Title
Three-dimensional hydraulic fracturing simulation in heterogeneous materials using Lattice Element Method

Author
Su, Zhenxiang

Publication Date
2022

Peer reviewed|Thesis/dissertation

Three-dimensional hydraulic fracturing simulation in heterogeneous materials using Lattice Element Method

by

Zhenxiang Su

A dissertation submitted in partial satisfaction of the

requirements for the degree of

Doctor of Philosophy

in

Civil and Environmental Engineering

and the Designated Emphasis

in

Computational and Data Science and Engineering

in the

Graduate Division

of the

University of California, Berkeley

Committee in charge:

Professor Kenichi Soga, Chair
Professor Nicholas Sitar
Professor Per-Olof Persson

Fall 2022

Three-dimensional hydraulic fracturing simulation in heterogeneous materials using Lattice Element Method

Abstract

Three-dimensional hydraulic fracturing simulation in heterogeneous materials using Lattice Element Method

by

Zhenxiang Su

Doctor of Philosophy in Civil and Environmental Engineering

and the Designated Emphasis in

Computational and Data Science and Engineering

University of California, Berkeley

Professor Kenichi Soga, Chair

Hydraulic fracturing is a technique for extracting unconventional resources by injecting high pressure fluid to crack the reservoir layer. This is a multi-scale and multi-physics problem that involves the behavior of rock matrix and injected fluid flow, as well as their interaction and resulting fracture propagation. The heterogeneities in the reservoir rocks make the fracture propagation a complex phenomenon and hydraulic fracturing an even more challenging problem.

In this study, a C++ based three dimensional Lattice Element Method (LEM) simulator is developed, which is capable of simulating both mechanical and fluid induced fracturing behavior in heterogeneous media. In this model, the mechanical response of solid is represented with a 3D lattice structure. The Timoshenko beam with embedded discontinuity is used as a solid lattice model, and exponential softening law is incorporated. The fracture surface is represented by the discontinuity generated in the lattice once it yields. While the fluid lattice network is a pipe flow system generated at fracture surfaces. This fluid lattice model follows Darcy's law and the principle of mass conservation, and interacts with solid lattice network through hydrostatic pressure. The 3D multi-physics problem is simplified into a network composed of 1D beam and pipe lattice, which can be simulated with a relatively low computational cost. The validations and comparisons between numerical and experimental results indicate that LEM is a promising tool for investigating the process of fracture development. Its simplicity makes it capable of simulating branching and complex interactions between multiple fractures, which is extremely difficult in continuum-based methods. A nonlinear softening law is implemented in the solid lattice model, which allows the simulation of the

failure of materials with different degrees of ductility. In addition, the potential application of LEM to early crack detection is explored.

The model is used to investigate the influence of rock heterogeneities on the hydraulic fracturing process, especially the fracture pattern. The results show that, all the factors, including in situ stress field, scale of weakness and statistical distribution of properties, affect the results to a different degree. The nodal arrangement is one of the main factors that affect potential fracture path. The interactions between hydraulic fractures and pre-existing natural joints are also investigated. The hydraulic fracture penetrates into a joint when the normal stress on the joint surface is too small to stop the joint from opening under fluid pressure. Whereas a fracture crossing is more likely to occur when there is little or no slippage between two sides of the joints. This implies a possible mechanism of fracture crossing in which the fracture reinitiates on the other side of the joint due to tensile stress generated by the friction applied on the joint surface.

To my parents, and grandparents

Contents

List of Figures

List of Tables

Acknowledgments

First and foremost, I am deeply grateful to my doctoral advisor, Professor Kenichi Soga, for giving me the opportunity to pursue my doctoral studies. His continuous support, patience and guidance throughout this study cannot be overstated. He is a great mentor not only in academics but also in life and personal development. He is always friendly and approachable, which influences my way of getting along with others. I particularly admire his passion for research. And I will never forget the integrity he taught me.

I would want to express my gratitude to Professor Krishna Kumar, who guided me with C++ coding and the LEM algorithm. Some preliminary works about this research should be credited to him. I could not start this research smoothly without his help. I also owe gratitude to Dr. John Kam Wing Wong. He developed the fluid model used in this research and patiently addressed my inquiries. I sincerely thank them for their patience and time.

I am grateful to the GeoSystems faculty at Berkeley, who taught me during my Master's year, with the background knowledge and skills needed to start the work of this research. They are, in no particular order, Professor Jonathan D. Bray, Professor Michael Riemer, Professor Robert Kayen and Professor Yoram N. Rubin. Recall the other courses I took in Berkeley, I particularly enjoyed the classes from Professor Sanjay Govindjee, Professor James Demmel, Professor Per-Olof Persson, Professor Panos Papadopoulos and Professor Jonathan Shewchuk. Their great instruction provided me with knowledge for my research, as well as fulfilling my curiosity. I greatly appreciate Professor Sanjay Govindjee, Professor Michael Riemer, Professor Jonathan D. Bray, Professor Per-Olof Persson and Professor Nicholas Sitar for their willingness to serve in my qualifying exam and thesis committee.

I want to express my special gratitude to Dr. Ezra Setiasabda, who is my senior in many ways. I enjoy the time when we share the same office. He gave me lots of advice in academics, life and personal development.

I would like to thank all my colleagues and friends at Berkeley. In particular, Dr. Xiang Sun for the constructive advice on the Finite Element Method and numerical simulations. Dr. Zorana Mijic for the help and advice in preparing for the qualifying exam. Dr. Bingyu Zhao, Dr. Peng Tan, Kecheng Chen, Bodhinanda Chandra, Dr. Renjie Wu, Dayu Apoji, Bofei Xu and Hanze Yao for the helpful advice and discussion about my academic and research problems. Special thanks to Dr. Peng Tan, Kecheng Chen, Yaobin Yang and Tianchen Xu for picking me up and hanging out together.

This research was supported in part by the Jane Lewis Fellowship, National Science Foundation, under "Modelling and Monitoring of Urban Underground Climate Change (MUC2)", and the Department of Energy, under "Community Resilience through Low-Temperature Geothermal Reservoir Thermal Energy Storage". I am grateful to these funding sources for making this research possible.

Finally, I would like to thank my family. They give me the freedom to decide my life and always love and support me. I would not be who I am today and make this accomplishment without them.

Chapter 1

Introduction

1.1 Background and Motivation

Shales are sedimentary rocks composed of silt or clay size mineral particles, and some of them may have high organic content. Under high subsurface pressure and temperature for an extended period of time, these organic materials may be transformed into oil and gas that are trapped in the rock, thereby becoming the so-called unconventional resources. As shown in Figure 1.1, the unconventional resources, including shale gas and tight oil, contribute to over 60 percent of the U.S. dry natural gas and crude oil production in 2018[3]. And the U.S. Energy Information Administration projects that the majority of U.S. dry natural gas production through 2050 will be from shale and tight gas resources[2]. This is due to the development of horizontal drilling and hydraulic fracturing techniques.

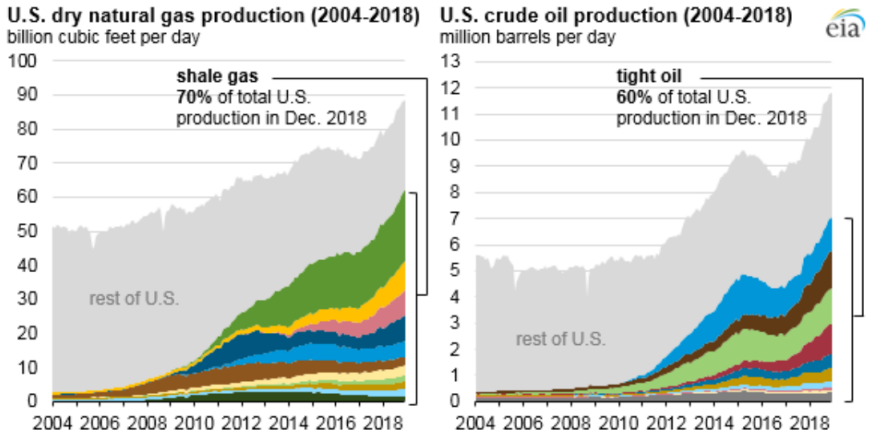

Figure 1.1: U.S. dry natural gas and crude oil production (2004-2018) from the U.S. Energy Information Administration[3]

Unlike the conventional resources such as coal or oil in porous rock, which are easily acces-

sible, extraction of unconventional resources usually requires hydraulic fracturing. Hydraulic fracturing has been in use since the 1950's to crack petroleum reservoir rocks by injecting high pressure fluid, in order to create pathway for the trapped oil and gas[39]. However, the process is not free of environmental concerns, such as a potential for contaminating potable water and causing induced seismicity. Therefore, it is important to understand this process, both for hydraulic fracturing design and environmental assessment.

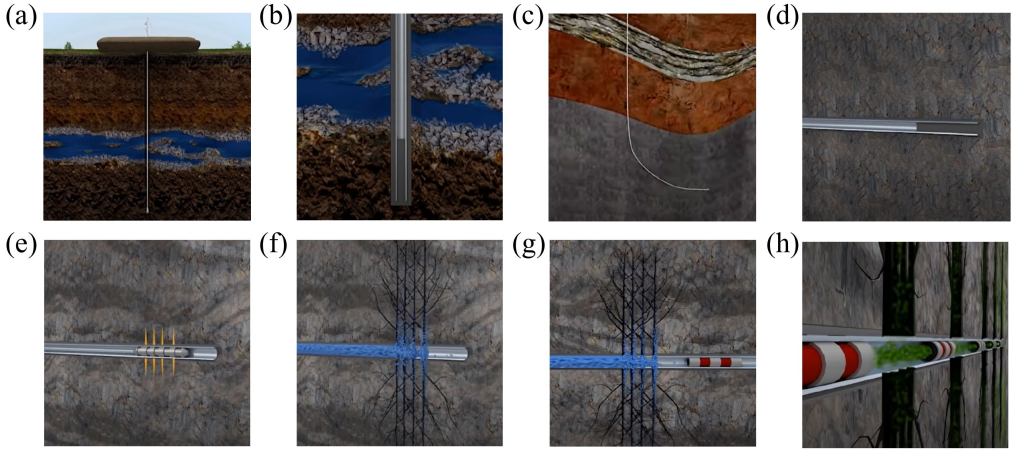

Figure 1.2: Simple procedure of hydraulic fracturing [25]
((a) vertical drilling; (b) applying casing; (c) turning; (d) horizontal drilling;
(e) perforation; (f) fluid injection; (g) isolation plug and fluid injection; (h) production)

Figure 1.2 depicts the process of hydraulic fracturing. First, a vertical borehole is drilled in stages, followed by the installation of steel and cement casings to support the borehole and prevent leakage. This will typically go down between 1 to 4 kilometers before reaching the reservoir rock layer, resulting in an in situ stress level in the range from 20 to 80 MPa [43]. Once it hits the target layer, it will gradually turn and start to drill and install casings horizontally in stages. This will usually run for several kilometers before the drilling is completed. A perforation gun is then used to create small holes through the casing into the target reservoir layer near the end of the borehole, followed by the injection of high pressure fluid to create fractures. The amount and rate of injected fluid vary site by site, from 400 to 4000 m^3 of fluid may be injected in one stimulation stage, and typically the injection rate ranges are approximately 10 m^3/min [51], which is relatively slow in such large scale and thus hydraulic fracturing could be treated as a static process. In most cases, water is used as the injected fluid and there is also sand as a proppant to keep the fractures open after pressure is released. An isolation plug is installed after this part of hydraulic fracturing is completed, perforation and hydraulic fracturing are then performed on the intact side. This process is repeated through the whole length of the horizontal well, after which the isolation plugs are removed for gas and oil production.

As a multi-scale and multi-physics problem, the hydraulic fracturing may be the most complicated among above mentioned processes, as it involves the behavior of rock matrix and injected fluid flow, as well as their interaction and resulting fracture propagation. The special features of rock materials, such as in-situ stress conditions, heterogeneous mechanical properties, different scales of layered, grain and flaw structures, make the fracture propagation in rock a complex phenomenon and make hydraulic fracturing an even more challenging problem. While these complex factors are hard to be reproduced in lab experiments, theoretical models of hydraulic fracturing have been developed since the 1960's for the design and investigation of its physical mechanisms, such as the early classic 2D models (PKN, KGD), and later on the pseudo-3D models (P3D, PL3D) [166]. These classic models are easy to apply in practice due to their simplicity, but on the other hand they may be oversimplified to represent the complex fully 3D fracture propagation and interactions in reality. This leads to the development of more sophisticated numerical models[93][22]. Simplification is still required as it is infeasible and unnecessary to model all the details, which results in the different applicability and limitations of various numerical methods depending on their corresponding assumptions. For example, the standard Finite Element Method usually requires very fine mesh near the crack or remeshing scheme and predefining the fracture path. As a discontinuum-based method, the Discrete Element Method can represent the fracture explicitly, but the high computational cost in contact detection limits its application in large scale problems. The Extended Finite Element Method may currently be one of the best methods to simulate a moderate number of cracks, but it has difficulties in modeling the complex fracture interactions, and the additional degrees of freedom to represent the cracks make it computationally intensive thus hindering its application in 3D scenarios.

The Lattice Element Method (LEM) is a discontinuous numerical model using a truss or frame structure to effectively simulate the mechanical response of a solid. This method represents the initiation and propagation of fractures by breaking corresponding yielding lattices, thus it could simulate random fracture development and the singularity related issues in continuum-based methods like FEM could be easily avoided[129]. Another advantage that makes LEM particularly suitable for simulating rock fracturing processes is that it is convenient to introduce different scales of weakness and heterogeneities into the model. For example, the size of the lattice could be selected in the scale of micro-crack or weakness of the rock, while larger pre-existing fractures could be represented by pre-breaking certain lattices. Weak regions, layered structures and statistical distribution of mechanical properties in rocks could be modeled by modifying the strength and stiffness of corresponding lattices.

Based on LEM, Wong proposed the Dual Lattice Model (DLM), which is a novel technique to simulate hydraulic fracturing[172]. As illustrated in Figure 1.3, the 3D solid material and fracture flow are represented by two fully coupled 3D lattice networks. The Rigid Body Spring Model (RBSM) is used as the lattice model of the solid network[12]. While the fluid lattice network is a pipe flow system generated at fracture surfaces. This fluid lattice model follows Darcy's law and the principle of mass conservation, and interacts with the solid lattice network through hydrostatic pressure. The 3D multi-physics problem is simplified into a network composed of 1D beam and pipe lattice, which can be simulated with a relatively

low computational cost so that it is able to deal with large scale problems, but still provides an opportunity to examine the complex interactions of tensile and shear fracture generations in heterogeneous 3D porous media.

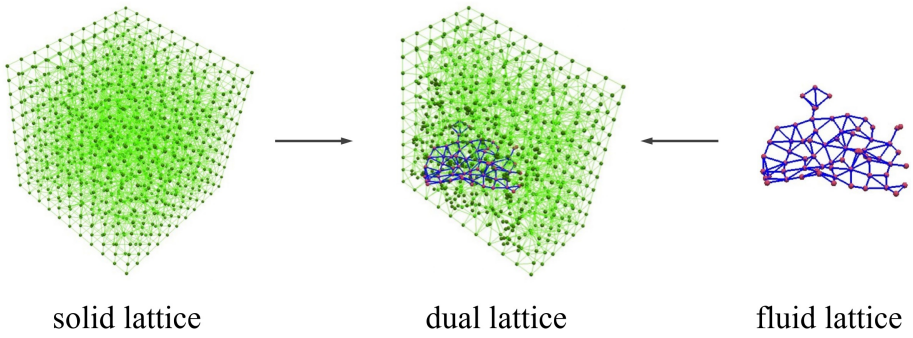

Figure 1.3: Schematic illustration of Dual Lattice Model [172]

A relatively simple lattice model and solution scheme are adopted in Wong's original work. The solid lattice is perfectly brittle, which means it initially behaves linearly elastically, and loses all the load bearing capacity once its strength is reached. The total displacements of nodes against the initial state following the secant modulus are solved every time step, which assumes that the model behaves elastically until the end of the reloading process and may potentially result in a different stress path from that obtained by an incremental scheme. The step size is limited as only a small number of lattices are allowed to break in each time step to preserve accuracy. This study is a continuation of Wong's work. A more robust solid lattice model proposed by Nikolic is adopted, which uses a linear elastic Timoshenko beam with embedded discontinuity as a single lattice[119]. In this model, the lattice can develop plastic strain in both axial and transversal directions once yielded. The post-peak strength of the lattice follows the exponential softening law and its decreasing rate could be adjusted by an input material parameter. This model is physically more realistic compared with the previous elastic-perfectly plastic model, and enables the original method to simulate materials with different degrees of ductility. And the corresponding implicit solution scheme computes incremental nodal displacements with respect to the last time step, which provides more accurate stress paths and eases the limit on step size.

The main objective of this research is to develop a C++ based LEM simulator that couples this solid lattice model with the pipe network approach for fluid flow. Due to the discrete nature of the LEM and the simplified representation of solid, it is expected that LEM could easily simulate complex fracture behavior, such as branching and interactions between multiple fractures, including crossing and arrest. Additionally, due to the nonlinear softening law implemented in the solid lattice model, it is anticipated that this model is capable of simulating the failure of materials with different degrees of ductility, which would be reflected in the loading curve and fracture pattern. The capability of this simulator to

achieve these expectations will be examined. In addition, with this efficient tool for hydraulic fracturing simulation, the influence of rock heterogeneities on the development of hydraulic fractures will be investigated. And the possible factors that affect the interactions between hydraulic fractures and pre-existing natural joints will also be explored.

1.2 Outline of the Thesis

The outline of this thesis is as follows.

Chapter 2 gives a literature review on fracture mechanics, various numerical methods developed to simulate rock fracture and hydraulic fracturing, with an emphasis on the LEM. Some experimental studies on various factors that affect the propagation of hydraulic fractures are also reviewed.

Chapter 3 first describes the method for generating a solid lattice network and its geometric features, then illustrates the solid and fluid lattice models and their coupling scheme. The implementation of this method is then discussed, including the structure of the code, the parallelization scheme for the matrix assembler and solver, and a comparison of different preconditioners for the iterative solver. And finally the performance is presented.

Chapter 4 presents the simulations conducted using the solid lattice model. The model is first verified with some typical problems, including an elastic cantilever beam, the Brazilian test and a sample with a pre-existing flaw. Four-point-bending tests on mortar beams with pre-existing notches under different loading conditions are simulated and compared with experimental results. The potential application of LEM to early crack detection is discussed. Uniaxial compression tests on cylindrical samples composed of lattices with various post-peak softening curves are conducted to demonstrate the capability of this model in simulating ductile materials.

Chapter 5 presents hydraulic fracturing simulations conducted with the solid fluid coupled lattice model. This coupled model is first verified elastically using the classic penny shaped crack problem. A series of fluid injection tests are performed to investigate the influence of rock heterogeneities on hydraulic fracture propagation. The interactions between hydraulic fracture and pre-existing joints are also simulated and various factors that affect the interactions, especially fracture crossing, are discussed.

Chapter 6 summarizes this study and gives some recommendations for potential future works.

Chapter 2

Literature Review

2.1 Fracture Mechanics

The fracture phenomena could be viewed from three different scales. Atomically, the fracture is the process that breaks the inter-atomic bonds; For materials with micro-structures, the fracture could happen around those features, such as the grains in a polycrystalline material, or the fibers in a composite; While macroscopically, which is also the standpoint of engineering applications, the material is generally assumed to be homogeneous continuum with some flaws. Micro-cracks nucleate and grow around these flaws and finally coalesce into macroscopic fractures[182]. Fracture mechanics is the subject that studies the propagation of cracks in continuum under a wide variety of loadings and environments, based on the theory of solid mechanics. Extensive research has been done in this area and there are a large number of publications that review or introduce this field with different depth[41][142][182].

The pioneering work in the field of fracture mechanics was done by Griffith[58]. Before the 1920's, it was already noticed that even for geometrically similar structures with the same homogeneous material and micro-structure, smaller size structures generally have larger strength, which is the so-called 'size effect'. And there were elasticity solutions that showed the stress singularity near a wedge apex. But the validity of the maximum stress criterion on predicting material failure was not questioned[41]. In his series of experiments on glass and metal, Griffith observed that the bulk strength of a solid is two orders of magnitude smaller than the theoretical strength to break the material's molecular bonds[58]. Griffith suggested that the microscopic flaws in the material contribute to this inconsistency and the size effect. And he proposed a new theory that interprets the propagation of fracture as the formation of new surfaces inside the solid, the surface energy required in this process is balanced by the work done from external loading and strain energy released from the material. With this assumption, Griffith derived the fracture stress for a plate containing an elliptical crack under uniaxial tension as,

$$\sigma = \sqrt{\frac{2\gamma E}{\pi a}} \tag{2.1}$$

for plane stress condition and,

$$\sigma = \sqrt{\frac{2\gamma E}{\pi(1-\nu^2)a}} \tag{2.2}$$

for plane strain condition. Where E is the Young's modulus, γ is the surface energy and a is the half length of the elliptical crack. This model was extended to a biaxial compression case by Griffith in 1924[57]. This criterion was applied to rock and extended to 3D later on by other researchers[117].

However, it was soon discovered that the energy required to fracture the material is orders of magnitude larger than the corresponding surface energy, especially for ductile materials. And experiments on metal showed that plastic deformation happens even on absolute brittle crack surfaces, which prevents the stress at the fracture tip from going to infinite[126]. Therefore, Griffith's work was largely ignored by the engineering community until the 1950's[41]. In the 1950's and early 1960's, Irwin and Orowan reinterpreted and extended Grifiith's classical work, which started the modern developments of fracture mechanics[142]. In addition to the surface energy, they independently proposed to add the work of plastic deformation around the crack tip as a dissipative energy into Griffith's energy balance relation[81][126]. The magnitude of plastic work varies largely depending on the material. In his later work, Irwin expressed the singular part of any component of the Cauchy stress tensor near the crack tip as,

$$\sigma_{ij} = \frac{K}{\sqrt{2\pi r}} f_{ij}(\theta) \tag{2.3}$$

Where r is the distance from any point to the crack tip, f_{ij} is a function of the polar angle θ. This shows that different stress tensors have the same dependence on coordinates and differ only by the constant factor K. Irwin named this coefficient as the stress intensity factor and designated the quantity K^2/E as the energy release rate G[79]. Irwin classified cracks into three types according to the directions of displacements of their lips in the vicinity of the

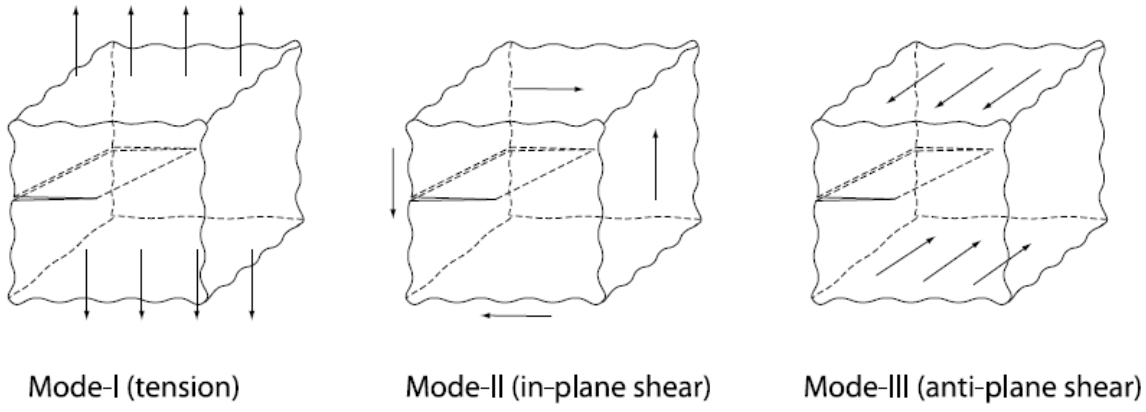

Figure 2.1: Modes of fracture[182]

crack tip as shown in Figure 2.1 and expressed the stress intensity factor for each mode as,

$$K_I = \lim_{r\to 0}\sqrt{2\pi r}\sigma_n \quad K_{II} = \lim_{r\to 0}\sqrt{2\pi r}\tau_n \quad K_{III} = \lim_{r\to 0}\sqrt{2\pi r}\tau_t \tag{2.4}$$

Where σ_n, τ_n, τ_t are the normal and two shear stresses that are normal and tangential to the crack front respectively[80]. The stress intensity factors are proportional to the load and attain their critical values at the time of crack initiation. With the assumption that the plastic zone only appears in the small vicinity of the crack for brittle fracture cases, Irwin applied the theory of elasticity and used the single parameter, fracture toughness, to characterize the fracture resistance of the material, which made the energy balance theory an effective design tool. Irwin and his colleagues made numerous contributions to the field of fracture mechanics. Their works are summarized in [180].

However, under large operation loads, most engineering materials show some inelastic behavior in the region whose size is comparable to the crack length. And the size of this plastic zone will generally increase with the crack length. This makes the small scale yielding assumption in Irwin's theory not hold[41]. Therefore, several more general theories were proposed to evaluate the fracture in elastic-plastic materials. One of the attempts is the crack growth resistance curve (R-Curve), which is a plot of the total energy dissipation rate (crack growth resistance) versus crack length. Together with another plot of energy release rate versus crack length for a given loading configuration as the driving force, the stability of a given crack could be determined[182]. Rice developed a way to compute the energy release rate using the path-independent line integral encircling the crack tip in two dimensional nonlinear elastic solid as,

$$J = \int_\Gamma (W dy - \mathbf{T}\cdot\frac{\partial \mathbf{u}}{\partial x} ds) \tag{2.5}$$

Where W is the strain energy density, $\mathbf{T}$ and $\mathbf{u}$ are traction and displacement vectors respectively, x, y are coordinate directions and ds is the increment along the path Γ that encircles the crack tip. This is the so-called J-Integral[141]. This integration could be straightforwardly computed and easily implemented in numerical methods. Thus J became attractive in analyzing asymptotic stress, characterizing crack-tip deformation and as a crack extension criterion.

Theoretical methods provide accurate solutions for relatively simple geometries and idealized material properties. The results could be implemented in numerical methods and also as benchmarks. They could be used to interpret experimental data as well. But in reality, the problems are usually much more complex, thus experiments and numerical simulations are also necessary for investigating the fracture behavior.

2.2 Numerical Simulation of Fracture and Hydraulic Fracturing

2.2.1 Rock Fracture

As rocks are generally heterogeneous and nonlinear materials, and the fracture process involves complicated interactions between cracks of different scales, analytical theories, such as linear elastic fracture mechanics, cannot satisfactorily describe this process. And although many laboratory and in situ experimental methods have been developed, they are frequently costly or infeasible in practice. Thus numerical method, which is able to simulate a variety of test scenarios at a much lower cost, is a necessary tool in investigating the fracture behavior in rocks. Especially with the rapid development of computational mechanics and computer technology in the last few decades, numerous robust numerical methods have been developed and applied in the field of rock mechanics. Some recent publications provide state-of-the-art reviews on the various computational methods for simulating the fracture in rocks[121][113][84]. This section will give an overview on some of the most popular methods.

The numerical techniques for fracture simulations could be classified into two categories, continuum and discontinuum based methods. Generally, continuum-based methods are suitable for modeling the global responses in a large rock system. But they usually have difficulties modeling the fragmentation process, detailed crack tip behavior and interactions between fractured rock blocks. Discontinuum-based methods model the crack initiation and propagation explicitly and are easy to simulate block movements. Thus while they are suitable for simulating fracture interactions, they may have difficulties modeling the pre-failure macroscopic response of rocks. There are also some attempts to develop hybrid methods, which bring together the advantages of both continuum and discontinuum-based methods.

Continuum-based Methods

The Finite Element Method (FEM) is one of the most popular numerical methods in engineering, including geomechanics, due to its robustness and flexibility for the treatment of material heterogeneity, plasticity and complex boundary conditions[85]. However, as a continuum-based method, FEM itself is not able to describe the fractures, which involve discontinuities and singularities. Various techniques have been proposed to facilitate the simulation of fracture processes in rocks by FEM. One type of approach is the smeared crack model, where cracks are smeared over a distinct area and constitutive calculations are performed independently at each integration point. The stress and material stiffness would be affected by the presence of cracks[169][34]. These models are easy to implement but not true localization limiters[84]. Within the framework of FEM, element erosion may be one of the simplest methods that incorporate the discrete nature of fractures. Instead of representing the topology of the crack, this method models fractures by deactivating failure elements. And the deactivation is done by either deleting those elements directly or setting

their stresses to zero[10][87]. However, this method is extremely sensitive to the mesh and not well suited for brittle fracture analysis[156]. In addition, it has difficulties modeling fragmentation and is computationally expensive[113]. The inter-element crack methods, which are usually combined with cohesive zone models, are generally considered a better alternative. In this method, constitutive relation is imposed between finite elements, and the crack propagation is modeled explicitly by separating corresponding elements along edges once the stress reaches cohesive strength[176][19]. Many problems have been investigated with this method, especially those involving dynamic fracture or complex fracture patterns. The major shortcoming of this method is that the cracks can only develop along the edges of elements, which results in overestimation of the fracture energy and strong mesh dependency[137]. Therefore, much finer mesh or special meshing schemes may be required to remedy this problem[156][130]. Another commonly used approach is the joint element, which is an indirect representation of discontinuities. The influence of fractures is modeled through constitutive laws of these elements[52]. Due to the continuum assumption, no real detachment occurs and only small displacement is allowed. Ill-conditioning of the global stiffness matrix would possibly arise as such elements have high aspect ratios. Various regularization techniques have been developed for FEM, and details can be found in [137].

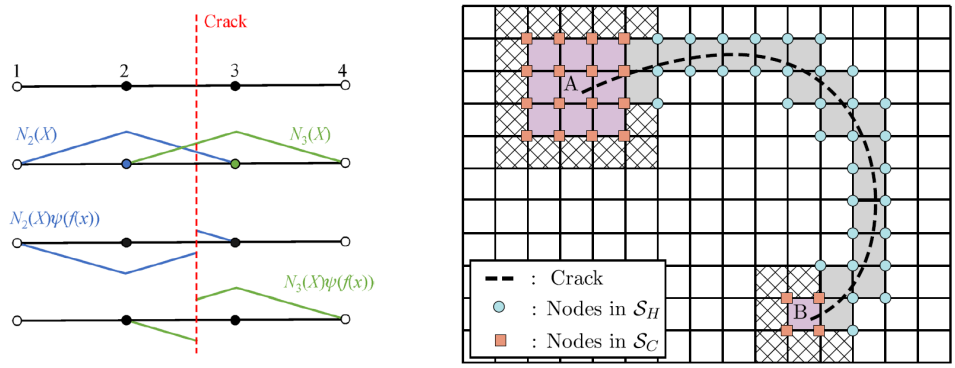

Figure 2.2: (a) Standard and enriched shape functions [84]; (b) An arbitrary crack (dashed line) in a structured XFEM mesh with step enriched (light gray) and tip enriched (purple) elements [9] (S_C: set of tip enriched nodes; S_H: set of step enriched nodes).

Generally, one common shortage of the standard FEM approaches in simulating the fracture process is the mesh dependency, such as requiring very fine mesh size, remeshing, or a predefined fracture path. The extended finite element method (XFEM) was developed to overcome these difficulties[8][116], with the idea of enrichment originating from the Partition of Unity[111]. In this method, the nodal displacement field is composed of both continuous and discontinuous parts. The continuous part is the standard FEM interpolation. While for the discontinuous part, additional degrees of freedom are introduced and multiplied with the

enriched shape functions, which are the products of standard shape functions and enrichment functions (Figure 2.2a). Different enrichment functions are used for the crack tip and the rest respectively (Figure 2.2b). The propagation of strong (cracks) and weak (material interfaces) discontinuities can thus be modeled by these enriched elements independently of the mesh. Detailed review about XFEM can be found in [44][9]. Although XFEM performs well in problems involving a few to a moderate number of cracks, one of its key challenges is modeling numerous cracks and complex interactions between fractures, such as branching and coalescence, due to the increasing complexity in the formulation and the absence of reliable crack branching criteria [137][156]. And its computational cost is relatively high, especially in three dimensional scenarios, which also hinders its application. Despite these drawbacks, XFEM may be one of the most powerful numerical techniques in simulating rock fracture process and has been implemented in various commercial software, such as ANSYS and ABAQUS. The Finite Element Method with embedded discontinuities (EFEM) is another extension of the standard FEM with a similar enrichment idea, but using an element enrichment scheme instead of the nodal enrichment[127][38]. The approximation of the displacement field is enriched with additional parameters that are inherent to the element. The jump in the displacement field can thus be captured within the single element. Both the EFEM and XFEM are capable of representing strong and weak discontinuities without the need for remeshing [75]. One major advantage of EFEM over XFEM is that the enrichment is completely embedded inside the element so that the additional unknowns can be condensed at the element level. Therefore, its implementation is more straightforward with existing FEM code[137]. However, there are some studies that indicate the piece-wise constant crack opening of EFEM generates some inaccuracies, such as stress locking, violation of traction continuity, and an inaccurate representation of the displacement field[86]. Some comparative studies between EFEM and XFEM suggest that EFEM has higher accuracy in some cases for coarse meshes and a reduced computational cost, but its accuracy may strongly depend on the fault orientation with respect to the element. While XFEM is independent of fault alignment and more promising in modeling fractured reservoirs[124][33].

The Finite Difference Method (FDM) is another widely used continuum-based method for solving ordinary or partial differential equations, which discretizes the domain into a grid of nodes and approximates the derivatives using finite difference computed over the grid with different schemes. It is a direct technique to solve problems without interpolation functions or iterative solutions. There are some researches that simulate rock fractures using FDM by incorporating micro-cracks into cells and checking propagation criteria based on linear elastic fracture mechanics[91][100]. A major disadvantage of standard FDM is that it requires a regular grid, which would cause difficulties in representing irregular geometries and heterogeneities, especially when simulating rock materials. But this has been overcome by more general FDM that is able to work on irregular meshes[134]. And eventually this led to the development of the Finite Volume Method (FVM), which discretizes the integral form of the PDEs with control volumes. FVM can be applied with an unstructured grid and varying material properties in different cells, which makes it as flexible as the FEM[85]. One can discretize the problem domain using a finite volume formulation and then solve it in

an FDM scheme [170][149]. However, despite the above improvements, it is still difficult for FDM/FVM to model fracture propagation appropriately due to the continuity requirement between the neighboring nodes. Although FVM is a popular method in rock engineering and has been used to study the mechanisms of fracturing processes, it is achieved by material failure at the nodes instead of creating strong discontinuities explicitly in the model[85]. Therefore, this method is usually not considered a robust technique for simulating rock fracture process[113].

Discontinuum-based Methods

In discontinuum-based methods, the discontinuities are incorporated explicitly. The Discrete Element Method (DEM) is one of the most popular methods in this category. DEM was first introduced by Cundall to model the rock system as rigid blocks[28], and then applied to model the granular material as particles by Cundall and Strack[31]. In this method, the domain of interest is represented by an assemblage of blocks or particles, which could be either rigid or deformable. The transnational and rotational displacements of each individual element follow the equations of motion. The contact between elements is modeled by appropriate constitutive laws and needs to be continuously updated. Therefore, the contact patterns keep changing and detachment could occur as the elements move. Thorough descriptions of DEM can be found in [27][67]. Due to the above features of DEM, fractures could be represented explicitly along the boundaries of elements. Thus this method has been extensively applied in the field of rock mechanics[85]. The Bonded Particle Model (BPM) is a particle-based DEM proposed for simulating rock fracturing process[136]. This model approximates rock materials by an agglomerate of cemented rigid discs (2D) or spheres (3D) with nonuniform size distribution, and the crack would be generated when the tensile or shear strength of the bond is reached. The key difficulties of DEM are the choice of contact laws and the calibration of material parameters. The procedures to uniquely determine the material parameters that capture a variety of macroscopic properties are still missing[84]. Efficient and accurate contact detection is another key challenge. The contact between polygonal/polyhedral blocks or irregular particles is complicated especially in 3D scenarios, which require high computational costs. Meanwhile, most contact detection algorithms are for convex bodies only. In addition, the explicit time integration scheme requires a relatively small time step, which further increases the computational cost of this method. A thorough discussion about these problems can be found in [30]. Despite these weaknesses, DEM has been employed successfully in the investigations of the rock fracturing process. A review of its wide variety of applications is given in [15].

The Discontinues Deformation Analysis (DDA) is an implicit type of DEM, which was first introduced by Shi and Goodman and has been developed rapidly in the field of rock mechanics since then[151][152]. Although DDA has a similar application area as explicit DEM, they are different theoretically. Instead, DDA shares some procedures with the FEM. This method uses standard FEM mesh generation, and calculates the motions and deformations of the blocks directly from the equations of equilibrium by minimizing the total potential

energy of the system[121]. Thus it is a displacement method instead of a force method like explicit DEM. But DDA also accounts for interactions between blocks along discontinuities, and thus shares similar challenges as DEM on the efficient and robust contact detection algorithms. As an implicit method, relatively larger time steps could be applied in DDA so that computational costs could be reduced. And due to its closed-form integration for the stiffness matrices of elements, it could be implemented based on current FEM code with all the advantageous features[85]. Therefore, DDA is an attractive method for solving rock mechanics problems. Its validation and wide range of applications are given in [107][150].

The Lattice Element Method (LEM) is another discontinuum-based method commonly adopted for fracture simulation. Its principle and application will be discussed in Section 2.3.

2.2.2 Hydraulic Fracturing

The hydraulic fracturing problems are more challenging than the rock fracture problems discussed above, as they involve the interactions and coupling of at least three basic processes: deformation of rock matrix under fluid pressure; fluid flow within the fracture; and fracture propagation[1]. Any one of these processes itself could be highly complicated. Therefore, they are usually simplified in some aspects in order to make the problem more tractable to simulate. For example, the intact rock matrix is typically assumed to behave linearly elastically; lubrication theory and Poiseuille's law are usually applied to model fluid flow; the fracture propagation criteria vary depending on the selected numerical method, but the Linear Elasticity Fracture Mechanics is often adopted[1][99]. Due to the different assumptions and simplifications, as well as the various combinations of solid and fluid schemes, numerous numerical approaches have been proposed for hydraulic fracturing simulations. State-of-the-art reviews on the various approaches can be found in [93][22]. As the fluid flows through the fractures, it typically has a lower dimension than the solid part and thus is normally a relatively simpler model. The selection of both fluid and fracture models usually depends on the solid model, which dominates the simulated behavior. Therefore, the numerical methods for hydraulic fracturing simulations usually share similar features and limitations as those mentioned in the last part that simulates rock fractures.

Continuum-based Methods

Among the continuum-based solid models, the standard FEM has also been used to simulate hydraulic fracturing. One type of approach utilizes the discrete fracture models, which represent the fractures explicitly in the mesh. For example, some early works combine FEM with classic hydraulic fracturing models. Specifically, FEM is used to model the rock deformation and fluid flows within the rock matrix, KGD type models are adopted to simulate the propagation of fractures, while the fluid flows inside fracture could be solved by either FEM or FDM following Poiseuille's law and the continuity equation[16][73]. The leakoff is usually handled by analytical models such as the Carter's model[69]. It is suggested that these pre-

liminary analytical 2D models should only be used in benchmark studies instead of practical design[177]. There are also some approaches that use more robust pseudo-3D fracture models such as P3D, which may be great pre-screening tools due to its simplicity, but the application is limited to planar fractures[177]. The cohesive zone models and zero-thickness joint element are also widely used in FEM to simulate hydraulic fracturing, which is capable of representing real-time crack growth and avoiding singularity problems[183]. Some relatively complicated scenarios, including the propagation of a fully 3D non-planar fracture, and the interactions between hydraulic and natural fractures, could also be simulated by these models[148][45]. However, similarly as in rock fracture simulations, these methods with discrete fracture models either require pre-defining the fracture path, or efficient remeshing schemes, which increases the computational cost and may induce accuracy problems due to the mapping between old and new elements[22]. Another type of approach with standard FEM is based on continuum damage mechanics, where the fractures are represented by the continuum elements with reduced strength and modulus, while the permeability is also related to the strain or stress state of corresponding elements[165][179]. Biot's consolidation theory could be used to solve the rock deformation and fluid flow inside the rock. Navier–Stokes equation and Darcy's law are also commonly adopted to describe fluid flow in the fracture and matrix in these methods. This type of approach is able to avoid mesh-related problems, and more advanced constitutive models, such as the Mohr-coulomb criterion, are easier to be implemented. However, the path and shape of hydraulic fractures cannot be precisely captured unless with very small elements. Thus adaptive mesh schemes are often used[99].

The damage-based smeared crack models are usually adopted in FDM types of methods for hydraulic fracturing simulations as well. In these methods, the rock deformation is computed with FDM, while the fluid flow inside the fracture also usually follows Poiseuille's law and the continuity equation, and could be solved by either FDM or FVM. Darcy's law is used to compute the leakoff and fluid transport inside the rock matrix. Different types of elements are used to represent the intact rock, fracture and crack tip. The transformation between different types for an element occurs when the corresponding failure criterion is achieved[192][138]. This type of approach usually shares similar limitations as the standard FEM with continuum damage crack models.

As a numerical method designed for simulating fracture propagation, XFEM is also popular in modeling hydraulic fracturing. In order to model the discontinuous pore pressure field across the media due to infiltrated fluid, different schemes have been proposed to enrich the finite element approximation of fluid pressure on nodes[114][42]. The fracture fluid is usually assumed to follow lubrication theory and should be coupled with rock deformation. Various coupling strategies are discussed in detail in [53], and a scheme that is capable of simulating viscous flow and fluid lag is developed. Besides LEFM, the cohesive zone models are also commonly adopted in XFEM to approximate the damage behavior at the crack tip[42]. The friction on fracture surfaces is incorporated in [90], and the corresponding model is used to investigate the interactions between hydraulic fracture and natural frictional joints. Simulating hydraulic fracturing using XFEM has also been implemented in FEM based commercial software. For example, non-planar fracture propagation from deviated well is simulated

using ABAQUS with Mohr-Coulomb plasticity model[162]. However, all of the above implementations are in 2D. Fully 3D implementation of XFEM is extremely difficult. Although there are some attempts, with strict assumptions, such as continuity of the fracture front and constant fluid pressure along fracture surfaces[62][61]. Compared with standard FEM, mesh-related problems are generally circumvented in XFEM due to the introduced discontinuous fields. But XFEM has the same limitations as FEM in simulating branching and complex fracture intersections. In addition, the computation of stress intensity factors is not as straightforward as that in FEM[22].

Discontinuum-based Methods

Different from the continuum-based methods, DEM simulates fracture propagation from a microscopic perspective. In order to model various hydromechanical behavior, different strategies to couple the solid DEM model with the fluid flow have been proposed. Detailed reviews can be found in [46][164]. An early DEM approach to simulate hydraulic fracturing utilizes the UDEC, which is a commercial package that implements 2D block based DEM[29][66]. The fluid flow along block edges is described by Darcy's law for contact and Poiseuille's law for joint. Fracture propagation is represented by the change of joint aperture. This approach is also extended to 3D with the package 3DEC[63]. The issue in these models is that the potential fracture path is biased as the fractures propagate along predefined block boundaries[177]. Another package, PFC2D, which implements 2D DEM with rigid disc elements, has also been used in hydraulic fracturing simulations[6]. Fractures are represented by voids and channels between particles, and the fluid flow within these spaces follows the Poiseuille's law and continuity equation. In addition, DEM is often coupled with the Computational Fluid Dynamics (CFD), which solves the Navier-Stokes equations typically by finite volume or finite element approximations. CFD calculates the flow field based on the particle positions and porosity given by DEM, and returns the drag forces back to DEM[71]. This model is used to investigate the interactions between Shale and proppants after hydraulic fracturing[36]. Traditional CFD-DEM has some fundamental limitations on the mesh size and computation cost, and may have convergence problems when the porosity changes rapidly[164]. The Lattice Boltzmann Method (LBM) is another numerical method often coupled with DEM for fluid simulations. Instead of solving the Navier–Stokes equations directly, LBM reproduces incompressible viscous flow by modeling the streaming and collision of fictive fluid particles. The interactions between fluid and DEM particles are computed based on the momentum exchange[64]. As an extension of LBM-DEM, LBM coupled with BPM has been used to simulate the hydraulic fracturing process[163]. Generally, LBM-DEM well captures the fluid particle interactions and enables multi-phase analysis, but is computationally inefficient and limited to low Reynolds number flows[164]. DEM has some notable advantages over continuum-based methods, such as no extra fracture criterion is required and no need to update the topology as fracture propagates. However, the computational cost increases rapidly with the number of particles, especially in 3D cases. Consequently, in large scale simulations, the particle size can only be much larger than the

rock grains, thus losing their physical meanings[22].

The Discrete Fracture Network (DFN) is a computational model that explicitly represents the geometrical properties and topological relationships between fracture sets, which could be generated through geological mapping, stochastic realization or geomechanical simulation[94]. As unconventional reservoirs are usually disjointed masses of rock, the interactions between fluid induced fractures and pre-existing natural joints greatly affect the hydraulic fracturing process[32]. Therefore, the DFN is commonly incorporated into the simulation to account for this effect. DFN could be integrated with various widely used numerical methods including FEM, FDM and DEM. A summary of these models is given in [94]. Example research that uses DFN to study hydraulic fracturing could be found in [112][140]. The application of DFN requires a significant amount of data to construct a reasonable model. In addition, the risk of over predicting the fracture network connectivity and treatment pressures should be noticed[177].

2.3 Lattice Element Method and Its Application in Fracture Simulation

The prototype of LEM was first proposed by Hrennikoff in 1941, which models the 2D elastic continuum with a truss framework[70]. This lattice analogy was utilized to investigate the fracture process of disordered media in the field of theoretical physics in the 1980's[193][68]. Due to the rapid development of computer technology, this method has gained increasing attention and continuously evolved. Various lattice type models have been proposed and also extended to 3D[102]. As a discontinuous numerical model, LEM represents a solid with a truss or frame structure, which is the assemblage of discrete 1D lattices. The initiation and propagation of fractures are modeled by breaking corresponding yielding lattices. The distinctions between different lattice models are mainly at the lattice level, including the regularity, type, constitutive relation and failure criterion.

Both regular and irregular lattice networks could be used in LEM. The regular network is a structured grid, commonly with triangular, square or hexagonal mesh. Heterogeneities could be introduced by varying lattice properties or removing certain lattices to create flaws. In general, the regular network is simple to generate and much easier to produce uniform strain throughout the sample. However, as the cracks can only occur at the lattice locations, such a network will usually generate over regular crack patterns, which is strongly biased and not realistic. Therefore, an irregular lattice network with disordered mesh is generally more favorable in fracture simulation. The unstructured grid automatically introduces geometric heterogeneity into the system, which greatly reduces the mesh dependence of the crack path. Various schemes have been proposed to generate the irregular lattice network, such as Voronoi construction[115], particle packing[4] and Delaunay triangulation[65].

Generally, there are two types of lattice models: the spring model and the beam model. In the early LEM models, the nodes are connected with normal springs, which only provide axial

resistance. This simple model results in a fixed Poisson's ratio for a 2D triangular structured network[133]. The shear and rotational springs were then introduced. By combining different types of springs and adjusting corresponding parameters, the elastic behavior of the lattice network varies and its Poisson's ratio could be adjusted in certain ranges. This approach is referred to as the Lattice Spring Model (LSM). Some typical examples include: the Kirkwood model with normal and rotational springs[128], the Distinct Lattice Spring Model (DLSM) with normal and multibody shear springs[187]. Another option named the Lattice Beam Model (LBM) uses beams as the lattice elements, which can resist axial and shear forces, as well as bending moments[146]. Nodes in these models have all the transitional and rotational degrees of freedom (3 DOFs in 2D and 6 DOFs in 3D). The classic Euler-Bernoulli beam and Timoshenko beam are commonly used as a lattice in LBM. Generally, LBM is an extension of LSM, while LSM keeps the intrinsic simplicity of the prototype. Thus both models have been widely used[129].

Various constitutive relations have been proposed for the lattice. The classic lattice model is linearly elastic and perfectly brittle, which would be completely removed from the network once yielded. Although this model would result in a very brittle macroscopic response of the structure, it is extensively used due to the principle of local simplicity in the lattice model[129]. In order to simulate more ductile responses, including local softening effects, more sophisticated models with different post-peak behavior are developed, such as the multilinear[89] and exponential[119] softening models. There are also models that incorporate nonlinear hardening behavior before the peak[118]. These models are able to simulate the degradation of material stiffness and redistribution of internal forces so that the progressive failure of the structure could be better captured. But they are more complex and the negative slope may lead to numerical instability and convergence problem. The selection of the constitutive model depends on the application. The lattice failure criteria are usually determined based on either critical stress or strain value. Yielding would be triggered once the threshold is reached. Various criteria combining the contributions of forces and bending moments have been proposed, especially for beam lattices[12][146][102]. These criteria are usually dependent on the mesh size, which leads to the recent development of fracture energy based criteria that solves the problem[185]. More detailed reviews about the lattice models can be found in [122][129].

LEM is an attractive numerical method for simulating material failure and fracturing behavior due to its advantageous features. It models complex 3D physical phenomena with a network composed of 1D lattices. Such simplification lowers the computational cost but still successfully represents the localized failure. The major challenges in continuum-based methods, such as the singularity related issues and simulating complex interactions between multiple cracks, are easily solved in LEM due to its discrete feature. In addition, material heterogeneity can be easily introduced by varying the lattice properties and orientations. LEM shares similar basic concepts with BPM but without the need for contact detection due to the fixed nodal connectivity in LEM. Consequently, LEM is much less computationally demanding than BPM or other DEM based methods, but its application is thus usually limited to small deformation scenarios. In addition, the lattice physically represents the bond

between solid grains, which ideally should have a similar size as the weak micro-structures in the material. Therefore, this method is not suitable for investigating the mechanisms related to smaller scales, such as the microscopic behavior at the crack tip. Despite these limitations, LEM has been extensively applied to simulate fracture propagation in various materials, including wood[159], bone[110], plain and reinforced concrete[89][103]. And because of its simplicity in incorporating heterogeneity, the application of LEM is especially common in the field of rock engineerings, such as fracture propagation in jointed rock mass[186], blasting[125] and earthquake rupture[97].

There are also a few studies that simulate fluid transport or hydraulic fracturing with lattice type models. In these methods, fluid is commonly represented using another set of lattices functions as pipes. Zhao and Khalili simulated the behavior of saturated soil using a lattice model that couples fluid flow with porous media. The soil skeleton is modeled with a lattice spring model, while pipelines connecting pore spaces represent the fluid network[188]. In a series of works by Grassl et al., a dual lattice model was developed to simulate fluid mass transport in quasi-brittle materials. The solid deformation is modeled by a lattice spring network generated from Voronoi tessellation. The fluid is assumed to flow along the boundaries of Voronoi cells and is represented by transport lattices. This model was also used to simulate hydraulic fracturing in a thick-walled cylinder under inner fluid pressure. But the solid and fluid models are not fully coupled in this approach, as the influence of solid deformation on transport properties is ignored[55][54][56]. A similar transport lattice was also proposed by Nikolic et al., but the solid and fluid lattice networks are coincident in their model. And the Timoshenko beam with an embedded discontinuity is used as a solid lattice. The failure of saturated poroplastic medium under drained compression test was simulated with this model[120]. Wong proposed a fully coupled dual lattice model for hydraulic fracturing simulation, which represents the 3D solid material and fracture flow by two fully coupled 3D lattice networks. The Rigid Body Spring Model is used as the solid lattice model, while the fluid flows along pipes connecting fracture surfaces, and follows Darcy's law and the principle of mass conservation[172]. Damjanac et al. developed a similar dual lattice model but originated from the idea of the Synthetic Rock Mass (SRM), which follows the formulation of BPM. The Smooth Joint Model (SJM) is used to represent the pre-existing natural joints[32]. This model was used to investigate the interactions between the hydraulic fractures and natural joints[189]. The linear elastic and perfectly brittle constitutive relation is used in both models.

2.4 Experimental Studies on Hydraulic Fracturing

Besides analytical and numerical studies on hydraulic fracturing, numerous field and laboratory experiments have been conducted to investigate the factors that influence the propagation of hydraulic fractures.

Field study is usually complex due to the unique mechanical properties and geologic conditions on site. Warpinski et al. examined hydraulic fracture behavior under various

conditions through a series of field experiments conducted in a tunnel complex at the U.S. DOE's Nevada Test Site, where realistic in situ medium and appropriate boundary conditions are provided[167][168]. These experiments demonstrate that the minimum principal stress is the predominant factor that affects hydraulic fracture containment, which limits the height of a fracture and confines it within a specific rock layer. Fractures are usually arrested at the formation interface due to the large gradient of the minimum principal stress[167]. The field hydraulic fractures are usually not planar, even in the most homogeneous formation. Multiple stranding, meandering and large scale surface roughness commonly occur especially in the vicinity of geologic discontinuities. Warpinski and Teufel observed that hydraulic fractures offset, divide and coalesce many times as they cross the joints. And they are usually terminated after a short distance across the fault (Figure 2.3) due to a change in stress field[168].

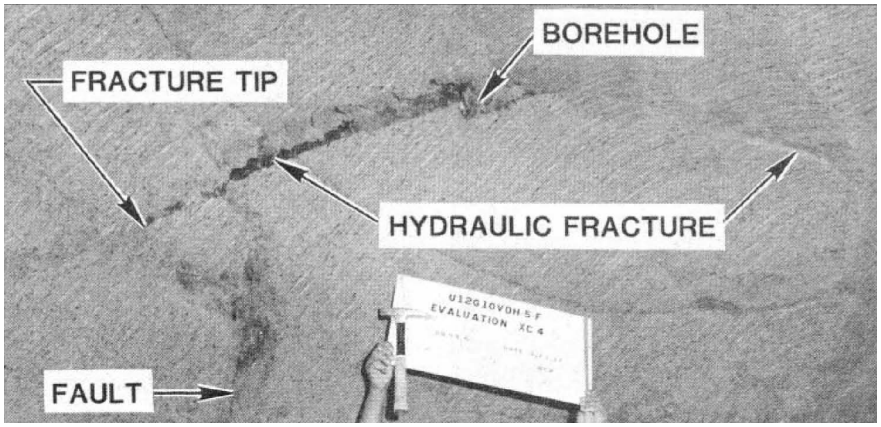

Figure 2.3: A colored-sand-propped hydraulic fracture terminates near a small displacement fault [168]

Laboratory study is generally much easier to conduct and control various conditions. Tan et al. conducted hydraulic fracturing experiments on shale specimens with well developed beddings[158]. The cubic samples were confined using a true triaxial machine before fluid was injected, and the maximum horizontal stress was applied along the wellbore direction. The results show that the propagation of hydraulic fracture is controlled by the in situ stress field and cemented strength of bedding planes. When the stress difference is large, hydraulic fracture develops perpendicular to the minimum stress direction and cuts through bedding planes as shown in Figure 2.4a. With the increment of minimum stress, hydraulic fractures start to have complex interactions with bedding planes and may even be arrested (Figure 2.4b, 2.4c). The experiments conducted by Zhou et al. on cement mortar samples show that the stress difference also affects the fracture propagation even in relatively homogeneous materials[190]. A dominant hydraulic fracture is formed in the case with a large horizontal stress difference. The resulting fracture pattern is increasingly random as the difference

reduces and eventually becomes net shaped when the difference is zero. El Rabaa found that the stress field changes as fracture develops, thus the direction of subsequently created fracture would be affected by the new stress field[40].

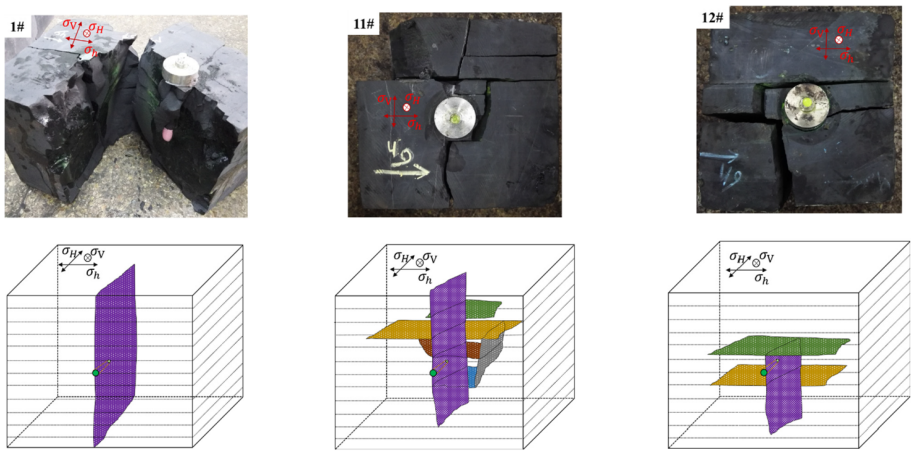

(a) σ_V:σ_h=3 (b) σ_V:σ_h=1.5 (c) σ_V:σ_h=1.2

Figure 2.4: Interactions between hydraulic fractures and bedding planes in some representative specimens[158]

Chen et al. showed that the path of hydraulic fracturing is affected by the fluid viscosity and rock heterogeneity through a series of tests conducted on Kurokami-jima granite specimens with different fluids (water, oil and CO_2)[23]. They found that a macroscopically straight fracture is tortuous and has many branches on the microscopic scale due to the interactions with rock heterogeneities such as pores, grains, pre-existing fissures and matrix with varying properties. Figure 2.5 depicts the interactions between fracture and mineral grains. They also indicate that fluid with a higher viscosity yields a smoother fracture pattern.

Blanton studied the interactions between hydraulic fracture and pre-existing joints through experiments performed on shale and gypsum[13]. He indicates that the differences in the in situ stress and the approaching angle between hydraulic fracture and joints are the key factors determining the type of interaction. The fractures are more likely to cross the joints under a high stress difference and a large approaching angle. Zhou et al. also conducted a series of experiments on cement mortar samples to investigate the fracture interactions[191][190]. Three types of interaction were identified, including crossing, arrest and penetration. They indicate that the occurrence of different interactions is dependent on the difference in the in situ stress, approaching angle and shear strength of the joints. They also related the injection pressure profile to the condition of the pre-existing joint network. More small natural joints on the fracture path would result in a higher frequency of fluctuation in the pressure profile.

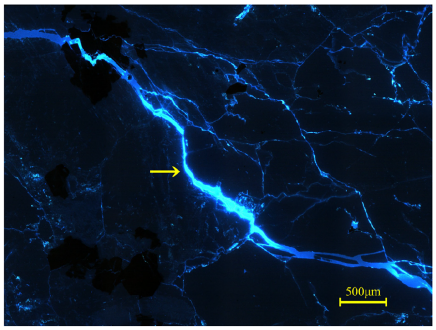

(a) Propagate along the grain boundaries

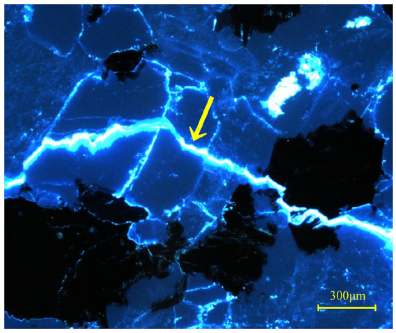

(b) Cut across the grain

Figure 2.5: Interactions between hydraulic fractures and mineral grains observed under ultraviolet light[23]

Chapter 3

LEM Theory and Implementation

3.1 Generation and Properties of the Solid Lattice Network

3.1.1 Generation of the Solid Lattice Network

In this study, in order to generate the solid lattice network, the domain that represents the specimen is discretized into cells by performing Voronoi tessellation on a set of disordered nodes distributed throughout the domain. Each Voronoi cell is a convex polyhedron that every point in this volume is closer to its corresponding node than any other nodes in the domain [123]. Non-intersecting lattice network can thus be generated by connecting neighboring nodes that share the same face of a Voronoi cell with a lattice. This node set would be used as computational nodes in the simulation. Physically, the Voronoi cell represents a grain of rock or similar structure with a corresponding scale of weakness. While the lattice represents the cohesive link between two grains [119]. A similar approach has been employed in other LEM research, such as [12][119][172].

In this study, considering that the grains of simulated materials (e.g., cement mortar, shale) are irregularly arranged but have relatively homogeneous sizes, and in order to have more control over the simulated scale of weakness, it is desired to use disordered node set, but have relatively small variations in the lattice length, which is also the distance between neighboring nodes. Therefore, the following scheme to generate the disordered node set is proposed, as shown in Figure 3.1a-d. The domain is defined by the bounding curves and surfaces. An open source mesh generator, GMSH [50], is then used to perform 3d unstructured tetrahedral mesh on the domain (Figure 3.1a-c). The curves are first discretized. The resulting 1D mesh is then used to mesh the surfaces, and similarly for the volume, both by Delaunay refinement [47]. The mesh size is controlled by an input factor, characteristic length, defined at the vertices of the domain. GMSH carries out the mesh generation procedure with both mesh quality and compliance with the prescribed mesh size taken into account. Therefore, the mesh sizes are not exactly equal to the characteristic length but

would be close. In this usage, a constant characteristic length is used throughout the domain, resulting in tetrahedrons with relatively uniform sizes. In case a different mesh size is required, such as local refinement around the potential crack path or simulating inclusion, it could also be achieved by dividing the domain and assigning different characteristic lengths to each subdomain. Finally, the centroids of these tetrahedral mesh elements are taken as the nodes of the lattice network, which are disordered, but with relatively homogeneous spacing (Figure 3.1d).

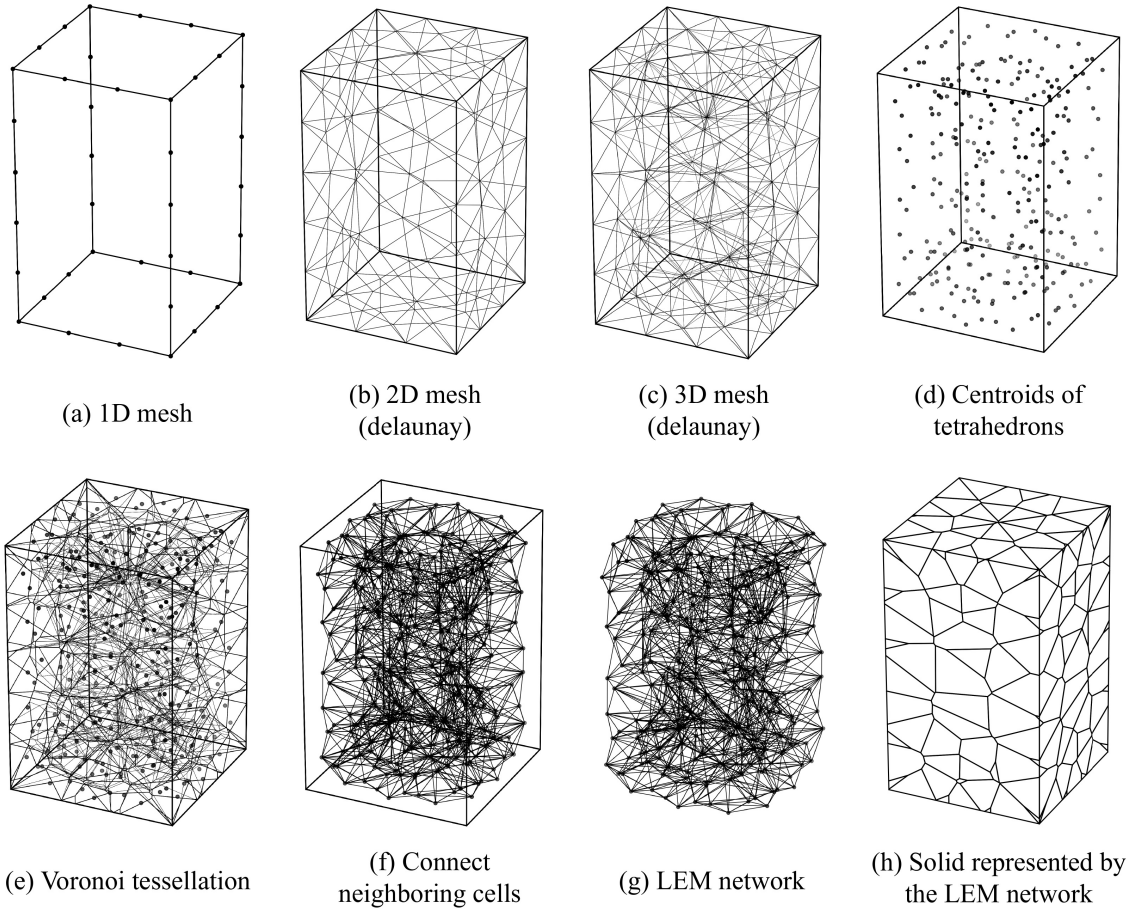

Figure 3.1: Process to generate lattice network in this study

Voronoi tessellation is then performed on this node set using the C++ library Voro++ [144] (Figure 3.1e). The neighboring nodes that share the same face are connected with a lattice (Figure 3.1f), which is also the dual Delaunay triangulation of this node set. The cross sectional area of a lattice is equal to the area of the corresponding face. These nodes and lattices form the solid lattice network that would be used in LEM simulation, and physically it represents a solid composed of bonded Voronoi cell shaped grains.

3.1.2 Geometrical Features of the Solid Lattice Network

In order to understand the geometrical features of the lattice network generated according to the above procedure, lattice models for a 10 × 10 × 20 m column were created with different mesh sizes by assigning different values of characteristic length. The size information about these models is summarized in Table 3.1, and example models are shown in Figure 3.2. This section will refer to the model by its normalized cell volume, which is the mean volume of its Voronoi cells divided by the total volume of the model.

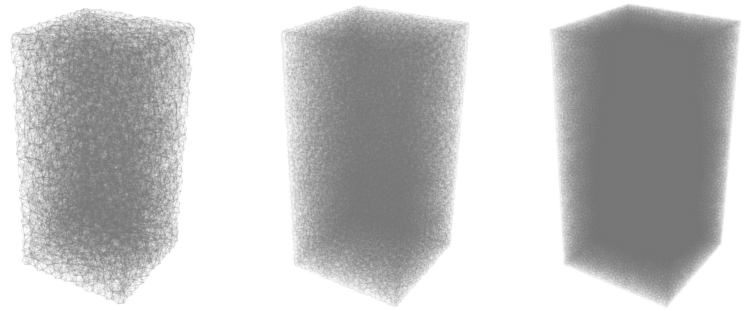

(a) v_n=1.01 × 10^{-4} (b) v_n=1.42 × 10^{-5} (c) v_n=1.87 × 10^{-6}

Figure 3.2: LEM column models with different normalized cell volumes

Characteristic length (m)	Number of nodes	Number of elements	Normalized cell volume v_n
1.00	9906	73768	1.01×10^{-4}
0.75	23793	180489	4.20×10^{-5}
0.65	34669	266204	2.88×10^{-5}
0.50	70411	548293	1.42×10^{-5}
0.35	198557	1570046	5.04×10^{-6}
0.25	534918	4274717	1.87×10^{-6}

Table 3.1: Summary of model sizes

For each model, several geometric properties of the cells and lattices were computed. Figure 3.3a depicts the probability density functions (PDF) of the cell sphericity, which is defined as,

$$\Psi = \frac{\pi^{\frac{1}{3}}(6V)^{\frac{2}{3}}}{A_s} \tag{3.1}$$

Where V and A_s are the volume and surface area of the Voronoi cell respectively. In order to facilitate comparisons, the cell volume, lattice cross sectional area A, and length L of

each model were normalized by dividing by their respective means. In addition, L was also normalized by the characteristic lengths. The resulting PDFs are shown in Figure 3.3b-e.

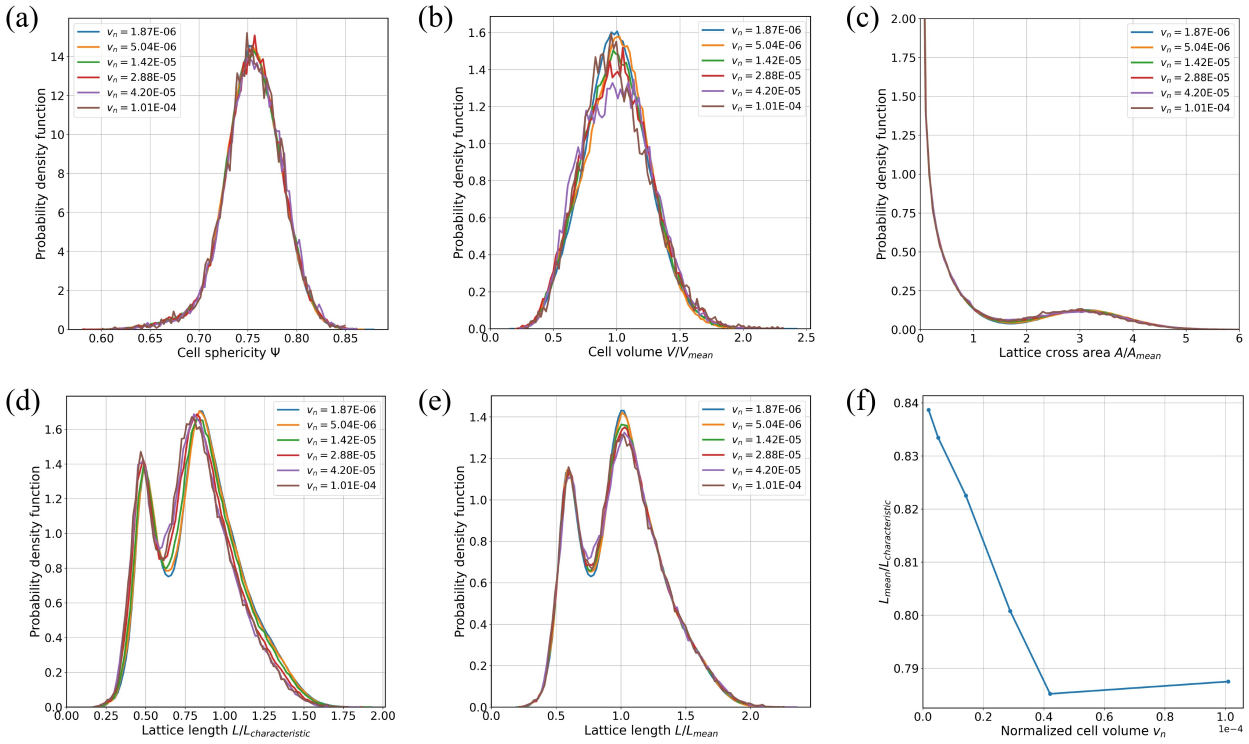

Figure 3.3: Geometrical features of lattice networks for models with different normalized cell volume v_n ((a) PDFs of cell sphericity Ψ; (b) PDFs of cell volume V/V_{mean}; (c) PDFs of lattice cross area A/A_{mean}; (d) PDFs of lattice length $L/L_{characteristic}$; (e) PDFs of lattice length L/L_{mean}; (f) $L_{mean}/L_{characteristic}$ vs v_n)

The PDFs of Ψ and A/A_{mean} nearly do not vary with the mesh size, while those of V/V_{mean} and L/L_{mean} become slightly more concentrated around the mean values as mesh refined. This indicates that the lattice network resulting from this discretization method has relatively homogeneous structural units throughout the domain. As the mesh is refined, the sizes of these structural units reduce while the patterns remain similar. This method generates more stable and consistent lattice networks, which gives more control over the results and unexpected randomness could be avoided. On the other hand, the heterogeneity due to lattice arrangement is reduced. The distribution of cell sphericity is concentrated around 0.75, indicating that the shape of resulting rock grains (Voronoi cells) is mostly in between tetrahedron ($\Psi = 0.671$) and cube ($\Psi = 0.806$). These grains have relatively uniform sizes, as the majority of the cell volumes are between 0.5 and 1.5 times their means. The PDFs of A/A_{mean} show that there are a large number of lattices that have very small cross

sectional areas, and the small concentration at around 3 indicates there are a certain number of lattices with relatively large cross sectional areas. While the PDFs of L/L_{mean} show that there are also two concentrations for lattice length. These two quantities are related, as depicted in Figure 3.4, which is the scatter plot of lattice cross sectional area versus length, taking all the lattices in the finest meshed model as an example. This plot demonstrates that there are two types of lattices in the network: those that are thick but short and those that are thin but long. Considering that the nodes of this network are the centroids of tetrahedrons generated by Delaunay refinement, the shape of cells resulting from Voronoi tessellation performed on this node set would still be similar to the tetrahedron (Figure 3.1h). It is actually a "rounded" tetrahedron: the four large triangular surfaces remain, but the parts around the four vertices are cut by multiple smaller faces. Similarly as the distance from the centroid of a tetrahedron to its faces and vertices, the short lattices connect neighboring nodes share the large face, while the long lattices connect neighboring nodes share the small face around the original vertex. Physically, such a long lattice represents the bond between two angular grains at the tip. While the majority of loads applied to the model would be sustained by the short lattices, which represent the bonds at large contact surfaces between grains. Therefore, these long lattices do not have much influence on the overall mechanical properties of the lattice network. Figure 3.3d shows the PDFs of lattice length normalized by corresponding characteristic length, where the peaks slightly shift toward characteristic length as the mesh is refined. Figure 3.3f also shows that, although the average lengths of lattices are smaller than the characteristic length, it becomes closer as the mesh is refined. For consistency and clarity, the characteristic length is used to describe the lattice size in the following part of this thesis. But it should be noted that this is not the average length of lattices, and the short lattices, which determine the mechanical properties of the lattice network, have lengths that are approximately half of this value.

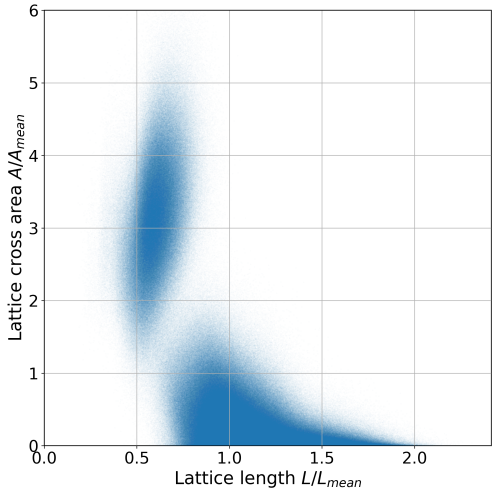

Figure 3.4: Lattice cross sectional area versus length ($v_n = 1.87 \times 10^{-6}$)

Figure 3.5 depicts the orientations of lattices in models with different mesh sizes. The numbers around the circumference and along the radius represent the polar and azimuthal angles respectively, of the lattice in spherical coordinates. The lattice is counted into the bin that represents its orientation and the bin counts are normalized by the mean value. The lattices show preference along 0° and 90° polar angle, and 90° azimuthal angle. And there is also a slight preference that orientates along 45° or 135° polar angle, and 45° azimuthal angle. This is due to the effect of boundary lattices that connect two cells at side faces (0° and 90° polar angle) or top and bottom faces (90° azimuthal angle). Note that the cell surface on the boundary could either be the large face, or the small face near its tip, thus resulting in these two preferred lattice orientations. The proportion of boundary lattices decreases as the mesh is refined, causing a reduction of this preference. Therefore, excluding the boundary lattices, the lattice orientation should be approximately isotropic.

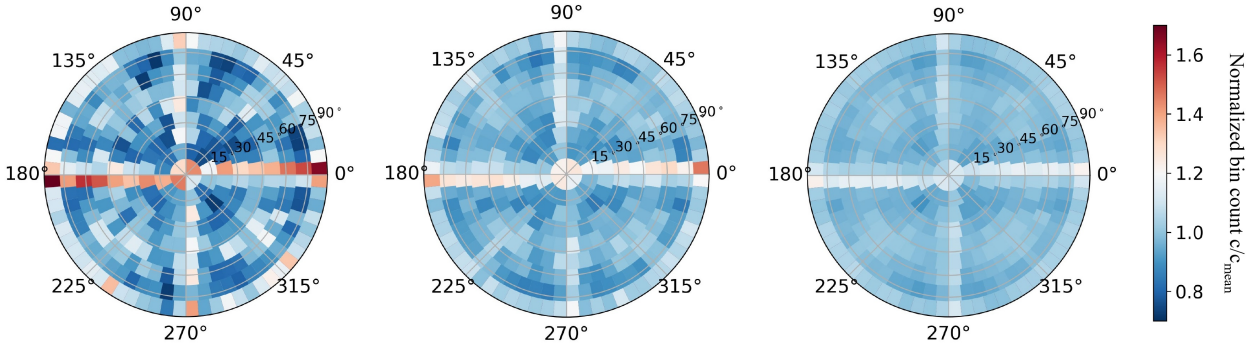

(a) v_n=1.01 × 10^{-4} (b) v_n=1.42 × 10^{-5} (c) v_n=1.87 × 10^{-6}

Figure 3.5: Lattice orientations for model with different mesh sizes

3.1.3 Embedding Rough Surface in the Network

The pre-defined rough surface within the model may be required in case of simulating the pre-existing fracture or weak plane with a certain degree of roughness. This can be achieved by utilizing the feature of GMSH, which allows the embedding of pre-defined mesh structures within the prescribed domain, and the generated mesh will conform to these embedded entities.

The rough surface is generated following the approach presented in [106] and with the script [105]. It starts from a smooth meshed surface, and roughness is introduced by applying deviation on every vertex of mesh elements along the normal direction of the surface. The deviation is treated as a stationary Gaussian stochastic process D, whose mean $< D >= 0$. In order to obtain a continuous pattern, D should be correlated in the tangential direction of the surface. Assume it has a Gaussian autocorrelation matrix R, that,

$$R =< DD^T >, \qquad R_{ij} = e^{-\frac{||t_i - t_j||^2}{2l^2}} \tag{3.2}$$

Where t_i and t_j are the coordinates of vertex i and j respectively, l is the prescribed correlation length. D could be constructed by applying transformation matrix L on Gaussian white noise W, where $< WW^T >= I$, by $D = LW$. There is,

$$R =< DD^T >=< LWW^TL^T >= L < WW^T > L^T = LL^T \tag{3.3}$$

Therefore, the matrix L could be computed from R by Cholesky decomposition. The deviation vector $\mathbf{d}$ that would be applied on the vertices, could be computed as,

$$\mathbf{d} = r_q L\mathbf{w} \tag{3.4}$$

Where $\mathbf{w}$ is a vector of random numbers following normal distribution, r_q is the root mean squared roughness, which is a scalar that controls the amplitude. In summary, the resulting degree of roughness is controlled by the two parameters, correlation length l in the tangential direction and root mean squared roughness r_q in the normal direction.

Once 3D mesh with this embedded rough surface is generated, the nodes above and below this surface would be recorded, and thus corresponding lattices that connect between these two node sets could be identified. The cross sections of these lattices form the rough surface in the LEM network. Although these two surfaces do not coincide, they should have similar roughness. Figure 3.6 shows the examples of surfaces (160×160 square) embedded in the GMSH model (top) and their resulting surface in the LEM network (bottom) with different l and r_q.

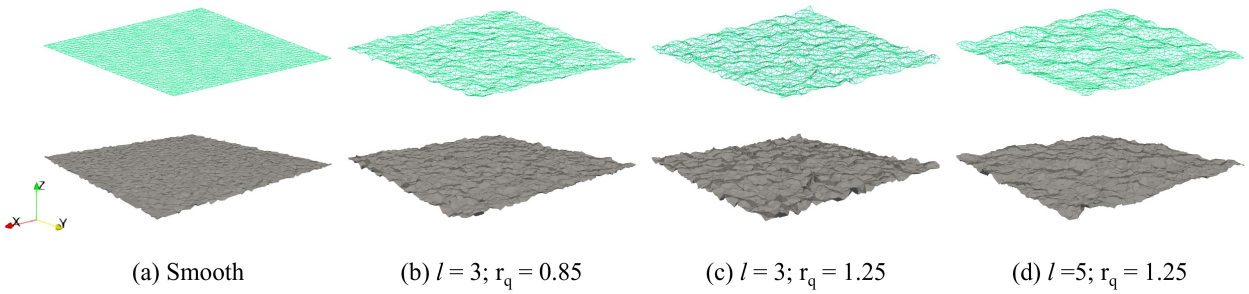

(a) Smooth (b) l = 3; r_q = 0.85 (c) l = 3; r_q = 1.25 (d) l =5; r_q = 1.25

Figure 3.6: Embedded surfaces with different roughness
(Top: GMSH model; Bottom: LEM network)

3.2 Solid Lattice Network Formulations and the Lattice Softening Model

The Timoshenko beam with an embedded discontinuity proposed by Nikolic is used as the solid lattice model. Following the derivation in [119][88].

3.2.1 Finite Element Approximation of the Lattice Model

Consider a 3D 2-node Timoshenko beam of length l_e in a local coordinate system (Figure 3.7a), the displacement vector $\boldsymbol{u}$ that has 6 degrees of freedom could be expressed as,

$$\boldsymbol{u}(x) = [u(x), v(x), w(x), \phi(x), \psi(x), \theta(x)]^T \tag{3.5}$$

Where x is the distance from starting node, u, v, w are the 3 transitional displacement (u is in the longitudinal direction while v and w are in the two transversal directions) and ϕ, ψ, θ are the 3 rotational displacement (ϕ is torsional while ψ and θ are bending). When the local coordinate axis is selected to pass through the shear centre of its cross-section, corresponding strain is,

$$\begin{aligned} \boldsymbol{\epsilon}(x) &= [\epsilon(x), \gamma_v(x), \gamma_w(x), \kappa_u(x), \kappa_v(x), \kappa_w(x)]^T \\ &= [\frac{du(x)}{dx}, \frac{dv(x)}{dx} - \theta(x), \frac{dw(x)}{dx} + \psi(x), \frac{d\phi(x)}{dx}, \frac{d\psi(x)}{dx}, \frac{d\theta(x)}{dx}]^T \end{aligned} \tag{3.6}$$

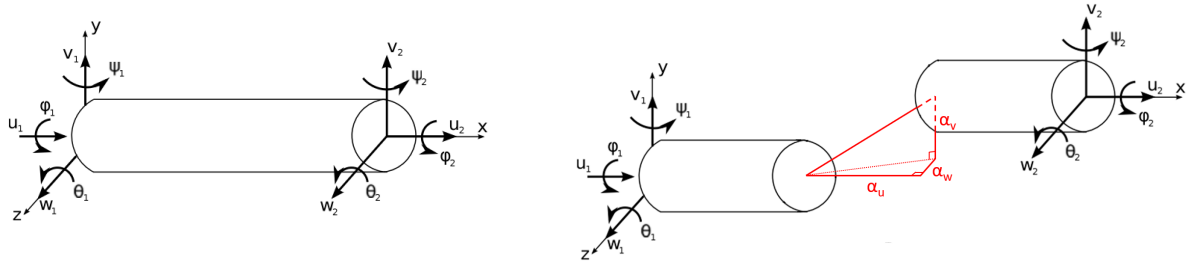

(a) Timoshenko beam [119] (b) Timoshenko beam with embedded discontinuity

Figure 3.7: Sketch of a 3D 2-node Timoshenko beam

In order to represent the tensile and shear failure modes of the lattice, discontinuity in displacement field is embedded at the middle of the beam, expressed as,

$$\boldsymbol{\alpha} = [\alpha_u, \alpha_v, \alpha_w, 0, 0, 0]^T \tag{3.7}$$

Its components represent the displacement jumps in the 3 transitional direction (Figure 3.7b). The displacement field becomes,

$$\begin{aligned} \boldsymbol{u}(x) &= \bar{\boldsymbol{u}}(x) + \boldsymbol{\alpha} H_{\frac{l_e}{2}}(x) \\ &= [\bar{u}(x), \bar{v}(x), \bar{w}(x), \bar{\phi}(x), \bar{\psi}(x), \bar{\theta}(x)]^T + [\alpha_u, \alpha_v, \alpha_w, 0, 0, 0] H_{\frac{l_e}{2}}(x) \end{aligned} \tag{3.8}$$

Where $\bar{\boldsymbol{u}}(x)$ represents the original displacement field, $H_{\frac{l_e}{2}}(x)$ is the Heaviside function, $H_{\frac{l_e}{2}}(x) = 0$ when $x \leq \frac{l_e}{2}$, $H_{\frac{l_e}{2}}(x) = 1$ when $x > \frac{l_e}{2}$. Using finite element approximation to express the displacement field along the 2-node element,

$$\boldsymbol{u}(x) = N_1 \boldsymbol{u_1} + N_2 \boldsymbol{u_2} + \boldsymbol{\alpha} H_{\frac{l_e}{2}}(x) \tag{3.9}$$

Where $\boldsymbol{u_1}$ and $\boldsymbol{u_2}$ are the nodal displacement vectors without discontinuity, $N_1 = 1 - \frac{x}{l_e}$ and $N_2 = \frac{x}{l_e}$ are the linear shape functions. This could be rearranged, and expressed in matrix form as,

$$\begin{aligned} \boldsymbol{u}(x) &= N_1\boldsymbol{u_1} + N_2(\boldsymbol{u_2} + \boldsymbol{\alpha}) + \boldsymbol{\alpha}(H_{\frac{l_e}{2}}(x) - N_2) \\ &= N_1\boldsymbol{u_{a1}} + N_2\boldsymbol{u_{a2}} + \boldsymbol{\alpha}(H_{\frac{l_e}{2}}(x) - N_2) \\ &= \boldsymbol{N}\boldsymbol{u_a} + \boldsymbol{M}\boldsymbol{\alpha} \end{aligned} \tag{3.10}$$

Where $\boldsymbol{u_{a1}} = \boldsymbol{u_1}$ and $\boldsymbol{u_{a2}} = \boldsymbol{u_2} + \boldsymbol{\alpha}$ are the total nodal displacement vectors, $\boldsymbol{u_a} = [\boldsymbol{u_{a1}}^T, \boldsymbol{u_{a2}}^T]^T$. The two shape function matrices are,

$$\boldsymbol{N} = \begin{bmatrix} N_1 & 0 & 0 & 0 & 0 & 0 & N_2 & 0 & 0 & 0 & 0 & 0 \\ 0 & N_1 & 0 & 0 & 0 & 0 & 0 & N_2 & 0 & 0 & 0 & 0 \\ 0 & 0 & N_1 & 0 & 0 & 0 & 0 & 0 & N_2 & 0 & 0 & 0 \\ 0 & 0 & 0 & N_1 & 0 & 0 & 0 & 0 & 0 & N_2 & 0 & 0 \\ 0 & 0 & 0 & 0 & N_1 & 0 & 0 & 0 & 0 & 0 & N_2 & 0 \\ 0 & 0 & 0 & 0 & 0 & N_1 & 0 & 0 & 0 & 0 & 0 & N_2 \end{bmatrix} \tag{3.11}$$

$$\boldsymbol{M} = \begin{bmatrix} M & 0 & 0 & 0 & 0 & 0 \\ 0 & M & 0 & 0 & 0 & 0 \\ 0 & 0 & M & 0 & 0 & 0 \\ 0 & 0 & 0 & 0 & 0 & 0 \\ 0 & 0 & 0 & 0 & 0 & 0 \\ 0 & 0 & 0 & 0 & 0 & 0 \end{bmatrix} \tag{3.12}$$

Where $M = H_{\frac{l_e}{2}}(x) - \frac{x}{l_e}$. In this formulation, $\boldsymbol{N}\boldsymbol{u_a}$ is the regular part of the displacement field with standard shape functions, while $\boldsymbol{M}\boldsymbol{\alpha}$ is the localized part requires treatment within the framework of incompatible modes [76]. The strain expression could be obtained by taking derivative, as,

$$\boldsymbol{\epsilon}(x) = \boldsymbol{B}\boldsymbol{u_a} + \boldsymbol{G}\boldsymbol{\alpha} + \delta_{\frac{l_e}{2}}\boldsymbol{\alpha} = \boldsymbol{B}\boldsymbol{u_a} + \boldsymbol{G}\boldsymbol{\alpha} + \boldsymbol{\delta}_{\frac{l_e}{2}}\boldsymbol{\alpha} \tag{3.13}$$

The two shape function matrices are,

$$\boldsymbol{B} = \begin{bmatrix} B_1 & 0 & 0 & 0 & 0 & 0 & B_2 & 0 & 0 & 0 & 0 & 0 \\ 0 & B_1 & 0 & 0 & 0 & -N_1 & 0 & B_2 & 0 & 0 & 0 & -N_2 \\ 0 & 0 & B_1 & 0 & N_1 & 0 & 0 & 0 & B_2 & 0 & N_2 & 0 \\ 0 & 0 & 0 & B_1 & 0 & 0 & 0 & 0 & 0 & B_2 & 0 & 0 \\ 0 & 0 & 0 & 0 & B_1 & 0 & 0 & 0 & 0 & 0 & B_2 & 0 \\ 0 & 0 & 0 & 0 & 0 & B_1 & 0 & 0 & 0 & 0 & 0 & B_2 \end{bmatrix} \tag{3.14}$$

$$\boldsymbol{G} = \begin{bmatrix} G & 0 & 0 & 0 & 0 & 0 \\ 0 & G & 0 & 0 & 0 & 0 \\ 0 & 0 & G & 0 & 0 & 0 \\ 0 & 0 & 0 & 0 & 0 & 0 \\ 0 & 0 & 0 & 0 & 0 & 0 \\ 0 & 0 & 0 & 0 & 0 & 0 \end{bmatrix} \tag{3.15}$$

Where $B_1 = G = \frac{dN_1}{dx} = -\frac{1}{l_e}$, $B_2 = \frac{dN_2}{dx} = \frac{1}{l_e}$. And $\delta_{\frac{l_e}{2}}$ is the Dirac function, which is derivative of the Heaviside function $H_{\frac{l_e}{2}}(x)$. Let $\boldsymbol{\delta}_{\frac{l_e}{2}}$ be the matrix that,

$$\boldsymbol{\delta}_{\frac{l_e}{2}} = \begin{bmatrix} \delta_{\frac{l_e}{2}} & 0 & 0 & 0 & 0 & 0 \\ 0 & \delta_{\frac{l_e}{2}} & 0 & 0 & 0 & 0 \\ 0 & 0 & \delta_{\frac{l_e}{2}} & 0 & 0 & 0 \\ 0 & 0 & 0 & 0 & 0 & 0 \\ 0 & 0 & 0 & 0 & 0 & 0 \\ 0 & 0 & 0 & 0 & 0 & 0 \end{bmatrix} \tag{3.16}$$

Noted that shear locking will occur when using a single element to represent a Timoshenko beam due to its linear nature [77]. This effect is mitigated by setting N_1 and N_2 in matrix $\boldsymbol{B}$ equal to $\frac{1}{2}$ in implementation [18].

According to the virtual work principle at the element level, the work done by internal force through a virtual strain $\delta\boldsymbol{\epsilon}$ could be expressed as,

$$W^{int,(e)} = \int_0^{l_e} (\delta\boldsymbol{\epsilon})^T \boldsymbol{\sigma} dx = \int_0^{l_e} (\boldsymbol{B}\delta\boldsymbol{u_a})^T \boldsymbol{\sigma} dx + \int_0^{l_e} (\delta\boldsymbol{\alpha})^T (\boldsymbol{G} + \boldsymbol{\delta}_{\frac{l_e}{2}})^T \boldsymbol{\sigma} dx \tag{3.17}$$

Where $\boldsymbol{\sigma} = \boldsymbol{C}(\boldsymbol{B}\boldsymbol{u_a} + \boldsymbol{G}\boldsymbol{\alpha})$ is the force in the element, $\boldsymbol{C}$ is the material matrix of Timoshenko beam,

$$\boldsymbol{C} = \begin{bmatrix} EA & 0 & 0 & 0 & 0 & 0 \\ 0 & GA\kappa & 0 & 0 & 0 & 0 \\ 0 & 0 & GA\kappa & 0 & 0 & 0 \\ 0 & 0 & 0 & GI_{pol} & 0 & 0 \\ 0 & 0 & 0 & 0 & EI_{11} & 0 \\ 0 & 0 & 0 & 0 & 0 & EI_{22} \end{bmatrix} \tag{3.18}$$

Where E, G, A, I_{pol}, I_{11}, I_{22} are the elastic modulus, shear modulus, cross sectional area, second polar moment of area and two moments of inertia of the beam respectively. κ is the shear coefficient of the Timoshenko beam. For simplicity, it is assumed that the beam has a circular cross section with the same area as the corresponding face of the Voronoi cell. Therefore, the shear coefficient is related to Poisson's ratio v, as [26],

$$\kappa = \frac{6(1+v)}{7+6v} \tag{3.19}$$

The first part on the right hand side of Equation 3.17 is the standard part of internal virtual work, the standard internal force vector is thus obtained, and it should be balanced by the external force applied on this element, that is,

$$\boldsymbol{f}^{int,(e)} = \int_0^{l_e} \boldsymbol{B}^T \boldsymbol{\sigma} dx = \boldsymbol{f}^{ext,(e)} \tag{3.20}$$

While the second part on the right hand side of Equation 3.17 is the enhanced part, which gives the element residual at discontinuity, that needs to be enforced to 0,

$$\boldsymbol{h}^{(e)} = \int_0^{l_e} (\boldsymbol{G}^T + \boldsymbol{\delta}_{\frac{l_e}{2}})\boldsymbol{\sigma} dx = \int_0^{l_e} \boldsymbol{G}^T \boldsymbol{\sigma} dx + \boldsymbol{t} = \boldsymbol{0} \tag{3.21}$$

Here $\boldsymbol{t} = \int_0^{l_e} \boldsymbol{\delta}_{\frac{l_e}{2}} \boldsymbol{\sigma} dx$ is the traction vector at discontinuity, thus,

$$\boldsymbol{t} = -\int_0^{l_e} \boldsymbol{G}^T \boldsymbol{\sigma} dx \tag{3.22}$$

Equation 3.20 and 3.21 are the two equations need to be satisfied to solve for the variables $\boldsymbol{u_a}$ and $\boldsymbol{\alpha}$.

3.2.2 The Constitutive Model and Failure Criteria of the Lattice

In each simulation step, the embedded discontinuity, or crack opening, $\boldsymbol{\alpha}$, is solved locally in each lattice with loading condition and constitutive model of the lattice. The softening model applies in each of the three transitional directions separately and has the same form. Thus in the following part of this section, subscript i is used to represent any of the three directions u, v, w. Initially, the lattice is intact ($\alpha_i = 0$) and behaves linearly elastically. When applied stress reaches its strength, the lattice enters the post-peak softening stage where the crack starts to open and its load capacity reduces.

Following the derivation in [74] to describe this behavior. The traction when intact lattice yields in tension ($i = u$) is,

$$t_{y,i} = A\sigma_{y,i} \tag{3.23}$$

Taking into account the contribution of friction and cohesion to shear resistance, when ($i = v, w$),

$$t_{y,i} = A\sigma_{y,i} + Ntan\phi + c \tag{3.24}$$

Where $\sigma_{y,i}$ is the tensile or shear strength in the corresponding direction, and A is the cross sectional area. ϕ and c are the friction angle and cohesion as lattice properties and N is compression force applied to the lattice. Define the parameter ξ_i, representing the accumulated absolute value of discontinuity increment, and the softening variable $q_i(\xi_i)$ is the reduction in load capacity. Therefore in the softening stage, the lattice's effective load capacity, or traction at yield, becomes,

$$t_{y,i}^{eff}(\xi_i) = t_{y,i} - q_i(\xi_i) \tag{3.25}$$

Note that the load capacity is reduced as ξ_i increasing, thus this model is not suitable to describe cyclic behavior. Define $G_{f,i}$ as the work done by applied traction during the crack opening process, it could be computed as,

$$G_{f,i} = \int_0^{\infty} t_{y,i}^{eff}(\xi_i) d\xi_i \tag{3.26}$$

Various softening laws could be assumed to relate $t_{y,i}^{eff}(\xi_i)$ with $t_{y,i}$ so that to obtain different post-peak behavior. As in [119], exponential softening law is used in this study, assuming that,

$$t_{y,i}^{eff}(\xi_i) = t_{y,i}e^{-c_{y,i}\xi_i} \tag{3.27}$$

Where $c_{y,i}$ is a constant coefficient. Thus the work done is,

$$G_{f,i} = \int_0^\infty t_{y,i}^{eff}(\xi_i)d\xi_i = \int_0^\infty t_{y,i}e^{-c_{y,i}\xi_i}d\xi_i = -\frac{t_{y,i}}{c_{y,i}}e^{-c_{y,i}\xi_i}|_0^\infty = \frac{t_{y,i}}{c_{y,i}} \tag{3.28}$$

Expressing $c_{y,i}$ with the work done,

$$c_{y,i} = \frac{t_{y,i}}{G_{f,i}} \tag{3.29}$$

Combining Equation 3.25, 3.27 and 3.29, the softening variable in this case is,

$$q_i(\xi_i) = t_{y,i} - t_{y,i}^{eff}(\xi_i) = t_{y,i} - t_{y,i}e^{-\frac{t_{y,i}}{G_{f,i}}\xi_i} = A\sigma_{y,i}(1 - e^{-\frac{A\sigma_{y,i}}{G_{f,i}}\xi_i}) \tag{3.30}$$

To make the softening behavior independent of lattice size, define the fracture energy as a material property, $G'_{f,i} = \frac{G_{f,i}}{A}$. Thus the softening variable becomes,

$$q_i(\xi_i) = A\sigma_{y,i}(1 - e^{-\frac{\sigma_{y,i}}{G'_{f,i}}\xi_i}) \tag{3.31}$$

Define the failure function as,

$$\Phi_i = |t_i| - t_{y,i}^{eff}(\xi_i) = t_i - (t_{y,i} - q_i(\xi_i)) \tag{3.32}$$

Where t_i is the applied traction in a simulation step. The lattice yields and crack opening changes in this step if $\Phi_i > 0$.

The element-wise procedure to compute crack opening is illustrated below. For time step $k+1$, with the updated nodal displacement from global lattice network $\boldsymbol{u_a}^{(k+1)}$, and crack opening related parameters form last time step $\boldsymbol{\alpha}^{(k)}$, $\boldsymbol{\xi}^{(k)}$, the trial traction vector could be computed as,

$$\boldsymbol{t}^{trial,(k+1)} = -\int_0^{l_e} \boldsymbol{G}^T\boldsymbol{C}(\boldsymbol{B}\boldsymbol{u_a}^{(k+1)} + \boldsymbol{G}\boldsymbol{\alpha}^{(k)})dx \tag{3.33}$$

Let $\boldsymbol{B}_i^T$ be the row of matrix $\boldsymbol{B}$, and C_i be the diagonal element of matrix $\boldsymbol{C}$, corresponding to direction i, the trial traction in this direction is a function of nodal displacement and crack opening,

$$t_i^{trial,(k+1)}(\boldsymbol{u_a}^{(k+1)}, \alpha_i^{(k)}) = -\int_0^{l_e} GC_i(\boldsymbol{B}_i^T\boldsymbol{u_a}^{(k+1)} + G\alpha_i^{(k)})dx \tag{3.34}$$

The failure function with this trial traction is,

$$\Phi^{trial,(k+1)} = |t_i^{trial,(k+1)}(\boldsymbol{u_a}^{(k+1)}, \alpha_i^{(k)})| - (t_{y,i} - q_i(\xi_i^{(k)})) \tag{3.35}$$

If $\Phi^{trial,(k+1)} \leq 0$, the loading on this lattice in this direction is less than its effective capacity, thus the lattice behaves elastically and the crack opening remain the same as last step,

$$\alpha_i^{(k+1)} = \alpha_i^{(k)}, \qquad \xi_i^{(k+1)} = \xi_i^{(k)} \tag{3.36}$$

While if $\Phi^{trial,(k+1)} > 0$ plastic deformation needs to happen at the discontinuity to release the loading and keep it right within the capacity. Thus the updated failure function is zero,

$$\Phi_u^{trial,(k+1)} = |t_i^{trial,(k+1)}(\boldsymbol{u_a}^{(k+1)}, \alpha_i^{(k+1)})| - (t_{y,i} - q_i(\xi_i^{(k+1)})) = 0 \tag{3.37}$$

Subtracting Equation 3.35 from Equation 3.37,

$$\begin{aligned}
\Phi_u^{trial,(k+1)} =& \Phi^{trial,(k+1)} + |t_i^{trial,(k+1)}(\boldsymbol{u_a}^{(k+1)}, \alpha_i^{(k+1)})| - |t_i^{trial,(k+1)}(\boldsymbol{u_a}^{(k+1)}, \alpha_i^{(k)})| \\
&+ q_i(\xi_i^{(k+1)}) - q_i(\xi_i^{(k)}) \\
=& \Phi^{trial,(k+1)} + \left| - \int_0^{l_e} GC_i(\boldsymbol{B}_i^T \boldsymbol{u_a}^{(k+1)} + G\alpha_i^{(k+1)})dx \right| \\
&- \left| - \int_0^{l_e} GC_i(\boldsymbol{B}_i^T \boldsymbol{u_a}^{(k+1)} + G\alpha_i^{(k)})dx \right| + q_i(\xi_i^{(k+1)}) - q_i(\xi_i^{(k)})
\end{aligned} \tag{3.38}$$

Noted that the sign of $t_i^{trial,(k+1)}$ is determined by the part $\boldsymbol{B}_i^T \boldsymbol{u_a}^{(k+1)}$, so does that of $G\alpha_i^{(k)}$ after being taken out from absolute value,

$$\begin{aligned}
\Phi_u^{trial,(k+1)} =& \Phi^{trial,(k+1)} - sign(t_i^{trial,(k+1)}) \int_0^{l_e} GC_i G\alpha_i^{(k+1)} dx \\
&+ sign(t_i^{trial,(k+1)}) \int_0^{l_e} GC_i G\alpha_i^{(k)} dx + q_i(\xi_i^{(k+1)}) - q_i(\xi_i^{(k)}) \\
=& \Phi^{trial,(k+1)} + sign(t_i^{trial,(k+1)}) GC_i(\alpha_i^{(k+1)} - \alpha_i^{(k)}) + q_i(\xi_i^{(k+1)}) - q_i(\xi_i^{(k)})
\end{aligned} \tag{3.39}$$

Let $sign(t_i^{trial,(k+1)})(\alpha_i^{(k+1)} - \alpha_i^{(k)}) = \lambda$, the update rule could be written as,

$$\alpha_i^{(k+1)} = \alpha_i^{(k)} + sign(t_i^{trial,(k+1)})\lambda, \qquad \xi_i^{(k+1)} = \xi_i^{(k)} + \lambda \tag{3.40}$$

And λ could be obtained by solving the nonlinear equation with respect to λ,

$$\Phi_u^{trial,(k+1)} = \Phi^{trial,(k+1)} + GC_i\lambda + q_i(\xi_i^{(k)} + \lambda) - q_i(\xi_i^{(k)}) = 0 \tag{3.41}$$

This is solved by the Newton-Raphson method in the implementation, and the updated crack opening under a given nodal displacement could be obtained.

Considering that the structure would be damaged by yielding, although the plastic deformation is computed in each of the three transitional directions separately, this model assumes that when the lattice is in tension, yielding would be triggered in all directions once the traction in any one direction reaches its capacity. This is achieved by updating the

load capacities in the otherwise non-yielding directions to the current traction values. For example, if the intact lattice starts to yield in u direction in step $k+1$, for $i = v, w$, the updated load capacity and strength are,

$$t_{yu,i} = A\sigma_{yu,i} = t_i^{(k+1)} \tag{3.42}$$

Noted that the softening variable q_i is related to the ratio $\frac{\sigma_{y,i}}{G'_{f,i}}$, the fracture energy $G'_{f,i}$ needs to be updated correspondingly in order to maintain the same normalized shape of the reaction curve. Because yielding occurs at lower traction, the corresponding strain decreases as well, and the work done should be related to the ratio by second order,

$$G'_{fu,i} = G'_{f,i}\left(\frac{t_{yu,i}}{t_{y,i}}\right)^2 \tag{3.43}$$

Figure 3.8 shows a 2D example of displacement controlled tests. The same tensile displacement increment was applied in each case, while the shear displacement increment varied. Yielding in the shear direction is triggered as the tensile reaction reaches the peak (0.4 kN). They have different updated shear capacities but the same shape as normalized softening curves.

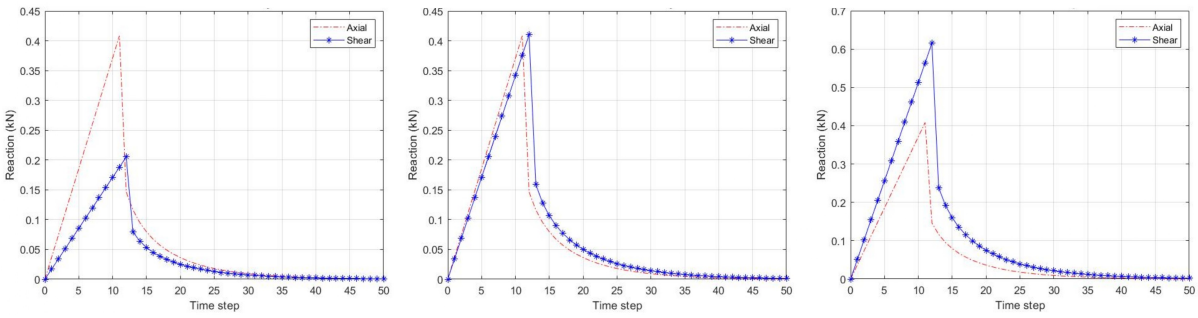

Figure 3.8: Tensile and shear reaction curves for single lattice with different shear displacement increment

3.2.3 Solving Procedures

The nodal displacement is obtained by solving the two equations (Equation 3.20 and 3.21) with variables $\boldsymbol{u_a}$ and $\boldsymbol{\alpha}$. If the crack opening does not change, the lattice behaves linearly in this step and the enhanced part of internal work vanishes. Therefore, in this case, only Equation 3.20 governs and it is linear. The change of nodal displacement could be obtained by solving,

$$\left[\boldsymbol{K}\right]\left(\Delta\boldsymbol{u_a}\right) = \left(\boldsymbol{f}^{ext} - \boldsymbol{f}^{int}\right) \tag{3.44}$$

Where

$$\boldsymbol{K} = \frac{\partial(\boldsymbol{f}^{int} - \boldsymbol{f}^{ext})}{\partial \boldsymbol{u_a}} = \int_0^{l_e} \boldsymbol{B}^T\boldsymbol{C}\boldsymbol{B}dx \tag{3.45}$$

If the lattice yields and crack opening changes, Equation 3.20 and 3.21 should be solved together, which is a nonlinear system and the Newton-Raphson method is used.

$$\begin{bmatrix} \boldsymbol{K} & \boldsymbol{F} \\ \boldsymbol{F}^T & \boldsymbol{H} \end{bmatrix} \begin{pmatrix} \Delta \boldsymbol{u_a} \\ \Delta \boldsymbol{\alpha} \end{pmatrix} = \begin{pmatrix} \boldsymbol{f}^{ext} - \boldsymbol{f}^{int} \\ \boldsymbol{0} \end{pmatrix} \tag{3.46}$$

Where

$$\boldsymbol{F} = \frac{\partial(\boldsymbol{f}^{int} - \boldsymbol{f}^{ext})}{\partial \boldsymbol{\alpha}} = \int_0^{l_e} \boldsymbol{B}^T \boldsymbol{C} \boldsymbol{G} dx \tag{3.47}$$

$$\boldsymbol{H} = \frac{\partial \boldsymbol{h}}{\partial \boldsymbol{\alpha}} = \int_0^{l_e} \boldsymbol{G}^T \boldsymbol{C} \boldsymbol{G} dx + \boldsymbol{K_s} \tag{3.48}$$

$\boldsymbol{K_s}$ is the matrix of consistent tangent stiffness components for the discontinuity [153], whose elements are zeros except the first three diagonal elements, as,

$$K_{s,i} = \frac{dq_i(\xi_i)}{d\xi_i} = \frac{A\sigma_{y,i}^2 \xi_i}{G'_{f,i}} e^{-\frac{\sigma_{y,i}}{G'_{f,i}}\xi_i} \tag{3.49}$$

The complete form of matrix $\boldsymbol{K}$, $\boldsymbol{F}$ and $\boldsymbol{H}$ are shown in Appendix A. To eliminate $\Delta\boldsymbol{\alpha}$ from the equation, from the second row of Equation 3.46,

$$\Delta \boldsymbol{\alpha} = -\boldsymbol{H}^{-1} \boldsymbol{F}^T \Delta \boldsymbol{u_a} \tag{3.50}$$

Substitute into the first row,

$$\boldsymbol{K} \Delta \boldsymbol{u_a} - \boldsymbol{F} \boldsymbol{H}^{-1} \boldsymbol{F}^T \Delta \boldsymbol{u_a} = \boldsymbol{f}^{ext} - \boldsymbol{f}^{int} \tag{3.51}$$

Define the matrix $\hat{\boldsymbol{K}} = \boldsymbol{K} - \boldsymbol{F}\boldsymbol{H}^{-1}\boldsymbol{F}^T$, Equation 3.46 becomes,

$$\left[\hat{\boldsymbol{K}}\right] \left(\Delta \boldsymbol{u_a}\right) = \left(\boldsymbol{f}^{ext} - \boldsymbol{f}^{int}\right) \tag{3.52}$$

In case the lattice is yielded only in some of the directions, the local stiffness matrix is assembled by corresponding rows of $\boldsymbol{K}$ and $\hat{\boldsymbol{K}}$. Finally, the local matrix system (Equation 3.44 or 3.52) is assembled into a global matrix system for solving.

Figure 3.9 shows the key steps in the solving process for this solid lattice network problem. The part in the dashed box takes the status of the solid lattice network and computes corresponding fluid forces under injection as part of force boundary conditions, which is used only in hydraulic fracturing problems and will be discussed in the next section. Details of this dashed box are shown below in Figure 3.12.

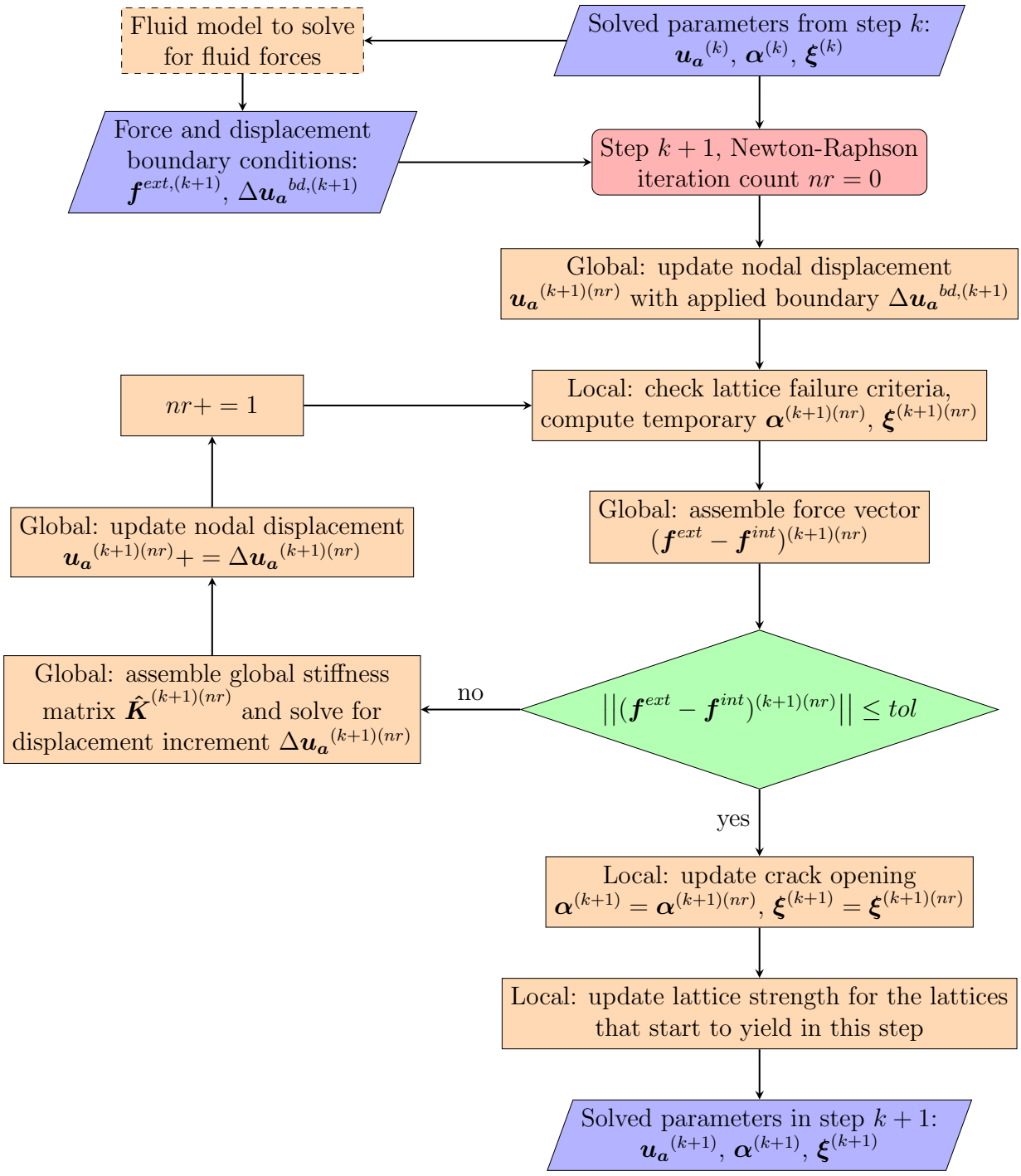

Figure 3.9: Solving process for solid lattice network in a time step

3.2.4 Nodal Stress Calculation

In every time step after the internal forces between lattices are obtained, the nodal stress is computed by summing the contributions from all the lattices connected to this node [20],

$$\sigma_{ij}^{n} = \frac{1}{2V_{cell}} \Sigma_{e=1}^{N_{ne}} F_i^e l_j^e \tag{3.53}$$

Where i and j represents the global coordinate directions (x, y, z), N_{ne} is the number of elements connecting to this node. F_i^e is the i-component of the force contributed from lattice e, l_j^e is the j-component of the vector joining the centroids of these two cells and V_{cell} is the volume of this cell.

3.3 The Fluid Model and Coupling Scheme

In order to simulate the hydraulic fracturing process, the fluid lattice model proposed by Wong is used in this study, which utilizes pipe flow networks to approximate the injected fluid flowing through fractures within rock mass [172]. This fluid lattice model follows Darcy's law and the principle of mass conservation, and interacts with the solid lattice network through hydrostatic pressure. In each simulation step with the prescribed injection rate and resulting fracture geometry from the previous step, pressure distribution across the fluid network could be computed, which is then converted to forces acting on solid nodes.

3.3.1 Generation and Formulation of the Fluid Lattice Network

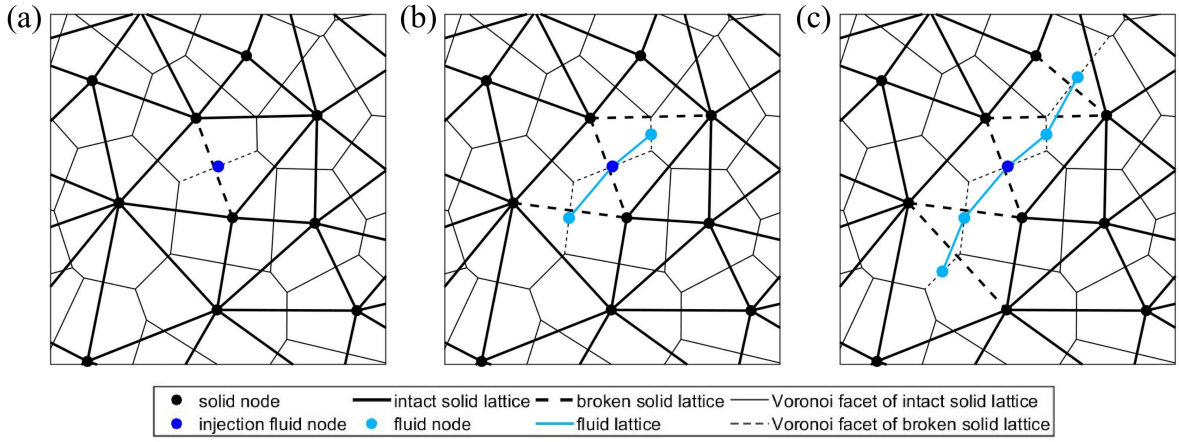

Figure 3.10: 2D example of fluid lattice network development

Figure 3.10 illustrates the idea of this model with a simple 2D example that shows the developing process of a fluid lattice network (fracture fluid) within a solid lattice network

(rock). Before the injection test begins, a solid lattice is broken to create the pre-existing fracture, represented by the Voronoi facet of the corresponding lattice. An injection fluid node is then placed at the centroid of this facet (Figure 3.10a). As fluid is injected, pressure will be generated within this fractured space and acts normally to the facet. In the lattice network, this pressure is converted to nodal forces acting on the solid nodes of this broken lattice in the longitudinal direction, which is also perpendicular to the facet. As pressure continues building up, adjacent solid lattices break and fracture propagates to corresponding facets. Because these facets are now connected to the one with the injection node, fluid nodes are placed on their centroids to represent the possible arrival of fracture fluid. Adjacent fluid nodes on facets that shares the same edge are connected with a fluid lattice (pipe) (Figure 3.10b). It should be noted that although a single pipe is straight visually for simplicity, the actual fluid path is assumed to follow the Voronoi facets. After pressure distribution across the updated fluid network is obtained, each fluid node is iterated to compute the nodal force applied on its corresponding solid lattice. Each solid node could possibly be subjected to multiple forces from different fluid nodes and their effects are superposed. These forces act as a boundary condition for the next time step and make the fracture further develops (Figure 3.10c).

In more complex scenarios with various isolated pre-existing fractures and multiple injection nodes distributed across the system, breadth first searches starting from each injection node should be conducted to identify all the fracture surfaces, and possibly other injection nodes, connecting to it. The fluid networks are then created in each group of fractures that contains at least one injection node and pressure distribution is computed within each fluid network separately. Therefore, the solid network is subjected to multiple isolated force boundary conditions in such cases. Regrouping of fracture should be performed each time step due to their development, closure or coalescence, and the fluid networks are updated correspondingly. As the fractures and corresponding fluid networks are 2D surfaces within the 3D solid lattice network, the fluid model is much smaller than the solid model. Consequently, the computational time within the fluid level is negligible compared with the solid part. But this model requires iterations between fluid and solid phases each time step to achieve convergence, which will be discussed in the following part. Therefore, simulating fluid injection problems is much more time consuming than solid problems.

Figure 3.11a shows a 3D example of elements in the system. The Voronoi cells representing rock grains are connected by solid lattices and fluid nodes are inserted at the centroids of facets corresponding to broken lattices (dash line). The fluid is assumed to fill up the fractured space, thus for a fluid node i, its storage S_i is equal to the volume of the space,

$$S_i = A_i \delta_i \tag{3.54}$$

Where A_i is the area of the facet and δ_i is the aperture, which are respectively also the cross sectional area and longitudinal crack opening of the corresponding solid lattice. Assume the fluid in the system flows between adjacent facets and follows Darcy's law, thus the volumetric

flow rate from fluid node i to j could be expressed as,

$$q_{ij} = \frac{k_{ij} a_{ij}}{\mu} \left(\frac{dp}{dl} \right)_{ij} \tag{3.55}$$

Where μ is the dynamic viscosity of the fluid, k_{ij} and a_{ij} are the permeability and cross sectional area of fractured space in between these two nodes, and $\left(\frac{dp}{dl}\right)_{ij}$ is the pressure gradient. For a laminar flow of incompressible fluid that follows Darcy's law and passes through fractures idealized as parallel planar plates, the permeability is given by the cubic law [171],

$$k = \frac{\delta^2 \rho g}{12} \tag{3.56}$$

Where ρ is the density of fluid and g is the gravitational acceleration.

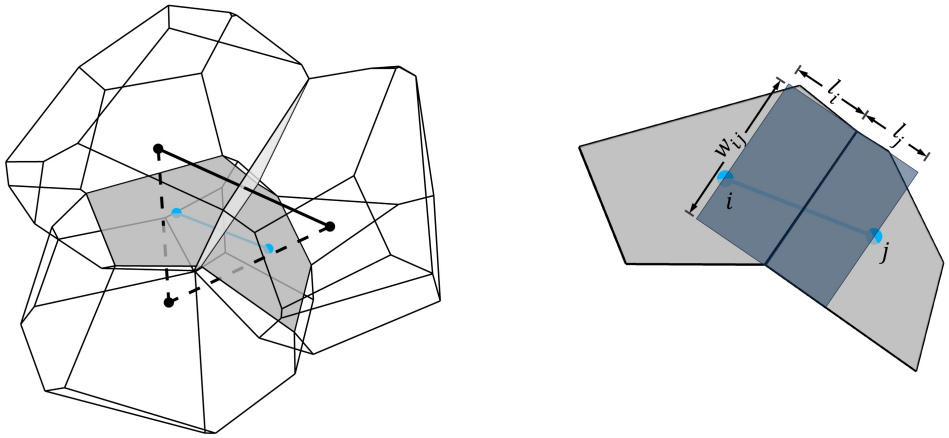

(a) 3D lattice system (b) Equivalent fluid channels

Figure 3.11: 3D lattice system and equivalent fluid channels

For simplicity, assume the fluid flows through the rectangular equivalent channels that connect the two fluid nodes and align perpendicular to the common edge, as shown in Figure 3.11b. Each channel represents the flow path between these two nodes within the corresponding facet, and has a width equal to the length of the common edge, w_{ij}, and a length equal to the distance from the corresponding fluid node to the edge, l_i and l_j. For an incompressible fluid, the flow rate is the same for the two channels. Therefore, the Darcy's law could be written for each segment,

$$q_{ij} = \frac{\delta_i^3 w_{ij} \rho g}{12\mu} \frac{p_i - p_e}{l_i} \tag{3.57}$$

$$q_{ij} = \frac{\delta_j^3 w_{ij} \rho g}{12\mu} \frac{p_e - p_j}{l_j} \tag{3.58}$$

Where p_e is the pressure at the common edge. Sum the two equations to eliminate p_e, obtain,

$$q_{ij} = \frac{w_{ij}\rho g}{12\mu(\frac{l_i}{\delta_i^3} + \frac{l_j}{\delta_j^3})}(p_i - p_j) = K_{ij}(p_i - p_j) \tag{3.59}$$

Here K_{ij} is used to represent the part that relates flow rate and pressure difference, define it as equivalent permeability. And there is $K_{ij} = K_{ji}$.

Consider fluid node i, which is connected to a set of adjacent fluid nodes whose indices are in the set $\mathbb{N}_i$. According to the conservation of mass at this node, there is,

$$q_i^{ext} - s_i - \sum_{j \in \mathbb{N}_i} q_{ij} = 0 \tag{3.60}$$

Where q_i^{ext} is the volumetric injection (+) or extraction (-) flow rate, s_i is the increment (+) or decrement (-) of fracture storage per unit time, q_{ij} is the outflow (+) from node i to j, or inflow (-) from node j to i. s_i could be computed from Equation 3.54,

$$s_i = \frac{S_i}{t} = \frac{A_i \delta_i}{t} \tag{3.61}$$

Or alternatively,

$$s_i = \frac{\Delta S_i}{\Delta t} = \frac{A_i \Delta \delta_i}{\Delta t} \tag{3.62}$$

Where t is the total simulated time, Δt and $\Delta \delta_i$ are the simulated time and change of aperture in this time step. Substitute Equation 3.59 into 3.54,

$$-\sum_{j \in \mathbb{N}_i} [K_{ij}(p_i - p_j)] = s_i - q_i^{ext} \tag{3.63}$$

This relation holds for all the nodes and could be assembled into a global matrix system,

$$\left[\boldsymbol{K}\right](\boldsymbol{p}) = (\boldsymbol{s}) - (\boldsymbol{q}^{ext}) \tag{3.64}$$

Each row of the system represents the mass conservation equation for the particular node. The elements in matrix $\boldsymbol{K}$ are,

$$\boldsymbol{K}_{ij} = \begin{cases} -\sum\limits_{j \in \mathbb{N}_i} K_{ij} & i = j \\ K_{ij} & j \in \mathbb{N}_i \\ 0 & j \notin \mathbb{N}_i \ \ and \ \ i \neq j \end{cases} \tag{3.65}$$

In each step, $\boldsymbol{s}$ and $\boldsymbol{K}$ could be obtained from fracture geometry computed in the solid phase, together with prescribed $\boldsymbol{q}^{ext}$ in fluid node, the pressure distribution $\boldsymbol{p}$ could be solved.

However, noted that the rank of matrix $\boldsymbol{K}$ is $row(\boldsymbol{K}) - 1$, as summing all the rows gives a zero row. There is one more unknown variable than the number of independent equations. The system could be solved by guessing one of the pressures at a random fluid node as a known boundary condition and then solving for the rest. While in implementation, the injection pressure (or one of them if there are multiple injection nodes in one fluid network) is chosen as the guessed variable.

Another problem with solving Equation 3.64 is that the distribution of fluid pressure will affect the fracture apertures in the solid network, and thus the permeability matrix and storage vector. Therefore, this is a nonlinear equation as both $\boldsymbol{K}$ and $\boldsymbol{s}$ are functions of $\boldsymbol{p}$. But the functional relation involves the solid phase in the lattice level, which is complex and cannot be expressed explicitly. In this case, fixed point iteration is used to solve the system with an initial guess $\boldsymbol{p}^{(0)}$. The pressure in the $(n+1)$-th fixed point iteration could be solved as,

$$\boldsymbol{p}^{(n+1)} = \left(\boldsymbol{K}(\boldsymbol{p}^{(n)})\right)^{-1} \left(\boldsymbol{s}(\boldsymbol{p}^{(n)}) - \boldsymbol{q}^{ext}\right) = \boldsymbol{g}(\boldsymbol{p}^{(n)}) \tag{3.66}$$

Let $\mathbb{F}$ be the set with indices of all the fluid nodes, the averaged pressure change in every fluid node is computed as the residual of fixed point iteration,

$$R_{fpi}^{n+1} = \frac{1}{|\mathbb{F}|} \sum_{i \in \mathbb{F}} \frac{\left| p_i^{(n+1)} - p_i^{(n)} \right|}{p_i^{(n+1)} + p_i^{(n)}} \tag{3.67}$$

Where $|\mathbb{F}|$ is the number of elements in set $\mathbb{F}$. The iteration is treated as converged when R_{fpi} is smaller than a specified tolerance ϵ_{fpi}.

After the pressure distribution under the guessed injection pressure is solved, the validity of this result is checked by the global mass conservation, which requires the total injected fluid volume to be approximately equal to the total increment of storage in the network. The relative difference between these two parts is defined as,

$$R_{gmc} = \frac{\sum\limits_{i \in \mathbb{F}} \boldsymbol{q}_i^{ext} - \sum\limits_{i \in \mathbb{F}} \boldsymbol{s}_i}{|\sum\limits_{i \in \mathbb{F}} \boldsymbol{q}_i^{ext}| + |\sum\limits_{i \in \mathbb{F}} \boldsymbol{s}_i|} \tag{3.68}$$

$R_{gmc} > 0$ indicates that the injected fluid volume is larger than that stored in the fractures, thus the guessed injection pressure needs to increase to achieve larger apertures. Similarly the guessed value needs to reduce when $R_{gmc} < 0$. With an initial guess $p_{in}^{(m+1)}$ and a prescribed constant c, the $(m+1)$-th guessed value is first determined as,

$$\begin{cases} p_{in}^{(m+1)} = c p_{in}^{(m)}, \;\; p_{in,min} = p_{in}^{(m)} & if \;\; R_{gmc}^{(m)} > 0 \\ p_{in}^{(m+1)} = \frac{1}{c} p_{in}^{(m)}, \;\; p_{in,max} = p_{in}^{(m)} & if \;\; R_{gmc}^{(m)} < 0 \end{cases} \tag{3.69}$$

The upper and lower bounds $p_{in,max}$ and $p_{in,min}$ are also assigned during this process. After the first time that the sign of the residual changes, that is, $R_{gmc}^{(m)} R_{gmc}^{(m+1)} < 0$, the guessed

value could be bounded and thus bisection method is used,

$$\begin{cases} p_{in}^{(m+1)} = \frac{p_{in}^{(m)}+p_{in,max}}{2}, \;\; p_{in,min} = p_{in}^{(m)} & if \;\; R_{gmc}^{(m)} > 0 \\ p_{in}^{(m+1)} = \frac{p_{in}^{(m)}+p_{in,min}}{2}, \;\; p_{in,max} = p_{in}^{(m)} & if \;\; R_{gmc}^{(m)} < 0 \end{cases} \tag{3.70}$$

The global mass conservation is satisfied when $|R_{gmc}|$ is smaller than a specified tolerance ϵ_{gmc}. It is also possible that the desired residual cannot be achieved due to the oscillation of the results. As a compromise, when convergence is still not achieved after a certain number of iterations, the guessed value would be accepted if the bound is small enough,

$$\frac{p_{in,max} - p_{in,min}}{p_{in}^{(m)}} \leq \epsilon_{pbd} \tag{3.71}$$

3.3.2 Solid-Fluid Coupling Scheme

Figure 3.12 shows the key steps of solving the process for fluid pressure distribution by coupling the solid and fluid lattice networks. Essentially the purpose of this process is to determine the force boundary conditions for solid parts at fracture surfaces due to the pressure generated by the prescribed injected fluid volume. Therefore, it could be incorporated into the process for solving the solid lattice network at the dashed box in Figure 3.9. This model assumes that the fracture forms much faster than the fluid flows, thus the solid fluid models are decoupled and fluid pressure does not change when solving for fracture development in the solid phase (the major part of Figure 3.9). While fluid pressure distribution is solved under a given fracture pattern, although it needs to iterate between the fluid and solid model to determine the corresponding fracture aperture, no new crack would be generated in this process. The pressure is non-negative values in the whole process. In case negative pressure is obtained by solving the matrix system, it is set to zero to indicate that the fluid has not yet reached this node.

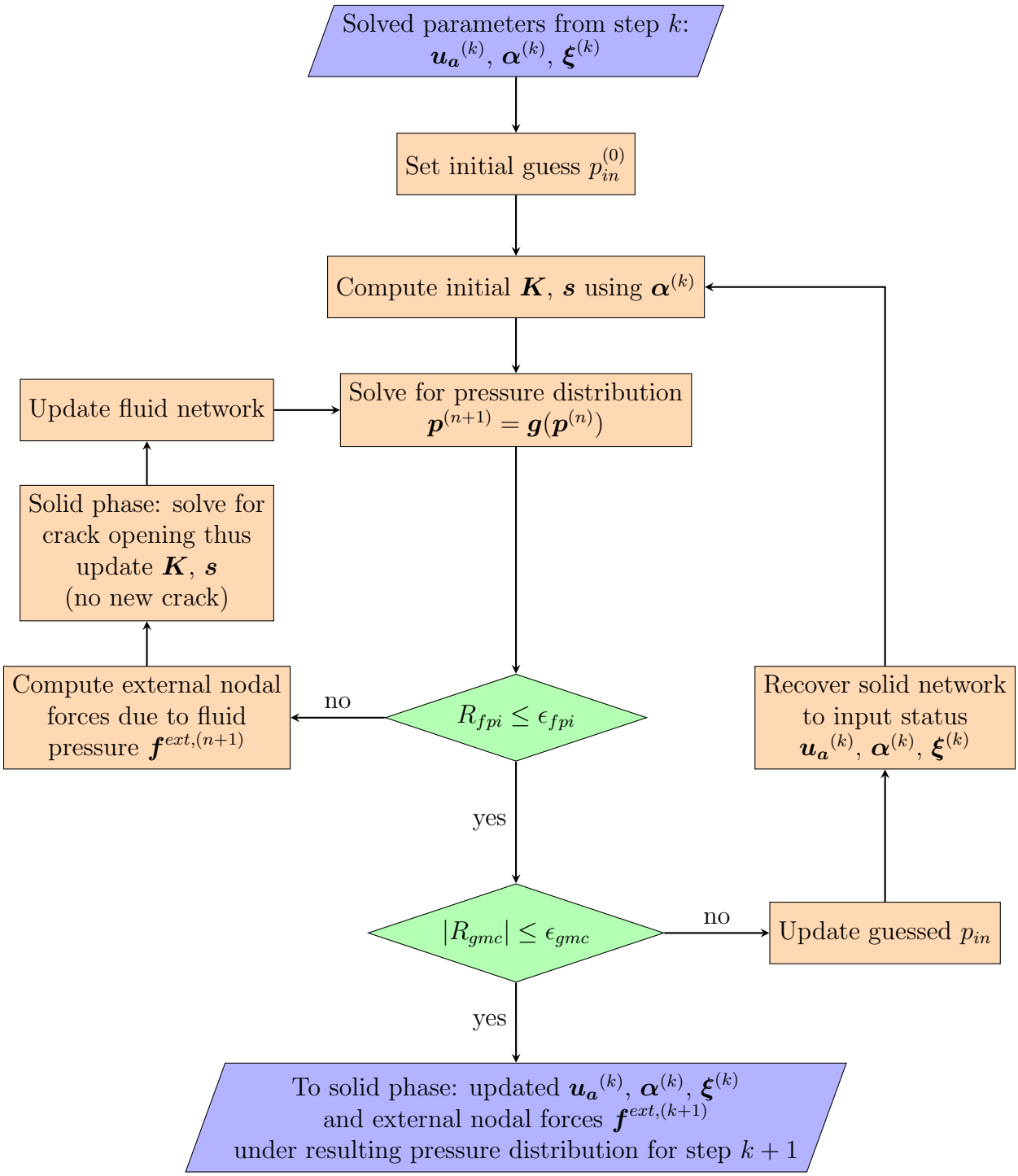

Figure 3.12: Solving process for fluid pressure distribution in a time step

3.4 Implementation

3.4.1 Structure of the Code

The LEM code is written on a generic template-based modern C++14 code with the class-orientation paradigm. Figure 3.13 shows the Unified Modelling Language (UML) diagram of this code.

The `LEM` class owns all the other related classes for the LEM method and controls the whole process. Three main types of classes directly controlled by `LEM` are the mesh, assemblers and solver. Functions for various simulation cases are implemented here, including time stepping and the solving processes for solid or solid-fluid coupled models illustrated in Figure 3.9 and 3.12.

The `Mesh` class reads the text file for solid node coordinates generated as described in Section 3.1, initializes the network and then stores the vectors of pointers to the classes of the lattice network's basic structures, including nodes and elements (lattice) for both solid and fluid parts. `NodeBase` is the base class that stores the index and coordinates for a particular node and is inherited by the `SolidNode` and `FluidNode` classes, which respectively store specific information of a solid (e.g., nodal forces, displacements and geometries of corresponding Voronoi cell) or fluid (e.g., fracture geometries, storage and connectivity) node. The `ElementBase` class stores information for a solid lattice, such as local stiffness matrix and crack openings. And it has access to the corresponding `SolidNode` objects at its two ends. Classes representing different lattice models could inherit from `ElementBase`. Only `TimoshenkoBeam` class is related to this study, which implements the solid lattice model described in Section 3.2. `Mesh` also manages the `FluidNetwork`, which stores fluid lattices networks and has direct access to `FluidNode`, `FluidElement` and `FluidMaterial`. `FluidMaterial` stores properties of fluid and `FluidElement` computes the permeability of corresponding pipe. Breadth first search algorithm for updating the active fluid nodes and connectivity is also implemented in `FluidNetwork`. `DistributionGenerator` is a small independent class in `Mesh` for applying probability distribution on properties of solid lattices. In summary, the whole lattice network is established in the `Mesh` class. Operations on the networks, such as discretizing the domain, applying boundary conditions, computing lattice crack opening and extracting the results are implemented as functions in `Mesh` by iterating through corresponding structures. The Intel Threading Building Blocks (TBB) library [135] is utilized to accelerate the iteration process.

The `TimoshenkoMatrixAssembler` and `FluidMatrixAssembler` classes also have access to nodes and elements through pointers by communicating with `Mesh`, which allows them to extract corresponding information (local stiffness matrix and nodal forces for solid; permeability and storage for fluid) to assemble the global matrix system as described by Equation 3.52 and 3.64. `VectorXd` and `SparseMatrix` structures from Eigen library [60] are used to store the data. Boundary conditions are applied by modifying corresponding elements in the matrix and right hand side vector. After the system is solved, the assemblers apply resulting displacement increments or pressures back to corresponding solid or fluid nodes.

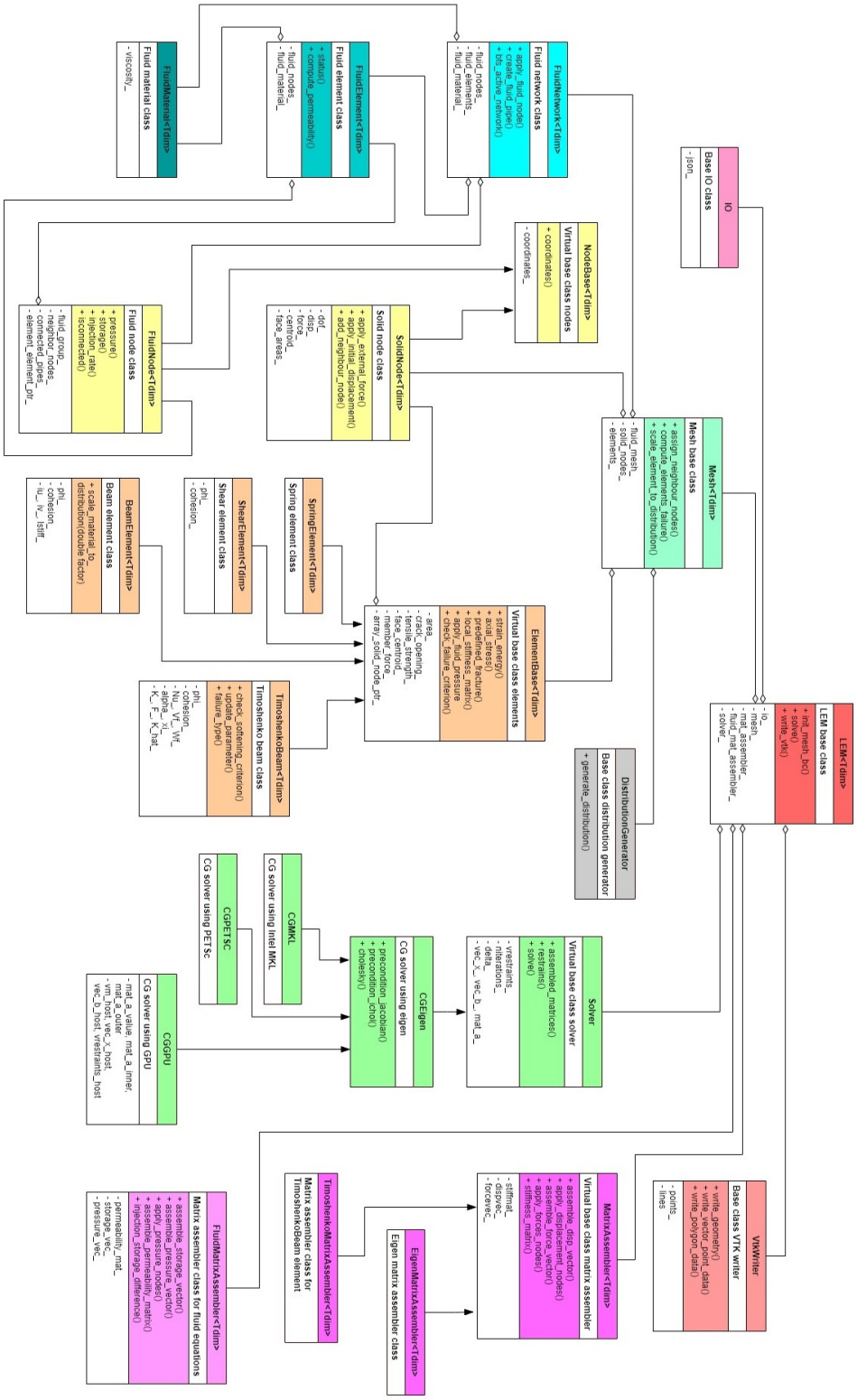

Figure 3.13: Structure of the LEM code

Assemblers pass the pointers to its stored global matrix and vectors to `Solver`, which solves the system of the form $\boldsymbol{Ax} = \boldsymbol{b}$. As the fluid network is one dimension less than the solid network, the size of its matrix system is also much smaller, allowing it to be solved by a direct solver nearly instantaneously. `SimplicialLDLT` from Eigen library [60], which performs a LDL^T Cholesky factorization, is used to solve the fluid matrix system. While the dimension of matrix systems for solid networks typically exceeds millions for models at the scale of interest. Iterative solvers are more suitable for such large sparse matrix systems. As the stiffness matrix is symmetric and positive definite, Conjugate Gradient (CG) solver is used. Self written CG solvers with matrix operation provided in Eigen or Intel Math Kernel Library (MKL) [161] are implemented in `CGEigen` and `CGMKL` classes. But eventually, the parallel CG solver implemented in PETSc library [7] is used for better performance.

The `IO` class reads JSON files for simulation setting such as material properties, boundary conditions and applied loading. It also writes required simulation results into text or CSV files, such as reaction, injection pressure histories and element status. In each simulation step, `VtkWriter` writes the resulting displacement and stress field across the network, as well as fracture patterns, into VTP files by utilizing the Visualization Toolkit (VTK) [147]. These data are visualized using ParaView [5].

3.4.2 Preconditioned Conjugate Gradient Solvers

For Conjugate Gradient method that solves matrix system of the form $\boldsymbol{Ax} = \boldsymbol{b}$, the error after n iterations is proportional to,

$$\left(\frac{\sqrt{\kappa(\boldsymbol{A})} - 1}{\sqrt{\kappa(\boldsymbol{A})} + 1}\right)^n \tag{3.72}$$

Where $\kappa(\boldsymbol{A})$ is the condition number of matrix $\boldsymbol{A}$, computed from its extreme singular values $\sigma_{max}(\boldsymbol{A})$ and $\sigma_{min}(\boldsymbol{A})$, as,

$$\kappa(\boldsymbol{A}) = \frac{\sigma_{max}(\boldsymbol{A})}{\sigma_{min}(\boldsymbol{A})} \tag{3.73}$$

Therefore, this method would converge in less number of iterations for a matrix with a smaller condition number. A standard approach to accelerate convergence is to select a nonsingular matrix $\boldsymbol{M}$ as preconditioner [35], and rewrite the system for left preconditioning as,

$$\boldsymbol{M}^{-1}\boldsymbol{Ax} = \boldsymbol{M}^{-1}\boldsymbol{b} \tag{3.74}$$

Such that the new matrix has a smaller condition number,

$$\kappa(\boldsymbol{M}^{-1}\boldsymbol{A}) < \kappa(\boldsymbol{A}) \tag{3.75}$$

A smaller condition number could be obtained when the matrix $\boldsymbol{M}$ is closer to $\boldsymbol{A}$. A trivial case is $\boldsymbol{M} = \boldsymbol{A}$, which solves the problem immediately but to obtain $\boldsymbol{M}^{-1}$ itself is as

complicated as the original problem. Two commonly used preconditioners are considered here. The first is Jacobi preconditioner,

$$\boldsymbol{M} = \boldsymbol{D} = diag(\boldsymbol{A}) \tag{3.76}$$

Where $\boldsymbol{D}$ is the diagonal matrix of $\boldsymbol{A}$. This is efficient for diagonally dominant matrices. The second is the incomplete Cholesky preconditioner,

$$\boldsymbol{M} = \boldsymbol{L}\boldsymbol{L}^T \tag{3.77}$$

Where $\boldsymbol{L}$ is a sparse lower triangular matrix that approximates Cholesky factorization of $\boldsymbol{A}$, but with lower cost.

A simple test problem that simulates one step of the uniaxial tension test on an elastic cuboid specimen of the size $0.8 \times 0.48 \times 0.48$, is used to understand the nature of the solid matrix system and to determine which preconditioner takes the least amount of time and is thus the best suitable for this application. Two models were created with lattice characteristic lengths 0.05 and 0.025 respectively. The information about their mesh sizes and features of corresponding stiffness matrices are shown in Table 3.2. The densities indicate that the stiffness matrix is quite sparse. While the resulting condition numbers are in the magnitude of 10^6, which is relatively large and thus preconditioner may be required for fast convergence.

Model	Number of nodes	Number of elements	Matrix dimension	Number of non-zero elements	Density	Condition number
$M_{0.05}$	7071	52081	42426^2	3135867	1.74×10^{-3}	400156
$M_{0.025}$	55467	430491	332802^2	26675678	2.41×10^{-4}	974601

Table 3.2: Summary of model sizes and matrix properties

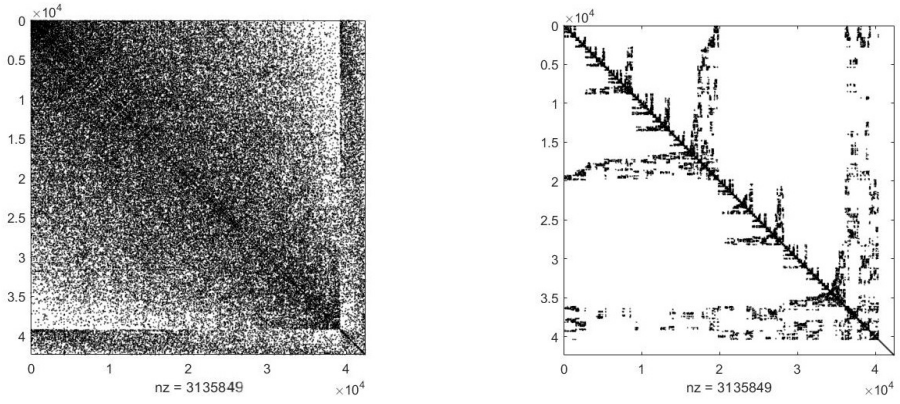

(a) Original matrix (b) Approximate minimum degree reordering

Figure 3.14: Sparsity patterns for stiffness matrices of model $M_{0.05}$

The sparsity plot for the stiffness matrix of model $M_{0.05}$ is shown in Figure 3.14a, which is quite random. Ordering of the matrix has a significant effect on the number of nonzero in Cholesky factorization and also on the rate of convergence of preconditioned CG [37]. Approximate minimum degree reordering is applied on the matrix and the resulting sparsity plot is shown in Figure 3.14b. The pattern of the sparsity plot for model $M_{0.025}$ is similar. The distribution of the magnitude of values in the stiffness matrix of model $M_{0.05}$ is shown in Figure 3.15. Most of the values are in between 10^{-4} to 10^{2}, which does not involve extremely large or small values. The magnitude varies with prescribed lattice properties, but the width of the range should remain similar.

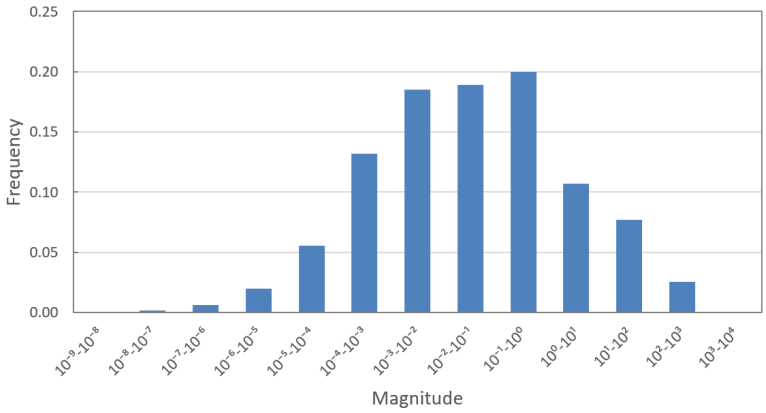

Figure 3.15: Magnitude distribution of non-zero elements in stiffness matrices of model $M_{0.05}$

The self written CG solver utilizing implemented matrix operations from the MKL library is used in this test. Matrix vector multiplication is accelerated with the function `mkl_sparse_d_mv`. For the incomplete Cholesky preconditioner, the Eigen library is used to generate a preconditioner with approximate minimum degree reordering. And after each CG iteration is completed, the multiplication of $\boldsymbol{M}^{-1}$ with a vector is computed by solving two triangular matrix systems using `mkl_sparse_d_trsv` function. A relative tolerance of $\epsilon_r = 10^{-7}$ is used as stopping criteria for all the cases. That is, the method is converged when the residual of n-th iteration satisfies,

$$||r^{(n)}||_2 \leq \epsilon_r ||r^{(0)}||_2 \tag{3.78}$$

The tests are run on a local laptop and the resulting convergence plots and duration for each iteration are shown in Figure 3.16 and 3.17. For the cases with incomplete Cholesky preconditioner, the duration for solving the triangular system in each iteration is also plotted in the same figure with the dashed line. In Figure 3.16b and 3.17b, the horizontal axis is cut at 500 and 1000 iterations, as the right parts are only for no preconditioner cases and are nearly the same as the left parts. The total number of iterations and time taken in this process for each case are listed In Table 3.3.

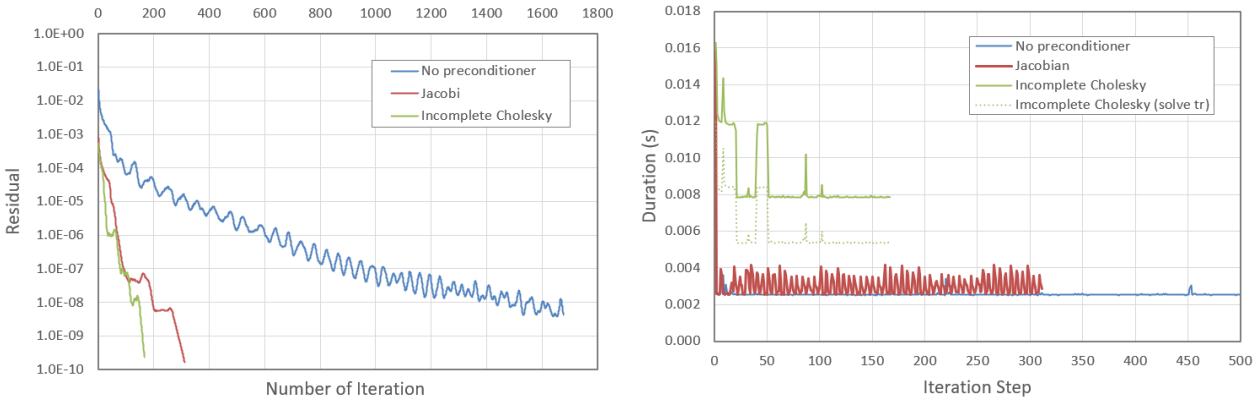

(a) Convergence plot (b) Duration per iteration

Figure 3.16: Solver performance for model $M_{0.05}$

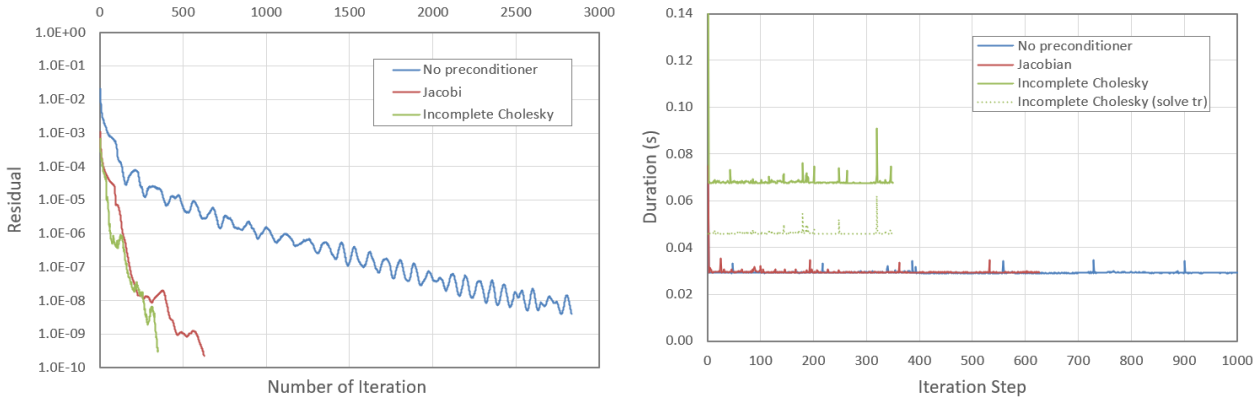

(a) Convergence plot (b) Duration per iteration

Figure 3.17: Solver performance for model $M_{0.025}$

Preconditioner	$M_{0.05}$			$M_{0.025}$		
	# iterations	Total time (s)	Condition number	# iterations	Total time (s)	Condition number
None	1677	4.28	400156	2833	82.80	974601
Jacobi	311	0.95	18123	626	18.53	84270
Incomplete Cholesky	167	1.00	1958	350	23.93	8150

Table 3.3: Number of iteration, condition number and total time used for each preconditioner

According to Figure 3.16a and 3.17a, CG with either Jacobi or incomplete Cholesky preconditioner converges in much fewer iterations and thus shorter time than the cases

without preconditioner. While compared with Jacobi, incomplete Cholesky reduces the number of iterations by nearly half. However, it still takes slightly more time than Jacobi, as shown in Table 3.3. This is because in each iteration, incomplete Cholesky needs to solve two additional triangular matrix systems on account of $\boldsymbol{M}^{-1}$. In dense case, this is an $\mathcal{O}(N^2)$ operation, where N is the dimension of the matrix, which is in the same magnitude of matrix vector multiplication (the main source of computation for one CG step). In sparse cases, the cost of this operation is also comparable with the cost of the rest of the CG operation in this step. While for the Jacobi preconditioner, only $\mathcal{O}(N)$ operation for this step, as $\boldsymbol{M}$ is a diagonal matrix. Therefore as shown in Figure 3.16b and 3.17b, the duration for each step of Jacobi is nearly the same as no preconditioner, while that of incomplete Cholesky is more than double, and the difference comes from solving the triangular matrix systems. In summary, according to this set of tests, Jacobi may be the most efficient preconditioner for this application. It reduces the number of iterations significantly compared with no preconditioner, in the cost of a negligible number of additional flops, resulting in the shortest time for convergence.

3.4.3 Performance of the Code

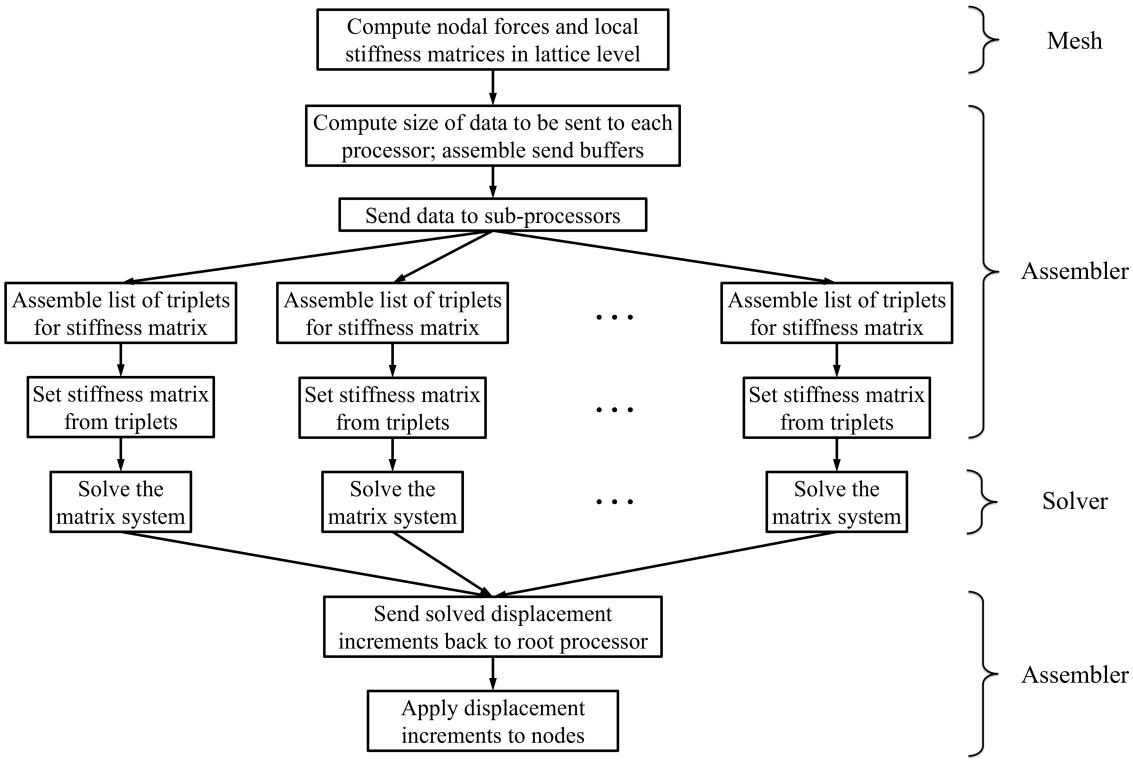

Figure 3.18: Parallelized assembler and solver

Solving the large matrix system for a solid network is the most time consuming part of the serial code. Assembling the global stiffness matrix also takes a substantial amount of time. Therefore, while the majority of the code is in serial, these two parts are parallelized using the Message Passing Interface (MPI) standard with MPICH [59]. Although such local parallelization is not as efficient as the fully parallelized code, it deals directly with the most time consuming part of the whole process and better utilizes the parallel solver implemented in the PETSc library, thus accelerating the code substantially with considerably less amount of effort.

The parallelization scheme is shown in Figure 3.18. After the root processor computes the nodal forces and stiffness matrices locally in each lattice, it determines the partition of the matrix system evenly by rows for each sub-processor, places the data (nodal forces, elements in stiffness matrix and corresponding indices) into vectors as buffers, and then distributes these data to each sub-processor. Upon receiving the data, sub-processors start to assemble lists of `Triplet` for elements and corresponding indices in the global stiffness matrix, then create the `SparseMatrix` by `setFromTriplets`. All of these data structures and functions are from the Eigen library. In the solver class, the data in Eigen containers passed from the assembler are converted to PETSc data structures, then preconditioned with Jacobi (`PCJACOBI`) and solved by the parallelized CG solver (`KSPCG`), all from PETSc library. The solved displacement increments in sub-processors are then sent to the root processor and the code is back to serial.

Model	Number of nodes	Number of elements	Matrix dimension
M_7	100504	788079	603034^2
M_5	240179	1899382	1441074^2
M_4	489847	3911253	2939082^2
$M_{3.5}$	738050	5912644	4428300^2
$M_{3.25}$	915194	7350725	5491164^2

Table 3.4: Summary of model sizes

Uniaxial compression tests on cubic specimens of the size $200 \times 200 \times 200$ with different lattice characteristic lengths (from 3.25 to 7) were conducted to evaluate the performance of this code. Table 3.4 lists the sizes of these models. The code was run in the Skylake (SKX) compute nodes of the supercomputer Stampede2 from the Texas Advanced Computing Center (TACC). Considering that models with around 250000 nodes are the most commonly used in simulations conducted for this study (mainly in Chapter 4 and 5), the code was run with varying numbers of MPI processors for model M_5, and the time spent for one assembler and solver step in each part was recorded and shown in Figure 3.19. The time spent reduces significantly with the increasing number of MPI processors initially. When the number of processors exceeds 12, the effect becomes marginal. Figure 3.19a shows that for assembler, when the number of processors is large, the time spent is dominated by the

serial part (assemble send buffers) and communication (send data), thus it cannot be further optimized with this scheme. Figure 3.19b shows that nearly all the time spent by the solver is in solving the system iteratively, which utilizes implemented function in PETSc and has better efficiency. While Figure 3.20 shows the time spent for one assembler and solver step for models of different sizes run with 24 MPI processors.

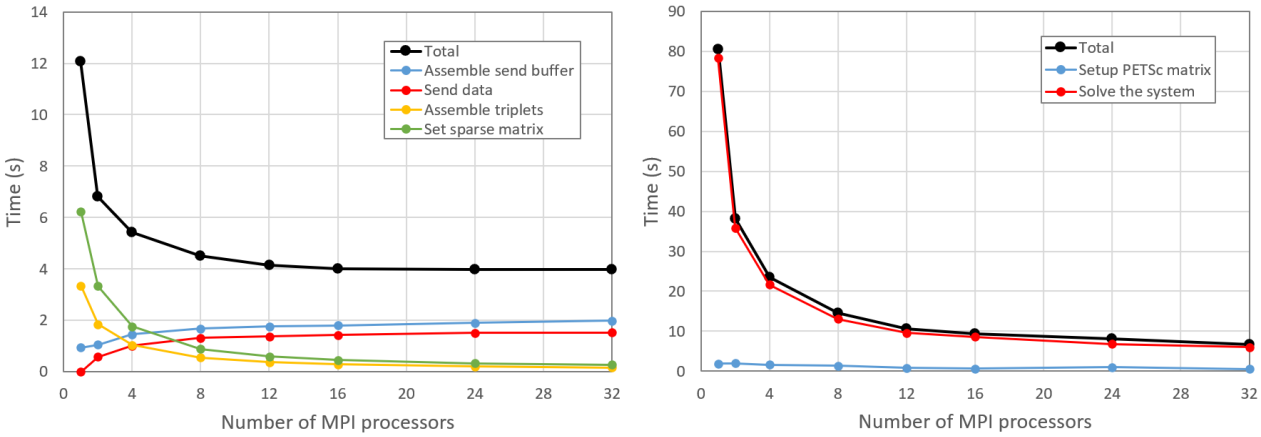

(a) Assembler (b) Solver

Figure 3.19: Time spent for one assembler and solver step for model M_5 with different number of MPI processors

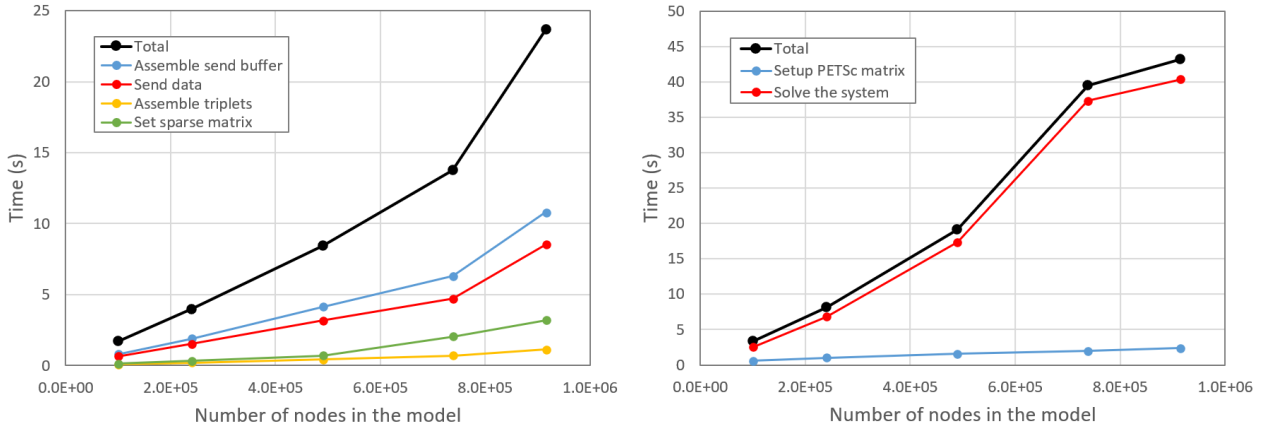

(a) Assembler (b) Solver

Figure 3.20: Time spent for one assembler and solver step for models of different sizes with 24 MPI processors

Table 3.5 shows the time spent on main operations in 10 elastic steps of uniaxial compression test on model M_5 ran with 24 MPI processors. The whole test finished in around 15 min. The mesh initialization takes approximately 10% of the simulation time. But this operation is only required once when the code starts, thus it is negligible in large simulations with lots of time steps. The solver is still the most time consuming part, and the global matrix assembler also takes a substantial amount of time, but they are comparable to the rest and are acceptable. This also shows the importance of parallelizing these two parts. It should be noted that the model behaves elastically through this test and the Newton-Raphson method converges in 2 iterations in all the time steps. When simulating fracture development that involves breakage of lattice, the required number of Newton Raphson iterations may largely increase. And line search method would be used for more complicated scenarios where the Newton-Raphson method becomes difficult to converge. Therefore, the time spent on this part could significantly increase in practice. In addition, hydraulic fracturing problems require iterating between solid and fluid phases, thus would take even more time. In simulations run for this study with models of similar sizes, it usually takes 5 to 10 hours to simulate dry crack scenarios for 70 to 100 steps. And it may take over one day to simulate hydraulic fracturing scenarios also for 70 to 100 steps. This may not be fast, but it is more due to solution methods for this numerical problem. The time spent may possibly be further optimized by utilizing other numerical methods. The code itself has a decent speed for these operations. In this example, writing VTK files takes nearly the same amount of time as the solver. But this is in the post processing stage and requires only once every time step. Thus it would not be a problem for complicated cases as discussed above.

	Procedure		Time (s)	Percentage (%)
	Total time (10 steps)		913.189	100.00
	Initialize mesh		87.202	9.55
NR iterations	Check lattice softening criteria		63.601	6.96
NR iterations	Compute nodal forces		69.07	7.56
NR iterations	Assemble stiffness matrix	local	48.144	5.27
NR iterations	Assemble stiffness matrix	global	87.576	9.59
NR iterations	Solver		254.789	27.90
Post processing	Compute nodal stress		4.431	0.49
Post processing	Write VTK files		238.821	26.15
	Sum		853.634	93.48

Table 3.5: Time spent for 10 elastic steps of uniaxial compression test on model M_5 with 24 MPI processors

Chapter 4

LEM Simulations on Fractures in Solid

4.1 Validation

4.1.1 Elastic Cantilever Beam Tests

The solid lattice model was first validated elastically using the cantilever beam problem. Seven LEM models for a $0.4 \times 0.4 \times 10$ m beam with different mesh sizes were created. The characteristic lengths of the lattice vary from 0.02 to 0.1 m, and the models are named as $B_{0.02}$ to $B_{0.1}$ correspondingly, where the subscript represents its lattice characteristic length in meters. The beam was chosen to have a high aspect ratio so that the Euler–Bernoulli beam theory is applicable [48]. The microscopic elastic modulus and Poisson's ratio for a single lattice were chosen to be 50 GPa and 0.2 respectively.

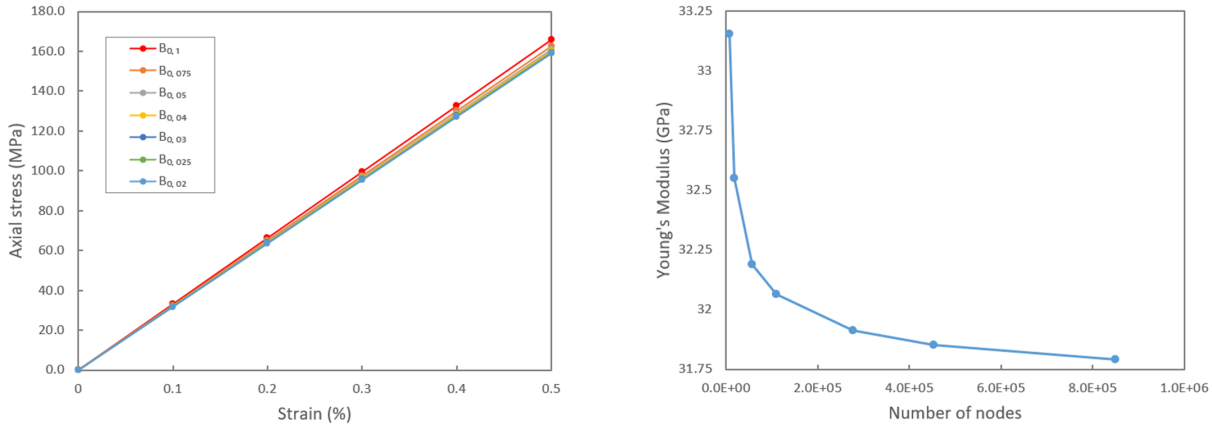

(a) Stress strain curves

(b) Young's modulus versus model size

Figure 4.1: Results of uniaxial compression tests on the beams

Uniaxial compression tests were first conducted. Roller support was applied at one end of the beam, while 0.01 m constant longitudinal displacements were applied on the other end in each of the five incremental steps. In all the cases, the beam behaves linearly throughout the test, as the stress-strain curves show in Figure 4.1a. The slope of each curve represents the macroscopic Young's modulus of the corresponding beam, which decreases slightly as the mesh is refined but tends to converge at the end, as depicted in Figure 4.1b. The model sizes and corresponding macroscopic Young's modulus are listed in Table 4.1.

Model	Number of nodes	Number of elements	Young's modulus (GPa)	Maximum deflection		Averaged maximum stress	
				value (m)	error (%)	value (MPa)	error (%)
$B_{0.1}$	8080	54016	33.16	0.360	-8.45	63.84	-14.88
$B_{0.075}$	18759	131806	32.55	0.372	-5.29	73.64	-1.82
$B_{0.05}$	57409	422807	32.19	0.380	-3.4	70.26	-6.32
$B_{0.04}$	110173	828418	32.06	0.382	-2.79	77.48	3.30
$B_{0.03}$	276511	2130217	31.91	0.386	-1.90	77.85	3.80
$B_{0.025}$	453149	3527008	31.85	0.388	-1.41	76.26	1.67
$B_{0.02}$	850290	6683699	31.79	0.389	-0.98	75.91	1.21
*Theoretical value:				0.393		75.00	

Table 4.1: Summary of properties and point load test results for cantilever beam models

The point load test was then conducted, as sketched in Figure 4.2. Rigid boundary condition was applied at left end of the beam, while 0.5 MPa stress acting transversely was applied at the surface of right end to simulate the 80 kPa point load P.

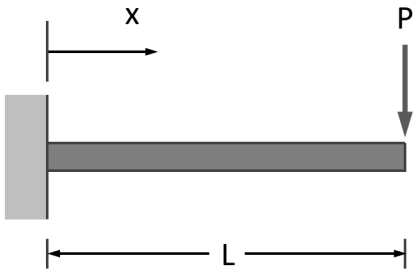

Figure 4.2: Sketch of point load test on a cantilever beam

According to the Euler–Bernoulli beam theory [48], deflection of the beam as a function of distance to the fixed end, x, is,

$$w(x) = \frac{Px^2}{6EI}(3L - x) \tag{4.1}$$

Where E is the macroscopic Young's modulus, L is the length of the beam, I is the second moment of inertia of the cross section. The maximum deflection of 0.393 m is achieved when $x = L = 10$ m. While the maximum moment in the beam occurs at the fixed end, resulting in the maximum normal stress at the edge of this cross section,

$$\sigma_m = \frac{PLc}{I} \tag{4.2}$$

Where c is the distance from the centroid of the cross section to the edge. In this case, the maximum stress is 75 MPa.

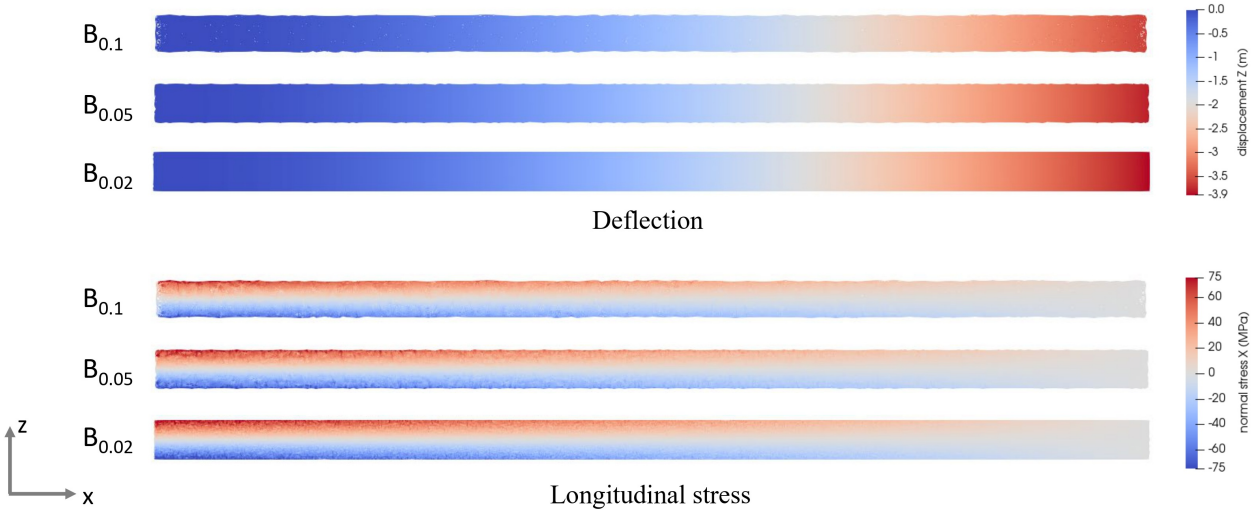

Figure 4.3: LEM simulated deflection and longitudinal stress fields

Figure 4.3 depicts the simulated deflection and longitudinal normal stress fields for model $B_{0.1}$, $B_{0.05}$ and $B_{0.02}$. It is observed that the stress profiles have small local fluctuations but decrease as the mesh is refined. For each beam, the average stress at the edge of the left end surface was computed and compared with the theoretical value, as listed in Table 4.1. Although error exists due to mesh heterogeneity, the results are close enough when the characteristic length is finer than 0.04 m. The deflection at the center line of each beam is plotted in Figure 4.4, together with the theoretical deflection profile calculated according to Equation 4.1. The Young's modulus of $B_{0.02}$ was used in the calculation as the closest value to convergence. The resulting maximum deflections at the right end are also listed in Table 4.1. The simulated results approach the theoretical profile as mesh refined. Although they are not identical as full convergence has not been achieved, the errors are smaller than 2% when the characteristic length is finer than 0.03 m.

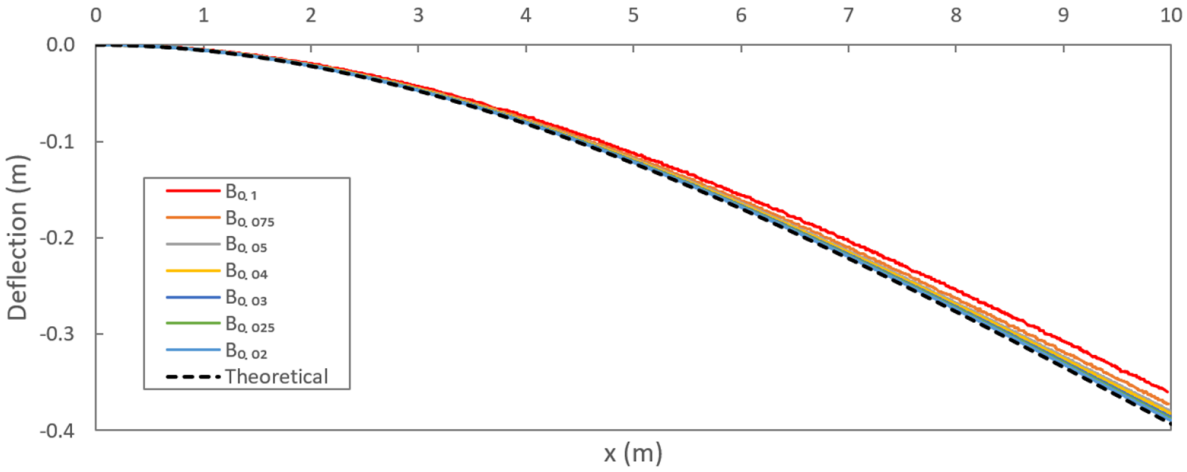

Figure 4.4: Theoretical and simulated deflection profiles

4.1.2 The Uniaxial Tension Test and Brazilian Test

The solid lattice model was also validated using both the uniaxial tension test and the Brazilian test to examine the fracture development process and prediction of model strength.

The uniaxial tension test was first conducted on a cylindrical sample with 0.03 m in radius and 0.15 m in height to measure its macroscopic tensile strength for comparison. The completely brittle lattice was used and it has the following microscopic properties: elastic modulus of 50 GPa, Poisson's ratio of 0.2, tensile strength of 6.45 MPa, shear strength of 21 MPa, and its characteristic length is 0.002 m. 10^{-6} m longitudinal displacement was applied in every step.

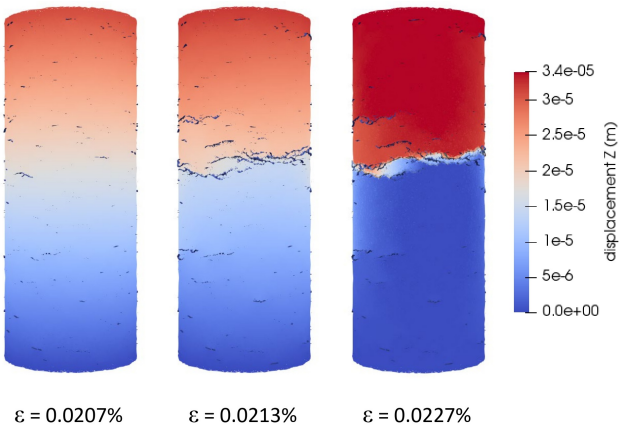

(a) Displacement fields and fracture patterns

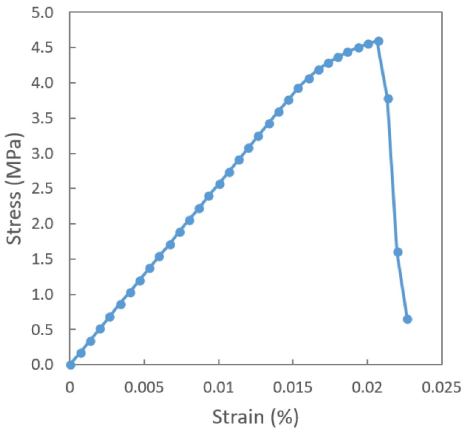

(b) Stress strain curve

Figure 4.5: Results of uniaxial tension tests on cylindrical sample

The fracture development process and stress strain curve of the test are shown in Figure 4.5. Before the peak stress is reached, small cracks start to develop and are distributed randomly across the sample, which weakens the structure. The stress continues increasing with strain, but the slope decreases. As the number of these small individual cracks increases, they start to quickly coalesce into localized fractures at multiple locations, which leads to stress drop. The largest fracture keeps developing rapidly and eventually cuts through the sample. The peak stress is observed before fracture localization, which is 4.60 MPa.

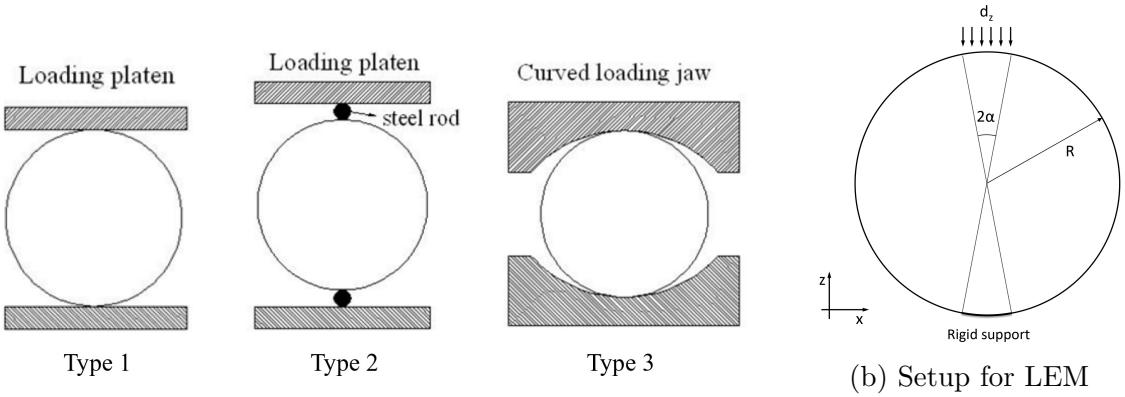

(a) Typical loading types in Brazilian test [96]

(b) Setup for LEM simulations

Figure 4.6: Sketch of setup for Brazilian test

The Brazilian tests were conducted on cylindrical samples with 0.05 m in radius and 0.1 m in height, whose lattices have the same characteristic length and microscopic properties as those used in the above uniaxial tension test. Some studies suggested that early shear failure fracture may occur due to stress concentration near the loading jaw, thus additional simulations were conducted on samples with large shear strength lattice [95]. The lattice properties for each test case are summarized in Table 4.2.

The boundary condition is an important factor that would significantly affect the estimated tensile strength from the Brazilian test [96][143]. Three typical loading types are shown in Figure 4.6a. Experimental studies indicated that the Type 2 condition gives a much smaller measured strength than Type 1 and 3, because large stress is concentrated around the boundary due to the small contact area, which would cause localized premature fracture [96]. While the contact area for Type 1 and 3 cases is a curved surface instead of an idea line as assumed theoretically, due to the deformation of rock and loading jaw, which increases the measured loading [108]. The setup for LEM simulations is shown in Figure 4.6b. The bottom contact arc over 2α central angle was set as a rigid boundary, while a constant displacement increment 3×10^{-6} m in $-z$ direction was applied to the top arc in each step. In this setup, the arc of contact has a constant central angle and moves downward rigidly, which is actually different from each of the three loading types in Figure 4.6a. But when α is small, it becomes similar to the Type 2 condition, indicating the simulation may

possibly underestimate the tensile strength. Cases with different angles of contact arc were also tested.

Case	Lattice strength (MPa)		Angle of contact	Maximum load	Tensile strength	
ID	tensile σ_{st}	shear σ_{ss}	arc 2α (°)	P (kN)	value (MPa)	error (%)
1	6.45	21	2.3	16.78	2.14	-53.54
2	6.45	21	4.6	22.75	2.90	-37.00
3	6.45	21	8.0	28.71	3.66	-20.49
4	6.45	210	2.3	31.81	4.05	-11.92
5	6.45	210	4.6	32.57	4.15	-9.82
6	6.45	210	8.0	34.05	4.34	-5.71
*Tensile strength from uniaxial tension test:					4.60	

Table 4.2: Summary of lattice properties and Brazilian test results

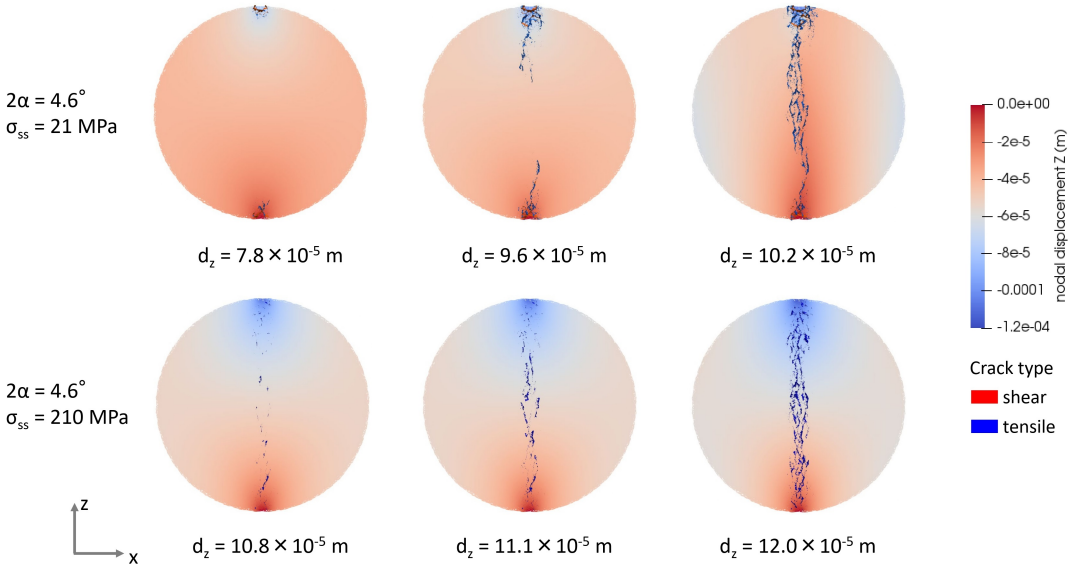

Figure 4.7: Fracture pattern and z displacement field at different applied displacement d_z for Brazilian tests Case 2 and 5

Figure 4.7 demonstrates examples of the fracture development process for Case 2 and 5, with different shear strengths. Varying the angle of the contact arc does not have a significant influence on this process. Figure 4.8 depicts the reaction-displacement curves for all the cases.

For the case with $\sigma_{ss} = 21$ MPa, lattices near the two boundaries start to break in shear (colored in red) at around 80% of peak stress. As the shear fractures accumulate, the

boundaries slightly penetrate into the sample and start to split it. Consequently, tensile cracks (colored in blue) initiate from these two locations and propagate toward the center of the sample. During this stage, the reaction deviates from the linearly increasing trend and remains relatively constant until the tensile cracks connect together and cut through the sample, causing a significant drop in reaction. When α is small, the shorter contact arcs start to penetrate earlier, as fewer shear fractures are required, but the development of the splitting process is also slower. This explains the earlier but longer plateau in the reaction curves for small α cases. This failure phenomenon is consistent with observations in some experiments, especially those with the type 2 boundary condition as discussed above [96]. But this is not the failure mechanism assumed in the Brazilian test and is likely to underestimate the strength.

Due to this simulated boundary condition, the presence of early shear fractures around boundaries is probably unavoidable. Therefore, simulations on models with large shear strength lattices (σ_{ss} = 210 MPa) were conducted to change the mechanism of fracture initiation. Theoretically, according to the Griffith criterion, tensile cracks should be initiated from the center of the sample under this loading condition [95]. However, in the simulation, due to mesh heterogeneity and the discrete nature of the sample, small fractures are randomly distributed across the middle part of the sample, both at the center and near the boundaries (Figure 4.7). But those fractures at the center have larger apertures and develop more rapidly. They quickly coalesce and propagate toward the boundaries and eventually cut through the sample.

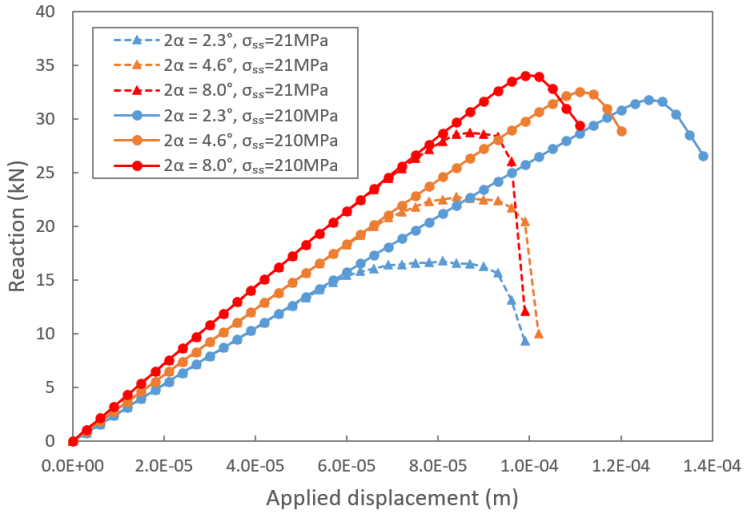

Figure 4.8: Reaction curves for Brazilian tests

The tensile strengths were estimated as,

$$\sigma_{t_{br}} = \frac{2P}{\pi D t} \tag{4.3}$$

Where P is the maximum load, D and t are the sample diameter and height respectively [82]. The results are compared with the value measured by the uniaxial tension test and listed in Table 4.2. According to experimental studies, the Brazilian test is more likely to overestimate the tensile strength [95]. While in this simulation, due to the boundary condition and relatively small central angle of the contact arc, all the cases underestimate the strength. But both simulated failure mechanisms were observed in experiments, and the cases with large lattice shear strength give close estimations.

4.1.3 Uniaxial Compression Test on a Specimen with an Inclined Pre-existing Open Flaw

Fracture patterns and processes in samples with pre-existing flaws under compression have been extensively studied. Wong and Einstein conducted a systematic evaluation of the crack behavior of such samples, with a single open flaw specifically, using a high speed camera [173]. They proposed to categorize the cracks emanating from the pre-existing flaws into seven types according to their trajectories and initiation mechanism, as shown in Figure 4.9.

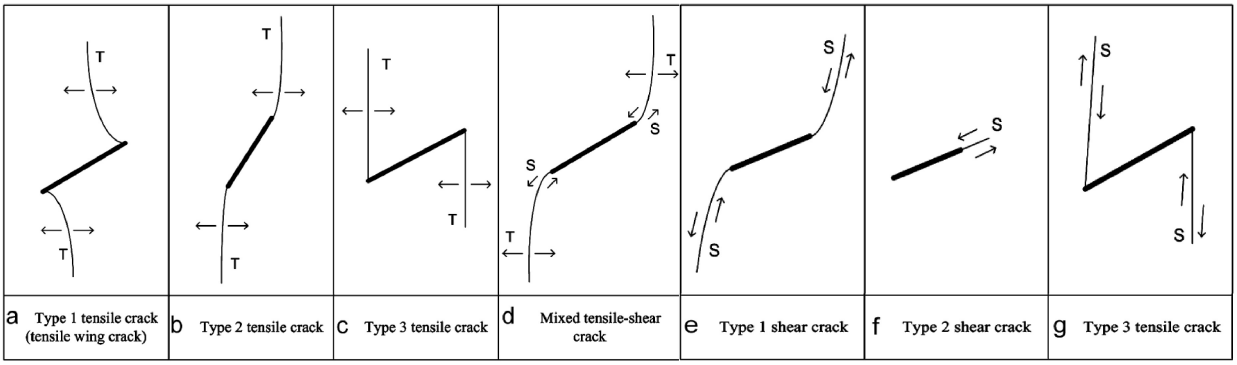

Figure 4.9: Various crack types initiated from the pre-existing flaws [173] (T = tensile cracking opening; S = shearing displacement)

A similar test was simulated using LEM to examine the macroscopic crack behavior induced by the solid lattice model. A rectangular plate sample with dimensions of 70 $\times$ 150 $\times$ 20 mm was created using lattices with a characteristic length of 1.7 mm, and the same microscopic properties as those used in the uniaxial tension test sample in the last section. The pre-existing open flaw, which is 20 mm long and has 45° inclination angle, was generated by removing corresponding lattices. The aperture is approximately 1.2 mm, which is much larger than the total applied displacement on the top surface (0.192 mm). Therefore, it could be ensured that there is no contact between the crack surfaces and that it remains open throughout the test. The sample was fixed at the bottom surface, and 0.003 mm downward displacement (strain increment $\Delta\epsilon = 0.002\%$) was applied on the top surface in each step.

The model configuration and fracture development process are shown in Figure 4.10. The fractures at the final step ($\epsilon = 0.128\%$) are classified into three groups and numbered based on the temporal sequence (Figure 4.11c). The tensile wing cracks (Group 1) start to emanate at the early stage ($\epsilon = 0.03\%$) and develop slowly afterward. The Type 2 tensile cracks (Group 2) initiate successively at the bottom and top tip of the flaw when ϵ is approximately 0.09% and 0.104% respectively, and subsequently develop in the vertical direction. When ϵ exceeds 0.12%, a large number of cracks emerge and develop rapidly in an inclined band roughly in the plane of the flaw, circled as Group 3 in Figure 4.11c. These cracks are distributed across the region instead of coalescing into a distinct major fracture. Nearly all the cracks in Group 1 and 2 originate from the tensile failure of the corresponding lattice, whereas Group 3 contains both tensile and sheared originated cracks. It should be noted that the origin of a single crack only represents the failure type of the corresponding lattice. Although it is strongly related to the macroscopic movement of the sample, it is not exactly equivalent. For example, the shear movement could generate both tensile and shear cracks, depending on the orientation and strength of lattices.

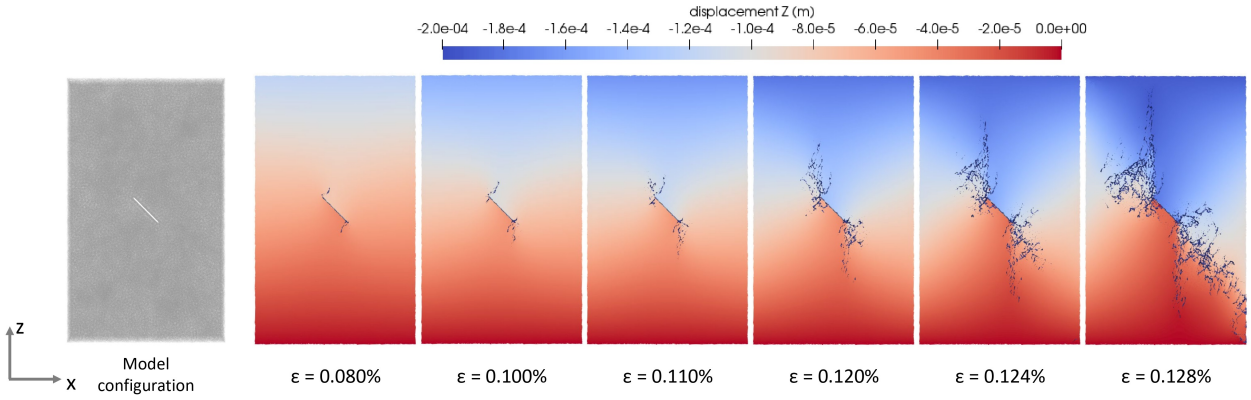

Figure 4.10: Model configuration, z displacement field and fracture pattern at different compressive axial strain ϵ

According to Wong and Einstein's experiments and review of other studies, the tensile wing cracks appear in every test and are the cracks that first develop in the vast majority of cases [173]. This is correctly simulated by the LEM model. While the types of subsequently emanated cracks vary from case to case, depending on various factors, such as material properties and geometry of the pre-existing flaw. In this simulation, the Type 2 tensile cracks develop following the tensile wing cracks. A similar pattern was observed in the experiments done by Ingraffea and Heuze [78], as shown in Figure 4.11a. Although in their case, these cracks originate from the circled locations, which are slightly away from the flaw tips. While the shear zone was observed by Lajtai, following the development of tensile wing cracks (Figure 4.11b) [92]. Although some of them combined into distinct shear cracks, which does not occur in this simulation.

In summary, the LEM simulation well predicts the pattern and temporal sequence of the tensile wing cracks. Due to the various factors that affect fracture behavior, overall fracture patterns vary between experiments. Therefore, the simulation does not exactly match the result of one particular experiment. But for each individual crack type generated by simulation, a similar pattern was observed in other studies.

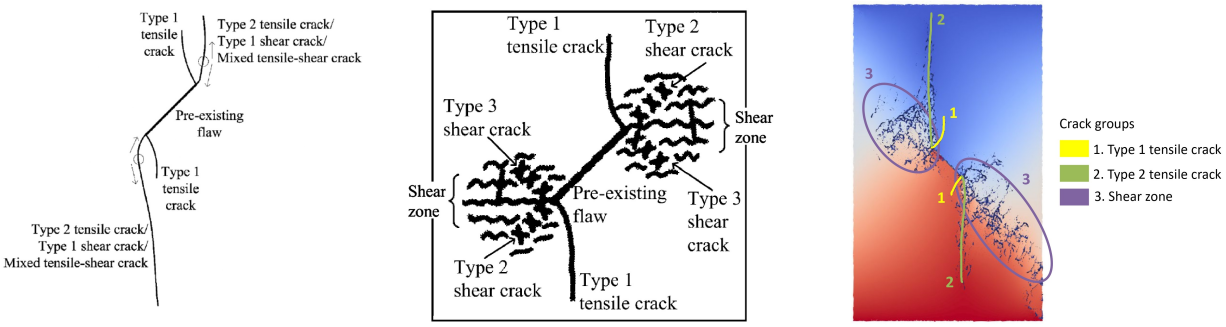

(a) Ingraffea and Heuze [78] (b) Lajtai [92] (c) Simulated crack groups

Figure 4.11: Sketch of crack patterns and types from other experimental studies [173] and the crack groups in this LEM simulation

4.2 Simulations of Four-Point-Bending Experiments on Mortar Beams

4.2.1 Background and Experimental Setup

In a previous experimental study aiming at investigating the feasibility of distributed fiber optic strain sensor (DSS) for early crack detection, four-point bending tests on mortar beams with a pre-installed single-edge notch were performed under different loading conditions. In this section, the same tests will be simulated using LEM and compared with the experimental results in order to investigate the capacity of LEM in modeling real fracture scenarios and its potential application in early crack detection.

Each mortar beam specimen has the dimension of 2000 × 200 × 240 mm, and a single notch with 0.5 mm aperture was installed in the middle of the top surface of the specimen. Three tests with different loading conditions and notch orientations were performed, as demonstrated in Figure 4.12. The specimens were subjected to symmetric loading in Case 1 and 3, while unsymmetric loading in Case 2. The notch is perpendicular to the longitudinal axis of the beam in Case 1 and 2, while it has a 45° inclination angle in Case 3. The depth of the notch is around 48 mm for Case 1 and 75mm for Case 2 and 3. With these configurations, it was expected that the failure modes would be tensile (Mode I), in-plane shear (Mode II) and anti-plane shear (Mode II) for Case 1, 2 and 3 respectively. The mortar was prepared by mixing standard Portland cement and fine aggregates, with a water-to-cement ratio of 0.5 and an aggregate-to-cement ratio of 3.0. The compressive strength of mortar in each case was measured by uniaxial compression test on cylindrical specimens, and the results are: 42.48 MPa for Case 1, 39.82 MPa for Case 2 and 49.47 MPa for Case 3.

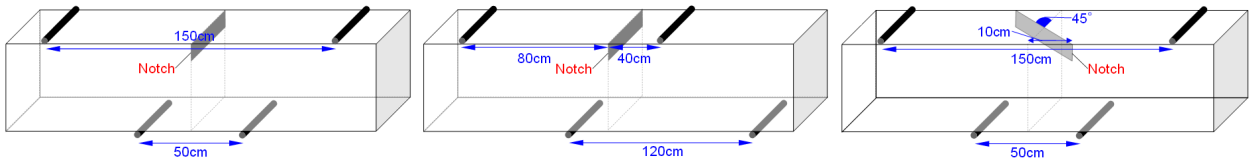

(a) Case 1 (b) Case 2 (c) Case 3

Figure 4.12: Sketch of setup for four-point-bending tests

The experimental setup is shown in Figure 4.13a and sketched in Figure 4.14a. The mortar beam was supported at the bottom by two steel rods serving as roller supports. The loading head was applied on top of the steel spreader beam, transferring the load to the two steel rods serving as top supports. Step-wise incremental displacement was applied on the loading head and DSS strain measurements from the interrogator units (IUs) were taken in between each loading step. The total displacements applied on the loading head at each step are shown in Figure 4.13b. The maximum applied displacements before failure

are 4.67 mm, 6.05 mm and 2.24 mm for Case 1, 2 and 3 respectively. The arrangement of DSS is shown in Figure 4.14a. The fibers were embedded in the specimens at seven different heights in four rows, and each cable of four rows was connected to different fiber optic IUs. The Rayleigh scattering based distributed sensors used in this study is in the second row from the left. The fibers are labeled Line 1 through Line 7 from top to bottom. The notch cuts through Line 1 in Case 1, and Lines 1 and 2 in Cases 2 and 3, respectively. The IU called the NBX 7020 based on TW-COTDR from Neubrex with 20 mm special resolution and 10 mm sampling interval was used. A 2.0mm diameter cable called NZS-DSS-C07 from NanZee was embedded in the mortar specimens. The cable structure is shown in Figure 4.14b. More detail about the theory and application of DSS can be found in [11][184]. Five linear variable differential transformers (LVDT) were set up at the bottom of the beam to measure the vertical displacements. The positions of supports and LVDTs for each case are listed in Table 4.3.

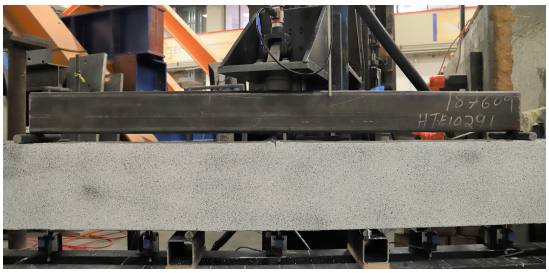

(a) Experimental setup (Case 1)

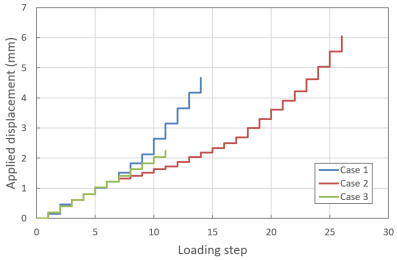

(b) Applied displacement on loading head at each loading step

Figure 4.13: Experimental setup and applied displacements

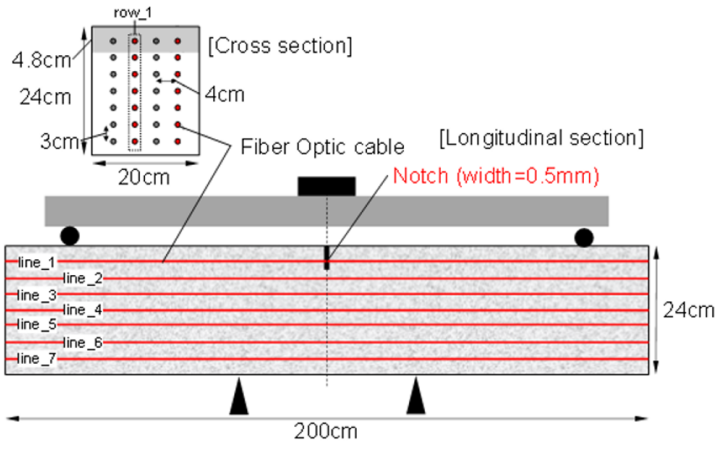

(a) Experimental setup and fiber arrangement (Case 1)

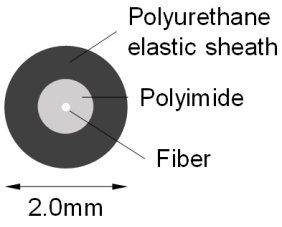

(b) Cable structure

Figure 4.14: Sketch of experimental setup and cable structure

Case	Support				LVDT				
	upper left	upper right	lower left	lower right	left outer	left inner	center	right inner	right outer
1	250	1750	750	1250	300	600	1000	1400	1700
2	200	1400	600	1800	300	700	1000	1300	1700
3	250	1750	750	1250	300	600	1000	1400	1700

*The values represent longitudinal distance to left end in mm

Table 4.3: Summary of positions of supports and LVDTs for each case

4.2.2 Numerical Model Setup

The LEM models are generated with the same dimensions as those mortar beams used in experiments. Figure 4.15 shows the Case 1 model as an example, which is 2000 mm in the x direction, 200 mm in the y direction and 240 mm in the z direction. The characteristic length of lattices is 12 mm. The elastic modulus of a single lattice is set to be 40 GPa and Poisson's ratio is 0.2, the resulting macroscopic Young's modulus is 27.1GPa, measured from the uniaxial tension test on these numerical beam samples. This value is close to the modulus of dry mortar materials. The notches are created by removing corresponding lattices across the notch planes. Ideally, the support should be a straight line parallel to the y axis, which intersects the faces of Voronoi cells on the bottom or top surface. The corresponding nodes of these cells are selected as support nodes to assign boundary conditions. The nodes at the bottom left support are fixed in all directions to simulate rigid support, while those at the bottom right support are fixed in the z direction as roller support. Constant displacement increment in the $-z$ direction is applied each time step on the nodes representing the two upper supports to simulate the displacement controlled test. In order to compare with the measurement from DSS, query lines are set at the fiber locations. Longitudinal displacements of the nodes within 1 mm of the line, which is the radius of the cable, would be recorded as measurements. As this is a discrete model, moving averages between adjacent seven nodes (spread over the length of approximately 20 mm, which is the special resolution of the IU) were taken to smooth the data. The gradient of displacement was computed as strain. Moving averages between the adjacent 25 data points were taken to further smooth the strain data.

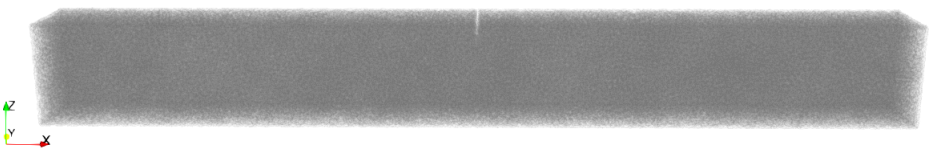

Figure 4.15: Experimental setup (Case 1)

4.2.3 Elastic Tests for Model Validation

The LEM models were first validated by comparing simulated deformations against the results from FEM simulations using the COMSOL Multiphysics [24]. Finite element models of these beams were created in the software with the same configurations. For each of the three cases, the same amount of downward displacement, 0.36 mm, was applied on the two upper supports of both the LEM and FEM models. The deformations were small such that these models were kept in the elastic range. Longitudinal displacements and strains at fiber locations were output, as shown in Figure 4.16 and 4.17. The results of LEM simulations match well with FEM.

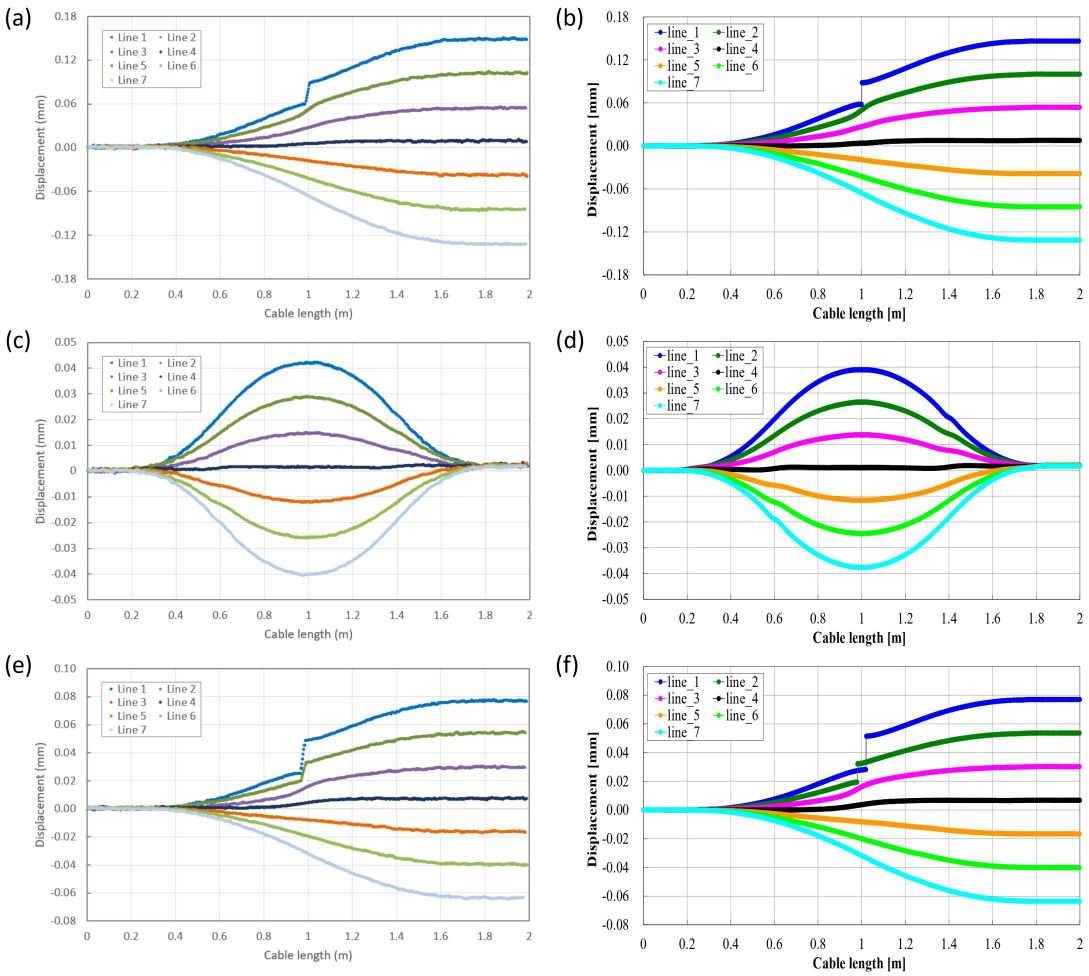

Figure 4.16: Longitudinal displacement at fiber locations ((a)Case 1 LEM; (b)Case 1 FEM; (c)Case 2 LEM; (d)Case 2 FEM; (e)Case 3 LEM; (f)Case 3 FEM)

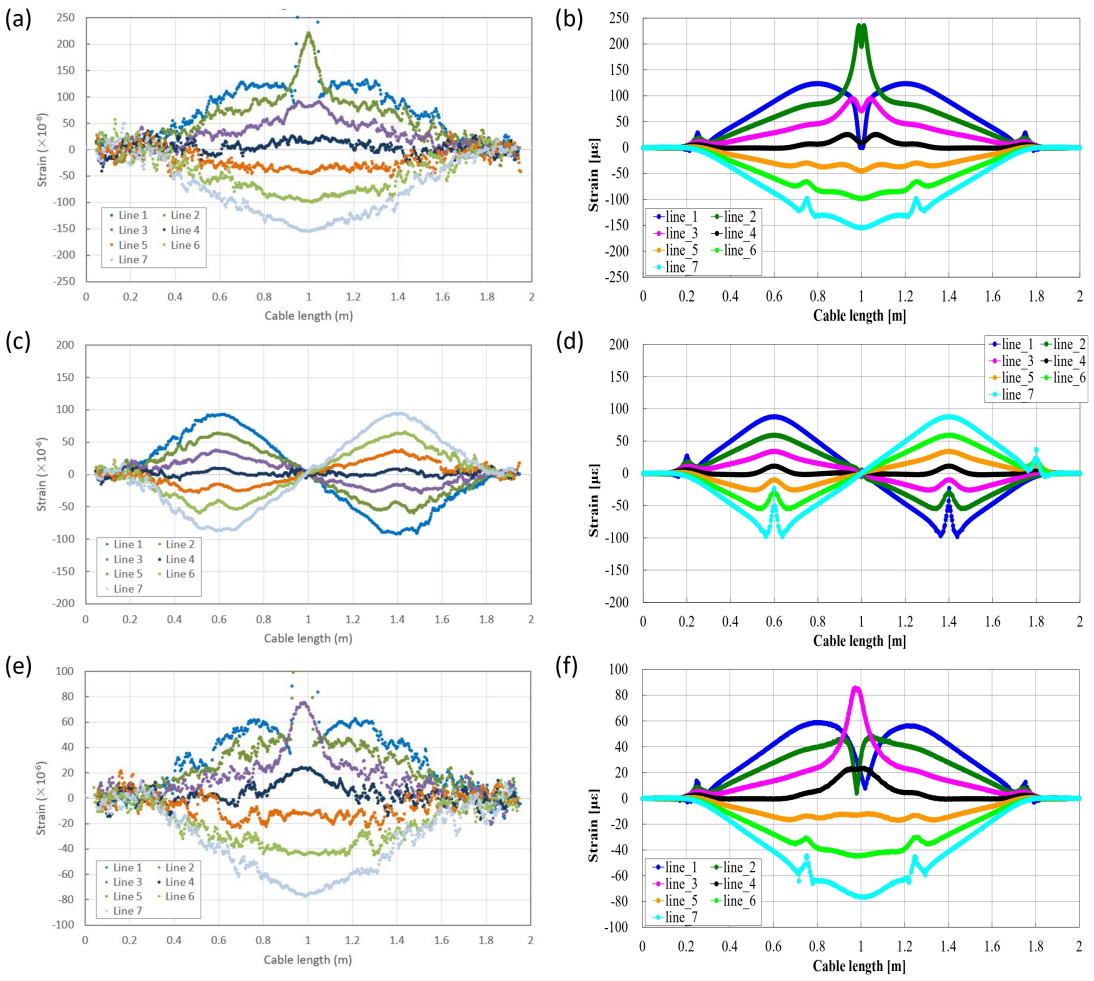

Figure 4.17: Longitudinal strain at fiber locations
((a)Case 1 LEM; (b)Case 1 FEM; (c)Case 2 LEM; (d)Case 2 FEM; (e)Case 3 LEM; (f)Case 3 FEM)

4.2.4 Comparison between Numerical and Experimental Results

There are three sets of data recorded in the experiments: 1) reactions and displacements of the loading head recorded by the loading system; 2) vertical displacements at the bottom surface measured by the five LVDTs; 3) longitudinal strains at the seven heights measured by the DSS.

According to these measurements and resulting fracture patterns, the vertical displacements of the two upper supports are approximately the same in Case 1 and 3 during the tests. However, due to the unsymmetric setup of Case 2, the displacement of the upper left support is larger (will be discussed later in this section). Therefore, in each step of the LEM

simulation, 0.01 mm downward displacements were applied on the two upper supports in Case 1 and 3, and on the upper left support in Case 2, while the displacement increment on the upper right support in Case 2 needs to be calibrated. Considering the mortar is a brittle material, the completely brittle lattice is used in the LEM model. Simulations with different lattice strengths and displacement increments on the upper right support for Case 2 were conducted to calibrate these parameters by comparing the results with experimental measurements. Finally, they were determined as: tensile strength $\sigma_{st} = 6.45$ MPa, shear strength $\sigma_{ss} = 10.5$ MPa, the ratio of displacement increment between the upper left and right support for Case 2 $d_{left}/d_{right} = 0.38$.

The experimental and simulated results with the calibrated parameters are shown below.

Fracture patterns

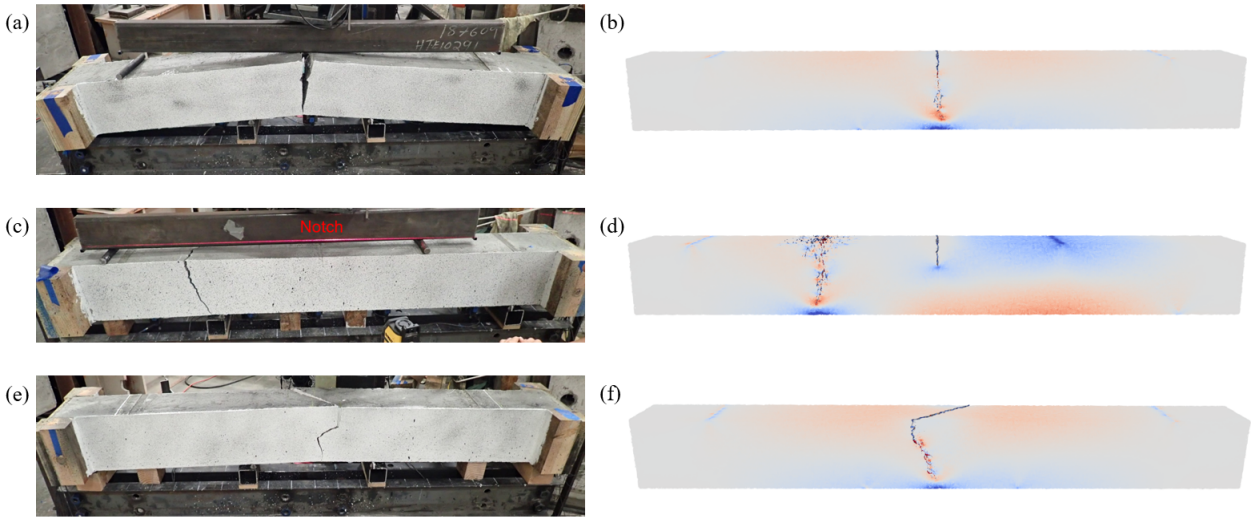

Figure 4.18: Fracture patterns and LEM stress fields (blue in compression, red in tension) ((a) Case 1 exp.; (b) Case 1 LEM; (c) Case 2 exp.; (d) Case 2 LEM; (e) Case 3 exp.; (f) Case 3 LEM)

As depicted in Figure 4.18, the simulated fracture patterns well match the experimental results of Case 1 and 2. In Case 1, the specimen was subjected to symmetric loading and the maximum moment occurred in between the two lower supports. Therefore, a tensile (Mode I) crack was developed from the notch and cut through the beam vertically. In Case 2, the specimen was subjected to unsymmetric loading, and the purpose of this setup was to generate an in-plane shear crack (Mode II) from the notch. However, a tensile crack developed at the location of the lower left support, which was intact initially, and the beam failed in bending. This behavior was also captured by LEM. The reason why this happened will be discussed later. For Case 3, the specimen with a 45° inclined notch against the

longitudinal axis was subjected to the same loading as Case 1. It was expected that anti-plane shear (Mode III) would occur at the notch. But this location was also subjected to the bending moment as in Case 1, thus the beam could also fail in tension, or more possibly the mixed behavior. The simulated and experimental fracture patterns are slightly different. The fracture developed straightly to the bottom in the simulation. In terms of the fracture tip, which was originally at the notch tip, it gradually rotated and eventually became approximately perpendicular to the longitudinal direction at the bottom surface. However, the experimental fracture shows a sharp turn in the path. The fracture tip was approximately perpendicular to the beam axis in the middle, where this turn occurred. The lower part of this pattern looks more like a tensile crack as in Case 1. This indicates that the angle between the initial crack path and vertical direction is larger in the experiment than simulation, which is possibly due to the combined effect of tensile and shear stress. While almost all the simulated fractures originated from tensile failure. Therefore, in this case, although the simulated and experimental fracture looks similar, the mechanism that generated them may be different.

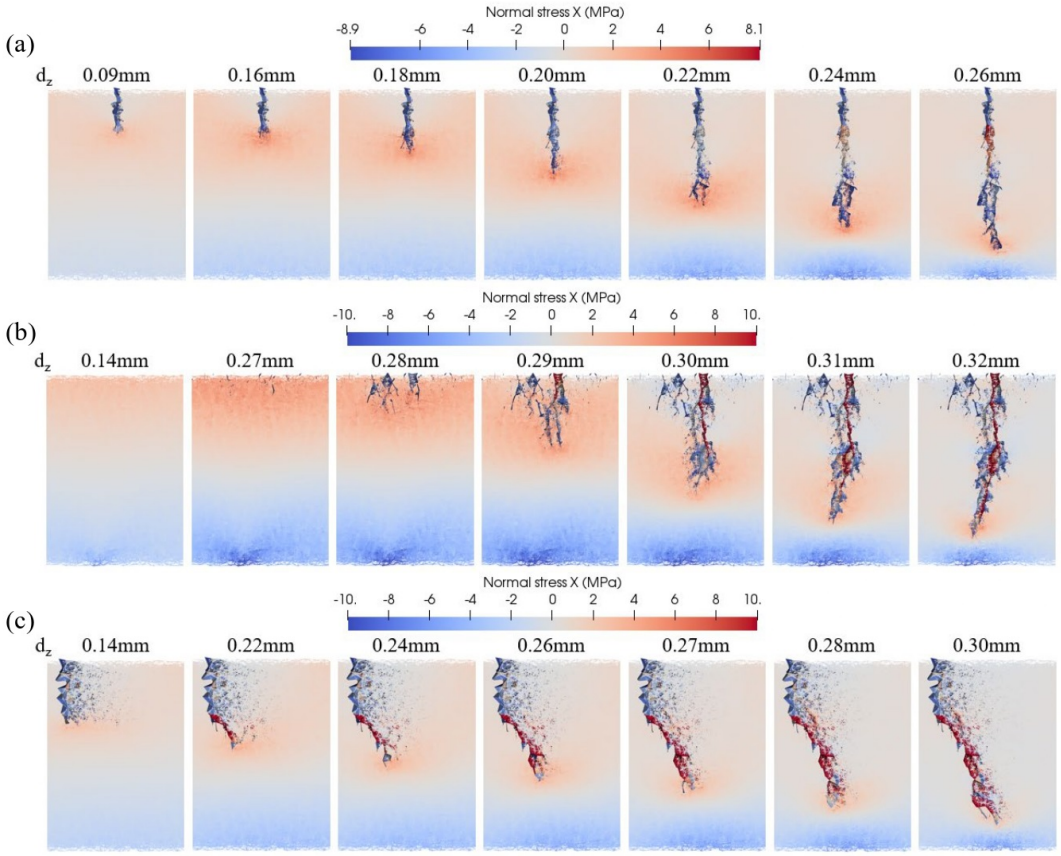

Figure 4.19: Main fracture development and stress field
((a) Case 1; (b) Case 2; (c) Case 3)

Figure 4.19 shows the fracture development processes for the three cases. For Case 1 and Case 3, the fracture only initiates from the tip of the pre-existing notch. Except for some micro-cracks that develop near the main fracture, other parts of the beam remain intact. Because tensile stress is concentrated at the notch tip, the stress levels of the lattices in this region are much higher and reach their strength, which leads to the breakage of lattices and results in the generation of micro-cracks. And as the fracture develops, the stress level on other parts of the beam is reduced due to the rebound of intact parts, thus no other fracture is generated. While no stress concentration occurs in Case 2, because the location that initiates the major fracture was originally intact. Instead, the stress levels over a relatively larger region are increased due to the bending moment. The breakage of lattices happens more randomly under the effect of heterogeneous lattice arrangement. Therefore, the initially developed fractures are more scattered. The stress could be concentrated once initial fractures appear, thus eventually forming a major fracture as in the other cases.

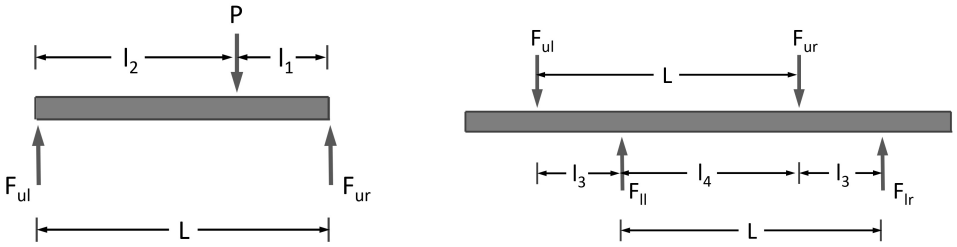

(a) Spreader beam (b) Mortar beam

Figure 4.20: Force equilibrium diagram (Case 2)

The reason that the expected shear fracture did not occur from the notch in Case 2 could be explained by a simple analysis of the beams. Assume the force applied on the spreader beam is P, and the distance from the loading head to the upper right and upper left support is l_1 and l_2 respectively (Figure 4.20a). Also assume that the distance between two upper supports is the same as that between two lower supports, and let it be L. According to moment equilibrium, the resulting force at the two upper support could be computed as,

$$F_{ul} = \frac{l_1}{L}P, \qquad F_{ur} = \frac{l_2}{L}P \tag{4.4}$$

For the mortar beam, let the distances from the lower right to the upper right support, and from the lower left to the upper right support, be l_3 and l_4 respectively (Figure 4.20b). Note that l_2 should be larger than l_3 to keep the system stable. Also according to moment equilibrium, the resulting force at the two lower support could be computed as,

$$F_{ll} = F_{ul} + \frac{F_{ul}l_3 + F_{ur}l_3}{l_3 + l_4} = F_{ul} + \frac{l_3}{L}P, \qquad F_{lr} = F_{ur} - \frac{F_{ul}l_3 + F_{ur}l_3}{l_3 + l_4} = F_{ur} - \frac{l_3}{L}P \tag{4.5}$$

Therefore, the shear force and moment diagram of the mortar beam could be obtained, as depicted in Figure 4.21. The shear force at the middle of the beam, where the notch is located, is $\frac{l_3}{L}P$, while the local maximal moments appear at the locations of the lower left and upper right support, is $\frac{l_1 l_3}{L}P$ and $\frac{(l_2-l_3)l_3}{L}P$ respectively.

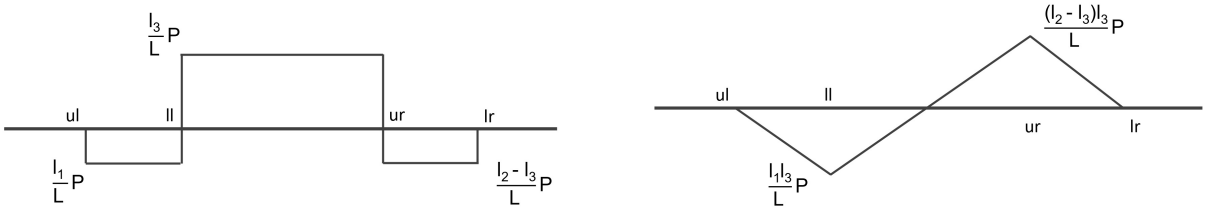

(a) Shear force diagram

(b) Moment diagram

Figure 4.21: Shear force and moment diagram for mortar beam (Case 2)

The shear stress on the cross section at middle of the beam is,

$$\tau = \frac{V}{A} = \frac{\frac{l_3}{L}P}{bh_n} = \frac{l_3}{Lbh_n}P \tag{4.6}$$

While the maximum tensile stresses on the cross sections at the lower left and upper right support, are,

$$\sigma_{ll} = \frac{M_{ll}c}{I} = \frac{\frac{l_1 l_3}{L}P\frac{1}{2}h}{\frac{1}{12}bh^3} = \frac{6l_1 l_3 P}{Lbh^2} \tag{4.7}$$

$$\sigma_{ur} = \frac{M_{ur}c}{I} = \frac{\frac{(l_2-l_3)l_3}{L}P\frac{1}{2}h}{\frac{1}{12}bh^3} = \frac{6(l_2-l_3)l_3 P}{Lbh^2} \tag{4.8}$$

Where b is the width of the beam, h_n and h are the heights at the middle and supports respectively. The values of l_1 and l_2 were not recorded in the experiment. According to the reactions at the upper supports recorded in simulation during the elastic stage, $F_{ur}/F_{ul} = l_2/l_1 = 1.5$, and $L = 1200$ mm inferring that, $l_1 = 480$ mm, $l_2 = 720$ mm. In this simulation, the other parameters, $l_3 = 400$ mm, $l_4 = 800$ mm, $b = 200$ mm, $h = 240$ mm, $h_n = 165$ mm. The shear and tensile stresses at the critical cross sections, expressed in terms of the applied force P, are,

$$\tau = 1.01 \times 10^{-5}P, \quad \sigma_{ll} = 8.33 \times 10^{-5}P, \quad \sigma_{ur} = 5.55 \times 10^{-5}P \tag{4.9}$$

Therefore, in this case, the maximum tensile stress occurs at the location of the lower left support and is around 8 times larger than the shear stress in the middle. This beam should fail in bending at the lower left support, and this is what was observed in both the experiment and simulation. As for the condition to initiate a mode II shear failure at the notch location, considering the ratio between shear and tensile stress in Equation 4.6, 4.7 and 4.8, both l_1 and $l_2 - l_3 = l_4 - l_1$ should be small, which means the lower left and upper right support should be much closer. Therefore, the experimental setup for Case 2 is problematic.

Reaction curves

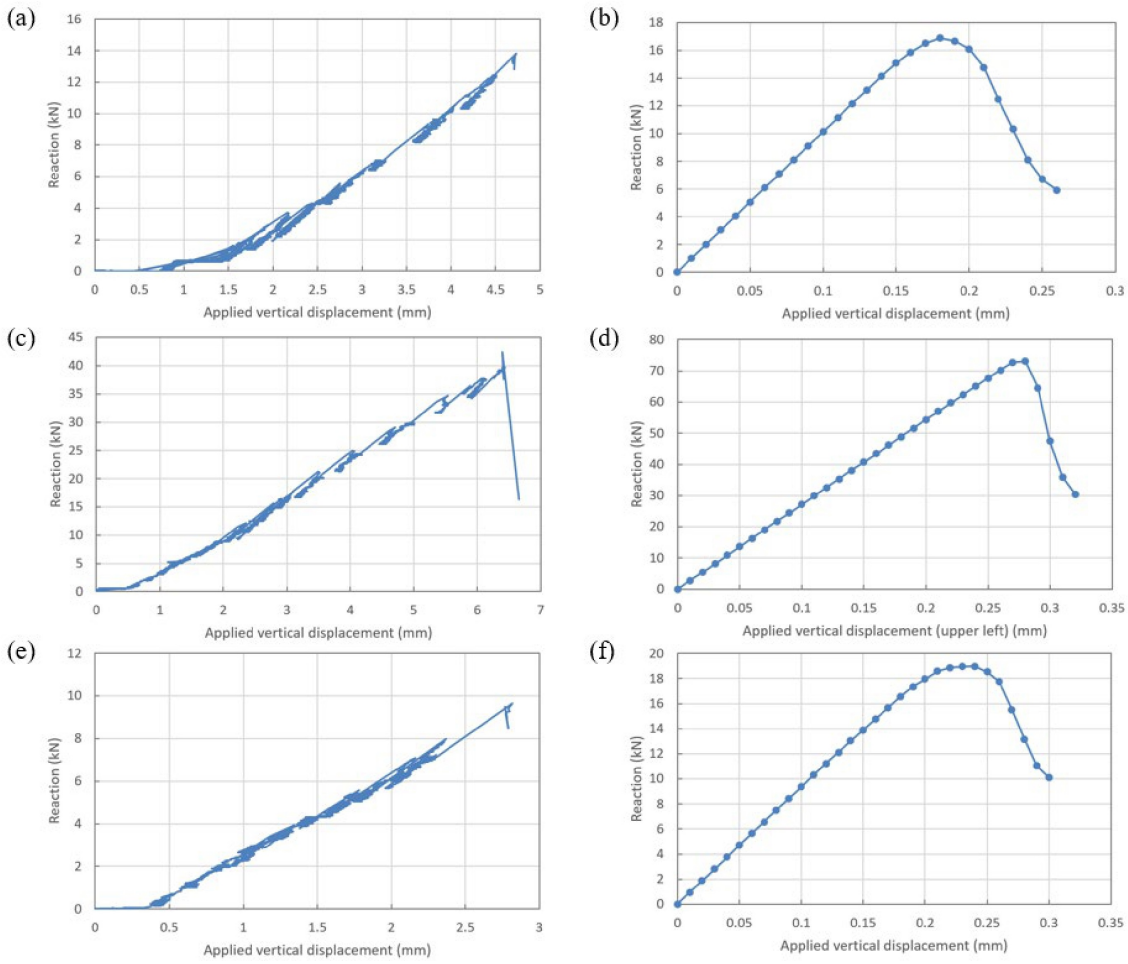

Figure 4.22: Reaction-Applied Displacement curves ((a) Case 1 exp.; (b) Case 1 LEM; (c) Case 2 exp.; (d) Case 2 LEM; (e) Case 3 exp.; (f) Case 3 LEM)

Figure 4.22 depicts the reaction curves for all the cases. Although the applied loading head displacements are step-wise in the experiments, as shown in Figure 4.13b, a slight rebound occurred in between each step as DSS measurements were taken, which are reflected in the reaction curves.

In the beam theory, under bending moment, yielding will occur at the edge of cross section, where resulting tensile stress is maximized. While microscopically in the LEM model, the lattices in this region are subjected to large tensile force, resulting in the failure in tension and development of mode I fracture. However, the lattices at the bottom surface would always be in compression under this loading condition. Because a lattice is the smallest unit

in this discrete model, and the bending failure of a single lattice is ignored in the model, these lattices would not break. Therefore, the bending initiated tensile crack cannot cut through the section, and its propagation slows down as it approaches the bottom. This explains the decreasing post-peak slope in the simulated reaction curves at the end stages. While due to the rapid development of the main fracture after the peak reaction, the experiment was not able to capture the post-peak behavior of the beam. Although the simulated results in this stage cannot be validated, they are likely not affected by the bottom lattices before the fracture approaches and the occurrence of decrement in slope.

The simulated peak reaction is close to the experiment in Case 1 but is much larger in Case 2 and 3. As discussed in the last section, the failure in Case 3 is likely to be governed by the combined effect of tensile and shear stress in the notched section. However, in the lattice model, the failure criteria consider the effects of tensile and shear separately (Equation 3.32), which leads to overestimating the strength in the combined scenario as in Case 3, where the contribution from tensile and shear are comparable. Although further reducing the shear strength of lattices could possibly match the experimental results, this would result in an unreasonably low shear strength value and still could not precisely represent the failure mechanism. Therefore, this test case reflects a shortage of this lattice model. It may be adequate to model the case dominated by a single loading type. However, more sophisticated failure criteria that account for the combined effect should be established if it is to be used in such circumstances, especially when predicting the sample strength.

Note that the applied displacements on the upper supports in the simulation are much smaller than those recorded on the loading head in the experiment. Because of the experimental setup, the spreader beam and wooden supports at the bottom deformed during the loading process. Therefore, the actual displacement applied on the mortar beams should be much smaller. This is reflected by the photos recorded during the experiment and could also be shown by a simple beam analysis.

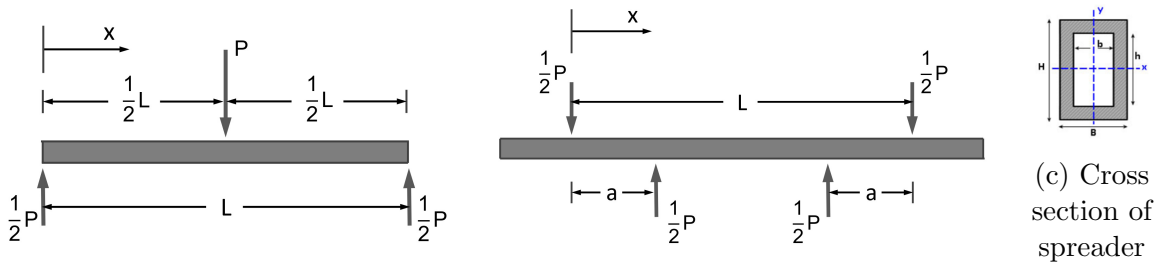

(a) Spreader beam (b) Mortar beam (c) Cross section of spreader beam

Figure 4.23: Force equilibrium diagram (Case 1)

Consider Case 1 as an example, assume the loading is P applied at the middle of spreader beam (Figure 4.23a), the deflection at this point, against the end, is given as [48],

$$\delta_{mid} = \frac{PL^3}{48EI} \tag{4.10}$$

The steel spreader beam has a rectangular hollow section (Figure 4.23c), with an estimated height of 0.121 m, outer width of 0.0387 m and thickness of 0.005 m, resulting in the second moment of inertia, $I = 2.442 \times 10^{-6}$ m^4. Assume its Young's modulus $E = 200$ GPa, the deflection at the middle of the spreader beam could be estimated, in terms of the loading, as,

$$\delta_{mid}(mm) = 1.439 \times 10^{-1} P(kN) \tag{4.11}$$

For the mortar beam, the deflection against upper left support is,

$$\delta(x) = \frac{\frac{1}{2}Px}{6EI}(3aL - 3a^2 - x^2) \qquad 0 \leq x \leq a \tag{4.12}$$

Thus the difference of deflection between upper and adjacent lower support, which is applied deflection on the mortar beam, is,

$$\delta_{applied} = \delta(a) - \delta(0) = \delta(0.5) - \delta(0) = \frac{5}{324}\frac{PL^3}{EI} \tag{4.13}$$

The second moment of inertia, I, is expected to be bounded by those of rectangular cross sections with heights 192 mm and 240 mm (without and with the notch). That is, $I = 1.180 \times 10^{-4}$ to 2.304×10^{-4} m^4, while $E = 27.14$ GPa, $L = 1.5$ m, thus the applied deflection on the mortar beam could be estimated, in terms of the loading, as,

$$\delta_{applied}(mm) = (0.833 \times 10^{-2} \ to \ 1.626 \times 10^{-2}) P(kN) \tag{4.14}$$

Therefore, the applied displacement on the upper supports of the mortar beam is approximately ten times the deflection at the middle of the spreader beam, which matches the magnitude of experimental and simulated displacements in the reaction curves. Therefore, the loading head displacement is unreliable for comparison purposes.

Relative displacements at bottom surface

Although the measurement of LVDTs on the bottom surface of the beam is affected by the possible deformation of bottom supports, the difference between these values reflects the differential displacement of the beam, which may be relatively more accurate and thus could be used to calibrate LEM results. As shown in Figure 4.24, the reference point is set at the middle of the beam, simulated vertical displacements of the bottom surface at peak reaction and during crack development processes are plotted together with measured values at the largest applied displacement in the experiment. The numbers in the legends represent the applied displacements. For Case 1 and Case 3, the simulated deformation during crack development matches experimental results. While due to the unsymmetric loading in Case 2, more deformation occurred at the bottom left support, which led the mortar beam to slightly rotated. The simulated deformation matches measured results after rotating approximately 0.03° against bottom right support (Figure 4.24c).

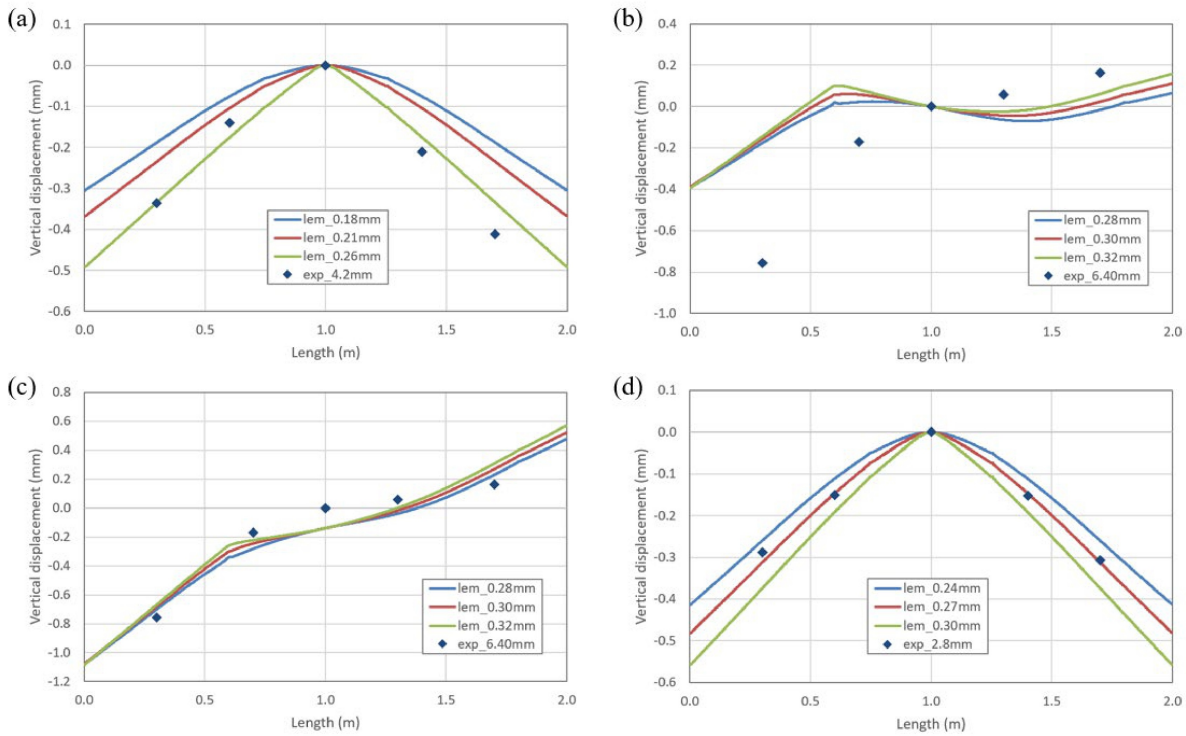

Figure 4.24: Vertical displacement at bottom surface along the beam ((a) Case 1; (b) Case 2; (c) Case 2 (rotated); (d) Case 3)

Longitudinal strains

The experimental and simulated longitudinal strain along fibers are shown in Figure 4.25 to 4.27. The experimental data were measured at the largest applied loading head displacement, while the simulated data presented here were recorded at peak reaction, and two steps afterward in the post-peak stage, to show the influence of crack development on the strains. The DSS were embedded in the beams so that the measurements would not be affected by the supports or loading frames as other data. Therefore, this strain data is more reliable to compare and be used for calibration.

For Case 1, generally the simulated strain at peak reaction (Figure 4.25b) matches experimental values at the top and bottom layers of fiber. The main difference is that Line 5 is in tension in the experiment while in compression in the simulation. The most possible reason is that this fiber was not precisely placed at the indicated location during installation. This is supported by the measurements from the same fiber during earlier stages, which also gives tensile strain consistently. Another possibility is that the development of cracks near the notch shifts the cross sectional neutral axis below this line. However, this should affect the entire section, including measurements from other fibers, which is not the case. Micro-cracks initiated near this fiber may generate tensile stress, but this influence should be limited lo-

cally within a small region instead of resulting in tensile measurements throughout the entire fiber. Therefore, it is more probable that there are installation issues with this fiber. As the crack develops, stress within the beam is released and thus the overall simulated strain decreases, except at the middle part in front of the crack tip, which becomes in tension and increases rapidly as the crack approaches. The measurements become discontinuous once the fiber is cut through by the crack, which indicates the position of the crack tip.

For Case 2, more deformation happens on the left part of the beam due to the unsymmetric loading. The strain is expected to have a similar magnitude at the top (Line 1) and bottom (Line 7) layers of fiber. However, the measurement indicates that the strain at the top is approximately 50% less than that at the bottom. As this difference appears throughout the entire fiber, it may be due to the installation problem as well. It is also possible that the development of micro-cracks near the top surface under tension reduces the strain level at this part. The simulated strains at peak reaction (Figure 4.26b) match the measurement of the bottom fiber. As the crack initiate and develop from the top surface, the strains at the top fiber reduce and become close to the measurements (Figure 4.26c), but only at the left part of the beam where fractures occur.

For Case 3, the strain distribution looks similar to that in Case 1 due to the same loading condition. The experimentally measured strains are smaller than the simulated values, indicating that the failure occurred with less deformation. This is due to the combined failure mechanism as discussed in previous sections.

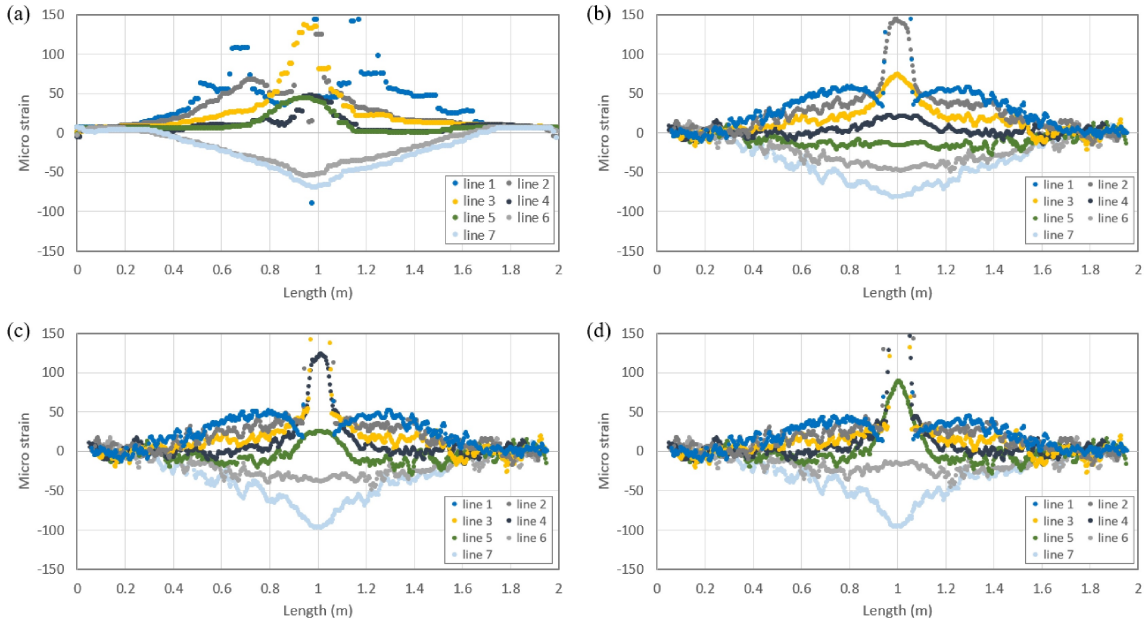

Figure 4.25: Axial strain at the fiber locations (Case 1)
((a) exp (4.17mm); (b) LEM (0.18mm); (c) LEM (0.21mm); (d) LEM (0.22mm))

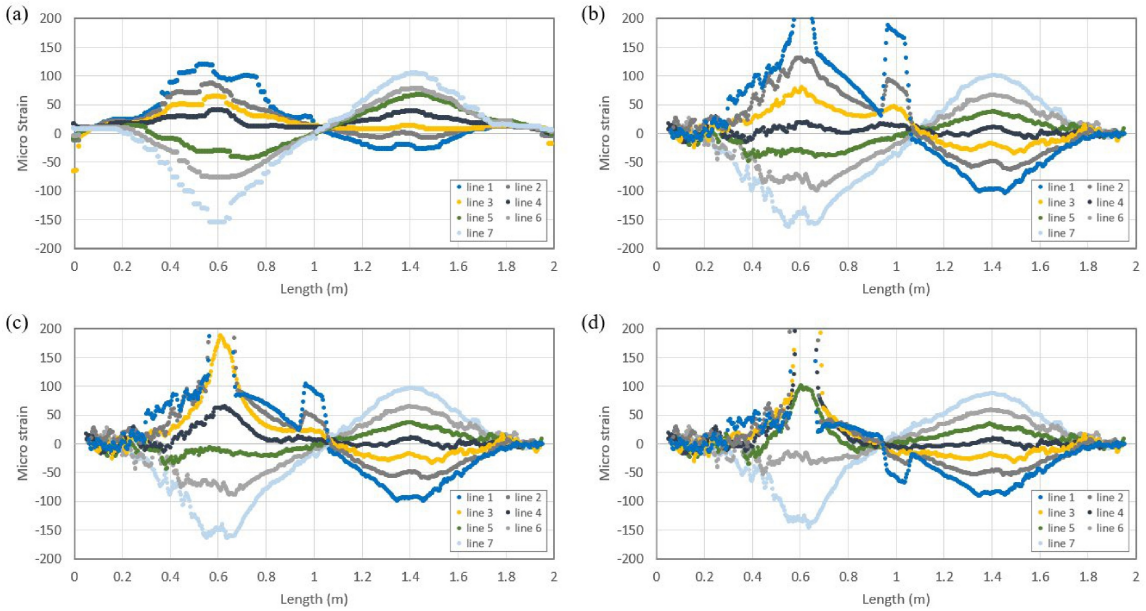

Figure 4.26: Axial strain at the fiber locations (Case 2)
((a) exp (6.05mm); (b) LEM (0.28mm); (c) LEM (0.29mm); (d) LEM (0.30mm))

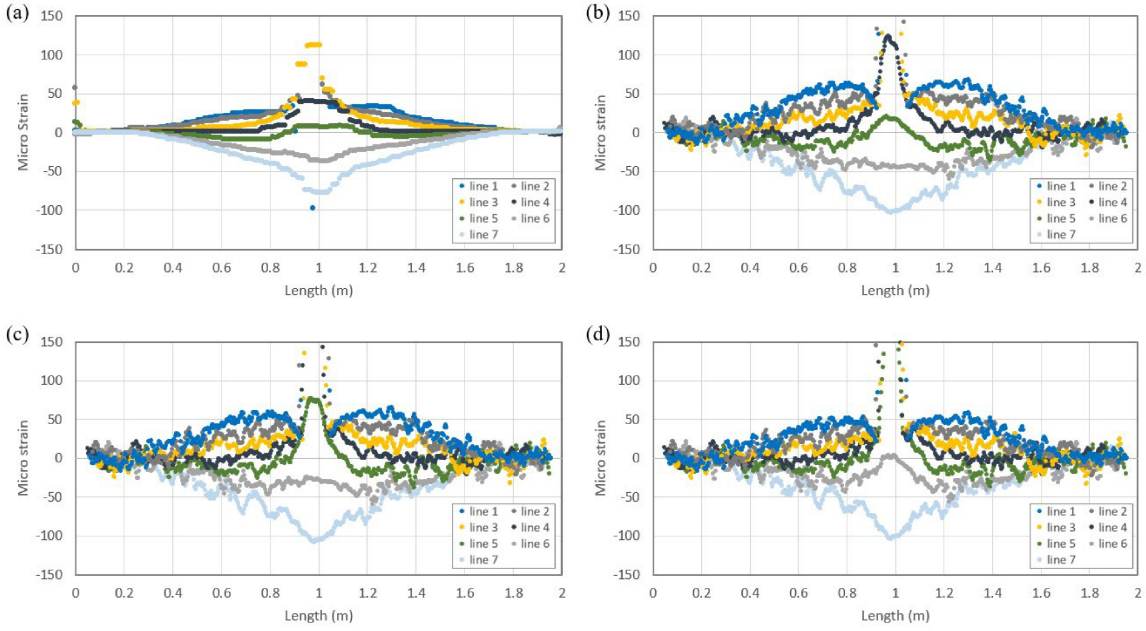

Figure 4.27: Axial strain at the fiber locations (Case 3)
((a) exp (2.24mm); (b) LEM (0.24mm); (c) LEM (0.25mm); (d) LEM (0.27mm))

4.2.5 Potential Usage of the LEM in Crack Detection

One of the strengths of LEM is that it can capture the states of a specimen during the rapid process of fracture propagation, which is hard to achieve in experiments. The strain field is one of the quantities that could be measured in structural health monitoring [11], and it is affected by the stress field induced by crack development. The simulation could possibly provide a correlation between the strain field and crack location, which may be helpful in interpreting the monitored strain values for crack detection.

Estimation of experimental strain and crack tip distance

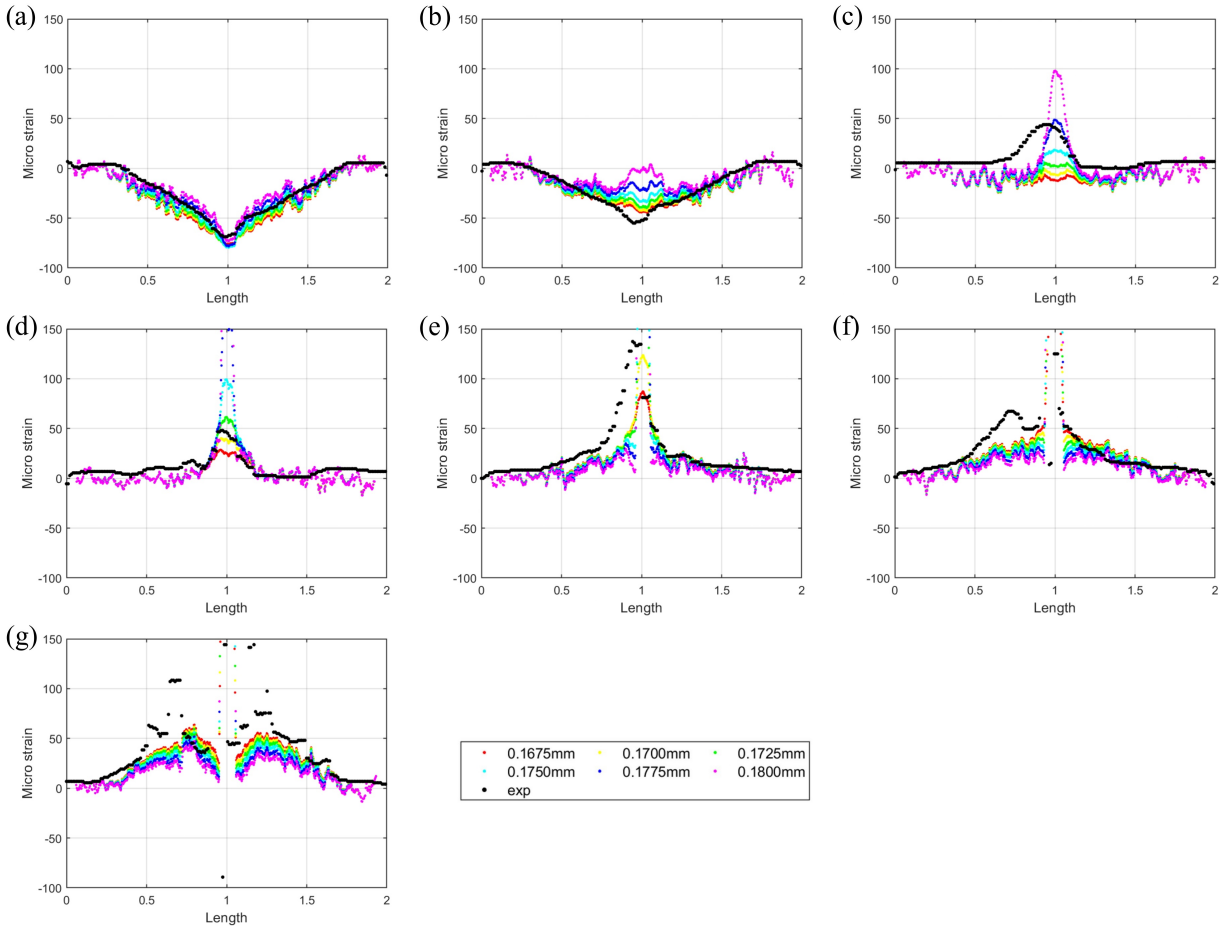

Figure 4.28: Matching experimental strain curve with simulation at different applied support displacements (Case 1)
((a) Line 7; (b) Line 6; (c) Line 5; (d) Line 4; (e) Line 3; (f) Line 2; (g) Line 1)

The tip position of the main fracture is recorded at every time step in the simulation. For each fiber location that is in front of the fracture, its distance to the fracture tip could be computed. Together with strain value at these points, the relation between strain and distance to fracture tip could be established. But in the experiment, only the strain values are measured by the fibers, while the distance from the corresponding fiber to the fracture tip remains unknown. The simulated strains at different time steps could be utilized to compare with measured values to correlate each experimental step with the possible simulation step, thus using the simulated crack tip distance at this step as an approximation for the experimental value.

As shown in Figure 4.28, take experimental measurements at the largest applied loading head displacement (4.17 mm) in Case 1 as an example. For each fiber location, the overall shape of the experimental strain curve is compared with simulated strain curves under different applied upper support displacements in order to determine which simulation step most closely matches the experiment. The similarity between experimental and simulated curves is evaluated both by eyes and some statistical measures, such as Procrustes distance. However, as some of the adjacent simulation steps give very similar strain curves, there are several possible simulation steps matched for each experimental curve. And different experimental curves match different simulation steps. Also considering the experimental results at smaller loading head displacements, the final results, which relate the measured strain and estimated crack tip distance, are shown in Figure 4.29. For each strain value at the middle of the beam, measured by a fiber at certain applied loading head displacement, there are several possible values of crack tip distance and the range (connected by the dashed line) is relatively large. In this case, the uncertainty may be excessive and render this plot meaningless. This process may be more useful if the uncertainty could be reduced.

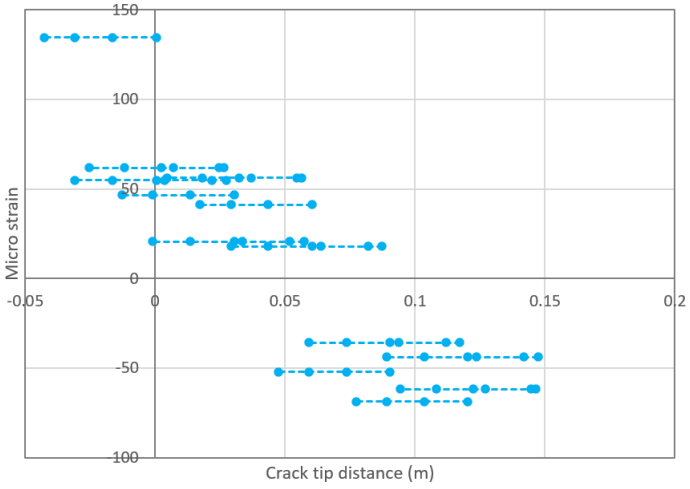

Figure 4.29: Measured strain values (at notched section) with possible range of crack tip distance (Case 1)

Simulated strain vs crack tip distance

Now consider the relation between strain and crack tip distance established by purely the simulation results. In the four-point-bending case, besides the influence of the crack tip, the strain at the notched section is also affected by the bending moment and varies with the cross section as fracture develops. In order to eliminate the contribution to the strain field by the loading, and investigate the influence of mesh size, another set of simulations was conducted.

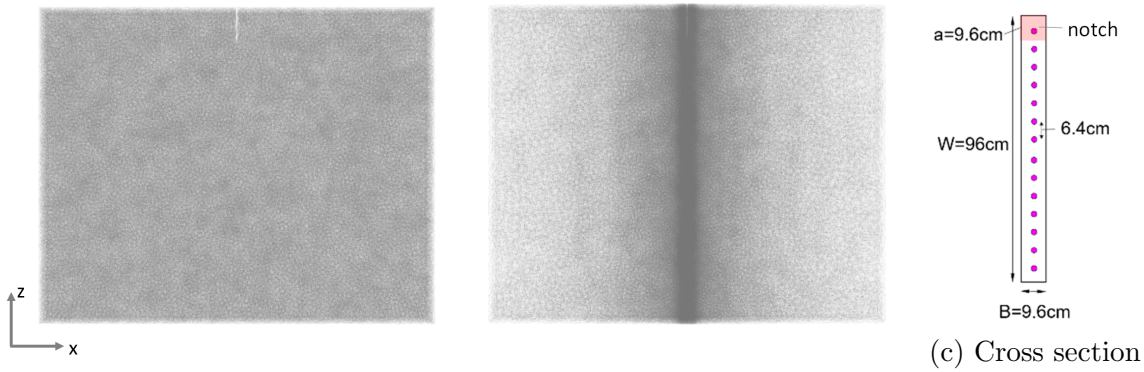

(a) Plate 1 (b) Plate 2 (c) Cross section at middle

Figure 4.30: Configurations of plate model and fiber arrangement

Two plate models of the dimension 1200 × 96 × 960 mm, with a 96 mm height single notch at the middle, were created. The characteristic length of lattices in Plate 1 is 12 mm, while that in Plate 2 varies from 25 mm (edge) to 5 mm (center). The model configurations and cross section are shown in Figure 4.30. The query lines (fibers) are labeled from top to bottom, as Line 1 to Line 14. All the lattice properties are the same as those in the four-point-bending tests. The $-x$ surface of the model is fixed and 0.0025 mm tensile displacement is applied on the $+x$ surface. The longitudinal strain field induced by this uniaxial tensile loading could be easily computed and is approximately constant throughout the sample. According to the principle of superposition, the strain value due to the influence of the crack tip could be obtained by subtracting this value from the recorded strain at the fiber location.

Under prescribed loading, mode I fracture initiates from the notch and propagates toward the $-z$ direction. In each simulation step, the longitudinal strains along each fiber were computed by taking the gradient of longitudinal displacement of the nodes whose distance from the query line is within the sampling radius r_q (10 mm for Plate 1, 10 mm and 2 mm for Plate 2). The strain value at the notched section (middle plane) was recorded, together with the distance from the crack tip to the corresponding fiber. The relation between strain and crack tip distance could thus be established, as shown in Figure 4.31. The strains are approximately zero before the crack tip approaches, except the bottom fiber (Line 14), which is slightly in compression. This is because constant displacement increment was applied on

the two side faces ($-x$ and $+x$), the forces acting on the parts above the crack tip generate a bending moment on the lower part of the plate, which, in this case, is similar as a beam under bending. As the fracture propagates downward, the cross sectional area decreases, which increases the influence of this moment. Therefore, the bottom fiber is in compression when the crack tip is far away. Similarly, this bending moment is likely to generate tensile strain on the parts close to the crack. But this effect is relatively small compared with that of the crack tip, especially for the fibers in the upper part of the plate, when the cross sectional area is large and the influence of this moment is negligible. Regardless of the bottom fiber, in each case, the records at different fiber locations follow a similar trend and form a curve. Despite the difference in mesh size and sampling radius, the curves from different cases look nearly the same, which shows the rapid strain increment as the crack tip approaches. Because the completely brittle lattice is used in the model, this demonstrates the capability of LEM to capture the purely elastic strain field induced by the crack tip before its arrival. But in case the crack tip distance is smaller than the sampling radius, the nodal displacements may be averaged from elastic deformation (intact lattice) and free movement (broken lattice), which is physically meaningless. Thus the computed strain value in this small crack tip distance is unreliable. It should be noted that the value of crack tip distance when strain starts to increase, and the strain value when the crack arrives, varies with lattice properties such as elastic modulus and strength, as well as the loading condition. These factors should be calibrated before utilizing this method to give predictions in practice.

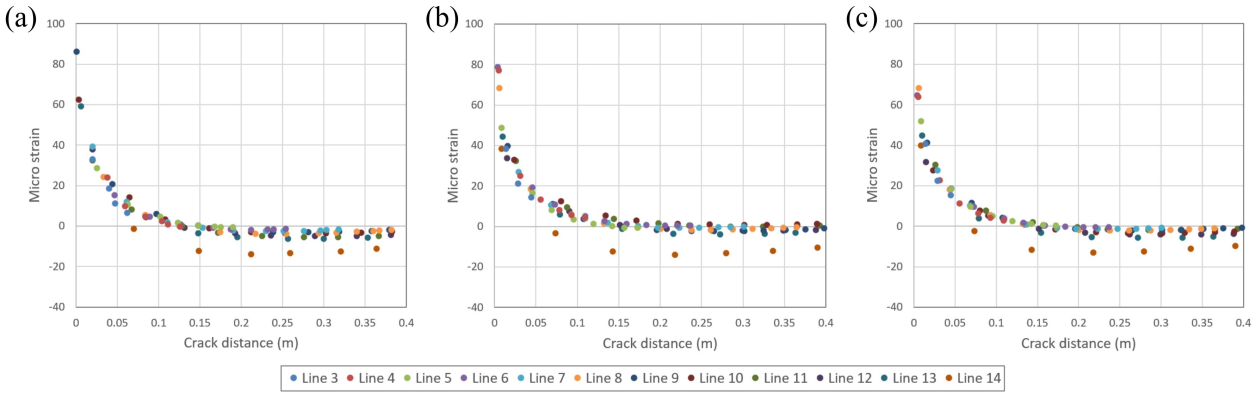

Figure 4.31: Strain vs crack tip distance
((a) Plate 1, $r_q = 10$ mm; (b) Plate 2, $r_q = 10$ mm; (c) Plate 2, $r_q = 2$ mm)

However, in most materials, there would be a plastic zone around the crack tip and resulting in plastic strain, which cannot be ignored. Since the softening behavior is implemented in this lattice model, it potentially could also be used to simulate this combined elastic and plastic strain, but it needs very careful calibration and possibly extremely fine mesh size, which may be difficult in practice. As illustrated in Figure 4.32, the size of the plastic zone should be first estimated [17], then appropriate lattice fracture energy and strength could be

selected so that the lattice reaches peak stress and starts yielding once it enters the plastic zone, and its residual stress becomes zero as the crack tip arrives.

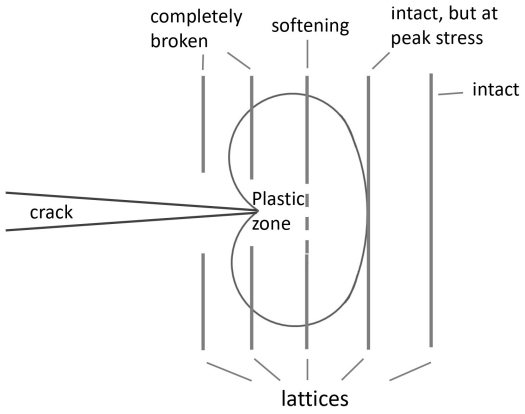

Figure 4.32: Sketch of possible way to simulate plastic strain around crack tip

4.3 Uniaxial Compression Tests on Cylindrical Samples with Different Ductility

The implementation of the softening lattice model facilitates LEM to simulate ductile materials. Although there are multiple definitions of ductility, one commonly accepted description is that, the capacity for enduring substantial, non-localized post-yield strain without notable strength loss and gross fracturing on the scale of the specimen [132]. This is a purely macroscopic or phenomenological definition, without any implication on the microscopic mechanisms, which involve various factors, such as crystal plasticity, micro cracking and pore collapse, and are highly dependent on the materials and loading types [174][160]. Similarly in this lattice model, although the implemented softening behavior does not physically represent the actual mechanism, it enables the lattice to sustain loading after yielding. Consequently, as an assemblage of lattices, the whole model is expected to endure greater strain for the same amount of strength loss, which corresponds to the definition of ductile behavior.

Laboratory studies indicate that confining pressure in the triaxial test significantly affects the ductility of the samples [132][174]. For example, Figure 4.33 depicts the triaxial test results of marble samples at various confining pressures conducted by Paterson [131]. As the confining pressure increases, the stress strain curves show greater peak stress value and strain level at macroscopic failure. There is also an increasing tendency for the curve to continue rising and eventually exhibit strain hardening behavior. The failure mode changes from axial splitting to localized shear fracture, conjugate fracture pairs, and eventually cataclastic flow. With increasing ductility, the shear zone broadens and deformation occurs outside the shear zone as well.

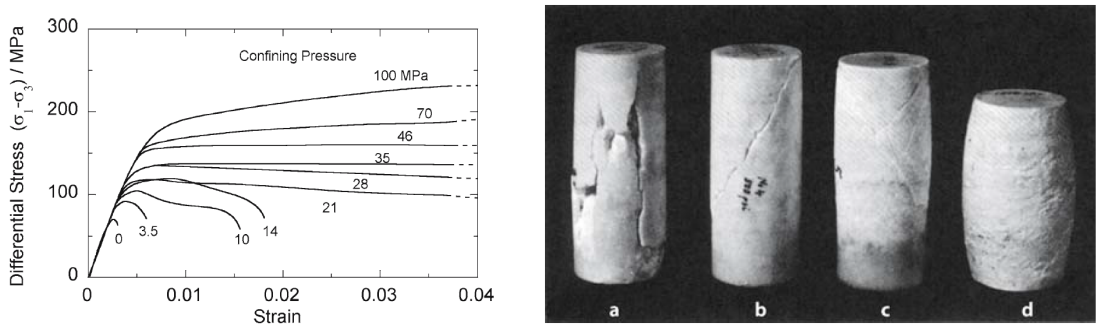

(a) Stress strain curves (b) Failure patterns

Figure 4.33: Triaxial test results at various confining pressures by Paterson[131]

In this set of simulations, uniaxial compression tests were conducted on cylindrical samples with different lattice fracture energy to show the influence of plastic lattices on the macroscopic behavior of the samples. The sample dimensions are 0.02 m in radius and 0.1 m in height. The lattice has the following microscopic properties: elastic modulus of 40 GPa, Poisson's ratio of 0.2, tensile strength of 6.45 MPa, shear strength of 10.5 MPa, and its characteristic length is 0.0013 m. Different values of axial and transversal fracture energy were assigned to lattices in different models. The resulting reaction curves for a single lattice are shown in Figure 4.34. The samples are fixed at the bottom, and 2×10^{-6} m longitudinal compressive displacement was applied on the top surface in every step.

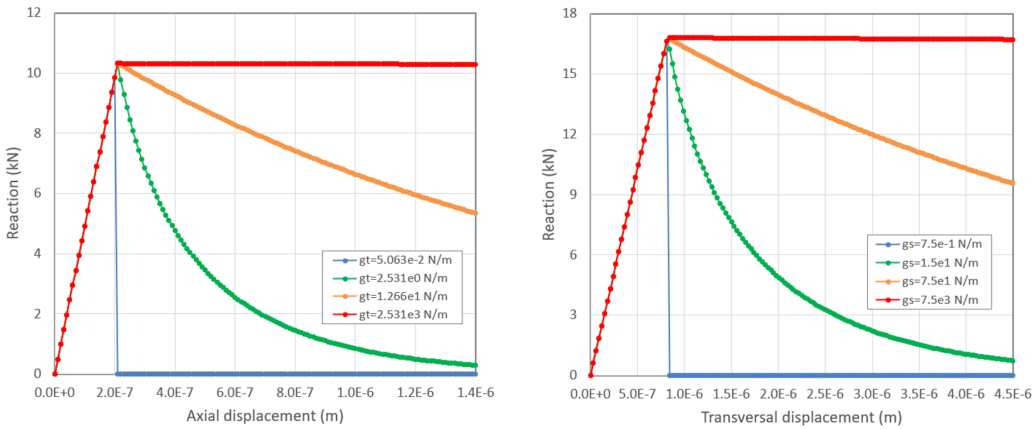

(a) Axial (b) Transversal

Figure 4.34: Reaction curves for single lattice with different fracture energy

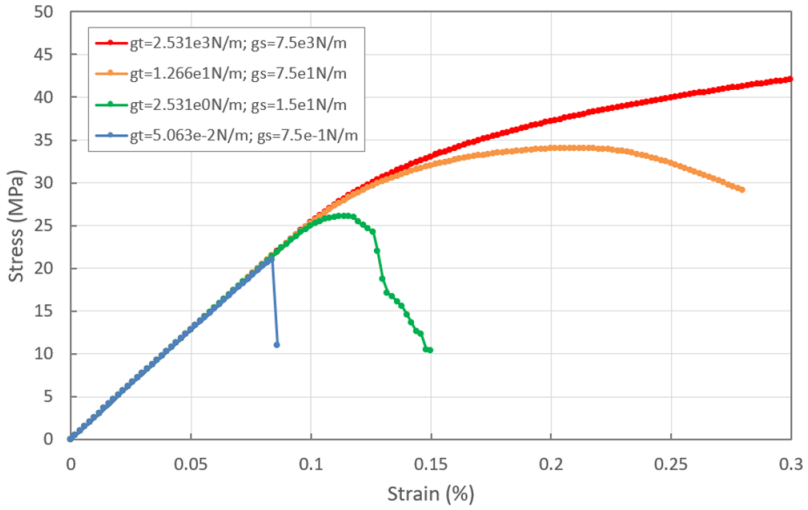

Figure 4.35: Stress strain curves of uniaxial compression tests on cylindrical samples with different ductility

The resulting stress strain curves and fracture patterns are shown in Figure 4.35 and 4.36. The stress strain curves exhibit similar trends as the experimental curves under different confining pressure, indicating the macroscopic ductile behavior could be simulated using this LEM model by varying the softening behavior of single lattices. The transition in fracture patterns was also captured. The samples failed with a localized shear fracture in the most brittle. As the fracture energy increases, conjugate fracture pairs appear and the distribution becomes increasingly scattered across the sample. It should be noted that in the most ductile case, the lattices are perfectly plastic after reaching the peak, thus the fracture surfaces shown in the figure represent yielding instead of broken lattices. However, the axial splitting failure mode was not captured in these simulations, even in the model with perfectly brittle lattices. This implies that either this method cannot simulate the particular mechanism that initiates the axial splitting, or there are other factors besides the behavior of each individual lattice that contributes to the ductility of the whole model.

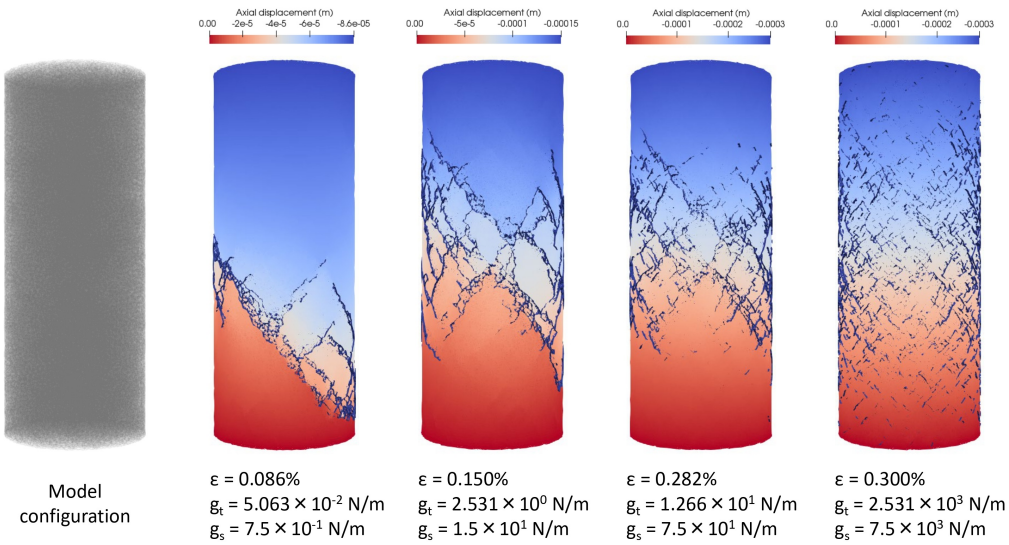

Figure 4.36: Stress strain curves

4.4 Summary

In this chapter, besides being verified elastically, the solid lattice network gives similar values of tensile strength from both uniaxial tension and Brazilian tests, and it is capable of predicting the pattern and temporal sequence for the development of tensile wing cracks.

In the four-point-bending tests, the simulated deformations, strain fields and fracture patterns well match the experimentally measured values. These examples indicate that although LEM is a simplified model, it is still a reliable tool to simulate and investigate rock fracturing behavior. Besides, it is shown that LEM is capable of capturing the purely elastic strain field induced by the crack tip before its arrival, which may potentially be applied in early crack detection. However, it should be noted that as the lattice is a simplified representation of the bond between solid grains, it ideally should have a similar size as the grain, which limits its application in investigating microscopic phenomena, such as crack tip behavior. Another limitation of this solid model is that the lattice failure criteria evaluate loading in three orthogonal directions separately, which may possibly overestimate the strength in combined loading scenarios.

The simulated compression tests on cylindrical samples with different lattice softening curves give a similar trend in stress strain curves as the experimental curves under different confining pressure, and the transition in fracture patterns are also captured, which indicates the macroscopic ductile behavior could be simulated using this LEM model by varying lattice parameters. However, in the case of the perfectly brittle lattice, although the stress strain curve implies an extremely brittle macroscopic failure behavior, the expected corresponding axial splitting failure mode did not occur. Pre-existing imperfections in rock materials, such

as pores and micro-cracks, are usually attributed as the cause of axial splitting in some literature [49]. Recall that in Section 4.1.3, vertically developed fractures did occur in the samples with a pre-existing inclined flaw but were not observed in these cylindrical specimens. The heterogeneity introduced by the lattice geometry may not be enough to represent those imperfections in rock.

Chapter 5

LEM Simulations on Hydraulic Fracturing

5.1 Validation by the Penny Shaped Crack Problem

Before conducting hydraulic fracturing simulation, the elastic behavior of the solid fluid coupled model was validated using the penny shaped crack problem, which has been extensively studied and one of the important analytical solutions was given by Sneddon [155][154][21]. The hydraulic fracturing simulations in the following sections will also start from this geometry.

The circular crack with a radius R is located in an infinite domain with homogeneous material and subjected to internal hydrostatic pressure P_0. The aperture of this crack is given as,

$$\delta(r) = \frac{8P_0R}{\pi E'}\sqrt{1-(\frac{r}{R})^2} \qquad (r \leq R) \tag{5.1}$$

Where E' is the plane strain Young's Modulus, $E' = E/(1-v^2)$, v is the Poisson's ratio and r is the distance from the crack center. And the induced normal stress at the crack plane ($z = 0$), acting in the perpendicular direction, is derived as,

$$\sigma_{zz}(r) = \frac{2P_0}{\pi}(\frac{R}{\sqrt{r^2-R^2}} - sin^{-1}\frac{R}{r}) \qquad (r > R) \tag{5.2}$$

The LEM model used for the validation test is shown in Figure 5.1a. A 0.25 m radius penny shaped crack was created at the center of a 2 × 2 × 2 m cube specimen. The lattice characteristic length is 0.05 m, which is also the size used in the following sections. And the microscopic elastic modulus and Poisson's ratio of a single lattice are 50 GPa and 0.2 respectively. A uniaxial compression test was conducted and gave the following macroscopic properties for the whole sample: Young's modulus $E = 32.16$ GPa and Poisson's ratio $v = 0.19$. Although a smooth plane was embedded as the crack surface, due to the way

the LEM code discretizes the domain and connecting nodes, the generated crack surface is not completely flat, which may cause some discrepancies with the analytical solutions. The analytical solution applies to an infinite domain, which cannot be modeled due to the limit of model size. Therefore, the simulations were conducted with two types of boundary conditions. The fixed boundary applies rigid constraints on all six faces, while the released boundary applies rigid constraints only at the four corners of the bottom face. It is reasonable to use these two conditions as the upper and lower bounds of the analytical scenario. 5 MPa hydrostatic pressure was applied on the crack surface.

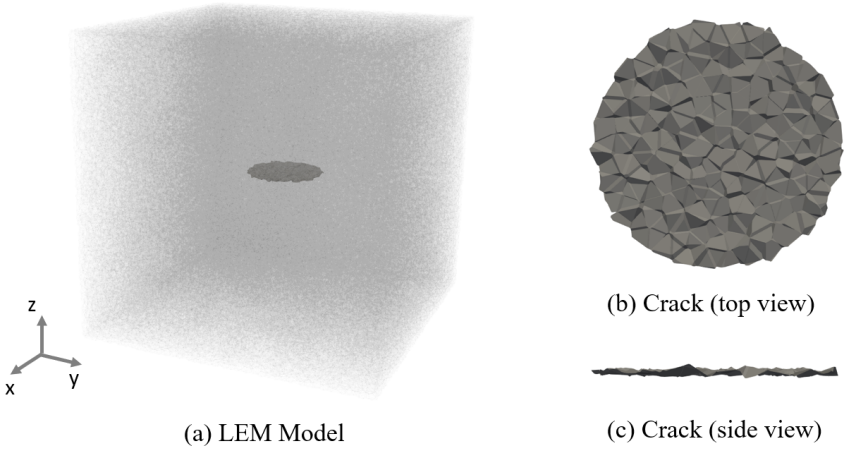

Figure 5.1: LEM model for validation test

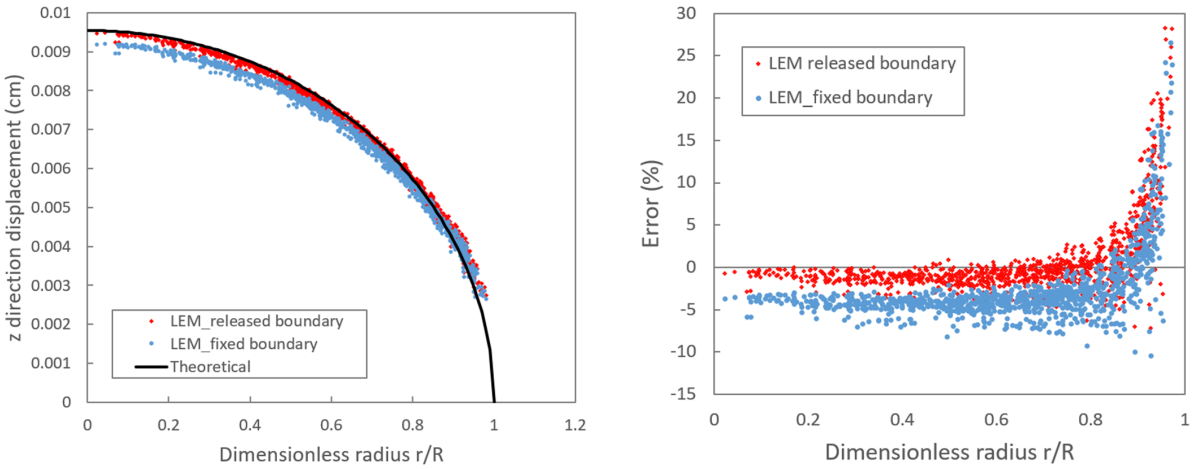

(a) Aperture (b) Error against analytical solution

Figure 5.2: Resulting crack aperture from analytical solution and LEM simulations (Lattice characteristic length = 0.05 m)

Figure 5.2a depicts the analytical and simulated crack aperture along the normalized radius r/R. The analytical curve was computed using Equation 5.1 with measured sample plane strain Young's modulus $E' = 33.36$ GPa. There is a small difference in the simulation results for fixed and released boundaries. The corresponding simulated aperture for an infinite domain is expected to fall between these two conditions. The errors between analytical and simulated results were computed as,

$$err = \frac{u_{sim} - u_{ana}}{u_{ana}} \times 100\% \tag{5.3}$$

Where u_{sim} and u_{ana} are the simulated and analytical displacement respectively, and the results are shown in Figure 5.2b. There are constant errors less than 5% when the normalized radius is below 0.8, indicating that the simulation gave slightly smaller deformations. This is due to the effect of the mesh size. Another set of simulations with the same configuration, but a smaller lattice characteristic length (0.04 m), was conducted and the results are shown in Figure 5.3. The errors decrease as the mesh becomes finer. The other part of the error appears after the normalized radius is beyond 0.8 and increases sharply as it approaches the edge. This is expected in the discrete model with a relatively homogeneous lattice size. Because there is a discontinuity in the apertures of adjacent broken and intact lattices, the smooth transition to 0 aperture cannot be represented. Despite these errors, the simulation results generally fit the analytical solution.

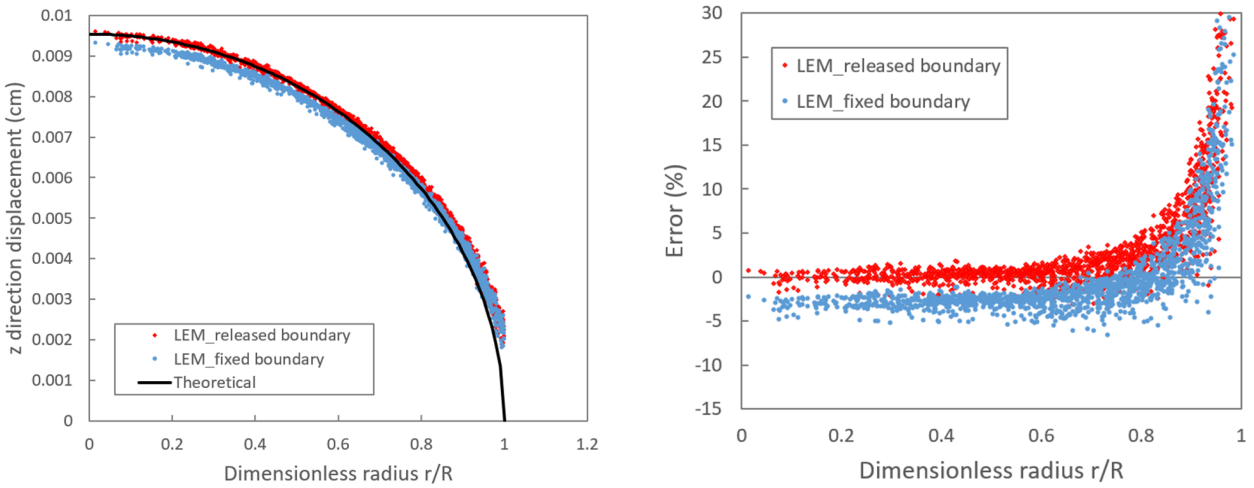

(a) Aperture

(b) Error against analytical solution

Figure 5.3: Resulting crack aperture from analytical solution and LEM simulations (Lattice characteristic length = 0.04 m)

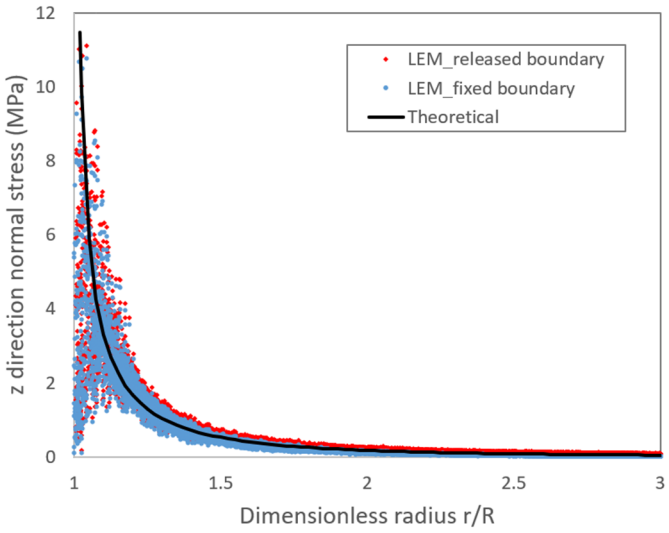

Figure 5.4: Resulting normal stress from analytical solutions and LEM simulations

The nodal stresses in a 0.05 m slice centered on the crack plane were computed and compared with analytical solutions. The results and the analytical curve are plotted in Figure 5.4. A positive value represents in tension. A small discrepancy is expected as this is a discrete model, and the nodes are not perfectly laid on the plane. Although the simulated results are slightly scattered especially when it is close to the crack, they are centered around the analytical curve and generally fit well. The exception happens in the close vicinity of the crack, where some nodes have small stresses even close to 0. Because the calculation of nodal stress (Equation 3.53) considers the contributions from all the lattices connecting to the node. A lattice connected to an adjacent node above or below the crack, which is in the compressive zone, could be in compression and provide a negative contribution to the stress. The lattice size, which is around 0.2 (dimensionless), also contributes to this error, as this relatively coarse grid cannot capture the rapid change of stress in this region. The induced stresses of the released boundary case are slightly greater than those of the fixed boundary case because of larger deformation. However, the difference is smaller enough and negligible.

5.2 Hydraulic Fracturing Simulations on Penny Shape Crack with Various Heterogeneities

5.2.1 Model Setup and Material Properties

This series of simulations aims to examine the effect of several types of heterogeneities, including mesh size, property distribution, and background stress field, on the development of fractures. The model setup is depicted in Figure 5.5, a 0.2 m radius, penny-shaped fracture was created in the center of a 2 m cube specimen. As input dimensions for simulation are digits, their magnitude could be scaled so long as the length-related units also change correspondingly. The dimensions described in Figure 5.5a were multiplied by 100 in simulation and thus the unit was converted to centimeter to avoid small digits. Noticed that Figure 5.5a depicts a smooth pre-existing crack within the sample. However, as described in the previous chapter, the cross sections of these randomly oriented lattices that are cut through by the prescribed planar area form a rough surface, as shown in Figure 5.5b. Therefore, the pre-existing crack surfaces in the actual LEM models used in this set of simulations are tortuous and their areas are thus larger than the circular plane. Compressive stress fields were applied to the samples after the pre-existing cracks were created to close the crack. Therefore, the initial aperture sizes are zero.

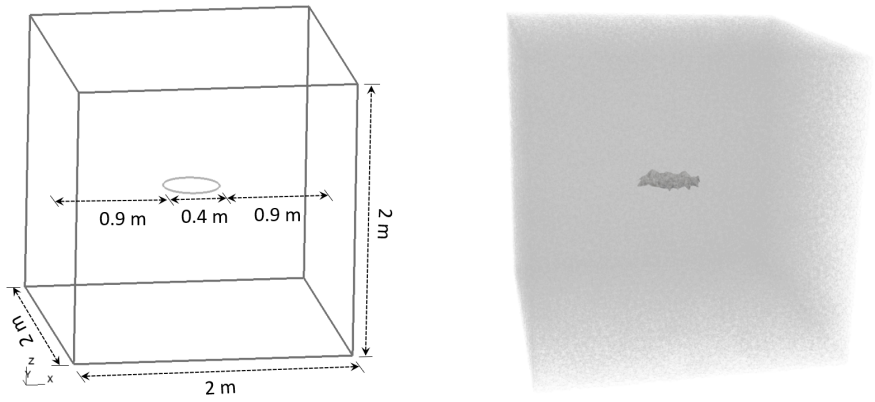

(a) Sketch (b) LEM model

Figure 5.5: Model configuration

In all the tests, the fluid would be injected from the center of the penny-shaped crack. On the $-x$, $-y$ and $-z$ faces, roller supports were applied, while uniform pressures σ_x, σ_y, and σ_z were applied to the $+x$, $+y$ and $+z$ faces, respectively. Several megapascals to tens of megapascals are used to represent the subsurface stress field at several hundred meters depth. In test cases subjected to an isotropic stress field (stress ratio $\sigma_z/\sigma_x = 1$), the applied pressure in all three directions was 2.5 MPa. In cases of anisotropic stress fields, x is the

minor stress direction and σ_x remains 2.5 MPa, z is the major stress direction, and the stress ratio varies as σ_z increases from 7.5 to 15 MPa. While σ_y is fixed at 5 MPa to make it the intermediate stress direction. The value of the coefficient of lateral earth pressure is related to the soil friction angle for normally consolidated soil [83]. Therefore, it typically falls between 0.3 and 0.7. While in overconsolidated cases, the value is also affected by the overconsolidation ratio and usually exceeds 1 [109]. Because of the simulation setting, the largest stress should always be applied along the z axis to ensure it is the major stress direction. Therefore, cases with a stress ratio of less than 3.5 may be more realistic. But tests with higher stress ratios were still conducted to simulate extreme scenarios.

Rock is usually composed of multiple materials and contains large numbers of defects. The statistical theory that models the progressive mechanical breakdown of materials assumes that these defects are statistically distributed throughout the material and could be appropriately described by the Weibull distribution[181]. This kind of elemental scale heterogeneity could be easily modeled in LEM by varying individual lattice properties. Uniform and Weibull distributions were applied to the lattice strength and modulus to account for this effect. The dispersion of the Weibull distribution is controlled by the shape parameter k. The distribution is more concentrated around the mean value as k increases. Figure 5.6 shows the probability density functions of Weibull distributions with mean value 1 but different shape parameters. The reasonable range limit of the shape parameter for describing the brittle failure of rock is between 1 and 6 [178], commonly between 2 to 3.5 [175]. Considering 1 is the lower bound of k and would result in a large number of extremely weak lattices (Figure 5.6), which are uncommon in reality. When k is greater than 3, the distribution tends to be concentrated and the model behaves similarly to uniform cases. In this set of simulations, k is selected to be 2 or 3.

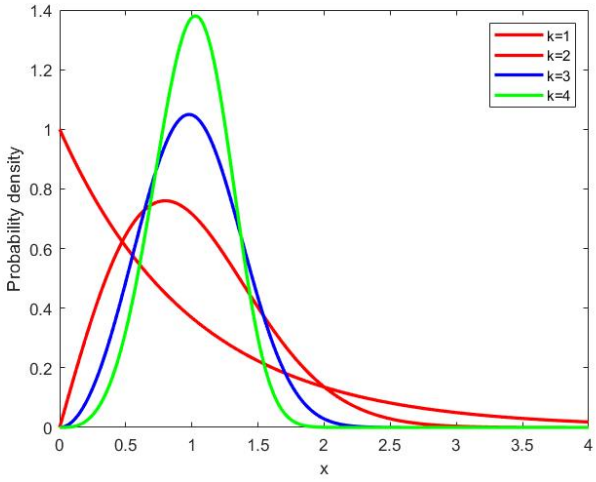

Figure 5.6: Probability density function of Weibull distribution with mean value $u = 1$ and different shape parameters k

Three models with different lattice characteristic lengths, including 3.5 cm, 5 cm and 7 cm, were constructed to study the effect of mesh size. And one additional model with the same nodal density but a different arrangement was created for the 5 cm case to investigate the influence of nodal arrangement. These four models are referred to as $M_{3.5}$, M_{5_1}, M_{5_2} and M_7, where the first subscription represents the lattice characteristic length of the model in centimeters, while the second subscription (5 cm cases only) is used to distinguish the models with the same nodal density. These models' approximate number of nodes and lattices are listed in Table 5.1.

Model	**Number of nodes (million)**	**Number of lattices (million)**
$M_{3.5}$	0.75	6
M_{5_1}, M_{5_2}	0.25	2
M_7	0.1	0.8

Table 5.1: Approximate number of nodes and lattices of the models

The values of above mentioned heterogeneity-related factors are provided in Table 5.2. For the uniformly distributed cases, the lattice has the following microscopic properties: tensile strength of 17.2 MPa, shear strength of 28 MPa, elastic modulus of 50 GPa, and Poisson's ratio of 0.2. While in circumstances where the lattice strengths and modulus follow a Weibull distribution, the above values are used as the distribution's mean. The injection rate is 1.25×10^{-4} m^3/s and the time step length is 0.05 s. The viscous effects are ignored in this set of simulations, meaning the fluid fills out the whole fracture network connected to the source, and constant hydrostatic pressure is applied throughout the network in each step. Therefore, the time resolution is actually governed by the injection volume in each time step, which is the multiple of injection rate and time step length, and is 2.5×10^{-3} m^3. Calibrations were conducted before choosing this value, such that the simulation is stable, has enough time resolution, and can be completed within a reasonable amount of time.

Parameters	**Values**
σ_x (MPa)	2.5
σ_y (MPa)	2.5, 5
σ_z (MPa)	2.5, 7.5, 8.75, 10, 15
Stress ratio (σ_z/σ_x)	1, 3, 3.5, 4, 6
Distribution	uniform, Weibull (k = 2, 3)
Characteristic length of mesh (cm)	3.5 ($M_{3.5}$), 5 (M_{5_1}, M_{5_2}), 7 (M_7)

Table 5.2: Simulation parameters for the fluid injection tests

Before the hydraulic fracturing simulations, uniaxial compression tests were conducted on all the models and their Young's modulus was measured, as listed in Table 5.3. In addition, the ratios of Young's modulus between different models and the model M_{5_1} were computed. The model M_{5_2} has approximately the same Young's modulus as M_{5_1} (around 0.1% difference). This small discrepancy could be attributed to the different nodal arrangements. Although the Young's modulus decreases slightly as the lattices become finer, the changes are minor (less than 1%), indicating that the mesh sizes of these models are sufficiently small that the macroscopic modulus is unaffected. While the application of Weibull distribution produces a more noticeable difference (between 5% to 10%). The Young's modulus decreases as the lattice properties become more scattered, which is consistent with the results in literature [181].

Model	**Young's Modulus E (GPa)**	**Ratio between Young's Modulus E/E$_{M_{5_1}}$**
M_{5_1}	32.135	1.000
M_{5_2}	32.173	1.001
$M_{3.5}$	31.952	0.994
M_7	32.382	1.008
M_{5_1}, Weibull k=3	31.149	0.969
M_{5_1}, Weibull k=2	30.152	0.938

Table 5.3: Young's modulus of different models

5.2.2 Results and Discussions

Injection pressure, fracture area and opening

Figures 5.7 to 5.9 depict the relationships between fracture area, injection volume, mean aperture, and injection pressure during the whole injection process for model M_{5_1} under different stress ratios, as well as for different models, or model with different property distributions, under the same stress ratio 4. As changing the unit of length of the input model is equivalent to scaling its size, some related quantities are normalized in the analysis for greater generalizability. The mean apertures are normalized by the radius of the penny shape crack (0.2 m). In addition, for models other than M_{5_1}, or in cases Weibull distributions were applied, the mean apertures are also multiplied by the ratio Between Young's modulus specified in Table 5.3 to eliminate the influence on deformation caused by different macroscopic Young's modulus. As illustrated above, the actual fracture surfaces are tortuous due to the randomly oriented lattices. Consequently, the real fracture area, which is obtained by summing the cross sectional areas of corresponding lattices, is greater than the area covered by a smooth surface. Therefore, the fracture areas are normalized by the

total pre-fractured area (approximately 0.19 m^2), both taking tortuosity into account. The injection volumes are normalized by the volume of the original penny shape crack during the process, which is equal to its total area multiplied by the mean aperture. Considering that the fracture would eventually grow along the direction of the major principal stress, which means it needs to overcome the minor principal stress to open the aperture and develop. The injection pressures are normalized by the minor principal stress, which is 2.5 MPa for all the cases.

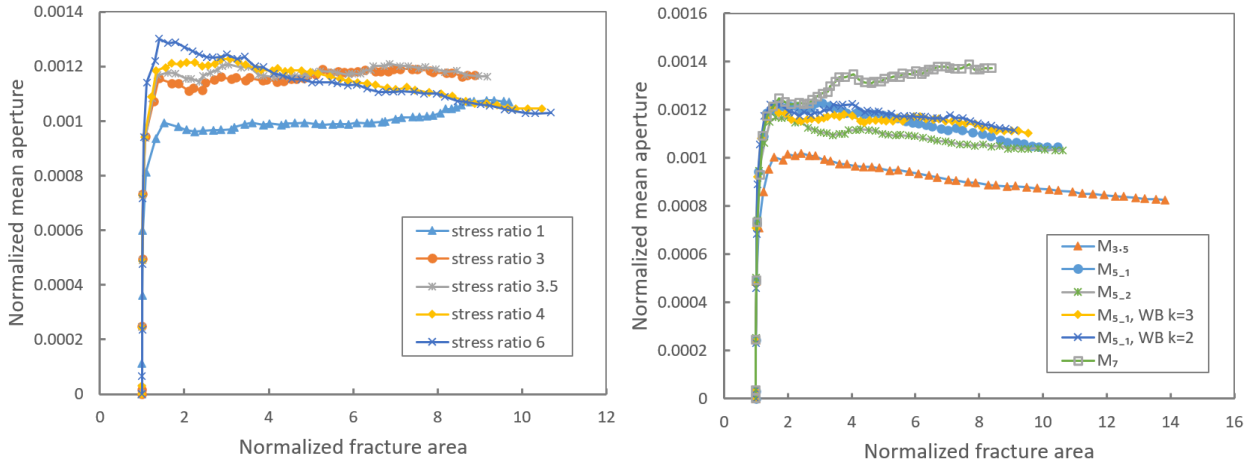

(a) Model M_{5_1} under different stress ratio (b) Different models under stress ratio 4

Figure 5.7: Mean aperture at different fracture area

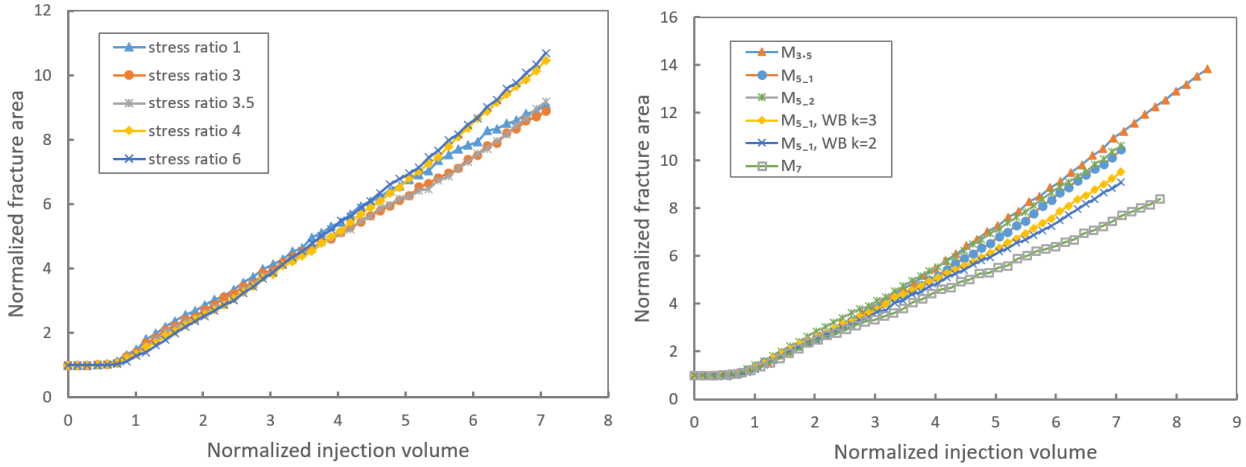

(a) Model M_{5_1} under different stress ratio (b) Different models under stress ratio 4

Figure 5.8: Fracture area history

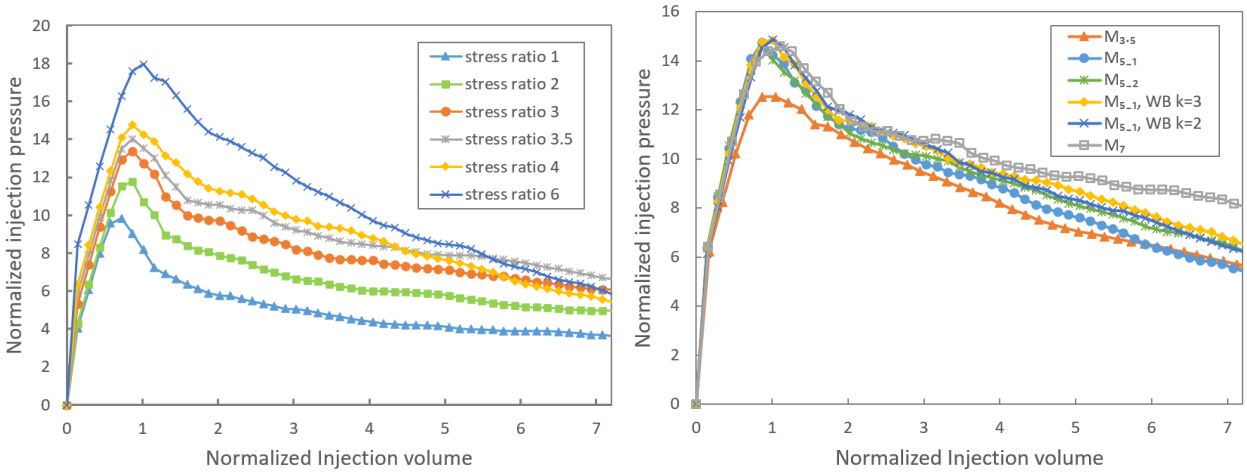

(a) Model M_{5_1} under different stress ratio

(b) Different models under stress ratio 4

Figure 5.9: Injection pressure history

At the initial stage when the normalized injection volumes are below around 0.8, the fractures do not develop (Figure 5.8) while the pre-existing cracks keep opening (Figure 5.7). After that, the number of fractures starts to increase approximately linearly with injection volumes, while the mean apertures remain relatively unchanged. This result is reasonable based on the injection pressure and crack radius history. Because although the injection pressures decrease in the later stage, the fracture developments result in larger crack radii and thus increase the total force. Some crack radius related quantities were computed using the results of model M_{5_1} under stress ratio 1, as shown in Figure 5.10. Because the fracture occurs on the original plane and is roughly circular, the analytical solution for the aperture of a penny-shaped crack (Equation 5.1) is applicable in this instance. Prior to analysis, the radius was calculated as the mean value of radii in different directions and normalized by the original crack radius (0.2 m). The normalized injection pressure was subtracted by 1 to eliminate the part that overcomes the applied compressive stress field. Figure 5.10b depicts the products of normalized net injection pressure and radius at different normalized fracture areas. The products are approximately constant after the fracture starts to develop, and the trend is similar to that of the mean aperture shown in Figure 5.7. This result is consistent with Equation 5.1, which states that the aperture is proportional to the product of applied pressure and crack radius for a given location.

Figure 5.9 demonstrates that injection pressures initially grow nearly linearly as injection volumes approach 1 and reach a maximum shortly after fractures begin to develop. All cases reach the peak pressure at almost the same normalized injection volume, indicating that the maximal injection pressure is required to open the pre-existing fracture to the point that initiates the fracture development process. Also consider the case of model M_{5_1} under stress ratio 1, the classic solution in the theory of linear elastic fracture mechanics is applicable. The mode I stress intensity factor at the fracture tip for this geometry is,

$$K_I = P\sqrt{\pi r}F(\frac{2r}{L}) \tag{5.4}$$

Where P is the injection pressure, r is the fracture radius and L is the sample length [157]. F is a monotonically increasing function with the ratio $2r/L$ as the variable. The fracture would start to propagate when K_I exceeds the critical stress intensity factor, also known as the fracture toughness, which is a material property and keeps constant. In LEM simulation, appropriate pressure is applied to initiate new fractures in each step. Therefore, the above criteria could be applied for analysis. As the fracture toughness is constant, stress intensity fracture must reach a similar level in each step to initiate the crack. As shown in Figure 5.10c, the computed stress intensity factor drops following fracture initiation. This results from the sudden decline of the injection pressure after it reaches the peak, whereas the radius does not have a dramatic increment. But the stress intensity factor does not change significantly at a later stage when the fracture stably develops, which is consistent with the theory. As the radius of the crack expands as the fracture propagates, the injection pressure must drop to attain equivalent stress intensity factors, and this was reflected in results shown in Figure 5.9. Figure 5.10a further demonstrates that the rate of growth of radius is decreasing because the less incremental radius is required to create the same annular area while the injection rate remains unchanged. This explains the decline in the rate of pressure decreasing. However, even if the rate is slow, if the model is sufficiently large to allow the radius to grow indefinitely, the pressure would continue to decrease and eventually approach the magnitude of the applied stress field.

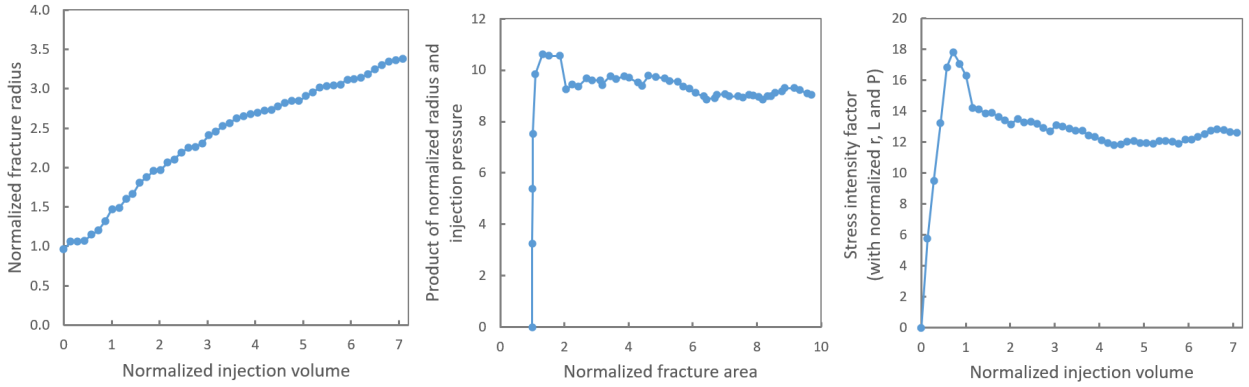

(a) (b) (c)

Figure 5.10: Crack radius related quantities for the simulation on model $M_{5\text{-}1}$ with stress ratio 1

The influence of stress ratio

According to Figure 5.9a, a greater stress ratio results in a steeper slope at the initial stage and higher peak pressure. This is because, with a higher stress ratio, the stress in the

direction perpendicular to the fracture surface is greater, necessitating a higher injection pressure to open the aperture for the same injection volume. Initial post-peak slopes are identical in all circumstances. However, when the normalized injection volumes exceed 2, the slopes of cases with stress ratios of 4 and 6 decrease slightly more quickly than those of the other cases. This is because, as depicted in Figure 5.12, fractures develop along the major stress direction for these two cases at this stage. Therefore, the pressures required to open these parts of fractures are reduced. Consequently, the mean apertures are slightly smaller (Figure 5.7a), and to maintain the same volume for the injected fluid, the fractured areas are greater (Figure 5.8a), that is, fractures develop more easily for these two cases at the later stage.

In order to understand the influence of the applied stress field on the peak injection pressure, some additional simulations were conducted on model M_{5_1}, with different dip angles (0°, 45°) of pre-existing cracks and under various stress ratios. The dip angle α is the angle between the initial crack plane and the major principal stress direction (z axis), as demonstrated in Figure 5.11a. And Figure 5.11b shows the results. When $\alpha = 90°$, which are the previous cases where the major principal stress is imposed perpendicular to the pre-existing fracture surface, the peak injection pressure increases linearly with the stress ratio. The injection pressure could be divided into two parts. The first part overcomes the applied compressive stress field before the aperture is able to open. This thus forms the linearly increasing part of the data in the Figure. While the second part of injection pressure opens the crack and contributes to the stress for crack initiation. For the same geometry, the same net pressure is required to achieve the critical stress intensity factor. Therefore, this part of the pressure remains constant even as the stress ratio increases.

The scenario differs when α is less than 90°. Depending on the dip angle, the applied stress field generates tensile or shear stress around the crack tip, which also contributes to the fracture initiation instead of closing the crack [49][173]. When $\alpha = 0°$, the surface normal of pre-existing crack is along the direction of minor principal stress, which keeps constant for all the cases. Therefore, regardless of the stress ratio, the part of injection pressure that overcomes this applied stress field remains the same. However, the major principal stress field would open the crack and generates tensile stress at the crack tip, which becomes part of fracture initiation stress and reduces the required injection pressure. Consequently, there is a slight decrement in peak pressure for the case under stress ratio 6. When the dip angle increases from 0 to 45, the crack initiation stress decreases, as different crack modes would be generated [101]. Therefore, for the cases that $\alpha = 45°$, the stress induced by the major principal stress field contributes a larger portion of fracture initiation and further reduces the extra injection pressure required. However, there is also a component of the major principal stress field that is perpendicular to the crack surface, which tends to close the crack and requires injection pressure to overcome. The combination of the above two effects results in the curve for $\alpha = 45°$ in Figure 5.11b, which increases with stress ratio, but at a decreasing rate.

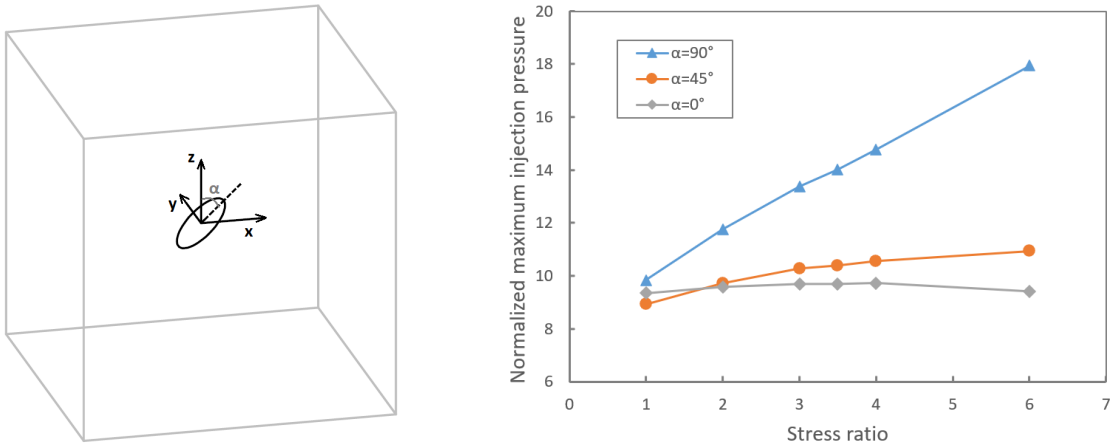

(a) Sketch of the model

(b) Peak stress versus stress ratio

Figure 5.11: Peak stress versus stress ratio, for model M_{5_1} with different dip angles of pre-existing cracks

The influence of mesh size and nodal arrangement

The influence of mesh size and property distribution on the injection pressure history is depicted in Figure 5.9b. The injection pressure for the model M_{5_1} and M_{5_2} are approximately identical until having slight deviation after normalized injection volume 2, and they exhibit nearly the same fracture area history throughout the test (Figure 5.8b). This suggests that, while the mesh size is the same for samples with similar fracture patterns, the node arrangement does not significantly alter the general behavior. The discrepancy at a later stage may be the result of a deviation in fracture pattern due to a different potential crack path restricted by the arrangement of the nodes (Figure 5.12).

Comparing the results of models with different mesh sizes ($M_{3.5}$, M_{5_1}, and M_7) under the same normalized injection volume reveals that the models with smaller mesh sizes are subjected to lower injection pressure (Figure 5.9b) and have larger normalized fracture areas (Figure 5.8b), indicating that fractures are easier to develop in the model with smaller mesh size. This is because finer mesh results in shorter and more slender lattices, whose strength is reduced due to their smaller cross sectional areas. These lattices would break under a lower stress level generated by a narrower aperture. Thus, microcracks are generated, which further weaken the structure and cause the fractures to propagate.

The influence of property distribution

For the influence of property distribution, as shown in Figures 5.8b and 5.9b, under the same normalized injection volume, more scattered cases (smaller shape parameter k for Weibull distribution) have slightly higher injection pressures and smaller fracture areas, but the

differences are relatively small. This may indicate that a more scattered distribution may make the fracture slightly more difficult to propagate in the model. In general, though, this may not have as much impact as the other factors. However, the heterogeneity induced by property distribution has some noticeable influence on the fracture pattern, which will be discussed in the next section.

Fracture pattern

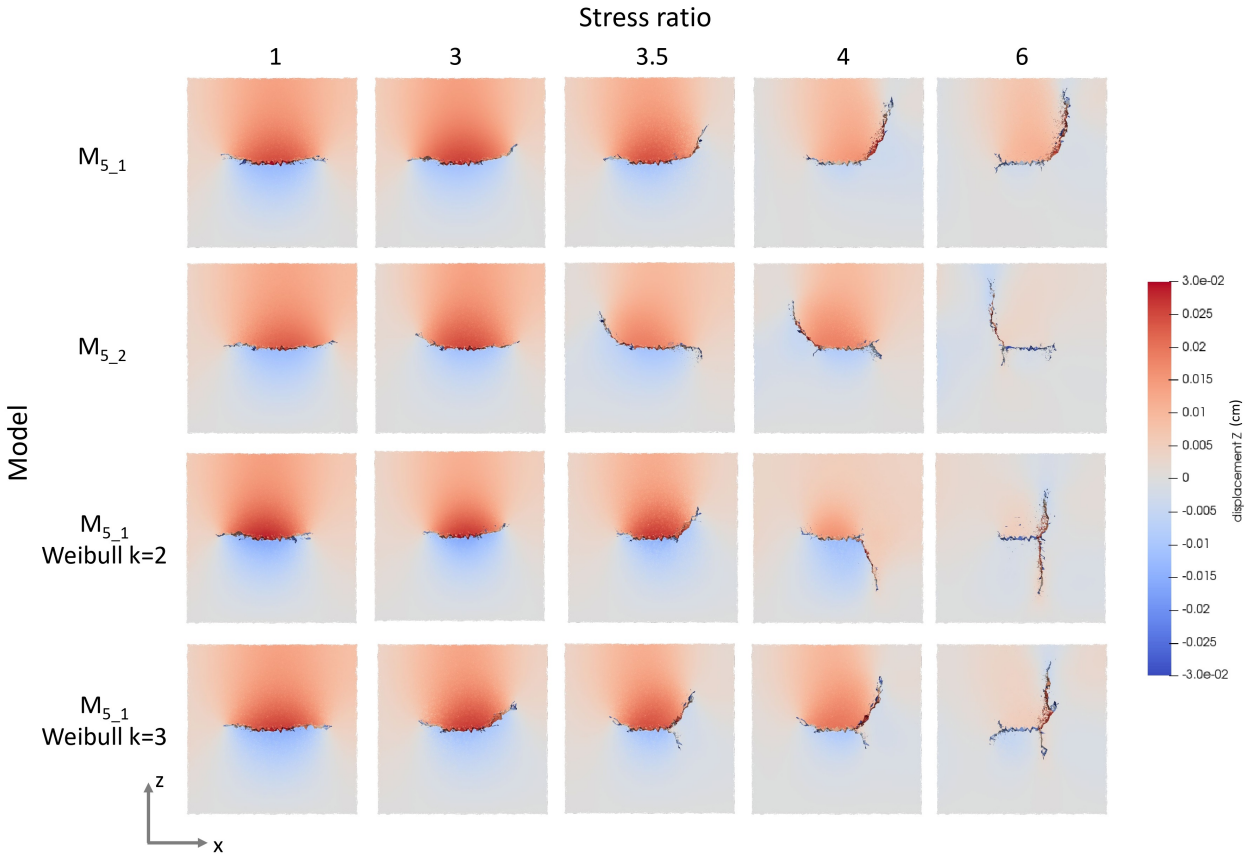

Figure 5.12: Fracture patterns and z displacement fields at final stage (normalized injection volume 7) for samples with different nodal arrangements and property distributions

Figure 5.12 shows the final stage fracture patterns and displacement fields in the major stress direction (z) at the xz-plane cross sections that cut through the middle of the samples. Generally, the fractures develop first along the pre-existing crack direction, then turn to the major stress direction. This transformation occurs more rapidly in cases with a greater stress ratio. It was also observed that z deformations are reduced when fractures develop along the z axis. This is because these cracks are able to open in the direction of minor stress (x), which

is easier under the same pressure and also provides volume for the injected fluid. Except for the isotropic cases (stress ratio 1), all of these fractures develop predominately on one side of the model, especially in cases where the stress ratio is high and the fractures turn to the z axis. The fractures in model M_{5_1} grow on the right, while those in model M_{5_2} develop on the left. This variation may be due to the different potential crack paths defined by the node arrangement in these models. Although the preferred development directions are different, the fracture patterns in M_{5_1} and M_{5_2}, under the same stress ratio and uniform property distribution, are similar.

As the property distribution is applied, the fractures become increasingly dispersed in the more heterogeneous scenarios, as shown in Figure 5.13. For the uniform and k=3 cases, the fractures are almost continuous. The majority of newly generated fracture surfaces are connected to the main fracture. While as k decreases, more isolated fracture surfaces are formed, mostly around the front of the main fracture. This is due to the heterogeneous lattice properties. Weak lattices would break under a lower stress level, which could be achieved even away from the main fracture. While some strong lattices have high strength and do not break even within the main fracture. These strong lattices reduce the fracture openings by sustaining part of the loading. This may be one of the reasons why fracture is more difficult to propagate in models with more dispersed lattice properties.

The fracture paths are also affected by the property distribution, but they generally remain comparable. For the cases under stress ratio 6, the fractures develop two-way at one side of the pre-existing fractures, along the z direction. Under such a large stress field, the pre-existing fractures are nearly closed, while the newly formed fractures open in the x direction. For k=3 cases, there are branches on the right side even under stress ratios of 3.5 and 4, albeit the bottom one does not develop eventually. For the k=2 case with a stress ratio of 4, the fracture grows downward, unlike the other cases. The reason may be that, there are multiple potential crack paths in each simulation, and fractures typically develop along the weakest one. While the randomly applied property distribution results in a varying number of weaker lattices on each path, this alters the order of weak paths and, thus, the path along which fractures eventually develop. Another thing to notice is that, compared to uniform cases with the same stress ratio, it appears that fractures in samples applied property distribution turn to the major stress direction faster.

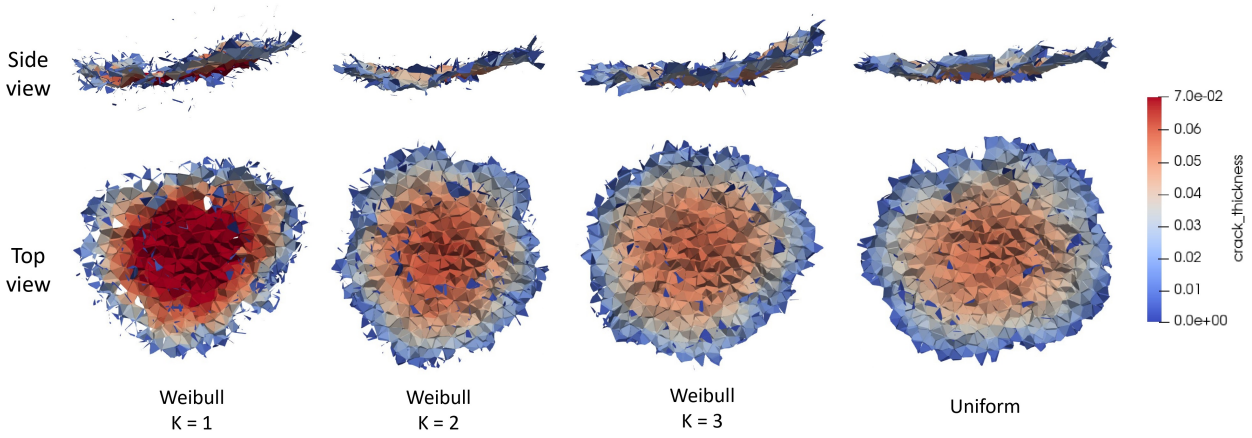

Figure 5.13: Fracture patterns of the model M_{5_1}, under stress ratio 3, with different property distributions

Figure 5.14 depicts the final stage fracture patterns and z displacement fields for the tests on the models $M_{3.5}$ and M_7, which have different mesh sizes. Also compared with the results of model M_{5_1} in Figure 5.12, it is seen that, at the same stress ratio, the fractures turn to the major stress direction earlier as the meshes become finer. This indicates that the rate at which fractures turn is related to the nodal density, or equivalently, the scale of weakness. A similar number of lattices may need to be traversed for the transition of fractures developing from minor to major principal stress direction. In the model with a finer mesh, the transition zone is smaller, therefore this process could be either completed earlier or developed to a later stage. Also due to weaker individual lattices, microcracks are easier to occur in finer models, as mentioned previously. Consequently, the injection pressure and crack opening are reduced, but the fracture area is increased, causing the fractures to develop further.

Fractures in model $M_{3.5}$ are more likely to occur on both sides of the pre-existing cracks. The reason may be that, denser and shorter lattices may reduce the heterogeneity induced by the lattice orientation. As the model becomes more homogeneous, the fractures may not have a strong preference to develop on one particular side. For the case under stress ratio 6, the fracture at the left initially develops in two-way with similar rates and results in the bifurcation. But at some point the lower branch stops developing. This bifurcation may also be generated due to the relatively homogeneous lattice orientations along the potential crack path. But the tie is eventually broken by heterogeneity.

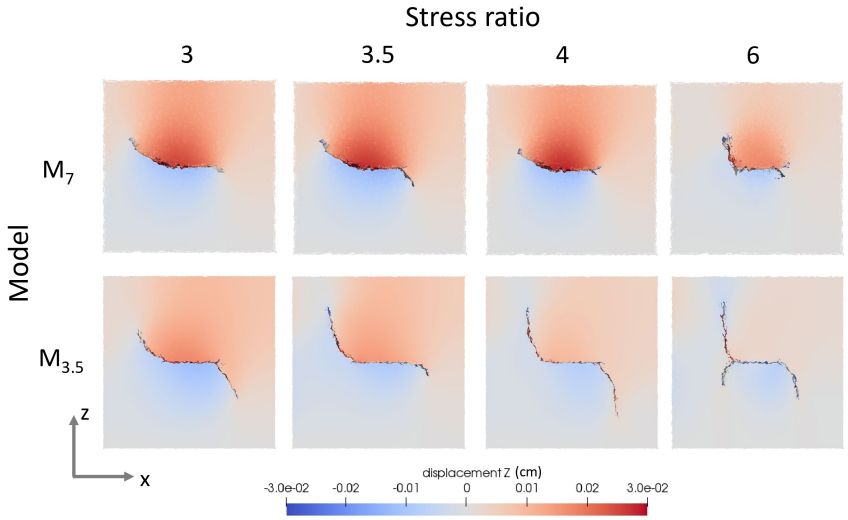

Figure 5.14: Fracture patterns and z displacement fields at final stage (normalized injection volume 7) for samples with different nodal densities

Inclination angle

To investigate the rate of change in fracture direction at the xz-plane, 10 cm stripes of fractures at the center line of the samples were taken for analysis. The fractures developed in different stages (10 time steps per stage, converted to normalized injection volumes in the figures) were distinguished with different colors as shown in Figure 5.15a. The normal vectors of newly developed fracture surfaces at the right part in each stage were recorded and their average was computed. The inclination angle between the averaged vector and z axis, which is also the angle between the direction of fracture development and xy plane, was computed and plotted in Figure 5.15b.

Figure 5.15a demonstrates that the fractures developed at the 1st stage (0-1.16) are nearly identical for all the cases, even though under different stress ratios, and are almost along the direction of pre-existing fractures. This indicates that, at the initial stage, either the influence of stress ratio is insufficient to alter the fracture direction, or the mesh size is not fine enough to capture the different influences of various stress ratios. While in subsequent stages, the fractures start to turn to the major stress direction at different rates, depending on the stress ratio. The lengths of colored fractures indicate the number of fractures that have developed and how far they have progressed in the corresponding stage.

Figure 5.15a further demonstrates that, as the stress ratio rises, more fractures develop on the right side of pre-existing cracks, while fractures on the left side are fewer and stop developing earlier. For example, fractures in cases with stress ratios of 3 and 3.5 develop on both sides at all stages, but are more concentrated on the right side in the 3.5 case. While in cases with stress ratios of 4 and 6, few fractures develop on the left in the third stage (2.60-4.04), and their development ceases thereafter. The reason is that, fractures start to develop

unevenly due to heterogeneities such as lattice length, orientation or properties. While the newly developed inclined fractures would be easier to open, as the stress field perpendicular to the fracture surfaces decreases. So once the balance is broken by heterogeneity, the side with more fractures would be more vulnerable and continue to fracture. This further leads to the shift of the maximum opening position. As shown in Figure 5.16, it reduces the opening of fractures on the opposite side, away from the maximum opening position, making the fractures more difficult to develop there. In addition, as the stress ratio increases, fractures develop more unevenly. In order to maintain the same volume for injected fluid, fractures need to extend further in the preferred direction.

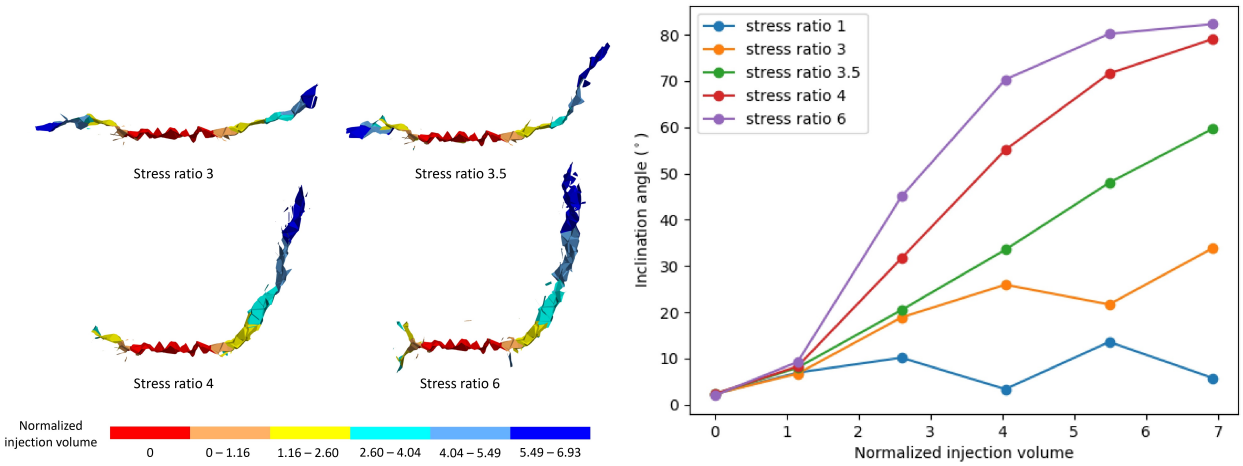

(a) Fractures developed at different stages

(b) Inclination angle

Figure 5.15: Inclination angle of the fractures (10 cm stripe at the middle of the sample)

As shown in Figure 5.15b, the computed inclination angle of the pre-existing crack is not exactly zero because it is averaged over a number of randomly oriented small fracture surfaces. Similarly in the later stage, but these averaged values are close enough to represent the orientation of macroscopic fracture directions. The changes of inclination angle in the 1st stage are almost the same for all cases and relatively small compared to the later stages, which is consistent with Figure 5.15a showed. In later stages, the rate of change increases as the stress ratio rises. When the inclination angles are below 70°, they increase approximately linearly with the injection volume. Then the rates decrease and the angles nearly do not increase after 80°, as they are already developing along the major stress direction. They do not reach 90° for the same reason mentioned above, as they are approximations using the averaged normal vector. For the isotropic case (stress ratio 1), the fluctuation indicates that locally the fractures may not develop exactly in the plane, but generally they do.

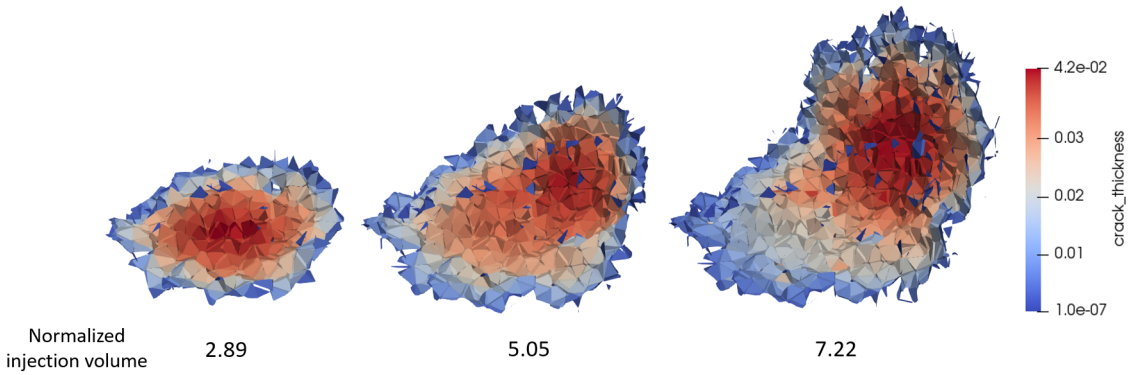

Figure 5.16: 3D view of the fracture development in model M_{5_1} under stress ratio 4. Notice the shift of maximum opening position

Effects of applied boundary conditions

Note that in most simulations conducted on model M_{5_1}, the fractures mainly develop at the right part and turn toward the $+z$ direction. One potential cause of this behavior is the applied asymmetric boundary conditions. Fixing one side of the model and applying stress on the other side, together with induced deformation from the fracture, generates an asymmetric displacement field in the sample, which may possibly affect the path of fracture development. In order to examine the influence of boundary conditions, another two sets of simulations were conducted on model M_{5_1} under stress ratio 4, with uniform and Weibull distribution ($k = 2$) respectively. Reversed boundary conditions were applied: roller supports were applied on the $+x$, $+y$, and $+z$ faces, while uniform pressures σ_x, σ_y, and σ_z were applied to the $-x$, $-y$, and $-z$ faces respectively.

The final stage fracture patterns are shown in Figure 5.17 and 5.18. Original and reversed boundaries gave similar fracture patterns for both cases, especially when they developed on the same side and turned toward the same direction. Comparing the two patterns by overlaying the colored fracture surfaces (original boundary in red, reversed boundary in blue) together, it turns out that a large part of the surfaces from the two fractures is completely identical (results in purple). There are also some discrepancies that cannot be ignored, indicating that the applied boundaries affect fracture developments to some degree. This is expected due to the mesh heterogeneity (irregular arrangement of nodes). The resulting nodal forces converted from applied boundary pressure would not be identical, member stress would thus change and alter the broken status for some lattices. In general, however, the fracture paths and development trends remain similar and are mainly unaffected by the boundaries. Also considering that the preferred fracture paths vary in different models, it is more probable that this is due to model heterogeneity.

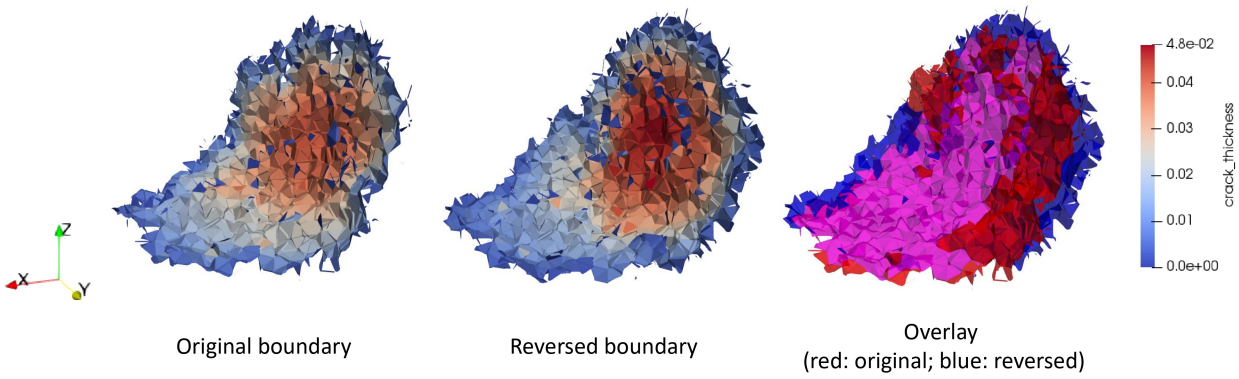

Figure 5.17: Fracture pattern resulted from original and reversed boundary conditions (Tests on model M_{5_1}, uniform distribution, stress ratio 4)

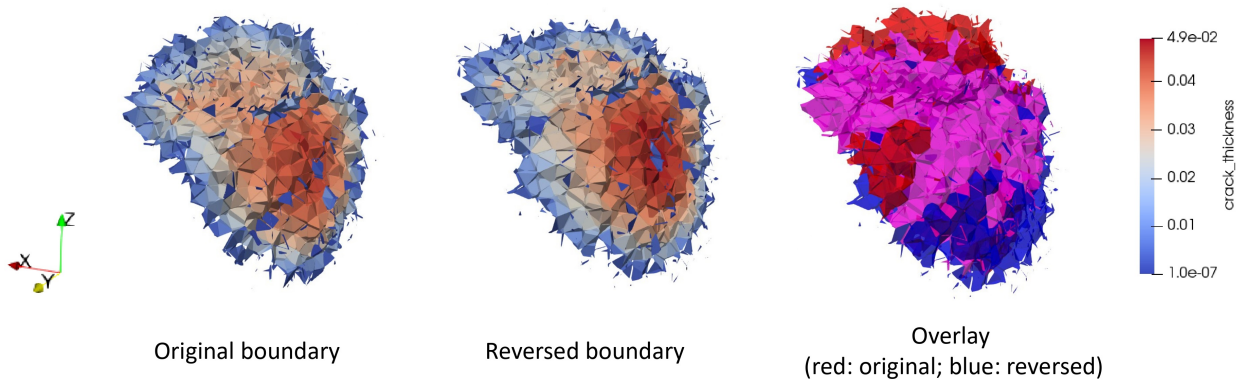

Figure 5.18: Fracture pattern resulted from original and reversed boundary conditions (Tests on model M_{5_1}, Weibull distribution with $k = 2$, stress ratio 4)

5.3 Simulations of the Interactions between Hydraulic and Pre-existing Fractures in the Penny Shape Cracked Samples

5.3.1 Model Setup and Material Properties

This series of simulations aims to investigate the interactions between hydraulic fractures and pre-existing fractures, with a focus on the factors that affect fracture crossing. The model setup is depicted in Figure 5.19, besides the 0.2 m radius penny-shaped crack created at the center of the 2 m cube specimen, which is identical to the model used in Section 5.2, two additional 1.6 m × 1.6 m pre-existing square fractures are created in the yz plane, 0.4 meters away from the center of penny shaped crack, as shown in Figure 5.19a. The model M_{5_1} from Section 5.2, with 0.25 million nodes, 2 million lattices and 5 cm lattice characteristic length, is used in all the simulation cases of this section. The LEM model is shown in Figure 5.19b, as explained previously, all the pre-existing fracture surfaces are rough, and their initial aperture sizes are also zero. The fluid would be injected from the center of the penny-shaped crack.

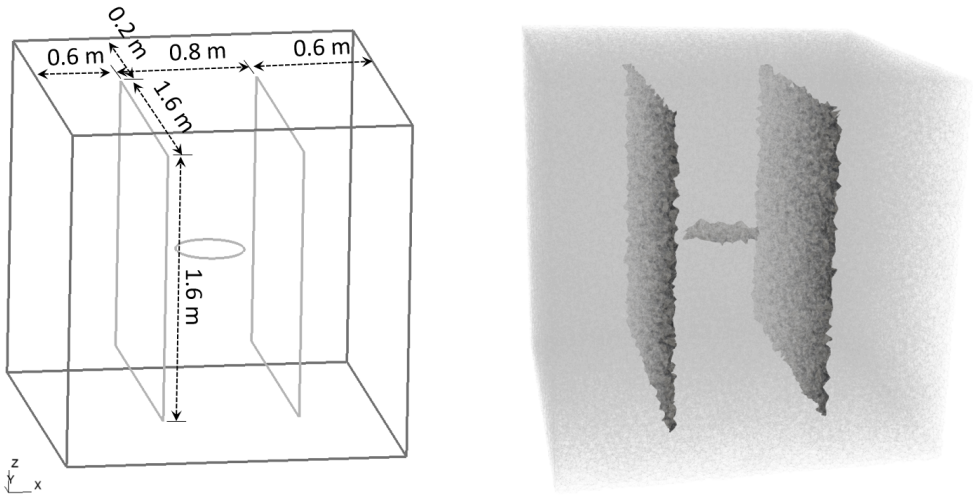

(a) Sketch (b) LEM model

Figure 5.19: Model configuration

Also similarly as in Section 5.2, roller supports were applied on the $-x$, $-y$, and $-z$ faces and uniform pressures σ_x, σ_y, and σ_z were applied to the $+x$, $+y$, and $+z$ faces, respectively. σ_y and σ_z are fixed at 5 MPa in all the cases. While σ_x, the stress field perpendicular to the pre-existing fracture surfaces, is one of the most important factors affecting fracture crossing. Because it determines whether the pre-existing square fractures could remain closed under

the injection pressure, and the magnitude of friction generated at the square fracture surface, which is a key element in the mechanism of fracture crossing. σ_x needs to be large enough to trigger the fracture crossing. Most of the cases were simulated under $\sigma_x = 40$ MPa, which is a relatively large value, to make the fracture crossing easier to occur so that the influence of other factors could be examined. Cases that $\sigma_x = 20$ or 30 MPa were also conducted for comparison and to show the influence of the applied stress field. This arrangement of stress field makes x the major principal stress direction, which ensures the fracture develops in a plane.

Cohesion c and friction angle ϕ are also important factors that affect fracture crossing, because they directly determine the magnitude of forces on the square fracture surfaces that resist the relative movements between adjacent solids. It should be noted that in this section, these two quantities refer to lattice parameters rather than the macroscopic properties of the sample. As defined in the LEM formulation, the ultimate shear strength of a lattice is,

$$V_u = V_f + N tan\phi + c \tag{5.5}$$

Where V_f is the material shear strength and N is the longitudinal compressive stress. Both cohesion c and friction angle ϕ contribute to the ultimate shear strength. c provides a constant increment, while the effect of ϕ depends also on the normal pressure. This equation applies to all the lattice statuses. V_f starts to decrease when the lattice begins to yield and soften, and finally becomes zeros when the lattice is completely broken. Therefore, for a completely broken lattice under compression, its resistance to shear yielding and transversal movement entirely comes from c and ϕ, which is the case for those pre-existing fractures. For intact lattices, increasing these two parameters would increase their shear strength. But this would not have a significant influence because in the hydraulic fracturing test, nearly all the lattices fail in tension. In this set of simulations, c varies from 0 to 5 MPa and ϕ varies from 0° to 45°.

The approach angle (dihedral angle, denoted as β in this section) between hydraulic and pre-existing fractures also affects fracture interactions. However, to ensure the hydraulic fractures develop in the original plane, the major stress direction needs to be fixed in the same plane. Variation of approach angle is achieved by rotating the pre-existing square fractures along the y axis, as shown in Figure 5.20. Consequently, the magnitude of stress applied perpendicular to the square fractures decreases. Therefore, the influence of the approach angle cannot be considered separately. 45°, 60° and 90° approach angles were tested in this set of simulations.

As discussed in Section 5.2, heterogeneity induced by lattice property distribution affects fracture propagation. Most of the cases were tested using models with uniform lattice properties. But a small number of tests were also conducted under Weibull distribution with different shape parameters k to examine its influence. Above mentioned parameters and their values are listed in Table 5.4.

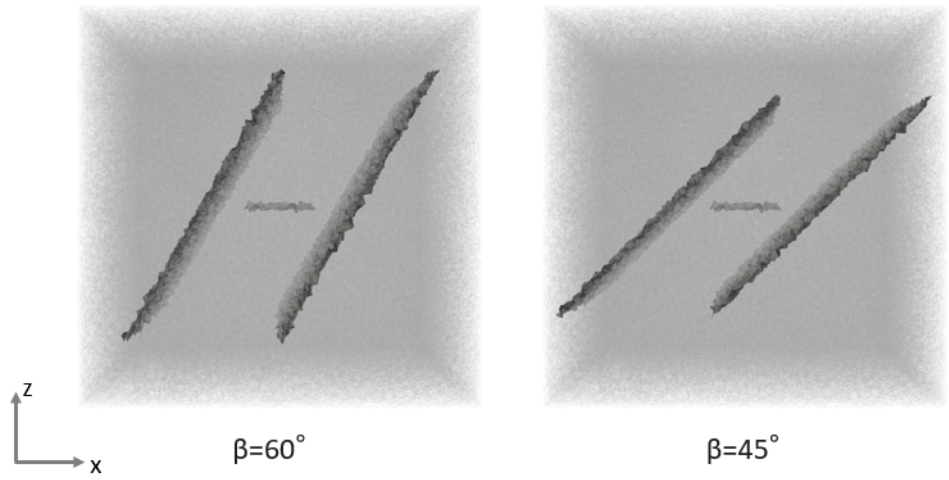

Figure 5.20: Side view of LEM models for different approach angles

Parameters	**Values**
Stress field σ_x (MPa)	10, 20, 30, 40
friction angle ϕ (°)	0, 15, 30, 45
cohesion c (MPa)	0, 2.5, 5
approach angle β (°)	45, 60, 90
Distribution	uniform, Weibull (k = 1, 2, 3)

Table 5.4: Simulation parameters for the fracture interactions tests

The same microscopic properties of lattices as in Section 5.2 are used here: tensile strength of 17.2 MPa, shear strength of 28 MPa, elastic modulus of 50 GPa, and Poisson's ratio of 0.2. The injection rate is 1.25×10^{-4} m^3/s and the time step length is 0.05 s. The viscous effects are also ignored in this set of simulations.

5.3.2 Mechanism of Fracture Crossing in the LEM

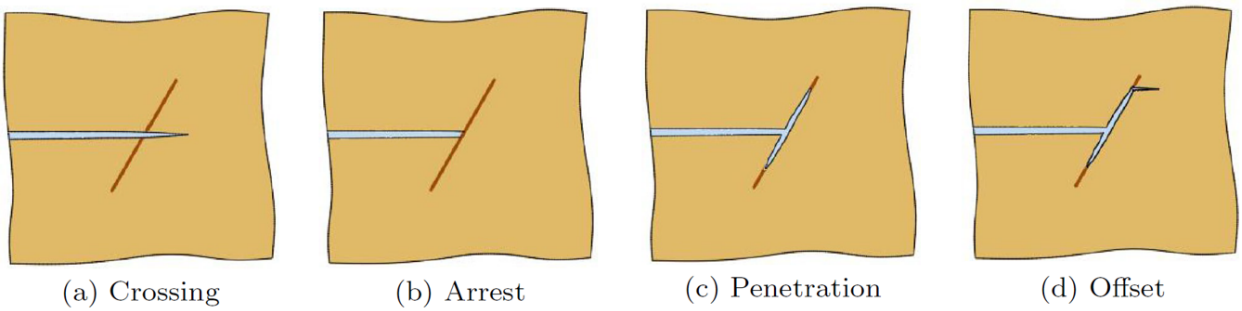

Figure 5.21: Four basic interaction types between hydraulic fracture and natural fracture [22]

The interactions between hydraulic fracture and pre-existing natural fracture could be classified into four basic types, including crossing, arrest, penetration and offset (Figure 5.21) [22]. A combination of different types, such as crossing and penetration, could also happen and form more complex scenarios. These basic interaction types could be observed in this set of simulations.

Figure 5.22 illustrates the mechanism of fracture crossing in this LEM code. As sketched in Figure 5.22a, the natural fracture is initially closed under the applied stress field σ_x. When the hydraulic fracture contacts the natural fracture, the rock matrix (solid lattices) on the hydraulic fracture side (left of natural fracture) is separated into upper and lower parts and subjected to the fluid pressure p, which leads to opposite z displacement field d_z in the rocks. As an example, Figure 5.22b shows the z displacement field at the cross section in the xz plane cutting through the middle of the sample, where red represents upward movement while blue stands for downward. Meanwhile, this contact allows fluid flows into the natural fracture and reduces the effective stress at the fracture surface. The natural fracture may open if the bond strength and applied stress field are not large enough to overcome the fluid pressure. In this case, hydraulic fracture develops along the natural fracture as fluid further flows into it, which is the penetration type of interaction (Figure 5.21c).

If the natural fracture surfaces are able to remain in contact, friction f_z would be generated due to relative movement, or the tendency of it, between rocks at two sides of the natural fracture. This joint friction and cohesion provide resistance to shear slip on the fracture surface. Because of the opposite tendency of movement, the resistance acts oppositely at the upper and lower part of the natural fracture. This results in tensile stress in the middle, which is in front of the hydraulic fracture tip. An example normal stress field is shown in Figure 5.22c, where red means in tension while blue represents in compression. Most part of the sample is in compression due to the applied stress field and fluid pressure, but high tensile stress is concentrated on the other side of the natural fracture, which is also

around the tip of the hydraulic fracture. The magnitude of this tensile stress is related to the shear resistance, which is determined by the combination of the applied stress field, friction angle and cohesion. If the tensile stress is not large enough to break the lattices, the hydraulic fracture would be arrested (Figure 5.21b). Otherwise, those lattices break in tension and small fracture surfaces are generated on this side. The hydraulic fracture propagates through the joint, which is the crossing type of interaction (Figure 5.21a). This mechanism is similar to the compressional crossing described in [139]. The occurrence of shear slip on the natural fracture surface is possible for both crossing and arrest cases, which depends on the magnitude of shear resistance and was observed in this set of simulations. This result was also verified by other research, both experimentally and numerically [104][189].

An offset scenario (Figure 5.21d) was observed in the case with 45° approach angle, though the crossed fractures were not fully developed. The cause of this scenario may be more likely due to fluid pressure instead of shear resistance, which will be discussed in detail in the next part.

Although all these interaction types were observed, it should be noted that viscosity is ignored in this simulation, which leads to constant fluid pressure developed in the whole natural fracture once it has contact with hydraulic fracture. This does not simulate real penetration or arrest scenarios due to the additional fluid pressure. And this is likely to cause crossing more difficult to happen because the effective stress is reduced.

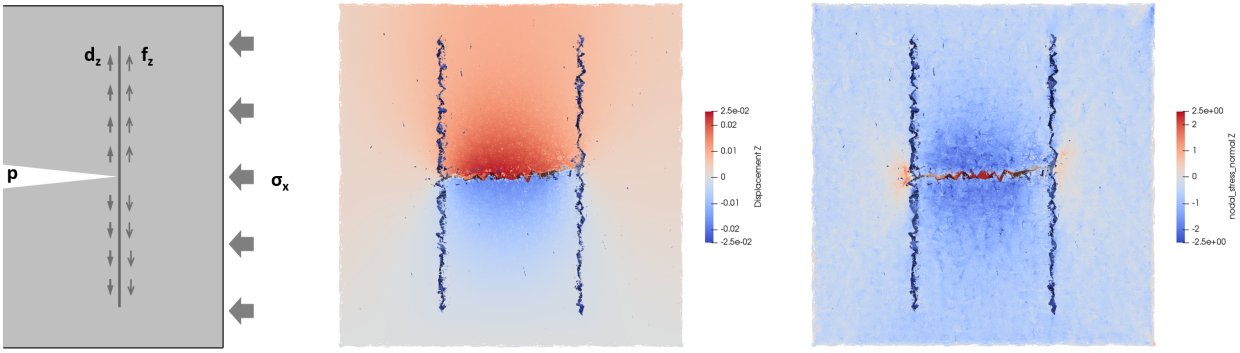

(a) Sketch (b) Z displacement field (c) Z normal stress field

Figure 5.22: Model configuration

In fracture crossing cases, the process may be classified into four stages. Figure 5.23 shows the fracture pattern (projected to xy plane) and normal stress field in z direction (cross section cut through the middle of sample in xy plane) at different stages.

The first stage begins with the injection of fluid and continues until the hydraulic fracture reaches the natural fracture (Figure 5.23a). Some studies suggested that shear failure of the pre-existing joint may occur before having contact with hydraulic fracture due to the increased stress level induced by approaching hydraulic fracture [189]. This could also be

observed in this simulation, where a very small number of new fracture surfaces were generated on the joints in this stage. But at least in this set of simulations, this effect has no substantial impact on the fracture interactions and could be ignored. As hydraulic fracture reaches the natural fractures, tensile stress develops in small regions across the joints. But this stress is small and the lattices remain intact. Because of this resistance, the hydraulic fracture develops mainly along the y axis, in between and parallel to the two joints.

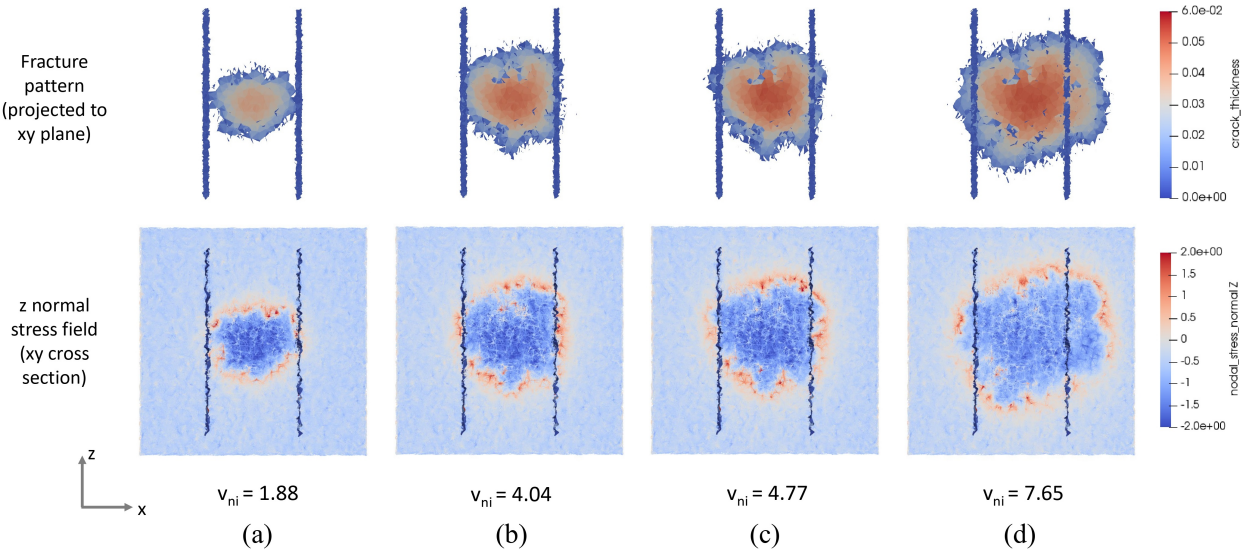

Figure 5.23: Fracture development process ($\sigma_x = 40$ MPa, $c = 2.5$ MPa, $\phi = 30°$) (v_{ni} represents normalized injection volume)

In the second stage, the contact length between hydraulic and natural fracture increases as the crack grows. This leads to greater regions on the other sides of the joints becoming in tension, and the magnitude of tensile stress also increases. Consequently, some lattices in these regions break and generate small fracture surfaces (Figure 5.23b). These fractures are randomly distributed in these regions and could be either adjacent to the joint or isolated, depending on the location of stress concentration, lattice strength and orientation. These small individual fractures continue to grow and coalesce in the third stage. They are eventually connected to the joints and filled with fluid (Figure 5.23c). Therefore, the hydraulic fracture crosses the joint in this stage. These crossed fractures are independent and may not be connected directly. Some parts adjacent to the contact line could remain intact at this stage. But it could be observed that higher tensile stress concentrates at the intact location between crossed fractures, which would subsequently break these lattices. The difference in injection volume between the second and third stages is relatively small, which indicates that fracture evolves quickly in this period and these two stages may not be clearly distinguished from each other. In simulation results, there are cases where fractures stop developing at

the second or third stage. The former is classified as arrest, while the latter is classified as partially cross.

It enters into the fourth stage if the fracture continues to develop. All the lattices adjacent to the contact line would break and the crossed fractures connect together. The hydraulic fracture becomes circular again with a continuous arc (Figure 5.23d). It appears that the joints do not significantly influence the propagation of hydraulic fracture once it is completely crossed. The type of interaction is classified as cross in this stage.

5.3.3 Results and Discussions

The influence of various parameters on the fracture interactions is directly reflected in the fracture patterns. For each set of parameters, simulation results, such as injection pressure histories, joint displacements, and stress fields around the contact region, would be investigated to explain how the corresponding fracture pattern was generated.

Similar to Section 5.2, the data is normalized for better generalizability. The injection volumes are normalized by the volume of the original penny shape crack during the process, which is equal to its total area multiplied by the mean aperture. Length related quantities, such as openings and shear slips of the joints, are normalized by the initial radius of the penny shaped crack (0.2 m). Stress related quantities, such as injection pressures and normal stress fields, are normalized by the applied stress field in z direction (5 MPa), which is the stress that hydraulic fractures need to overcome to develop. A 0.1 $\times$ 0.1 $\times$ 0.1 m box volume adjacent to each joint, on the opposite side of hydraulic fracture and aligned along the same x axis as the center of penny shaped crack (Figure 5.24), was taken to compute the mean nodal normal stress in z direction.

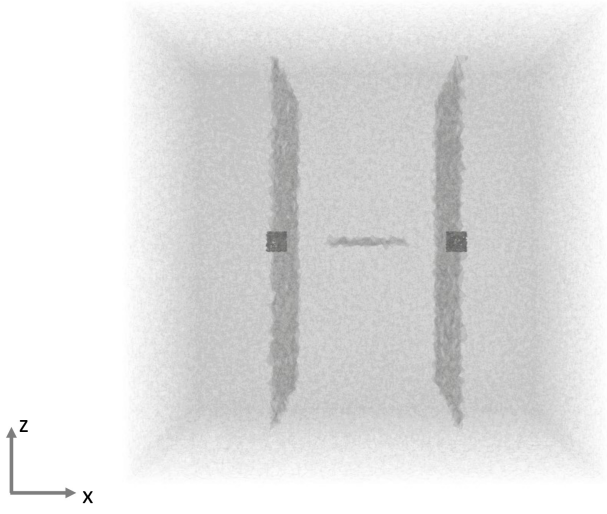

Figure 5.24: Cubic volumes for computing mean nodal stress

Cohesion and friction angle

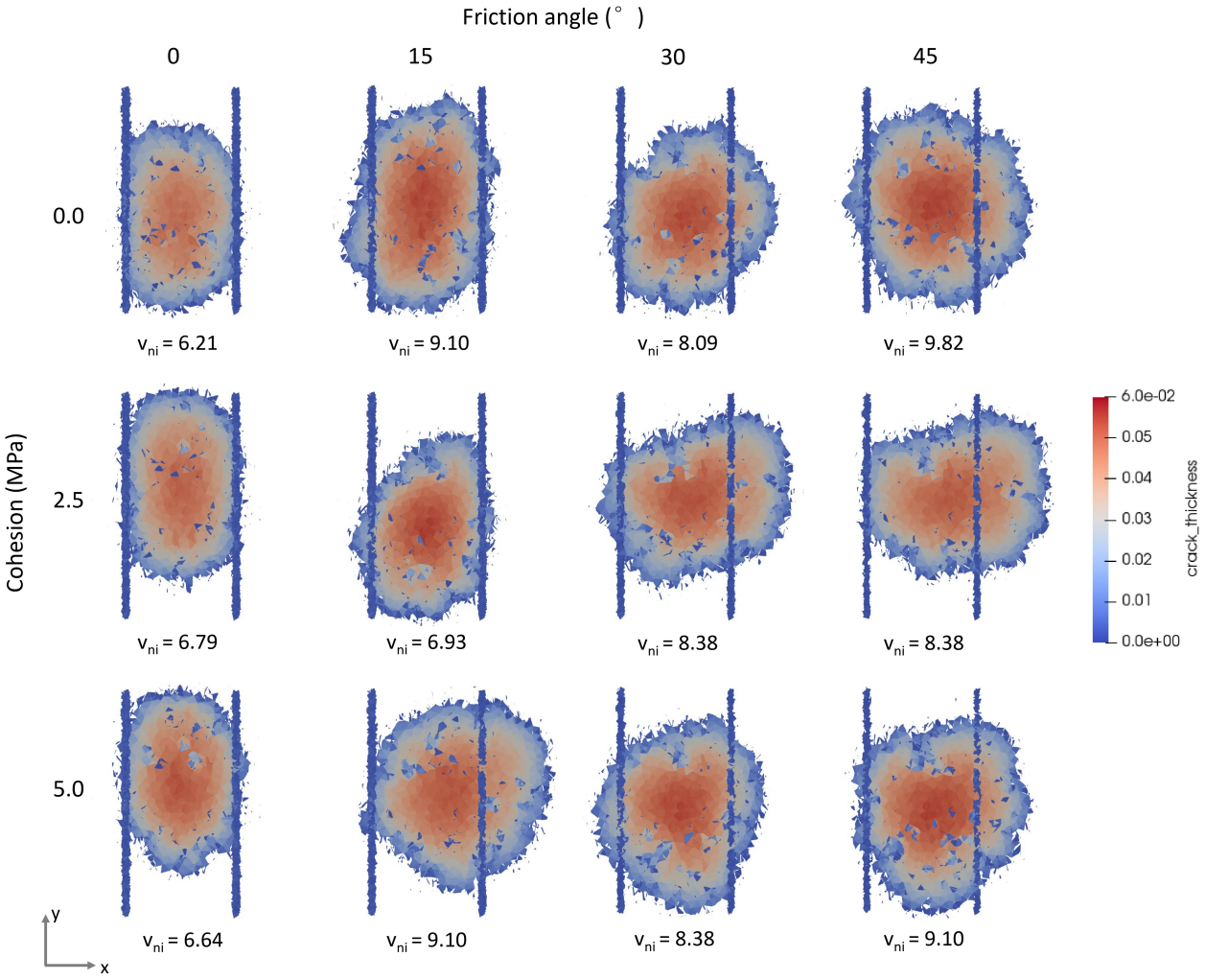

Figure 5.25: Fracture patterns for different values of friction angle and cohesion ($\sigma_x = 40$ MPa, $\beta = 90°$)

Figure 5.25 depicts the xy plane projected fracture patterns for cases with uniform lattice property, 90° approach angle and 40 MPa applied stress field, but different friction angles and cohesion values. It should be noted that due to the restriction of model size, the simulations were stopped when hydraulic fractures became close to model boundaries to eliminate possible influence on fracture development from the boundaries. Therefore, for different cases, the final stage fracture patterns shown in the figure are at different normalized injection volumes v_{ni}.

The types of interaction between hydraulic and natural fractures are summarized later in Table 5.5. Generally, as friction angle and cohesion increase, it becomes easier for the hydraulic fracture to cross the joints. The hydraulic fractures are mostly arrested on both sides for the cases with $\phi = 0°$, and mostly become partially crossed when $\phi = 15°$. When ϕ is larger than 30°, each case has at least one fully cross event. There are visible changes in fracture patterns when ϕ increases from 0° to 15°, and from 15° to 30°. However, similar fracture patterns are observed after ϕ is greater than 30°. This indicates that the resulting friction is already large enough to generate tensile stress that leads the hydraulic fracture to cross the joints. The increment of cohesion also makes crossing easier to occur, but the influence is not as great as the friction angle. Because a large stress field σ_x is applied on the joints, most part of the shear resistance is contributed by friction. Cohesion is expected to have more significant effects in cases with smaller σ_x.

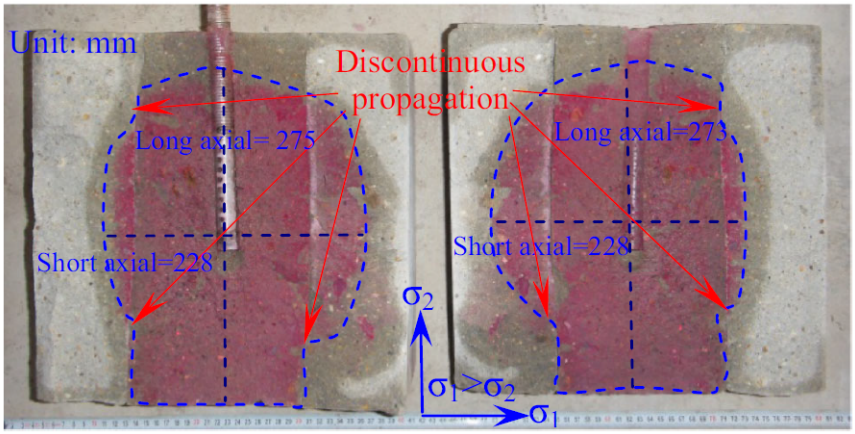

Figure 5.26: Interactions between hydraulic fracture and bedding layers in experiment [72]

In crossing cases under relatively large shear resistance, it is noticed that the crossing events could happen either on both sides, or on one side while the other is arrested or partially crossed. Therefore, this does not seem to be related to the shear resistance. Heterogeneity may explain the reason why, in some cases, the hydraulic fracture mainly develops and crosses on one side. Heterogeneity causes the hydraulic fracture arrives at the two joint at different time, and various tensile strength on the other side of the joints, due to lattice orientations or cross sectional areas. Consequently, the hydraulic fracture usually crosses one of the joints faster than the other. Crossing gives the hydraulic fracture new directions to develop, which reduces injection pressure and prevents the tensile stress adjacent to the other side of the joint from building up. Thus it becomes more difficult to cross the other joint. Figure 5.26 shows an unevenly developed fracture pattern observed in an experiment from literature [72], which looks similar to those shown in Figure 5.25.

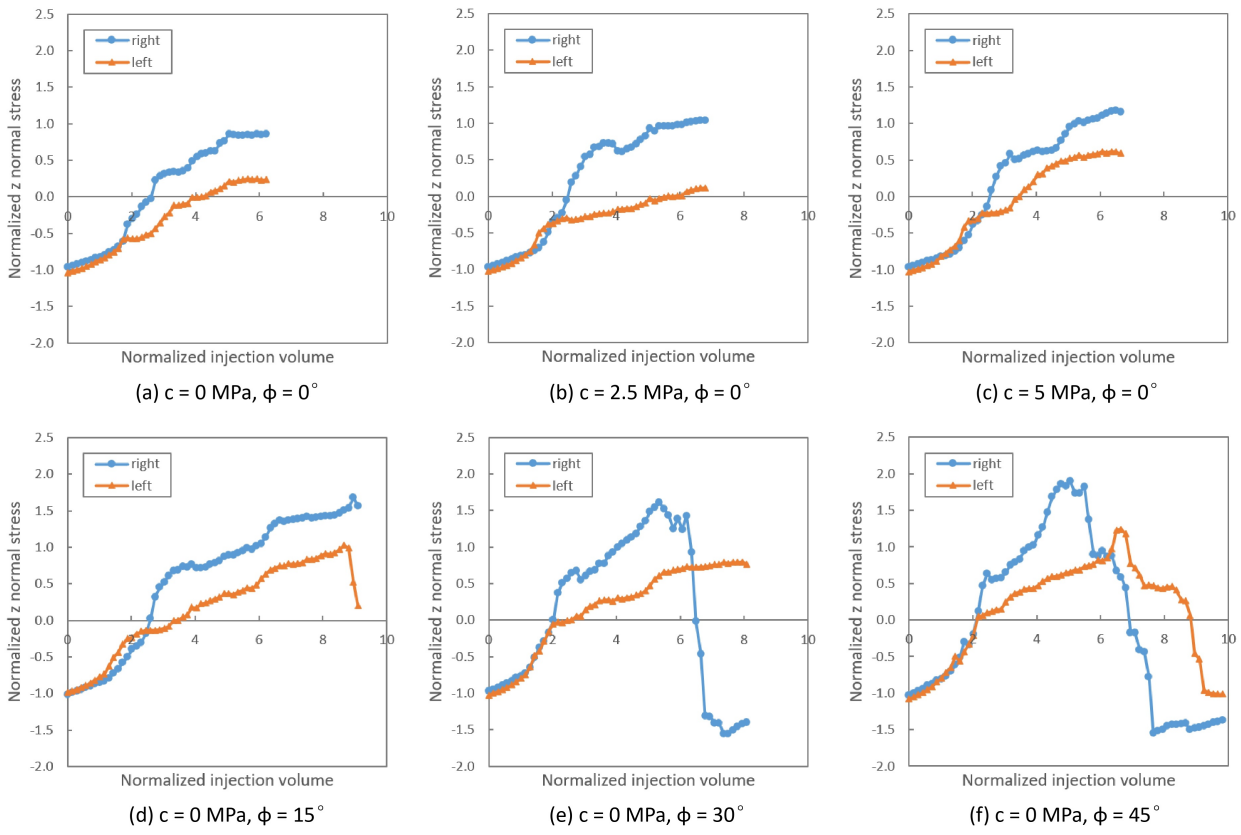

Figure 5.27: z normal stress for different values of friction angle and cohesion

Figure 5.27 depicts the normalized mean z direction normal stress history in small cubic volumes adjacent to the joints as shown in Figure 5.24. The initial values are -1 in all the cases, which is equal to the applied compressive stress field in z direction σ_z.

The change of these mean stress curves could be explained together with the fracture development process (Figure 5.28), using the case in Figure 5.27e as an example. The stress increases gradually at the initial stage as the fracture tip approaches. After hydraulic fracture reaches the joints, the continuing development of contact length increases the volume subjected to tension, and also the magnitude of shear resistance, which generates tensile stress (Figure 5.28a-b). These two factors cause the sudden increment in the slopes of the stress curves. When the tensile region covers the entire selected cubic volume, further increment of contact length only increases mean stress by increasing the shear resistance. Therefore, the mean stress keeps increasing but the slope decreases (Figure 5.28b-c). During this process, the hydraulic fracture mainly develops on the right side due to heterogeneity, resulting in larger stress observed on the right. Due to lattice breakage and compressive stress field by fluid pressure, the stress on the right starts to decrease when the hydraulic fracture crosses the joint (Figure 5.28c-d), and drops to negative (in compression) as completely

crossed (5.28d-e).

The slope in the third stage (Figure 5.28b-c), which is determined by shear resistance, increases as friction angle and cohesion. In cases with large friction angles, the stress builds up faster to the peak and leads to fracture crossing (5.27e,f). When ϕ is relatively small (5.27d), the stress increases slower and the hydraulic fracture can only be partially crossed at the end of the simulation. It can be observed that cohesion also slightly increases the slopes (5.27a,b,c), but the influence is not large enough.

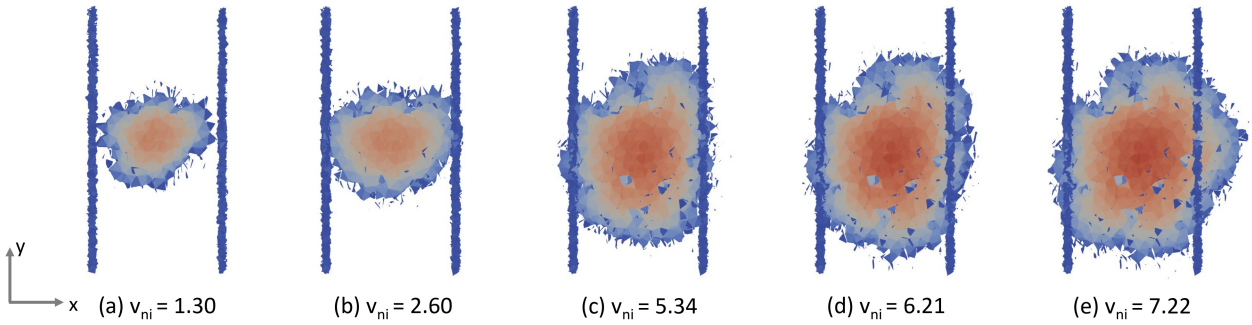

Figure 5.28: Fracture patterns at different injection volume ($\sigma_x = 40$ MPa, $c = 0$ MPa, $\phi = 30°$)

Applied stress field

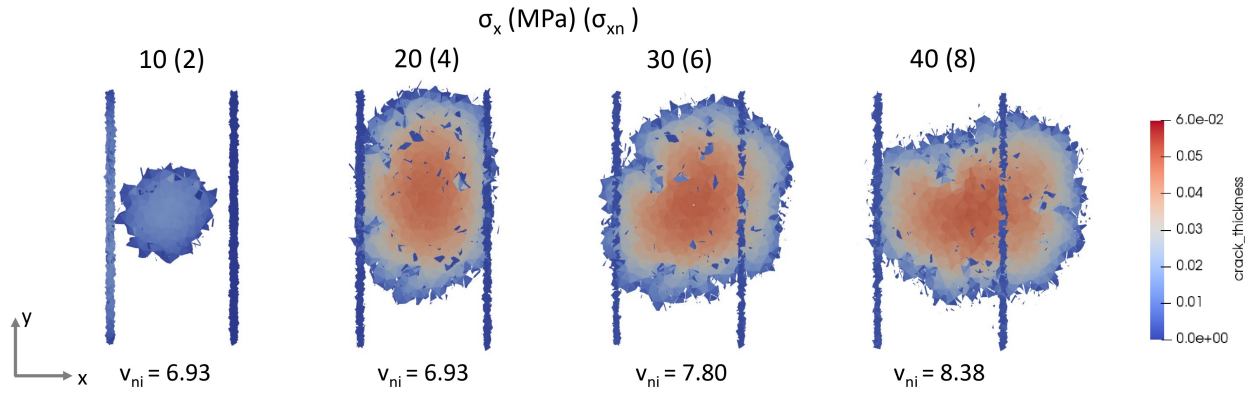

Figure 5.29: Fracture patterns for different applied stress field σ_x ($c = 2.5$ MPa, $\phi = 45°$)

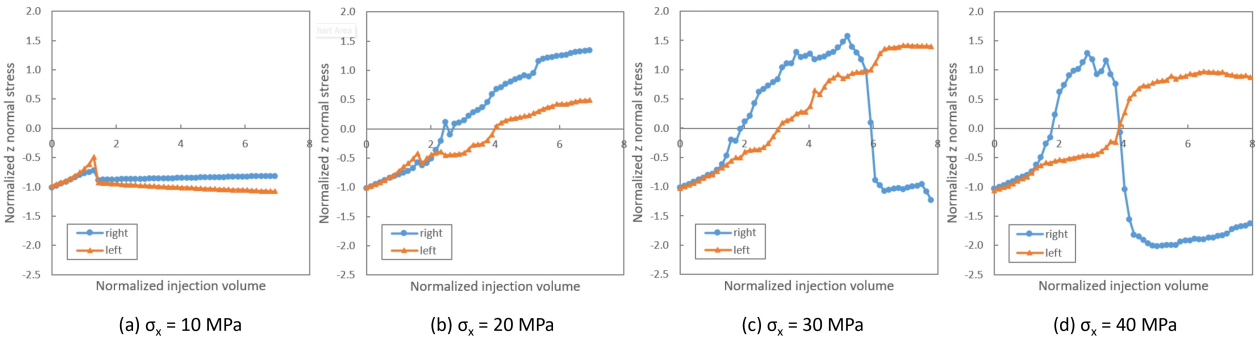

Figure 5.30: z normal stress for different applied stress field σ_x

Figure 5.29 depicts the fracture patterns for cases with uniform lattice property, 90° approach angle, 2.5 MPa cohesion and 45° friction angle, but under different applied stress fields σ_x. The normalized applied stress σ_{xn} is marked in the brackets for comparison with normalized injection pressure and mean stress. Figure 5.30 shows their mean normal stress history curves near the joints. Generally, as σ_x increases, greater shear resistance is generated on the joint surfaces and hydraulic fracture becomes easier to cross the joints.

For the case with $\sigma_x = 10$ MPa, hydraulic fracture stops developing once it reaches the left joint. As the joint connects to the fluid network, the total fracture surface area suddenly increases, thus less aperture is required to keep the constant injection rate. Therefore, the corresponding injection pressure is largely reduced (Figure 5.31a). However, the reduced pressure is still larger than σ_x, which completely opens the left joint. On the other hand, the pressure is much less than the threshold required for fracture development. Therefore, the system starts to behave linear elastically. As fluid is injected, the joint keeps opening and injection pressure increase slowly. Normal stress on the other sides of the joints remains in compression (5.30). The interaction type of this case is classified as penetration.

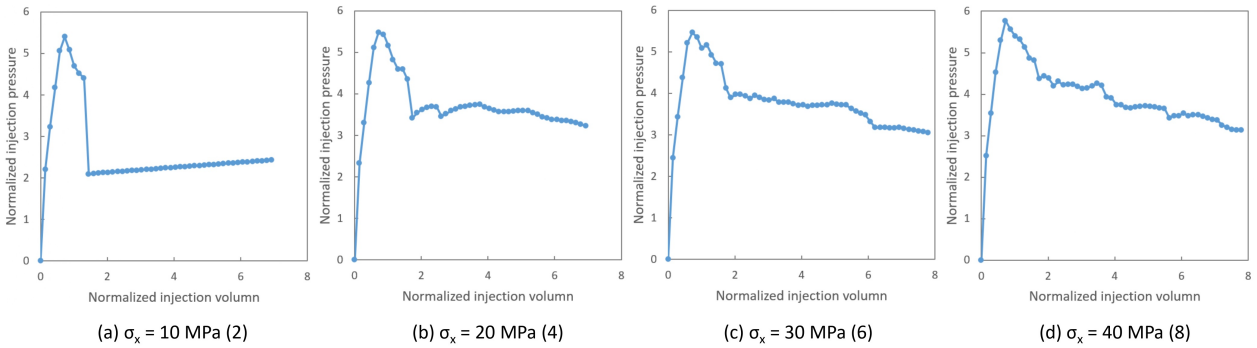

Figure 5.31: Injection pressure for different applied stress field σ_x

When $\sigma_x = 20$ MPa, the joint starts to become difficult to open under this relatively

large stress field. Thus the pressure drop when hydraulic fracture connects to a joint is much smaller than the previous case (Figure 5.31b). The reduced pressure is slightly less than σ_x, which allows most parts of the joint to remain close. However, this also results in a small normal compressive stress between joint surfaces, which could not provide enough shear resistance. Therefore, the tensile stress adjacent to joints builds up slowly (Figure 5.30b) and hydraulic fracture is arrested. As σ_x continues to rise, the slopes of mean stress curves increase and fracture crossing happens (Figure 5.30c,d). When $\sigma_x = 40$ MPa, the pressure drop at connection is very small (Figure 5.31d), indicating that the entire joints almost remain closed and injected fluid stays in the hydraulic fracture.

Approach angle

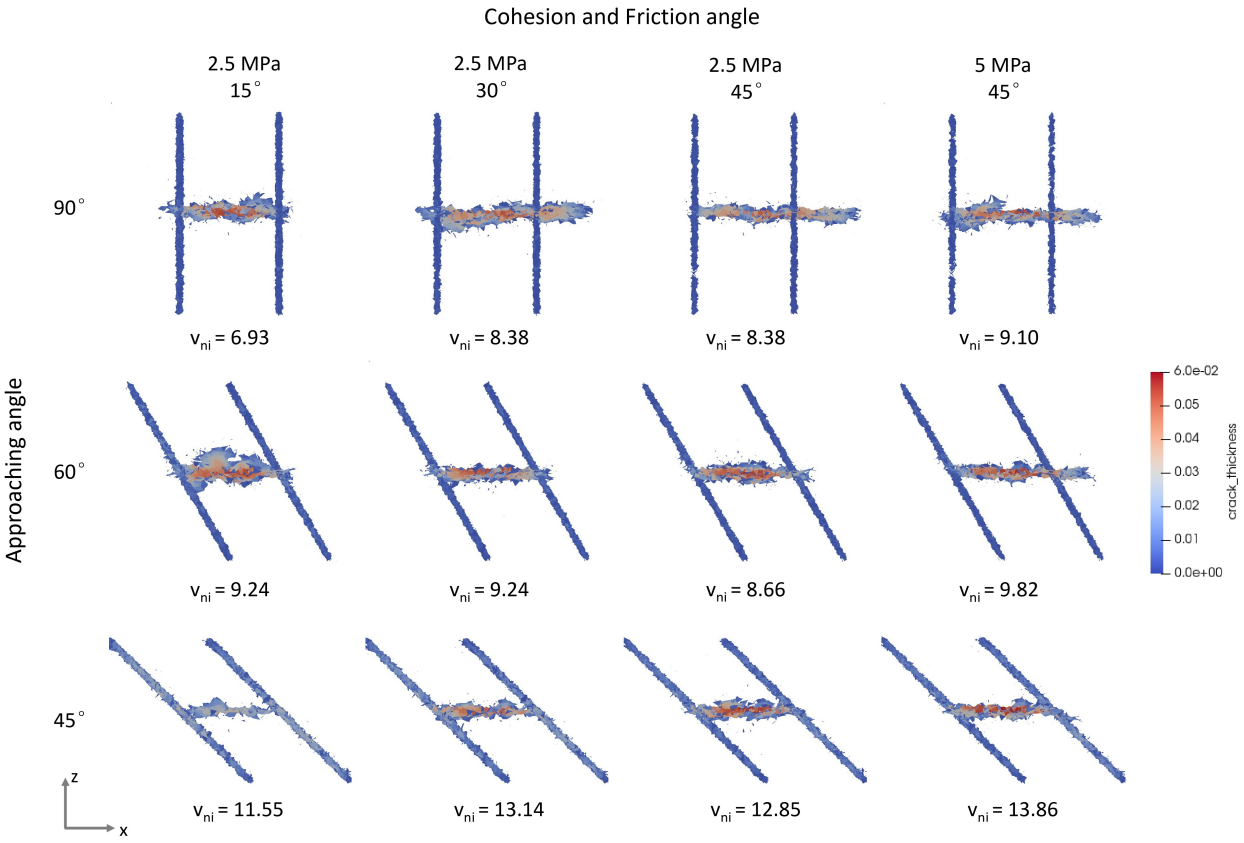

Figure 5.32: Fracture patterns for different approach angles β ($\sigma_x = 40$ MPa)

Figure 5.32 shows the fracture patterns for the cases with different approach angle β under the same applied stress field σ_x. The fracture patterns are taken at the steps where they are close to the model boundaries, or for most cases with $\beta = 45°$, until exceeding the simulation

time limit. Figure 5.33 and 5.34 depict the normalized injection pressure histories for cases with $\beta = 60°$ and $45°$ respectively. Generally, as β increases, the normal stress perpendicular to the square fracture surfaces rises, thus hydraulic fracture becomes easier to cross the joints.

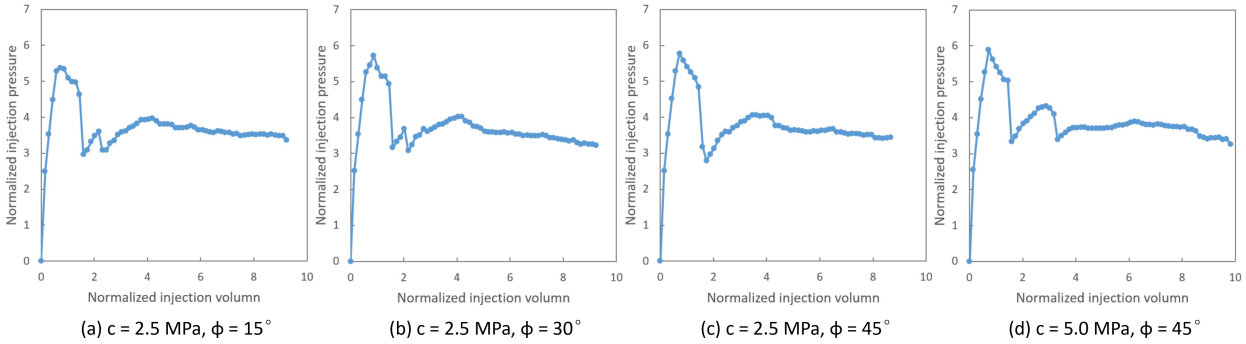

Figure 5.33: Injection pressure for different cohesion and friction angles ($\beta = 60°$)

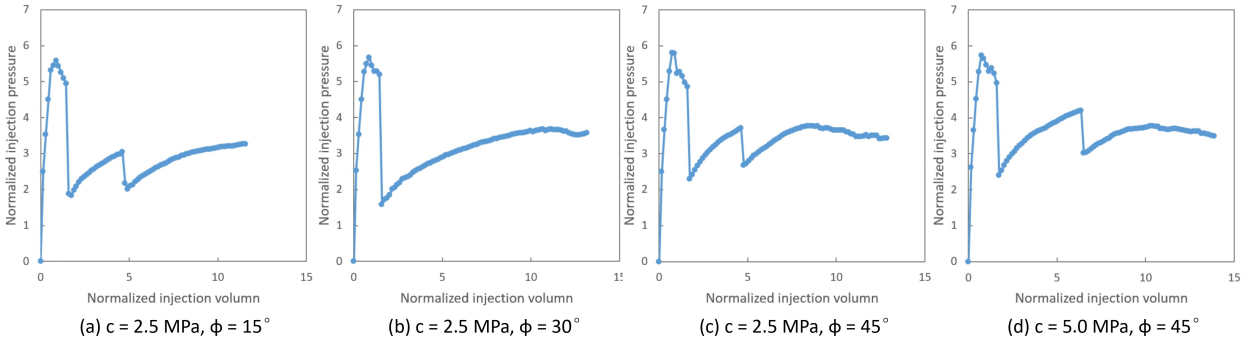

Figure 5.34: Injection pressure for different cohesion and friction angles ($\beta = 45°$)

Large injection pressure drops are observed in all the cases in Figure 5.33 and 5.34. The hydraulic fracture might contact the two joints at the same or in two successive steps, resulting in a single large drop. Alternatively, a large drop followed by a smaller drop appears when the two contacts happen at different steps. The stress field that is perpendicular to the joint surface, σ_n, is composed of components of the two orthogonal applied stress fields, σ_x (40 MPa) and σ_z (5 MPa). For $\beta = 60°$, σ_n is around 37 MPa, whereas when $\beta = 45°$, it is approximately 32 MPa. Noticed that σ_n are larger than those of the cases shown in Figure 5.31b,c. However, larger pressure drops are observed here, especially for the cases with $\beta = 45°$. This indicates that the inclined joints are easier to open under the same injection rate. The reason is, when the hydraulic fracture, which opens along the z axis, connects to the joints, the solid of joint surfaces also moves in this direction due to continuity. When $\beta = 90°$, this only results in a shear slip. However, this movement contributes to the

opening of the inclined joints. In addition, the components of σ_x and σ_z that are parallel to the joint surfaces may tend to induce shear slip of the joints. Although the surfaces are locked because of the roughness, this may also contribute to joint opening when the fluid pressure is applied. Therefore, as the normal stress on the joint surfaces decreases, hydraulic fractures are more difficult to cross the joints.

As the injection pressure builds up again after the drop, very few new fracture surfaces are formed and the hydraulic fracture develops very slowly. As discussed in Section 5.2, obvious fracture developments are only observed after the injection pressure approaches its peak. Therefore, for cases with $\beta = 60°$, the injection pressures reach the peak again and gradually reduce in the later stage (Figure 5.33), indicating the fractures continue developing. While when $\beta = 45°$, the fractures only have limited development in the case shown in Figure 5.34a, and only start to develop relatively faster at a very late stage in other cases (5.34b,c,d). The joints open visibly in these cases with $\beta = 45°$, thus penetration type of interaction is involved and no cross event is observed. However, for the case with $c = 5$ MPa and $\phi = 45°$, a small crossed fracture with an offset to the main hydraulic fracture appears on the other side of the right joint. Because the joint opens, the mechanism to form this offset fracture is different from the one discussed previously for crossing events. This fracture is likely to be initiated at a random location where fluid induced tensile stress is concentrated locally due to heterogeneity from the mesh and other previously formed fractures.

Property distribution

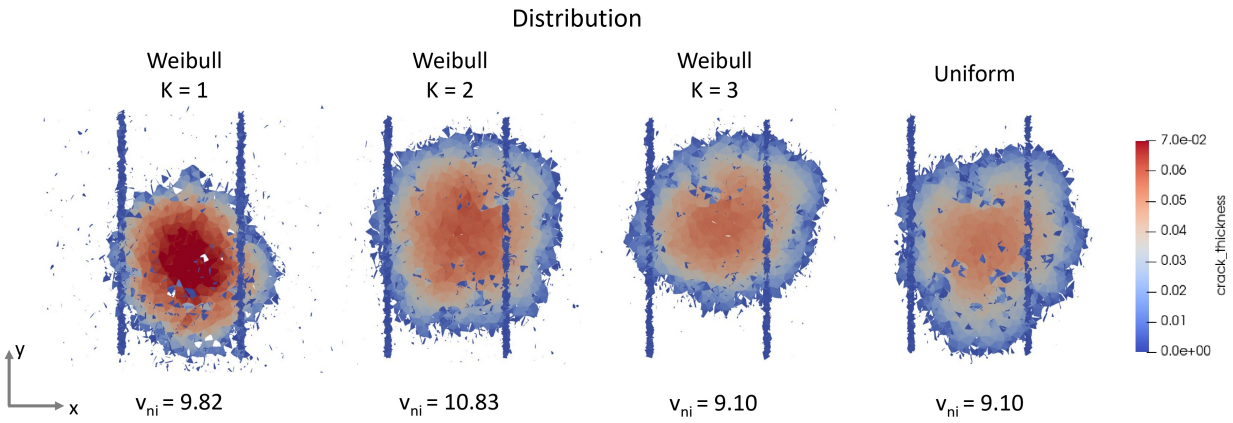

Figure 5.35: Fracture patterns for different property distributions ($\sigma_x = 40$ MPa, $c = 5.0$ MPa, $\phi = 45°$)

As discussed in Section 5.2, when the property distribution is applied, the fractures become increasingly dispersed and more difficult to propagate in the more heterogeneous scenarios. This also happened here, as shown in Figure 5.35. The heterogeneity reduces Young's modulus of the sample, resulting in a greater aperture of hydraulic fracture, which also makes

it develop slower. It seems the influence of heterogeneity on fracture crossing only becomes relatively significant for the extreme case ($k = 1$). Although The crossing events start earlier in more uniform cases, full crossing happens eventually, except for the $k = 1$ case, which is still in partial crossing. The slower development of hydraulic fracture may be part of the reason for this discrepancy.

Effects of applied boundary conditions

Also note that the fractures mainly develop on the right part in most simulations. Similarly to Section 5.2, reversed boundary conditions were applied to examine the influence of boundaries. The case under $\sigma_x = 40$ MPa, with $\phi = 45°$, $c = 2.5$ MPa and a uniform distribution was chosen, where the hydraulic fracture crosses the right joint but is arrested on the left. Roller supports were applied on the $+x$ and $+y$ faces, while uniform pressures σ_x and σ_y were applied to the $-x$ and $-y$ faces respectively. While the boundary conditions at $-z$ and $+z$ faces remain the same.

The projected fracture patterns are shown in Figure 5.36. The fractures that result from reversed boundary slightly shift to the left and partially cross the left joint. But the majority of these two patterns are the same (in purple), especially since both of them mainly develop on the right. Therefore, as in Section 5.2, the boundary conditions affect the fracture developments and interactions but do not significantly affect the results.

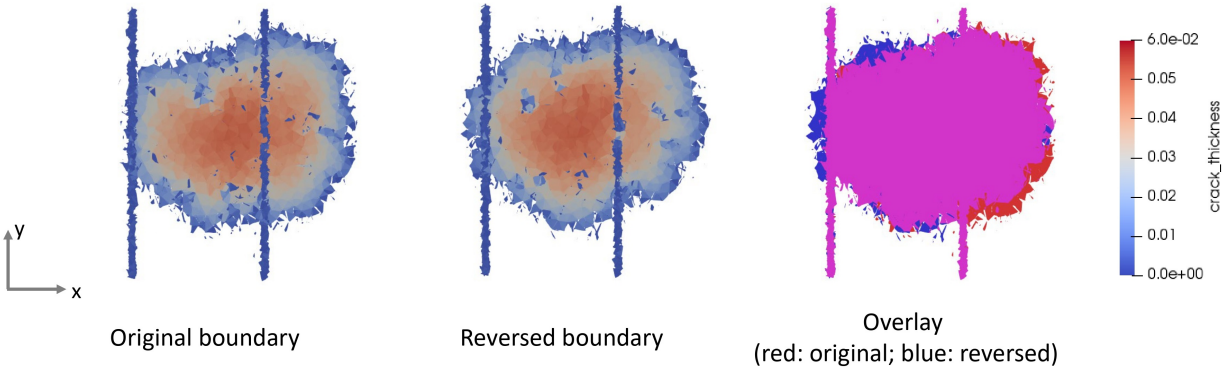

Figure 5.36: Fracture pattern resulted from original and reversed boundary conditions ($\sigma_x = 40$ MPa, $\phi = 45°$, $c = 2.5$ MPa, uniform distribution)

Summary and fracture crossing criteria

Table 5.5 summarizes the type of interaction on both joints for each scenario.

Case ID	Applied stress field σ_x (MPa)	Friction angle ϕ (°)	Cohesion c (MPa)	Approach angle β (°)	Distribution	Type of interaction	
						left	right
1	40	0	0.0	90	uniform	arrest	arrest
2	40	15	0.0	90	uniform	partially cross	partially cross
3	40	30	0.0	90	uniform	partially cross	cross
4	40	45	0.0	90	uniform	cross	cross
5	40	0	2.5	90	uniform	arrest	arrest
6	40	15	2.5	90	uniform	partially cross	partially cross
7	40	30	2.5	90	uniform	cross	cross
8	40	45	2.5	90	uniform	arrest	cross
9	40	0	5.0	90	uniform	arrest	arrest
10	40	15	5.0	90	uniform	arrest	cross
11	40	30	5.0	90	uniform	cross	partially cross
12	40	45	5.0	90	uniform	partially cross	cross
13	30	45	2.5	90	uniform	partially cross	cross
14	20	45	2.5	90	uniform	arrest	arrest
15	10	45	2.5	90	uniform	penetration	N.A.
16	40	15	2.5	60	uniform	partially cross	partially cross
17	40	30	2.5	60	uniform	partially cross	partially cross
18	40	45	2.5	60	uniform	arrest	partially cross
19	40	30	5.0	60	uniform	partially cross	partially cross
20	40	45	5.0	60	uniform	arrest	cross
21	40	15	2.5	45	uniform	penetration	penetration
22	40	30	2.5	45	uniform	penetration	penetration
23	40	45	2.5	45	uniform	penetration	penetration & offset
24	40	45	5.0	45	uniform	penetration	penetration & offset
25	40	45	5.0	90	Weibull k=1	partially cross	partially cross
26	40	45	5.0	90	Weibull k=2	partially cross	cross
27	40	45	5.0	90	Weibull k=3	cross	cross

Table 5.5: Interaction type summary for all the simulation cases

Several analytical criteria have been derived to predict whether a crossing event will happen when a hydraulic fracture encounters a natural joint [14][168][139]. As described above, the fracture crossing mechanism in this LEM code is similar to the compressional crossing proposed by Renshaw and Pollard (R&P), thus their crossing criterion developed based on this concept would be considered here [139]. This criterion is based on elastic fracture theory and specially designed for an orthogonal intersection between hydraulic fracture and non-cohesive natural joints, with an assumption that crossing will only occur when there is no slip between joint surfaces. This criterion states that the crossing will occur when,

$$\frac{-\sigma_{HMax}}{T_0 - \sigma_{hMin}} > \frac{1 + \mu_f}{3\mu_f} \tag{5.6}$$

Where σ_{HMax} and σ_{hMin} are the major and minor principal stress parallel and perpendicular to the hydraulic fracture respectively. μ_f is the coefficient of friction on the joint surface

and T_0 is the material tensile strength. The left hand side of this inequality is named as the crossing stress ratio. Because of the no slip assumption, which is in contrast with some experimental and numerical results [189], the crossing may occur at lower crossing stress ratios than predicted.

Sarmadivaleh and Rasouli further modified this criterion to extend its applicability to the non-orthogonal intersection between hydraulic fracture and cohesive joints [145]. For orthogonal intersection with a cohesive joint, the influence of joint cohesion c is treated as an additional frictional force,

$$c = -\mu_{f'}\sigma_{H'} \tag{5.7}$$

Where $\mu_{f'}$ is an equivalent coefficient of friction and $\sigma_{H'}$ is the normal stress applied on the joint surfaces, including the in situ stress field and induced stress from the tip of hydraulic fracture. The modified criterion shares the same form as Equation 5.6,

$$\frac{-\sigma_{HMax}}{T_0 - \sigma_{hMin}} > \frac{1 + \mu_{f''}}{3\mu_{f''}} \tag{5.8}$$

Where $\mu_{f''} = \mu_f + \mu_{f'}$, and $\mu_{f'}$ was derived as,

$$\mu_{f'} = -(1 + \mu_f)\frac{c}{\sigma_{HMax}} \tag{5.9}$$

Therefore, both sides of Equation 5.8 could be calculated for simulation results of orthogonal cases in Table 5.5 (Case 1∼15) and compared with this criterion. The major and minor principal stress here is σ_x and σ_z respectively. Because this analysis was conducted locally at the fracture tip, it is reasonable to use lattice properties as the tensile strength, cohesion and friction coefficient. The case is classified as complete crossing when at least one cross event exists. When there is no cross event but at least one partial cross event, it is classified as partial crossing. And the others are classified as no crossing. The results are shown in Figure 5.37. Note that as there are simulation cases with $\phi = 45°$ and $c \neq 0$, their equivalent friction coefficients are larger than 1. The simulation results are generally consistent with the R&P criterion. But as this criterion possibly overestimates the crossing boundary due to the no slip assumption, indicating that crossing is a bit difficult to happen in this simulation.

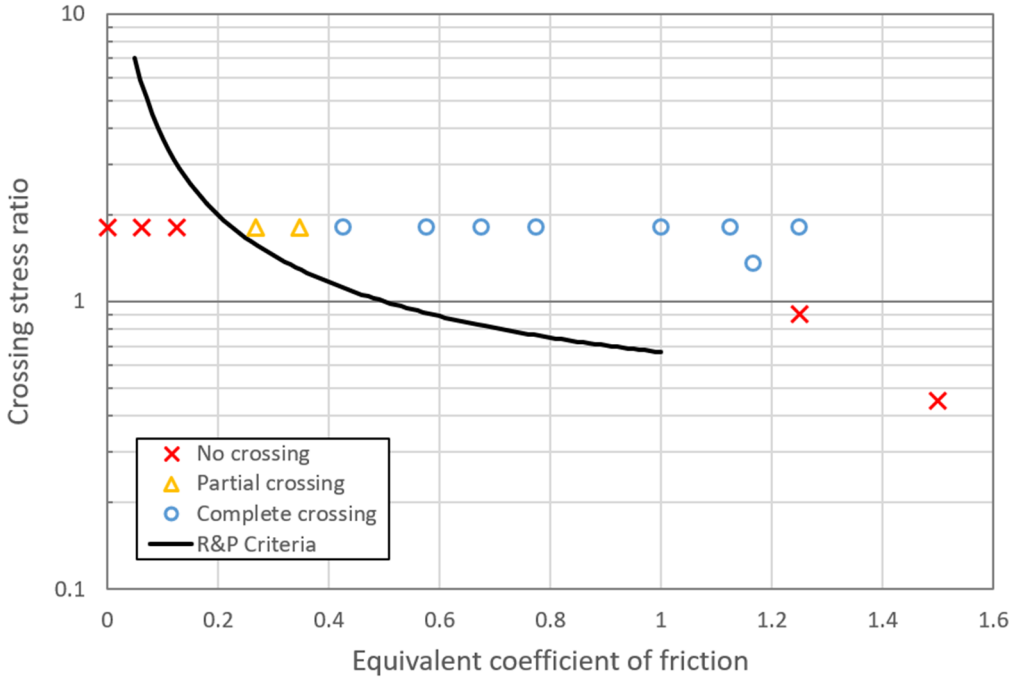

Figure 5.37: The R&P criteria for orthogonal intersection and simulation results (Case 1∼15)

For the non-orthogonal intersection case on cohesive joint with the approach angle β, the modified criterion becomes,

$$\frac{-\sigma_n}{T_0-\sigma_t} > \frac{(1-sin\frac{\beta}{2}sin\frac{3\beta}{2})+\frac{1}{\mu_{f''}cos\frac{\beta}{2}}(|sin\frac{\beta}{2}cos\frac{\beta}{2}cos\frac{3\beta}{2}+\alpha|)}{1+sin\frac{\beta}{2}sin\frac{3\beta}{2}} \tag{5.10}$$

Where σ_n and σ_t are the normal and tangential stresses applied on the joint surfaces transformed from the applied in situ stress field. And the parameter,

$$\alpha = \frac{\tau}{\frac{T_0-\sigma_t}{cos\frac{\beta}{2}(1+sin\frac{\beta}{2}sin\frac{3\beta}{2})}} \tag{5.11}$$

Which takes into account the shear stress generated at the inclined joint surfaces τ,

$$\tau = -\frac{\sigma_{HMax}-\sigma_{hMin}}{2}sin(\pi-2\beta) \tag{5.12}$$

$\mu_{f''} = \mu_f + \mu_{f'}$ still holds, but the equivalent friction coefficient from the cohesion becomes,

$$\mu_{f'} = \frac{\frac{c}{\sigma_n}}{\frac{1-sin\frac{\beta}{2}sin\frac{3\beta}{2}}{(1-sin\frac{\beta}{2}sin\frac{3\beta}{2})+\frac{1}{\mu_f cos\frac{\beta}{2}}|sin\frac{\beta}{2}cos\frac{\beta}{2}cos\frac{3\beta}{2}+\alpha|}-1} \tag{5.13}$$

The modified R&P criterion and simulation results are shown in Figure 5.10. Generally, the simulation results are consistent with the criterion. The cases with $\beta = 60°$ are mostly partial cross, which may be due to the fact that they are close to the crossing boundary. While none of the cases with $\beta = 45°$ crosses, as they are below the boundary.

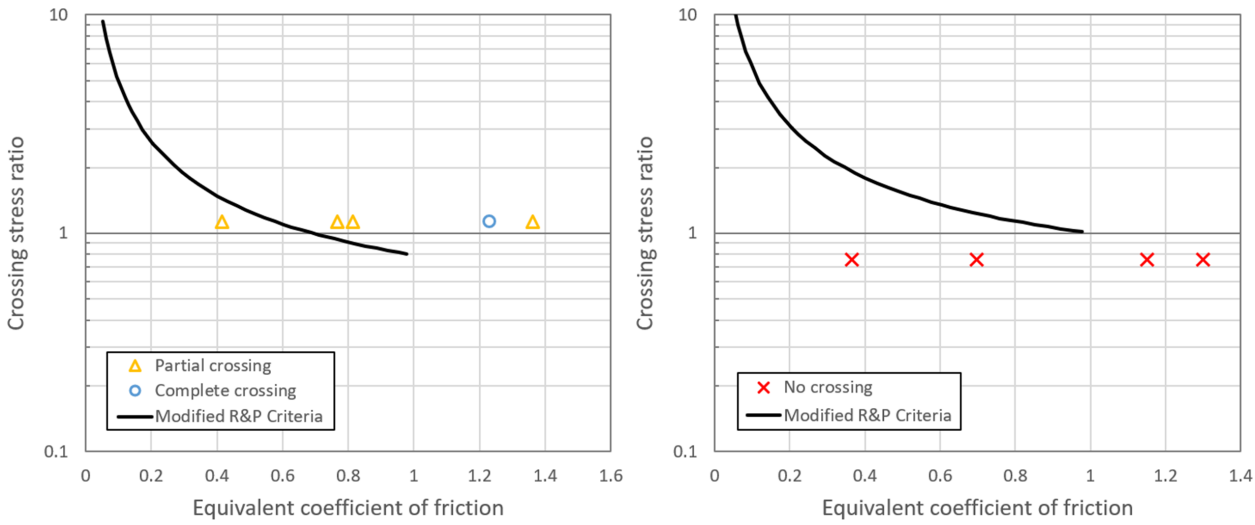

(a) $\beta = 60°$, Case 16∼20 (b) $\beta = 45°$, Case 21∼24

Figure 5.38: The modified R&P criteria for non-orthogonal intersection and simulation results

5.3.4 Summary

In this chapter, the solid fluid coupled lattice model is verified elastically using the classic penny shaped crack problem. The deformation and normal stress field match well with analytical values.

The fluid injection tests indicate rock heterogeneities affect the propagation of hydraulic fracture. The fractures tend to develop along the major stress direction, and the ratio between magnitudes of major and minor stress fields determines the turning rate of the fracture. The characteristic length of lattices represents the scale of weakness in the material, and the fracture is easier to develop in the model with finer mesh. Different arrangements of nodes represent the heterogeneous grain orientations and connectivities, and result in different potential paths for the fractures. As the statistical property distribution is applied to the lattices, the fractures become increasingly dispersed and slightly more difficult to propagate in the more heterogeneous scenarios. The interactions between hydraulic fracture and natural joints are mainly affected by the magnitude of normal stress and resistance against slip on the joint surface. The fracture crossing is more likely to occur when there

is little or no slippage between two sides of the joints. The simulation results give similar predictions on fracture crossing as the theory based on the compressional crossing mechanism.

These simulations demonstrate LEM is a promising tool for modeling and investigating hydraulic fracturing behavior. The discrete nature and simplicity of this method make it capable of modeling complex interactions between multiple fractures. However, also due to the simplified representation of fluid using steady state Darcy flow, some microscopic mechanisms, such as potential phase change at the crack tip, cannot be modeled. The simulations also indicate that lattice network geometry is one of the main factors that determine the potential crack path. This result suggests that when investigating fracture patterns with LEM, tests on multiple samples with different nodal arrangements may be necessary.

Chapter 6

Conclusions

6.1 Summary of This Study

In this study, the C++ based three dimensional LEM simulator is developed, which is capable of simulating both mechanical and fluid induced fracturing behavior in heterogeneous media. The Timoshenko beam with embedded discontinuity lattice model incorporates softening behavior into the single lattice, which allows this method to simulate materials with different degrees of ductility. The implicit incremental solution scheme allows a relatively larger step size. Together with the pipe flow model as the fluid lattice, this method simplifies the 3D multi-physics problem into a network of 1D lattices, which simulates the complex behavior with a relatively low computational cost. The validations and comparisons between numerical and experimental results indicate that LEM is a promising tool for investigating the process of fracture development. Its simplicity makes it capable of simulating branching and complex interactions between multiple fractures, as shown in fluid injection tests, which is extremely difficult in continuum-based methods. But this also hinders its application in investigating mechanisms related to microscopic scale.

With this solid lattice model, the potential application of LEM to early crack detection is explored. After calibrating simulation parameters by matching numerical and measured results, LEM could be used to interpret future measurements. As the numerical model is capable of capturing the strain field induced by the crack tip before its arrival, when abnormal strain is measured during monitoring, corresponding LEM simulations could be conducted to understand the status of the structure, such as overall deformation and potential fracture locations. The capability of this model to simulate materials with different degrees of ductility is also examined. The simulated stress strain curves match experimental curves representing different ductility, and the transition in fracture pattern is also captured. This indicates the macroscopic ductile behavior could be simulated using this LEM model by varying lattice parameters. However, axial splitting failure mode cannot be modeled even with the perfectly brittle lattice. Vertically developed fractures are observed in the specimen with a pre-existing open flaw but not in the intact cylinder. This possibly implies the

mechanism of splitting type failure, which is due to the axial tensile cracks initiated from small imperfections in the material. This also indicates that the heterogeneity introduced by the lattice geometry may not be enough to represent those imperfections.

The solid fluid coupled lattice model is used to investigate the influence of rock heterogeneities on the hydraulic fracturing process, especially the fracture pattern. All the factors, including in situ stress field, scale of weakness and statistical distribution of properties, affect the results to a different degree. Recall that the resulting fracture paths from simulations conducted on the same lattice model usually exhibit similar trends even when other types of heterogeneity are introduced. This indicates that one of the main factors that affect fracture pattern is the nodal arrangement, which determines the orientations of all the lattices in the network and thus the potential fracture path. Therefore, it is suggested that when investigating fracture patterns with LEM, tests on multiple samples with the same nodal density but different arrangements may be necessary. The interactions between hydraulic fractures and pre-existing natural joints are also investigated. The hydraulic fracture penetrates into a joint when the normal stress on the joint surface is too small to stop the joint from opening under fluid pressure. Whereas a fracture crossing is more likely to occur when there is little or no slippage between two sides of the joints. This implies a possible mechanism of fracture crossing in which the fracture reinitiates on the other side of the joint due to tensile stress generated by the friction applied on the joint surface.

6.2 Recommended Future Works

Some recommended future works based on this LEM model are as follows.

The capability of this LEM model is demonstrated by the simulations in this study. The influence of more types of rock heterogeneity could be explored with this model. For example, similar to applying probability distribution on the lattice properties, three dimensional noise could be utilized to generate random regions with continuously changing lattice properties. The effect of inclusions inside the rock matrix could be investigated, as this could also be directly achieved by modifying the lattice properties in certain regions[98].

As discussed in Section 4.2, one shortage of this solid lattice model is the lattice failure criteria, which evaluates the loading in three orthogonal directions separately. It is adequate to model the case dominated by a single loading type, but may overestimate the strength in combined loading scenarios. More sophisticated failure criteria could be developed to extend the applicability of this model.

As shown in Section 3.4.3, as a code primarily in serial, it has a decent speed for each of the individual operations. However, for a network with around 250000 solid nodes, it still takes hours to run the dry crack scenarios, and may need over one day to simulate hydraulic fracturing cases, which hinders it from simulating large real field scenarios. This is probably due to the low convergence rate of the adopted solution scheme, especially in solid fluid coupled cases, fixed point iteration is used to compute the pressure distribution and the bisection method is used to find the appropriate injection pressure. More sophisticated

numerical methods may be explored to accelerate the rate of convergence. In addition, fully parallelizing the code could also achieve substantial speed up and ease the memory limit when running on a multi-node high performance computer.

Although in the current fluid lattice model, leakages can be added into the mass conservation equation, LEM itself cannot reliably compute their values at each fluid node. In addition, it may be valuable to incorporate the thermal effect into the simulation. This could be achieved by coupling the current LEM model with a hydro-thermal FEM code. The Voronoi cells in LEM could be replaced with tetrahedrons or hexahedrons, thus these two codes can share the same solid mesh. Each cell in LEM is an element in FEM, while the fracture generated in LEM could be treated as an internal surface in FEM. In each step, LEM computes the fracture geometry and fluid pressure distribution, which are then used in FEM as boundary conditions to calculate fluid and thermal transports inside the rock matrix, the resulting values of leakages and thermal induced deformation are then sent to LEM.

Bibliography

[1] J. Adachi et al. "Computer Simulation of Hydraulic Fractures". In: *International Journal of Rock Mechanics and Mining Sciences* 44.5 (July 1, 2007), pp. 739–757. DOI: 10.1016/j.ijrmms.2006.11.006.

[2] The U.S. Energy Information Administration. *Annual Energy Outlook 2022 Narrative*. 2022. URL: https://www.eia.gov/outlooks/aeo/pdf/AEO2022_Narrative.pdf (visited on 11/14/2022).

[3] The U.S. Energy Information Administration. *EIA Adds New Play Production Data to Shale Gas and Tight Oil Reports*. 2019. URL: https://www.eia.gov/todayinenergy/detail.php?id=38372 (visited on 11/14/2022).

[4] R. Affes et al. "Tensile Strength and Fracture of Cemented Granular Aggregates". In: *The European Physical Journal E* 35.11 (Nov. 2012), p. 117. DOI: 10.1140/epje/i2012-12117-7.

[5] James Ahrens, Berk Geveci, and Charles Law. "Paraview: An End-User Tool for Large Data Visualization". In: *The visualization handbook* 717.8 (2005).

[6] A. Al-Busaidi. "Distinct Element Modeling of Hydraulically Fractured Lac Du Bonnet Granite". In: *Journal of Geophysical Research* 110.B6 (2005), B06302. DOI: 10.1029/2004JB003297.

[7] Satish Balay et al. *PETSc Web Page*. 2022. URL: https://petsc.org/.

[8] T. Belytschko and T. Black. "Elastic Crack Growth in Finite Elements with Minimal Remeshing". In: *International Journal for Numerical Methods in Engineering* 45.5 (June 20, 1999), pp. 601–620. DOI: 10.1002/(SICI)1097-0207(19990620)45:5<601::AID-NME598>3.0.CO;2-S.

[9] Ted Belytschko, Robert Gracie, and Giulio Ventura. "A Review of Extended/ Generalized Finite Element Methods for Material Modeling". In: *Modelling and Simulation in Materials Science and Engineering* 17.4 (June 1, 2009), p. 043001. DOI: 10.1088/0965-0393/17/4/043001.

[10] Ted Belytschko and Jerry I. Lin. "A Three-Dimensional Impact-Penetration Algorithm with Erosion". In: *Computers & Structures* 25.1 (Jan. 1987), pp. 95–104. DOI: 10.1016/0045-7949(87)90220-3.

[11] Carlos G. Berrocal, Ignasi Fernandez, and Rasmus Rempling. "Crack Monitoring in Reinforced Concrete Beams by Distributed Optical Fiber Sensors". In: *Structure and Infrastructure Engineering* 17.1 (Jan. 2, 2021), pp. 124–139. DOI: 10.1080/15732479.2020.1731558.

[12] Stefano Berton and John E. Bolander. "Crack Band Model of Fracture in Irregular Lattices". In: *Computer Methods in Applied Mechanics and Engineering* 195.52 (Nov. 2006), pp. 7172–7181. DOI: 10.1016/j.cma.2005.04.020.

[13] Thomas L. Blanton. "An Experimental Study of Interaction Between Hydraulically Induced and Pre-Existing Fractures". In: *All Days*. SPE Unconventional Gas Recovery Symposium. Pittsburgh, Pennsylvania: SPE, May 16, 1982, SPE–10847–MS. DOI: 10.2118/10847-MS.

[14] T.L. Blanton. "Propagation of Hydraulically and Dynamically Induced Fractures in Naturally Fractured Reservoirs". In: *SPE Unconventional Gas Technology Symposium*. SPE Unconventional Gas Technology Symposium. Louisville, Kentucky: Society of Petroleum Engineers, 1986. DOI: 10.2118/15261-MS.

[15] A. Bobet et al. "Numerical Models in Discontinuous Media: Review of Advances for Rock Mechanics Applications". In: *Journal of Geotechnical and Geoenvironmental Engineering* 135.11 (Nov. 2009), pp. 1547–1561. DOI: 10.1061/(ASCE)GT.1943-5606.0000133.

[16] Thomas J. Boone and Anthony R. Ingraffea. "A Numerical Procedure for Simulation of Hydraulically-Driven Fracture Propagation in Poroelastic Media". In: *International Journal for Numerical and Analytical Methods in Geomechanics* 14.1 (Jan. 1990), pp. 27–47. DOI: 10.1002/nag.1610140103.

[17] David Broek. *Elementary Engineering Fracture Mechanics*. 3rd rev. ed. The Hague: Martinus Nijhoff, 2013. ISBN: 978-94-010-8425-3.

[18] N.N. Bui et al. "Enriched Timoshenko Beam Finite Element for Modeling Bending and Shear Failure of Reinforced Concrete Frames". In: *Computers & Structures* 143 (Sept. 2014), pp. 9–18. DOI: 10.1016/j.compstruc.2014.06.004.

[19] G.T. Camacho and M. Ortiz. "Computational Modelling of Impact Damage in Brittle Materials". In: *International Journal of Solids and Structures* 33.20-22 (Aug. 1996), pp. 2899–2938. DOI: 10.1016/0020-7683(95)00255-3.

[20] Bernard Cambou, Michel Jean, and Farhang Radja, eds. *Micromechanics of Granular Materials*. London, UK: ISTE, Jan. 1, 2009. ISBN: 978-0-470-61161-6 978-1-84821-075-2. DOI: 10.1002/9780470611616.

[21] Sumitra Chaiyat et al. "Analytical and Numerical Evaluation of Crack-Tip Plasticity of an Axisymmetrically Loaded Penny-Shaped Crack". In: *Comptes Rendus Mécanique* 336.1-2 (Jan. 2008), pp. 54–68. DOI: 10.1016/j.crme.2007.10.015.

[22] Bin Chen et al. "A Review of Hydraulic Fracturing Simulation". In: *Archives of Computational Methods in Engineering* 29.4 (June 2022), pp. 1–58. DOI: 10.1007/s11831-021-09653-z.

[23] Youqing Chen, Yuya Nagaya, and Tsuyoshi Ishida. "Observations of Fractures Induced by Hydraulic Fracturing in Anisotropic Granite". In: *Rock Mechanics and Rock Engineering* 48.4 (July 2015), pp. 1455–1461. DOI: 10.1007/s00603-015-0727-9.

[24] COMSOL AB. *COMSOL Multiphysics*. Version 5.5. 2020. URL: https://www.comsol.com.

[25] Marathon Oil Corporation. *Animation of Hydraulic Fracturing (Fracking)*. 2012. URL: https://www.youtube.com/watch?v=VY34PQUiwOQ (visited on 11/14/2022).

[26] G. R. Cowper. "The Shear Coefficient in Timoshenko's Beam Theory". In: *Journal of Applied Mechanics* 33.2 (June 1, 1966), pp. 335–340. DOI: 10.1115/1.3625046.

[27] P.A. Cundall. "Formulation of a Three-Dimensional Distinct Element Model—Part I. A Scheme to Detect and Represent Contacts in a System Composed of Many Polyhedral Blocks". In: *International Journal of Rock Mechanics and Mining Sciences & Geomechanics Abstracts* 25.3 (June 1988), pp. 107–116. DOI: 10.1016/0148-9062(88)92293-0.

[28] Peter A Cundall. "A Computer Model for Simulating Progressive, Large-Scale Movement in Blocky Rock System". In: *Proceedings of the International Symposium on Rock Mechanics, 1971*. 1971.

[29] Peter A Cundall and Roger D Hart. *Development of Generalized 2-D and 3-D Distinct Element Programs for Modeling Jointed Rock*. ITASCA CONSULTING GROUP INC MINNEAPOLISMN, 1985.

[30] Peter A. Cundall and Roger D. Hart. "Numerical Modeling of Discontinua". In: *Analysis and Design Methods*. Elsevier, 1993, pp. 231–243. ISBN: 978-0-08-040615-2. DOI: 10.1016/B978-0-08-040615-2.50015-0.

[31] Peter A Cundall and Otto DL Strack. "A Discrete Numerical Model for Granular Assemblies". In: *geotechnique* 29.1 (1979), pp. 47–65.

[32] Branko Damjanac, Christine Detournay, and Peter Cundall. "Numerical Simulation of Hydraulically Driven Fractures". In: *Modelling Rock Fracturing Processes*. Ed. by Baotang Shen, Ove Stephansson, and Mikael Rinne. Cham: Springer International Publishing, 2020, pp. 531–561. ISBN: 978-3-030-35524-1 978-3-030-35525-8. DOI: 10.1007/978-3-030-35525-8_20.

[33] Kamal C. Das et al. "Efem vs. XFEM: A Comparative Study for Modeling Strong Discontinuity in Geomechanics". In: 13th ISRM International Congress of Rock Mechanics. May 10, 2015, ISRM–13CONGRESS–2015–183.

[34] René de Borst. "Fracture in Quasi-Brittle Materials: A Review of Continuum Damage-Based Approaches". In: *Engineering Fracture Mechanics* 69.2 (Jan. 2002), pp. 95–112. DOI: 10.1016/S0013-7944(01)00082-0.

[35] James W. Demmel. *Applied Numerical Linear Algebra*. Philadelphia: Society for Industrial and Applied Mathematics, 1997. 419 pp. ISBN: 978-0-89871-389-3.

[36] Shouchun Deng et al. "Simulation of Shale–Proppant Interaction in Hydraulic Fracturing by the Discrete Element Method". In: *International Journal of Rock Mechanics and Mining Sciences* 70 (Sept. 2014), pp. 219–228. DOI: 10.1016/j.ijrmms.2014.04.011.

[37] Iain S. Duff and Gérard A. Meurant. "The Effect of Ordering on Preconditioned Conjugate Gradients". In: *BIT* 29.4 (Dec. 1989), pp. 635–657. DOI: 10.1007/BF01932738.

[38] Eduardo N. Dvorkin, Alberto M. Cuitiño, and Gustavo Gioia. "Finite Elements with Displacement Interpolated Embedded Localization Lines Insensitive to Mesh Size and Distortions". In: *International Journal for Numerical Methods in Engineering* 30.3 (Aug. 20, 1990), pp. 541–564. DOI: 10.1002/nme.1620300311.

[39] Michael J. Economides and Kenneth G. Nolte, eds. *Reservoir Stimulation*. 3rd ed. Chichester, England ; New York: Wiley, 2000. 1 p. ISBN: 978-0-471-49192-7.

[40] W. El Rabaa. "Experimental Study of Hydraulic Fracture Geometry Initiated From Horizontal Wells". In: *SPE Annual Technical Conference and Exhibition*. SPE Annual Technical Conference and Exhibition. San Antonio, Texas: Society of Petroleum Engineers, 1989. DOI: 10.2118/19720-MS.

[41] F Erdogan. "Fracture Mechanics". In: *International Journal of Solids and Structures* 37.1-2 (Jan. 2000), pp. 171–183. DOI: 10.1016/S0020-7683(99)00086-4.

[42] M. Faivre et al. "2D Coupled HM-XFEM Modeling with Cohesive Zone Model and Applications to Fluid-Driven Fracture Network". In: *Engineering Fracture Mechanics* 159 (July 2016), pp. 115–143. DOI: 10.1016/j.engfracmech.2016.03.029.

[43] Kevin Fisher and Norm Warpinski. "Hydraulic-Fracture-Height Growth: Real Data". In: *SPE Production & Operations* 27.01 (2012), pp. 8–19.

[44] Thomas-Peter Fries and Ted Belytschko. "The Extended/Generalized Finite Element Method: An Overview of the Method and Its Applications: THE GEFM/XFEM: AN OVERVIEW OF THE METHOD". In: *International Journal for Numerical Methods in Engineering* 84.3 (Oct. 15, 2010), pp. 253–304. DOI: 10.1002/nme.2914.

[45] Pengcheng Fu, Scott M. Johnson, and Charles R. Carrigan. "An Explicitly Coupled Hydro-Geomechanical Model for Simulating Hydraulic Fracturing in Arbitrary Discrete Fracture Networks". In: *International Journal for Numerical and Analytical Methods in Geomechanics* 37.14 (Oct. 10, 2013), pp. 2278–2300. DOI: 10.1002/nag.2135.

[46] J Furtney, F Zhang, and Y Han. "Review of Methods and Applications for Incorporating Fluid Flow in the Discrete Element Method". In: *Proceedings of the 3rd International FLAC/DEM Symposium, Hangzhou, China*. 2013.

[47] Paul-Louis George and Houman Borouchaki. *Delaunay Triangulation and Meshing: Application to Finite Elements*. Paris: Hermès, 1998. ISBN: 978-2-86601-692-0.

[48] James M. Gere and Stephen Timoshenko. *Mechanics of Materials*. 4th ed. Boston: PWS Pub Co, 1997. 912 pp. ISBN: 978-0-534-93429-3 978-0-534-95102-3.

[49] L. N. Germanovich et al. "Mechanisms of Brittle Fracture of Rock with Pre-Existing Cracks in Compression". In: *Pure and Applied Geophysics PAGEOPH* 143.1-3 (1994), pp. 117–149. DOI: 10.1007/BF00874326.

[50] Christophe Geuzaine and Jean-François Remacle. "Gmsh: A 3-D Finite Element Mesh Generator with Built-in Pre- and Post-Processing Facilities: THE GMSH PAPER". In: *International Journal for Numerical Methods in Engineering* 79.11 (Sept. 10, 2009), pp. 1309–1331. DOI: 10.1002/nme.2579.

[51] Ahmad Ghassemi. *Rock Failure, Stimulated Volume & Permeability Enhancement in Gas Shale HF*. 2021. URL: https://www.epa.gov/sites/default/files/documents/rockfailurestimulatedvolumeandpermeabilityenhancementingasshalehf.pdf (visited on 11/14/2022).

[52] Richard E. Goodman, Robert L. Taylor, and Tor L. Brekke. "A Model for the Mechanics of Jointed Rock". In: *Journal of the Soil Mechanics and Foundations Division* 94.3 (May 1968), pp. 637–659. DOI: 10.1061/JSFEAQ.0001133.

[53] Elizaveta Gordeliy and Anthony Peirce. "Coupling Schemes for Modeling Hydraulic Fracture Propagation Using the XFEM". In: *Computer Methods in Applied Mechanics and Engineering* 253 (Jan. 2013), pp. 305–322. DOI: 10.1016/j.cma.2012.08.017.

[54] P. Grassl et al. "On a 2D Hydro-Mechanical Lattice Approach for Modelling Hydraulic Fracture". In: *Journal of the Mechanics and Physics of Solids* 75 (Feb. 2015), pp. 104–118. DOI: 10.1016/j.jmps.2014.11.011.

[55] Peter Grassl. "A Lattice Approach to Model Flow in Cracked Concrete". In: *Cement and Concrete Composites* 31.7 (Aug. 2009), pp. 454–460. DOI: 10.1016/j.cemconcomp.2009.05.001.

[56] Peter Grassl and John Bolander. "Three-Dimensional Network Model for Coupling of Fracture and Mass Transport in Quasi-Brittle Geomaterials". In: *Materials* 9.9 (Sept. 19, 2016), p. 782. DOI: 10.3390/ma9090782.

[57] A.A. Griffith. "The Theory of Rupture". In: *First Int. Cong. Appl. Mech.* 1924, pp. 55–63.

[58] A.A. Griffith. "VI. The Phenomena of Rupture and Flow in Solids". In: *Philosophical Transactions of the Royal Society of London. Series A, Containing Papers of a Mathematical or Physical Character* 221.582-593 (Jan. 1921), pp. 163–198. DOI: 10.1098/rsta.1921.0006.

[59] William Gropp and Ewing Lusk. *User's Guide for Mpich, a Portable Implementation of MPI*. 1996.

[60] Gaël Guennebaud, Benoît Jacob, et al. *Eigen V3*. 2010. URL: http://eigen.tuxfamily.org.

[61] P. Gupta and C. A. Duarte. "Coupled Formulation and Algorithms for the Simulation of Non-Planar Three-Dimensional Hydraulic Fractures Using the Generalized Finite Element Method". In: *International Journal for Numerical and Analytical Methods in Geomechanics* 40.10 (July 2016), pp. 1402–1437. DOI: 10.1002/nag.2485.

[62] P. Gupta and C. A. Duarte. "Simulation of Non-Planar Three-Dimensional Hydraulic Fracture Propagation". In: *International Journal for Numerical and Analytical Methods in Geomechanics* 38.13 (Sept. 2014), pp. 1397–1430. DOI: 10.1002/nag.2305.

[63] Farzin Hamidi and Ali Mortazavi. "A New Three Dimensional Approach to Numerically Model Hydraulic Fracturing Process". In: *Journal of Petroleum Science and Engineering* 124 (Dec. 2014), pp. 451–467. DOI: 10.1016/j.petrol.2013.12.006.

[64] Yanhui Han and Peter A. Cundall. "LBM-DEM Modeling of Fluid-Solid Interaction in Porous Media: LBM-DEM MODELING OF FLUID-SOLID INTERACTION IN POROUS MEDIA". In: *International Journal for Numerical and Analytical Methods in Geomechanics* 37.10 (July 2013), pp. 1391–1407. DOI: 10.1002/nag.2096.

[65] J.C. Hansen et al. "An Elastic Network Model Based on the Structure of the Red Blood Cell Membrane Skeleton". In: *Biophysical Journal* 70.1 (Jan. 1996), pp. 146–166. DOI: 10.1016/S0006-3495(96)79556-5.

[66] T. R. Harper and N. C. Last. "Interpretation by Numerical Modelling of Changes of Fracture System Hydraulic Conductivity Induced by Fluid Injection". In: *Géotechnique* 39.1 (Mar. 1989), pp. 1–11. DOI: 10.1680/geot.1989.39.1.1.

[67] R. Hart, P.A. Cundall, and J. Lemos. "Formulation of a Three-Dimensional Distinct Element Model—Part II. Mechanical Calculations for Motion and Interaction of a System Composed of Many Polyhedral Blocks". In: *International Journal of Rock Mechanics and Mining Sciences & Geomechanics Abstracts* 25.3 (June 1988), pp. 117–125. DOI: 10.1016/0148-9062(88)92294-2.

[68] Hans J. Herrmann, Alex Hansen, and Stephane Roux. "Fracture of Disordered, Elastic Lattices in Two Dimensions". In: *Physical Review B* 39.1 (Jan. 1, 1989), pp. 637–648. DOI: 10.1103/PhysRevB.39.637.

[69] George C Howard and CR Fast. "Optimum Fluid Characteristics for Fracture Extension". In: *Drilling and Production Practice*. 1957.

[70] A. Hrennikoff. "Solution of Problems of Elasticity by the Framework Method". In: *Journal of Applied Mechanics* 8.4 (Dec. 1, 1941), A169–A175. DOI: 10.1115/1.4009129.

[71] Zheng Hu, Yida Zhang, and Zhongxuan Yang. "Suffusion-Induced Deformation and Microstructural Change of Granular Soils: A Coupled CFD–DEM Study". In: *Acta Geotechnica* 14.3 (June 2019), pp. 795–814. DOI: 10.1007/s11440-019-00789-8.

[72] Bingxiang Huang and Jiangwei Liu. "Experimental Investigation of the Effect of Bedding Planes on Hydraulic Fracturing Under True Triaxial Stress". In: *Rock Mechanics and Rock Engineering* 50.10 (Oct. 2017), pp. 2627–2643. DOI: 10.1007/s00603-017-1261-8.

[73] Michael J. Hunsweck, Yongxing Shen, and Adrian J. Lew. "A Finite Element Approach to the Simulation of Hydraulic Fractures with Lag: FINITE ELEMENT APPROACH TO HYDRAULIC FRACTURES WITH LAG". In: *International Journal for Numerical and Analytical Methods in Geomechanics* 37.9 (June 25, 2013), pp. 993–1015. DOI: 10.1002/nag.1131.

[74] A. Ibrahimbegovic and D. Brancherie. "Combined Hardening and Softening Constitutive Model of Plasticity: Precursor to Shear Slip Line Failure". In: *Computational Mechanics* 31.1-2 (May 1, 2003), pp. 88–100. DOI: 10.1007/s00466-002-0396-x.

[75] Adnan Ibrahimbegovic and Sergiy Melnyk. "Embedded Discontinuity Finite Element Method for Modeling of Localized Failure in Heterogeneous Materials with Structured Mesh: An Alternative to Extended Finite Element Method". In: *Computational Mechanics* 40.1 (Mar. 28, 2007), pp. 149–155. DOI: 10.1007/s00466-006-0091-4.

[76] Adnan Ibrahimbegovic and EL Wilson. "A Modified Method of Incompatible Modes". In: *Communications in applied numerical methods* 7.3 (1991), pp. 187–194.

[77] Adnan Ibrahimbegović and FrançOis Frey. "Finite Element Analysis of Linear and Non-Linear Planar Deformations of Elastic Initially Curved Beams". In: *International Journal for Numerical Methods in Engineering* 36.19 (Oct. 15, 1993), pp. 3239–3258. DOI: 10.1002/nme.1620361903.

[78] Anthony R. Ingraffea and Francois E. Heuze. "Finite Element Models for Rock Fracture Mechanics". In: *International Journal for Numerical and Analytical Methods in Geomechanics* 4.1 (Jan. 1980), pp. 25–43. DOI: 10.1002/nag.1610040103.

[79] G. R. Irwin. "Analysis of Stresses and Strains Near the End of a Crack Traversing a Plate". In: *Journal of Applied Mechanics* 24.3 (Sept. 1, 1957), pp. 361–364. DOI: 10.1115/1.4011547.

[80] G.R. Irwin. "Fracture". In: *Elasticity and Plasticity / Elastizität Und Plastizität*. Ed. by S. Flügge. Red. by S. Flügge. Vol. 3 / 6. Handbuch Der Physik / Encyclopedia of Physics. Berlin, Heidelberg: Springer Berlin Heidelberg, 1958, pp. 551–590. ISBN: 978-3-642-45889-7 978-3-642-45887-3. DOI: 10.1007/978-3-642-45887-3_5.

[81] G.R. Irwin. "Fracture Dynamics". In: *Fracturing of metals* (1947).

[82] ISRM. "Suggested Methods for Determining Tensile Strength of Rock Materials". In: *International Journal of Rock Mechanics and Mining Sciences* 15.3 (June 1978), pp. 99–103. DOI: 10.1016/0148-9062(78)90003-7.

[83] J Jaky. "The Coefficient of Earth Pressure at Rest". In: *J. Soc. Hung. Archit. Eng.* 78 (1944), pp. 355–388.

[84] Ali Jenabidehkordi. "Computational Methods for Fracture in Rock: A Review and Recent Advances". In: *Frontiers of Structural and Civil Engineering* 13.2 (Apr. 2019), pp. 273–287. DOI: 10.1007/s11709-018-0459-5.

[85] L. Jing and J.A. Hudson. "Numerical Methods in Rock Mechanics". In: *International Journal of Rock Mechanics and Mining Sciences* 39.4 (2002), pp. 409–427. DOI: 10.1016/S1365-1609(02)00065-5.

[86] Milan Jirásek. "Comparative Study on Finite Elements with Embedded Discontinuities". In: *Computer Methods in Applied Mechanics and Engineering* 188.1-3 (July 2000), pp. 307–330. DOI: 10.1016/S0045-7825(99)00154-1.

[87] Gordon R. Johnson and Robert A. Stryk. "Eroding Interface and Improved Tetrahedral Element Algorithms for High-Velocity Impact Computations in Three Dimensions". In: *International Journal of Impact Engineering* 5.1-4 (Jan. 1987), pp. 411–421. DOI: 10.1016/0734-743X(87)90057-1.

[88] Emir Karavelić et al. "Concrete Meso-Scale Model with Full Set of 3D Failure Modes with Random Distribution of Aggregate and Cement Phase. Part I: Formulation and Numerical Implementation". In: *Computer Methods in Applied Mechanics and Engineering* 344 (Feb. 2019), pp. 1051–1072. DOI: 10.1016/j.cma.2017.09.013.

[89] B. L. Karihaloo, R. Ince, and A. Arslan. "An Improved Lattice Model for Fracture and Size Effect of Concrete Structures". In: *IUTAM Symposium on Analytical and Computational Fracture Mechanics of Non-Homogeneous Materials*. Ed. by B. L. Karihaloo. Red. by G. M. L. Gladwell. Vol. 97. Solid Mechanics and Its Applications. Dordrecht: Springer Netherlands, 2002, pp. 493–505. ISBN: 978-90-481-5977-2 978-94-017-0081-8. DOI: 10.1007/978-94-017-0081-8_55.

[90] A. R. Khoei et al. "An Enriched FEM Technique for Modeling Hydraulically Driven Cohesive Fracture Propagation in Impermeable Media with Frictional Natural Faults: Numerical and Experimental Investigations". In: *International Journal for Numerical Methods in Engineering* 104.6 (Nov. 9, 2015), pp. 439–468. DOI: 10.1002/nme.4944.

[91] H. Konietzky, A. Heftenberger, and M. Feige. "Life-Time Prediction for Rocks under Static Compressive and Tensile Loads: A New Simulation Approach". In: *Acta Geotechnica* 4.1 (Mar. 2009), pp. 73–78. DOI: 10.1007/s11440-009-0085-4.

[92] E. Z. Lajtai. "Brittle Fracture in Compression". In: *International Journal of Fracture* 10.4 (Dec. 1974), pp. 525–536. DOI: 10.1007/BF00155255.

[93] Brice Lecampion, Andrew Bunger, and Xi Zhang. "Numerical Methods for Hydraulic Fracture Propagation: A Review of Recent Trends". In: *Journal of Natural Gas Science and Engineering* 49 (Jan. 2018), pp. 66–83. DOI: 10.1016/j.jngse.2017.10.012.

[94] Qinghua Lei, John-Paul Latham, and Chin-Fu Tsang. "The Use of Discrete Fracture Networks for Modelling Coupled Geomechanical and Hydrological Behaviour of Fractured Rocks". In: *Computers and Geotechnics* 85 (May 2017), pp. 151–176. DOI: 10.1016/j.compgeo.2016.12.024.

[95] Diyuan Li and Louis Ngai Yuen Wong. "The Brazilian Disc Test for Rock Mechanics Applications: Review and New Insights". In: *Rock Mechanics and Rock Engineering* 46.2 (Mar. 2013), pp. 269–287. DOI: 10.1007/s00603-012-0257-7.

[96] Diyuan Li et al. "Evaluation on Rock Tensile Failure of the Brazilian Discs under Different Loading Configurations by Digital Image Correlation". In: *Applied Sciences* 10.16 (Aug. 10, 2020), p. 5513. DOI: 10.3390/app10165513.

[97] HL Li et al. "Damage Localization as a Possible Precursor of Earthquake Rupture". In: *pure and applied geophysics* 157.11 (2000), pp. 1929–1943.

[98] Ming Li et al. "Heterogeneous Rock Modeling Method and Characteristics of Multistage Hydraulic Fracturing Based on the PHF-LSM Method". In: *Journal of Natural Gas Science and Engineering* 83 (Nov. 2020), p. 103518. DOI: 10.1016/j.jngse.2020.103518.

[99] Quanshu Li et al. "A Review on Hydraulic Fracturing of Unconventional Reservoir". In: *Petroleum* 1.1 (Mar. 2015), pp. 8–15. DOI: 10.1016/j.petlm.2015.03.008.

[100] Xiang Li and Heinz Konietzky. "Numerical Simulation Schemes for Time-Dependent Crack Growth in Hard Brittle Rock". In: *Acta Geotechnica* 10.4 (Aug. 2015), pp. 513–531. DOI: 10.1007/s11440-014-0337-9.

[101] Z.Z. Liang et al. "A Three-Dimensional Numerical Investigation of the Fracture of Rock Specimens Containing a Pre-Existing Surface Flaw". In: *Computers and Geotechnics* 45 (Sept. 2012), pp. 19–33. DOI: 10.1016/j.compgeo.2012.04.011.

[102] G Lilliu and J.G.M van Mier. "3D Lattice Type Fracture Model for Concrete". In: *Engineering Fracture Mechanics* 70.7-8 (May 2003), pp. 927–941. DOI: 10.1016/S0013-7944(02)00158-3.

[103] J.X. Liu et al. "Modified Generalized Beam Lattice Model Associated with Fracture of Reinforced Fiber/Particle Composites". In: *Theoretical and Applied Fracture Mechanics* 50.2 (Oct. 2008), pp. 132–141. DOI: 10.1016/j.tafmec.2008.07.006.

[104] Ella María Llanos et al. "Hydraulic Fracture Propagation Through an Orthogonal Discontinuity: A Laboratory, Analytical and Numerical Study". In: *Rock Mechanics and Rock Engineering* 50.8 (Aug. 2017), pp. 2101–2118. DOI: 10.1007/s00603-017-1213-3.

[105] Fabian Loth. *Roughmesh*. 2020. URL: https://github.com/fabian-loth/roughmesh.

[106] Fabian Loth et al. "Surface Roughness in Finite Element Meshes". Version 1. In: (2020). DOI: 10.48550/ARXIV.2002.00894.

[107] M. M. MacLaughlin and D. M. Doolin. "Review of Validation of the Discontinuous Deformation Analysis (DDA) Method". In: *International Journal for Numerical and Analytical Methods in Geomechanics* 30.4 (Apr. 10, 2006), pp. 271–305. DOI: 10.1002/nag.427.

[108] Ch. F. Markides and S. K. Kourkoulis. "The Stress Field in a Standardized Brazilian Disc: The Influence of the Loading Type Acting on the Actual Contact Length". In: *Rock Mechanics and Rock Engineering* 45.2 (Mar. 2012), pp. 145–158. DOI: 10.1007/s00603-011-0201-2.

[109] Paul W Mayne and Fred H Kulhawy. "Ko- OCR Relationships in Soil". In: *Journal of the Soil Mechanics and Foundations Division* 108.6 (1982), pp. 851–872.

[110] Ashwij Mayya et al. "Splitting Fracture in Bovine Bone Using a Porosity-Based Spring Network Model". In: *Journal of The Royal Society Interface* 13.124 (Nov. 2016), p. 20160809. DOI: 10.1098/rsif.2016.0809.

[111] J.M. Melenk and I. Babuška. "The Partition of Unity Finite Element Method: Basic Theory and Applications". In: *Computer Methods in Applied Mechanics and Engineering* 139.1-4 (Dec. 1996), pp. 289–314. DOI: 10.1016/S0045-7825(96)01087-0.

[112] Bruce Roman Meyer and Lucas W Bazan. "A Discrete Fracture Network Model for Hydraulically Induced Fractures-Theory, Parametric and Case Studies". In: *SPE Hydraulic Fracturing Technology Conference*. 2011.

[113] Mojtaba Mohammadnejad et al. "An Overview on Advances in Computational Fracture Mechanics of Rock". In: *Geosystem Engineering* 24.4 (July 4, 2021), pp. 206–229. DOI: 10.1080/12269328.2018.1448006.

[114] T. Mohammadnejad and A.R. Khoei. "An Extended Finite Element Method for Hydraulic Fracture Propagation in Deformable Porous Media with the Cohesive Crack Model". In: *Finite Elements in Analysis and Design* 73 (Oct. 2013), pp. 77–95. DOI: 10.1016/j.finel.2013.05.005.

[115] C. Moukarzel and H. J. Herrmann. "A Vectorizable Random Lattice". In: *Journal of Statistical Physics* 68.5-6 (Sept. 1992), pp. 911–923. DOI: 10.1007/BF01048880.

[116] Nicolas Moës, John Dolbow, and Ted Belytschko. "A Finite Element Method for Crack Growth without Remeshing". In: *International Journal for Numerical Methods in Engineering* 46.1 (Sept. 10, 1999), pp. 131–150. DOI: 10.1002/(SICI)1097-0207(19990910)46:1<131::AID-NME726>3.0.CO;2-J.

[117] S. A. F. Murrell. "The Effect of Triaxial Stress Systems on the Strength of Rocks at Atmospheric Temperatures". In: *Geophysical Journal International* 10.3 (Dec. 1965), pp. 231–281. DOI: 10.1111/j.1365-246X.1965.tb03155.x.

[118] M. Nikolic, A. Ibrahimbegovic, and P. Miscevic. "Brittle and Ductile Failure of Rocks: Embedded Discontinuity Approach for Representing Mode I and Mode II Failure Mechanisms". In: *International Journal for Numerical Methods in Engineering* 102.8 (May 25, 2015), pp. 1507–1526. DOI: 10.1002/nme.4866.

[119] Mijo Nikolic and Adnan Ibrahimbegovic. "Rock Mechanics Model Capable of Representing Initial Heterogeneities and Full Set of 3D Failure Mechanisms". In: *Computer Methods in Applied Mechanics and Engineering* 290 (June 2015), pp. 209–227. DOI: 10.1016/j.cma.2015.02.024.

[120] Mijo Nikolic, Adnan Ibrahimbegovic, and Predrag Miscevic. "Discrete Element Model for the Analysis of Fluid-Saturated Fractured Poro-Plastic Medium Based on Sharp Crack Representation with Embedded Strong Discontinuities". In: *Computer Methods in Applied Mechanics and Engineering* 298 (Jan. 2016), pp. 407–427. DOI: 10.1016/j.cma.2015.10.009.

[121] Mijo Nikolić, Tanja Roje-Bonacci, and Adnan Ibrahimbegović. "Overview of the Numerical Methods for the Modelling of Rock Mechanics Problems". In: *Tehnički vjesnik* 23.2 (2016), pp. 627–637. DOI: 10.17559/TV-20140521084228.

[122] Mijo Nikolić et al. "Lattice Element Models and Their Peculiarities". In: *Archives of Computational Methods in Engineering* 25.3 (July 2018), pp. 753–784. DOI: 10.1007/s11831-017-9210-y.

[123] Atsuyuki Okabe. *Spatial Tessellations: Concepts and Applications of Voronoi Diagrams*. 2nd ed. Wiley Series in Probability and Statistics. Chichester ; New York: Wiley, 2000. 671 pp. ISBN: 978-0-471-98635-5.

[124] J. Oliver, A.E. Huespe, and P.J. Sánchez. "A Comparative Study on Finite Elements for Capturing Strong Discontinuities: E-FEM vs X-FEM". In: *Computer Methods in Applied Mechanics and Engineering* 195.37-40 (July 2006), pp. 4732–4752. DOI: 10.1016/j.cma.2005.09.020.

[125] Italo A. Onederra et al. "Modelling Blast Induced Damage from a Fully Coupled Explosive Charge". In: *International Journal of Rock Mechanics and Mining Sciences* 58 (Feb. 2013), pp. 73–84. DOI: 10.1016/j.ijrmms.2012.10.004.

[126] E Orowan. "Fracture and Strength of Solids". In: *Reports on Progress in Physics* 12.1 (Jan. 1, 1949), pp. 185–232. DOI: 10.1088/0034-4885/12/1/309.

[127] Michael Ortiz, Yves Leroy, and Alan Needleman. "A Finite Element Method for Localized Failure Analysis". In: *Computer methods in applied mechanics and engineering* 61.2 (1987), pp. 189–214.

[128] Martin Ostoja-Starzewski. "Lattice Models in Micromechanics". In: *Applied Mechanics Reviews* 55.1 (2002), pp. 35–60.

[129] Zichao Pan et al. "A Review of Lattice Type Model in Fracture Mechanics: Theory, Applications, and Perspectives". In: *Engineering Fracture Mechanics* 190 (Mar. 2018), pp. 382–409. DOI: 10.1016/j.engfracmech.2017.12.037.

[130] Katerina D. Papoulia, Stephen A. Vavasis, and Pritam Ganguly. "Spatial Convergence of Crack Nucleation Using a Cohesive Finite-Element Model on a Pinwheel-Based Mesh". In: *International Journal for Numerical Methods in Engineering* 67.1 (July 2, 2006), pp. 1–16. DOI: 10.1002/nme.1598.

[131] M. S. Paterson. "Experimental Deformation and Faulting in Wombeyan Marble". In: *Geological Society of America Bulletin* 69.4 (1958), p. 465. DOI: 10.1130/0016-7606(1958)69[465:EDAFIW]2.0.CO;2.

[132] Mervyn S. Paterson and Teng-fong Wong. *Experimental Rock Deformation — The Brittle Field*. Berlin/Heidelberg: Springer-Verlag, 2005. ISBN: 978-3-540-24023-5. DOI: 10.1007/b137431.

[133] A. Pazdniakou and P. M. Adler. "Lattice Spring Models". In: *Transport in Porous Media* 93.2 (June 2012), pp. 243–262. DOI: 10.1007/s11242-012-9955-6.

[134] Nicholas Perrone and Robert Kao. "A General Finite Difference Method for Arbitrary Meshes". In: *Computers & Structures* 5.1 (Apr. 1975), pp. 45–57. DOI: 10.1016/0045-7949(75)90018-8.

[135] Chuck Pheatt. "Intel Threading Building Blocks". In: *Journal of Computing Sciences in Colleges* 23.4 (2008), pp. 298–298.

[136] D.O. Potyondy and P.A. Cundall. "A Bonded-Particle Model for Rock". In: *International Journal of Rock Mechanics and Mining Sciences* 41.8 (Dec. 2004), pp. 1329–1364. DOI: 10.1016/j.ijrmms.2004.09.011.

[137] Timon Rabczuk. "Computational Methods for Fracture in Brittle and Quasi-Brittle Solids: State-of-the-Art Review and Future Perspectives". In: *ISRN Applied Mathematics* 2013 (Mar. 20, 2013), pp. 1–38. DOI: 10.1155/2013/849231.

[138] Xiangyan Ren et al. "A Three-Dimensional Numerical Investigation of the Propagation Path of a Two-Cluster Fracture System in Horizontal Wells". In: *Journal of Petroleum Science and Engineering* 173 (Feb. 2019), pp. 1222–1235. DOI: 10.1016/j.petrol.2018.10.105.

[139] C.E. Renshaw and D.D. Pollard. "An Experimentally Verified Criterion for Propagation across Unbounded Frictional Interfaces in Brittle, Linear Elastic Materials". In: *International Journal of Rock Mechanics and Mining Sciences & Geomechanics Abstracts* 32.3 (Apr. 1995), pp. 237–249. DOI: 10.1016/0148-9062(94)00037-4.

[140] Azadeh Riahi and Branko Damjanac. "Numerical Study of Interaction Between Hydraulic Fracture and Discrete Fracture Network". In: *Effective and Sustainable Hydraulic Fracturing*. Ed. by Rob Jeffrey. InTech, May 17, 2013. ISBN: 978-953-51-1137-5. DOI: 10.5772/56416.

[141] J. R. Rice. "A Path Independent Integral and the Approximate Analysis of Strain Concentration by Notches and Cracks". In: *Journal of Applied Mechanics* 35.2 (June 1, 1968), pp. 379–386. DOI: 10.1115/1.3601206.

[142] J. R. Rice. "Fracture Mechanics". In: *Applied Mechanics Reviews* 38.10 (Oct. 1, 1985), pp. 1271–1275. DOI: 10.1115/1.3143689.

[143] C. Rocco et al. "Size Effect and Boundary Conditions in the Brazilian Test: Experimental Verification". In: *Materials and Structures* 32.3 (Apr. 1999), pp. 210–217. DOI: 10.1007/BF02481517.

[144] Chris Rycroft. *Voro++: A Three-Dimensional Voronoi Cell Library in C++*. LBNL-1432E, 946741. Jan. 15, 2009, LBNL–1432E, 946741. DOI: 10.2172/946741.

[145] M. Sarmadivaleh and V. Rasouli. "Modified Reinshaw and Pollard Criteria for a Non-Orthogonal Cohesive Natural Interface Intersected by an Induced Fracture". In: *Rock Mechanics and Rock Engineering* 47.6 (Nov. 2014), pp. 2107–2115. DOI: 10.1007/s00603-013-0509-1.

[146] E. Schlangen and J. G. M. van Mier. "Simple Lattice Model for Numerical Simulation of Fracture of Concrete Materials and Structures". In: *Materials and Structures* 25.9 (Nov. 1992), pp. 534–542. DOI: 10.1007/BF02472449.

[147] Will Schroeder, Ken Martin, and Bill Lorensen. *The Visualization Toolkit: An Object-Oriented Approach to 3D Graphics ; Visualize Data in 3D - Medical, Engineering or Scientific ; Build Your Own Applications with C++, Tcl, Java or Python ; Includes Source Code for VTK (Supports Unix, Windows and Mac)*. In collab. with Inc Kitware. 4. ed. Clifton Park, NY: Kitware, Inc, 2006. 512 pp. ISBN: 978-1-930934-19-1.

[148] S. Secchi and B. A. Schrefler. "A Method for 3-D Hydraulic Fracturing Simulation". In: *International Journal of Fracture* 178.1-2 (Nov. 2012), pp. 245–258. DOI: 10.1007/s10704-012-9742-y.

[149] V. Selmin. "The Node-Centred Finite Volume Approach: Bridge between Finite Differences and Finite Elements". In: *Computer Methods in Applied Mechanics and Engineering* 102.1 (Jan. 1993), pp. 107–138. DOI: 10.1016/0045-7825(93)90143-L.

[150] Gen-hua Shi. "Recent Applications of Discontinuous Deformation Analysis and Manifold Method". In: The 42nd U.S. Rock Mechanics Symposium (USRMS). June 29, 2008, ARMA–08–108.

[151] Gen-Hua Shi and Richard E. Goodman. "Two Dimensional Discontinuous Deformation Analysis". In: *International Journal for Numerical and Analytical Methods in Geomechanics* 9.6 (Nov. 1985), pp. 541–556. DOI: 10.1002/nag.1610090604.

[152] Gen-Hua Shi. "Discontinuous Deformation Analysis: A New Numerical Model for the Statics and Dynamics of Deformable Block Structures". In: *Engineering Computations* 9.2 (Feb. 1, 1992), pp. 157–168. DOI: 10.1108/eb023855.

[153] J. C. Simo, J. Oliver, and F. Armero. "An Analysis of Strong Discontinuities Induced by Strain-Softening in Rate-Independent Inelastic Solids". In: *Computational Mechanics* 12.5 (1993), pp. 277–296. DOI: 10.1007/BF00372173.

[154] I. N. Sneddon and H. A. Elliott. "The Opening of a Griffith Crack under Internal Pressure". In: *Quarterly of Applied Mathematics* 4.3 (1946), pp. 262–267. JSTOR: 43633558.

[155] I.N. Sneddon. "The Distribution of Stress in the Neighbourhood of a Crack in an Elastic Solid". In: *Proceedings of the Royal Society of London. Series A. Mathematical and Physical Sciences* 187.1009 (Oct. 22, 1946), pp. 229–260. DOI: 10.1098/rspa.1946.0077.

[156] Jeong-Hoon Song, Hongwu Wang, and Ted Belytschko. "A Comparative Study on Finite Element Methods for Dynamic Fracture". In: *Computational Mechanics* 42.2 (July 2008), pp. 239–250. DOI: 10.1007/s00466-007-0210-x.

[157] Hiroshi Tada, Paul C. Paris, and George R. Irwin. *The Stress Analysis of Cracks Handbook, Third Edition*. ASME Press, 2000. ISBN: 978-0-7918-0153-6. DOI: 10.1115/1.801535.

[158] Peng Tan et al. "Analysis of Hydraulic Fracture Initiation and Vertical Propagation Behavior in Laminated Shale Formation". In: *Fuel* 206 (Oct. 2017), pp. 482–493. DOI: 10.1016/j.fuel.2017.05.033.

[159] Svetlana Vasić et al. "Deformation Rates Effects in Softwoods: Crack Dynamics with Lattice Fracture Modelling". In: *Engineering Fracture Mechanics* 76.9 (June 2009), pp. 1231–1246. DOI: 10.1016/j.engfracmech.2009.01.019.

[160] G. Walton et al. "Post-Yield Strength and Dilatancy Evolution Across the Brittle–Ductile Transition in Indiana Limestone". In: *Rock Mechanics and Rock Engineering* 50.7 (July 2017), pp. 1691–1710. DOI: 10.1007/s00603-017-1195-1.

[161] Endong Wang et al. "Intel Math Kernel Library". In: *High-Performance Computing on the Intel Xeon Phi*. Springer, 2014, pp. 167–188.

[162] HanYi Wang. "Numerical Modeling of Non-Planar Hydraulic Fracture Propagation in Brittle and Ductile Rocks Using XFEM with Cohesive Zone Method". In: *Journal of Petroleum Science and Engineering* 135 (Nov. 2015), pp. 127–140. DOI: 10.1016/j.petrol.2015.08.010.

[163] Min Wang, Y.T. Feng, and C.Y. Wang. "Numerical Investigation of Initiation and Propagation of Hydraulic Fracture Using the Coupled Bonded Particle–Lattice Boltzmann Method". In: *Computers & Structures* 181 (Mar. 2017), pp. 32–40. DOI: 10.1016/j.compstruc.2016.02.014.

[164] Tuo Wang et al. "A Review of Methods, Applications and Limitations for Incorporating Fluid Flow in the Discrete Element Method". In: *Journal of Rock Mechanics and Geotechnical Engineering* 14.3 (June 2022), pp. 1005–1024. DOI: 10.1016/j.jrmge.2021.10.015.

[165] Magnus Wangen. "Finite Element Modeling of Hydraulic Fracturing in 3D". In: *Computational Geosciences* 17.4 (Aug. 2013), pp. 647–659. DOI: 10.1007/s10596-013-9346-2.

[166] N. R. Warpinski et al. "Comparison Study of Hydraulic Fracturing Models—Test Case: GRI Staged Field Experiment No. 3". In: *SPE Production & Facilities* 9.01 (Feb. 1, 1994), pp. 7–16. DOI: 10.2118/25890-PA.

[167] Norman R. Warpinski, Richard A. Schmidt, and David A. Northrop. "In-Situ Stresses: The Predominant Influence on Hydraulic Fracture Containment". In: *Journal of Petroleum Technology* 34.03 (Mar. 1, 1982), pp. 653–664. DOI: 10.2118/8932-PA.

[168] N.R. Warpinski and L.W. Teufel. "Influence of Geologic Discontinuities on Hydraulic Fracture Propagation (Includes Associated Papers 17011 and 17074)". In: *Journal of Petroleum Technology* 39.02 (Feb. 1, 1987), pp. 209–220. DOI: 10.2118/13224-PA.

[169] S. Weihe, B. Kröplin, and R. De Borst. "Classification of Smeared Crack Models Based on Material and Structural Properties". In: *International Journal of Solids and Structures* 35.12 (Apr. 1998), pp. 1289–1308. DOI: 10.1016/S0020-7683(97)00104-2.

[170] M A Wheel. "A Geometrically Versatile Finite Volume Formulation for Plane Elastostatic Stress Analysis". In: *The Journal of Strain Analysis for Engineering Design* 31.2 (Mar. 1, 1996), pp. 111–116. DOI: 10.1243/03093247V312111.

[171] P. A. Witherspoon et al. "Validity of Cubic Law for Fluid Flow in a Deformable Rock Fracture". In: *Water Resources Research* 16.6 (Dec. 1980), pp. 1016–1024. DOI: 10.1029/WR016i006p01016.

[172] John Kam-Wing Wong. "Three-Dimensional Multi-Scale Hydraulic Fracturing Simulation in Heterogeneous Material Using Dual Lattice Model". In: (May 19, 2018). In collab. with Apollo-University Of Cambridge Repository, Apollo-University Of Cambridge Repository, and Kenichi Soga. DOI: 10.17863/CAM.17439.

[173] L.N.Y. Wong and H.H. Einstein. "Systematic Evaluation of Cracking Behavior in Specimens Containing Single Flaws under Uniaxial Compression". In: *International Journal of Rock Mechanics and Mining Sciences* 46.2 (Feb. 2009), pp. 239–249. DOI: 10.1016/j.ijrmms.2008.03.006.

[174] Teng-fong Wong and Patrick Baud. "The Brittle-Ductile Transition in Porous Rock: A Review". In: *Journal of Structural Geology* 44 (Nov. 2012), pp. 25–53. DOI: 10.1016/j.jsg.2012.07.010.

[175] Teng-fong Wong et al. "Microcrack Statistics, Weibull Distribution and Micromechanical Modeling of Compressive Failure in Rock". In: *Mechanics of Materials* 38.7 (July 2006), pp. 664–681. DOI: 10.1016/j.mechmat.2005.12.002.

[176] X.-P. Xu and A. Needleman. "Numerical Simulations of Fast Crack Growth in Brittle Solids". In: *Journal of the Mechanics and Physics of Solids* 42.9 (Sept. 1994), pp. 1397–1434. DOI: 10.1016/0022-5096(94)90003-5.

[177] Benyamin Yadali Jamaloei. "A Critical Review of Common Models in Hydraulic-Fracturing Simulation: A Practical Guide for Practitioners". In: *Theoretical and Applied Fracture Mechanics* 113 (June 2021), p. 102937. DOI: 10.1016/j.tafmec.2021.102937.

[178] Baicun Yang et al. "The Reasonable Range Limit of the Shape Parameter in the Weibull Distribution for Describing the Brittle Failure Behavior of Rocks". In: *Rock Mechanics and Rock Engineering* 54.6 (June 2021), pp. 3359–3367. DOI: 10.1007/s00603-021-02414-1.

[179] T. H. Yang et al. "Influence of Heterogeneity of Mechanical Properties on Hydraulic Fracturing in Permeable Rocks". In: *Rock Mechanics and Rock Engineering* 37.4 (Oct. 2004), pp. 251–275. DOI: 10.1007/s00603-003-0022-z.

[180] S. Ya. Yarema. "On the Contribution of G. R. Irwin to Fracture Mechanics". In: *Materials Science* 31.5 (1996), pp. 617–623. DOI: 10.1007/BF00558797.

[181] S.C. Yuan and J.P. Harrison. "A Review of the State of the Art in Modelling Progressive Mechanical Breakdown and Associated Fluid Flow in Intact Heterogeneous Rocks". In: *International Journal of Rock Mechanics and Mining Sciences* 43.7 (Oct. 2006), pp. 1001–1022. DOI: 10.1016/j.ijrmms.2006.03.004.

[182] Alan T. Zehnder. *Fracture Mechanics*. Lecture Notes in Applied and Computational Mechanics 62. London ; New York: Springer Science+Business Media, 2012. 223 pp. ISBN: 978-94-007-2594-2 978-94-007-2595-9.

[183] G.M. Zhang et al. "Three-Dimensional Finite Element Simulation and Parametric Study for Horizontal Well Hydraulic Fracture". In: *Journal of Petroleum Science and Engineering* 72.3-4 (June 2010), pp. 310–317. DOI: 10.1016/j.petrol.2010.03.032.

[184] Xiang-fei Zhang et al. "Numerical Simulation for Synergetic Deformation of Optical Fiber Sensor and Asphalt Mixture". In: *KSCE Journal of Civil Engineering* 23.7 (July 2019), pp. 3075–3087. DOI: 10.1007/s12205-019-2112-9.

[185] Zhennan Zhang et al. "A Hyperelastic-Bilinear Potential for Lattice Model with Fracture Energy Conservation". In: *Engineering Fracture Mechanics* 142 (July 2015), pp. 220–235. DOI: 10.1016/j.engfracmech.2015.06.006.

[186] Gao-Feng Zhao. "Modelling 3D Jointed Rock Masses Using a Lattice Spring Model". In: *International Journal of Rock Mechanics and Mining Sciences* 78 (Sept. 2015), pp. 79–90. DOI: 10.1016/j.ijrmms.2015.05.011.

[187] Gao-Feng Zhao, Jiannong Fang, and Jian Zhao. "A 3D Distinct Lattice Spring Model for Elasticity and Dynamic Failure". In: *International Journal for Numerical and Analytical Methods in Geomechanics* 35.8 (June 10, 2011), pp. 859–885. DOI: 10.1002/nag.930.

[188] GaoFeng Zhao and Nasser Khalili. "A Lattice Spring Model for Coupled Fluid Flow and Deformation Problems in Geomechanics". In: *Rock Mechanics and Rock Engineering* 45.5 (Sept. 2012), pp. 781–799. DOI: 10.1007/s00603-012-0291-5.

[189] Kaikai Zhao et al. "Investigating the Interaction of Hydraulic Fracture with Pre-Existing Joints Based on Lattice Spring Modeling". In: *Computers and Geotechnics* 122 (June 2020), p. 103534. DOI: 10.1016/j.compgeo.2020.103534.

[190] Jian Zhou, Yan Jin, and Mian Chen. "Experimental Investigation of Hydraulic Fracturing in Random Naturally Fractured Blocks". In: *International Journal of Rock Mechanics and Mining Sciences* 47.7 (Oct. 2010), pp. 1193–1199. DOI: 10.1016/j.ijrmms.2010.07.005.

[191] Jian Zhou et al. "Analysis of Fracture Propagation Behavior and Fracture Geometry Using a Tri-Axial Fracturing System in Naturally Fractured Reservoirs". In: *International Journal of Rock Mechanics and Mining Sciences* 45.7 (Oct. 2008), pp. 1143–1152. DOI: 10.1016/j.ijrmms.2008.01.001.

[192] Lei Zhou and Michael Z. Hou. "A New Numerical 3D-model for Simulation of Hydraulic Fracturing in Consideration of Hydro-Mechanical Coupling Effects". In: *International Journal of Rock Mechanics and Mining Sciences* 60 (June 2013), pp. 370–380. DOI: 10.1016/j.ijrmms.2013.01.006.

[193] J. M. Ziman. *Models of Disorder: The Theoretical Physics of Homogeneously Disordered Systems*. Cambridge [Eng.] ; New York: Cambridge University Press, 1979. 525 pp. ISBN: 978-0-521-21784-2 978-0-521-29280-1.

Appendix A

Local Stiffness Matrix

$$\boldsymbol{F} = \begin{bmatrix} \frac{AE}{l_e} & 0 & 0 \\ 0 & \frac{AG\kappa}{l_e} & 0 \\ 0 & 0 & \frac{AG\kappa}{l_e} \\ 0 & 0 & 0 \\ 0 & 0 & -\frac{AG\kappa}{2} \\ 0 & \frac{AG\kappa}{2} & 0 \\ -\frac{AE}{l_e} & 0 & 0 \\ 0 & -\frac{AG\kappa}{l_e} & 0 \\ 0 & 0 & -\frac{AG\kappa}{l_e} \\ 0 & 0 & 0 \\ 0 & 0 & -\frac{AG\kappa}{2} \\ 0 & \frac{AG\kappa}{2} & 0 \end{bmatrix} \tag{A.1}$$

$$\boldsymbol{H} = \begin{bmatrix} \frac{AE}{l_e} & 0 & 0 \\ 0 & \frac{AG\kappa}{l_e} & 0 \\ 0 & 0 & \frac{AG\kappa}{l_e} \end{bmatrix} + \begin{bmatrix} \frac{A\sigma_{y,u}^2\xi_u}{G'_{f,u}} e^{-\frac{\sigma_{y,u}}{G'_{f,u}}\xi_u} & 0 & 0 \\ 0 & \frac{A\sigma_{y,v}^2\xi_v}{G'_{f,v}} e^{-\frac{\sigma_{y,v}}{G'_{f,v}}\xi_v} & 0 \\ 0 & 0 & \frac{A\sigma_{y,w}^2\xi_w}{G'_{f,w}} e^{-\frac{\sigma_{y,w}}{G'_{f,w}}\xi_w} \end{bmatrix} \tag{A.2}$$

$$
\boldsymbol{K} = \begin{bmatrix}
\frac{AE}{l_e} & 0 & 0 & 0 & 0 & 0 & -\frac{AE}{l_e} & 0 & 0 & 0 & 0 & 0 \\
0 & \frac{AG\kappa}{l_e} & 0 & 0 & 0 & \frac{AG\kappa}{2} & 0 & -\frac{AG\kappa}{l_e} & 0 & 0 & 0 & \frac{AG\kappa}{2} \\
0 & 0 & \frac{AG\kappa}{l_e} & 0 & -\frac{AG\kappa}{2} & 0 & 0 & -\frac{AG\kappa}{l_e} & 0 & 0 & 0 & 0 \\
0 & 0 & 0 & \frac{GI_{pol}}{l_e} & 0 & 0 & 0 & 0 & -\frac{GI_{pol}}{l_e} & 0 & 0 & 0 \\
0 & 0 & -\frac{AG\kappa}{2} & 0 & \frac{AG\kappa l_e}{4} + \frac{EI_{11}}{l_e} & 0 & 0 & 0 & 0 & \frac{AG\kappa l_e}{4} - \frac{EI_{11}}{l_e} & 0 & 0 \\
0 & \frac{AG\kappa}{2} & 0 & 0 & 0 & \frac{AG\kappa l_e}{4} + \frac{EI_{22}}{l_e} & 0 & -\frac{AG\kappa}{2} & 0 & 0 & 0 & \frac{AG\kappa l_e}{4} - \frac{EI_{22}}{l_e} \\
-\frac{AE}{l_e} & 0 & 0 & 0 & 0 & 0 & \frac{AE}{l_e} & 0 & 0 & 0 & 0 & 0 \\
0 & -\frac{AG\kappa}{l_e} & 0 & 0 & 0 & -\frac{AG\kappa}{2} & 0 & \frac{AG\kappa}{l_e} & 0 & 0 & 0 & -\frac{AG\kappa}{2} \\
0 & 0 & -\frac{AG\kappa}{l_e} & 0 & \frac{AG\kappa}{2} & 0 & 0 & 0 & \frac{AG\kappa}{l_e} & 0 & 0 & 0 \\
0 & 0 & 0 & -\frac{GI_{pol}}{l_e} & 0 & 0 & 0 & 0 & \frac{GI_{pol}}{l_e} & 0 & 0 & 0 \\
0 & 0 & 0 & 0 & \frac{AG\kappa l_e}{4} - \frac{EI_{11}}{l_e} & 0 & 0 & 0 & 0 & \frac{AG\kappa l_e}{4} + \frac{EI_{11}}{l_e} & 0 & 0 \\
0 & \frac{AG\kappa}{2} & 0 & 0 & 0 & \frac{AG\kappa l_e}{4} - \frac{EI_{22}}{l_e} & 0 & -\frac{AG\kappa}{2} & 0 & 0 & 0 & \frac{AG\kappa l_e}{4} + \frac{EI_{22}}{l_e}
\end{bmatrix} \tag{A.3}
$$